Spring 2020

Role of Anisometric Particles in Ice-Templated Porous Ceramic Structure and Mechanical Properties

Mahesh Banda
Old Dominion University, bandamahesh25@gmail.com

ROLE OF ANISOMETRIC PARTICLES IN ICE-TEMPLATED POROUS CERAMIC STRUCTURE AND MECHANICAL PROPERTIES

by

Mahesh Banda
B. Tech. April 2012, Jawaharlal Nehru Technological University, India
M. Tech. July 2015, National Institute of Technology Warangal, India

A Dissertation Submitted to the Faculty of
Old Dominion University in Partial Fulfillment of the
Requirements for the Degree of

DOCTOR OF PHILOSOPHY

MECHANICAL ENGINEERING

OLD DOMINION UNIVERSITY
May 2020

Approved by:

Dipankar Ghosh (Director)

Abdelmageed Elmustafa (Member)

Xiaoyu Zhang (Member)

Oleksandr Kravchenko (Member)

Mileta Tomovic (Member)

ABSTRACT

ROLE OF ANISOMETRIC PARTICLES IN ICE-TEMPLATED POROUS CERAMIC STRUCTURE AND MECHANICAL PROPERTIES

Mahesh Banda
Old Dominion University, 2020
Director: Dr. Dipankar Ghosh

Open-cell macroporous ceramics have a significant impact on advancing various engineering endeavors such as bone-tissue engineering, lithium-ion batteries, filtration, thermal insulation, impact protection, etc. While pore orientation in conventional open-cell foams is random, in recent years, significant interest has grown in utilizing directionally porous ceramics in these applications to enhance performance. Ice-templating has emerged as a versatile technique that can synthesize directionally macroporous ceramics with low pore tortuosity. Although the fabrication is relatively straightforward, the challenge is that there are numerous variables associated with this technique, which can have significant effects on the final structure and macroscopic properties. As a result, understanding structure-property relationships in these materials is of continuing interest for the envisioned endeavors.

The central motivation of this dissertation is driven by understanding the role of particle size in tailoring ice-templated structure and compressive mechanical properties and address the underlying structure-mechanical property relationships. The notion for investigating particle size effects is that an increase in particle size can increase lamellar bridge density but without causing a considerable change in porosity. The proposed concept is that replacing a small volume fraction of fine particles with large particles provides a novel approach to tailor lamellar bridge density in ice-templated porous ceramics.

The results revealed that by inducing anisometric particles (ceramic platelets) within the equiaxed particles suspension led to dendritic microstructural development with increased lamellar bridging in ice-templated porous materials and thereby marked increase in the compressive mechanical properties. These platelet bridges offered resistance to the sideways deflection of the walls and contributed to the strength enhancement. Further, fine-equiaxed particles in the matrix phase packed more efficiently and offered better sinterability in the platelets-induced ice-templated porous ceramics; and showed enhanced mechanical properties than coarse-equiaxed matrix particles. Also, the mechanical properties of ice-templated porous ceramics are enhanced at high-strain rate regimes of loading. Finally, the porous ceramics containing platelets exhibited improved stability to structural deformation at higher temperatures compared to the materials without platelets. Thus, the findings of this dissertation can be helpful in tailoring the microstructure and mechanical properties of the ice-templated porous ceramics for structural and functional applications.

This dissertation is dedicated to my Teacher
who taught me the purpose of life and showed the path of perfection.

ACKNOWLEDGMENTS

First, I would like to thank my Ph.D. advisor Dr. Dipankar Ghosh who constantly guided me from the beginning of my journey towards doctoral study. I always revere his deep scientific knowledge, critical thinking, and exceptional scholarly skills. I am glad to have Dr. Ghosh as my adviser; any student could not wish for any better. Not only professionally, but also personally, he supported and advised me during my tough times. The discussions that we had during this dissertation led me to be a better researcher and a better person. Next, I thank my dissertation committee members for their valuable suggestions and critical review.

I would like to thank the chair of the Mechanical and Aerospace Engineering department of ODU, Dr. Sebastian Bawab, and staff for their help during this work. I would also like to appreciate the technical help of the Batten College Model Shop of ODU during the experiments. I also thank my colleagues at the Laboratory for Extreme and Energy Materials of ODU who helped me in several experiments and scientific discussions. You guys are great and it was fun working with you all.

I would like to acknowledge the encouragement and help by my Master's advisors Mr. Sairam K. and Dr. T.S.R.Ch. Murthy of Bhabha Atomic Research Center, Mumbai. They encouraged me to pursue a Ph.D. and referred me to Dr. Ghosh.

My life has not been molded to this shape without continuous direction, love, and support of my brother Late Mr. Ashok Banda. Whoever I am today is because of his training, motivation, and inspiration. I hope he is happy with my success and blesses me from his eternal position.

I am highly indebted to my parents without whose great sacrifice this wouldn't be possible. I have got these comforts at the expense of their sweat and blood. Although they do not have any formal education, they encouraged and supported me economically and morally to pursue higher studies.

I express my sincere thanks to Dr. Swadesh Kumar Singh by whose teachings I developed an interest in materials science. His explanations of fundamentals in materials science and mechanical engineering have laid a strong foundation upon which I am standing now. I would like to express my deepest gratitude to Mr. V. Anand who constantly supported me morally, despite my setbacks. I am also very much thankful to Mr. Harsh Pandya, Mr. Deepak Jain, Mr. Srinivasa Muktipaty, Mr. Subbu Garimella, Dr. Nagaraj Hegde and others who are like my family here in the United States. I would also thank my dearest friends Mr. N. Yugendher and Mr. Srinivasu Chadaram who constantly encouraged me to direct my energy in life on positivity.

Finally, I extend my gratitude to all those who directly or indirectly contributed to the success of this dissertation.

TABLE OF CONTENTS

Page

LIST OF FIGURES

Chapter 1

Figure Page

Chapter 2

Figure Page

Chapter 3

Figure Page

Chapter 4

Figure Page

Chapter 5

Figure Page

Chapter 6

Figure Page

Chapter 7

Figure Page

LIST OF TABLES

Chapter 5

Chapter 7

CHAPTER 1

ICE-TEMPLATED POROUS CERAMICS

1.1 Directionally porous materials

Ice-templated porous ceramics, as shown in Fig. 1, are a class of novel materials that exhibit unidirectional pore architecture [1-9]. Figure 1 (middle image) shows a schematic of an ice-templated ceramic sample and scanning electron microscope (SEM) images of vertical (left) and horizontal (right) cross-sections of the sample. In the SEM image of vertical cross-section, we can observe characteristic directional pores that run from bottom to top. Whereas, the SEM image of horizontal cross-section reveals parallel ceramic lamella walls, directional pores present between the walls, and lamellar bridges that connect the walls. Thus, ice-templated ceramics possess easily accessible pores with low tortuosity and exhibit high surface area [10]. The compressive strength of ice-templated ceramics along the ice-growth direction (described in the next section) is significantly higher compared to that of typical open-cell porous ceramics, which is another vital aspect of these materials [8].

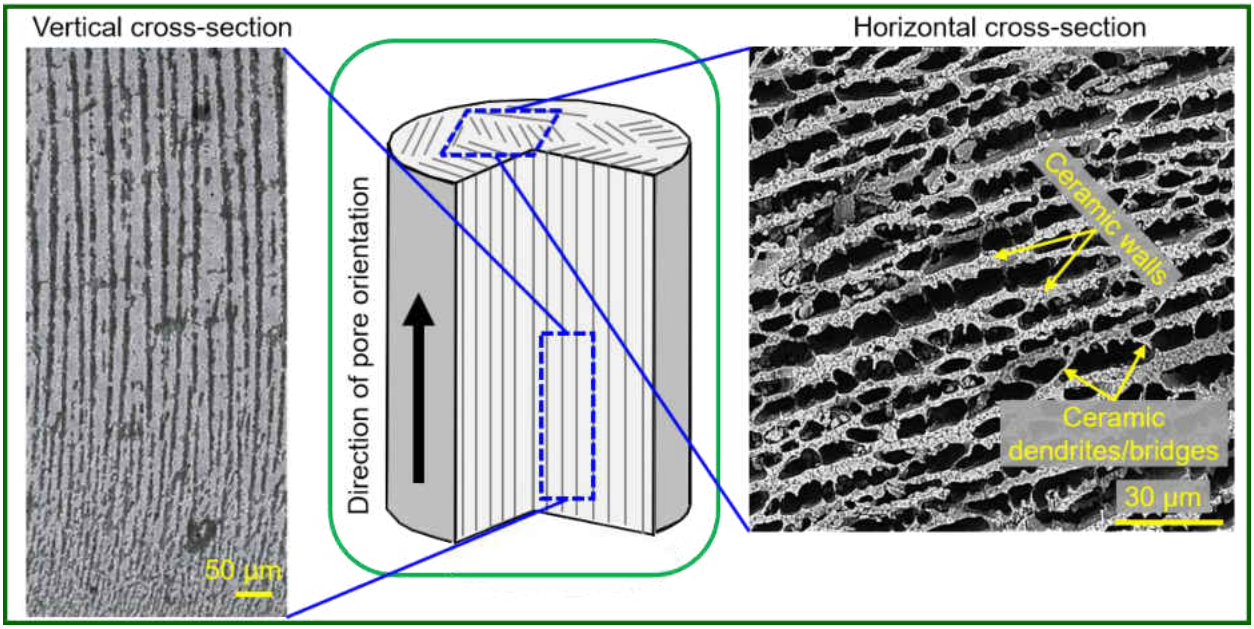

Figure 1: SEM images reveal vertical (left) and horizontal (right) cross-sections of an ice-templated sintered porous ceramic sample [8,9]. The middle picture is a schematic of an ice-templated porous sample.

Directional pore architecture offers several advantages in tissue engineering applications, such as slowing down the proliferation of cells due to the absence of pore interconnectivity and superior strength than their isotropic counterparts [11-17]. Filtration applications use porous materials; however, pore directionality can greatly enhance the performance of membranes by providing a combination of pressure drop and minimum resistance to fluid diffusion [18-21]. Anisotropic porous materials can also be advantageous for adsorption and depollution applications because they provide a combination of directional material properties, easily accessible pores, and high surface area [22-26]. Directionally porous solids can be infiltrated with a second phase to fabricate multilayered composites [7,27-29], which exhibit improved fracture resistance [7]. They are also potential candidate materials for applications such as electrochemical cells, batteries, capacitors,

supercapacitors, and solar cells [30-44]. Due to the strength and functional advantages, there has been a major interest in the development of directionally porous ice-templated ceramics and understanding structure-property relationships in these materials.

1.2 Growth velocity of ice crystals and particle rejection vs. entrapment

Freeze-casting is a novel technique to develop directional porous ceramics [10,45,46]. Initially, the freeze casting technique gained interest in fabricating complex-shaped ceramic components by freezing ceramic suspensions containing fine particles [47-50]. However, the interest in freeze-casting to develop directionally porous ceramic materials grew significantly after the work of Fukasawa et al. [1-4]. They showed the fabrication of ceramics with oriented pores by controlling the growth direction of ice crystals in a water-based ceramic suspension. Apart from water, other commonly used freezing vehicles to develop directionally porous materials are tetra-butyl alcohol (TBA) [51-54], camphene [55-60], and dioxane [61-65]. Thus, a fascinating aspect of freeze-casting is that variations in the shape and growth kinetics of different solvent crystals allow developing directionally porous freeze-cast ceramics with different pore morphologies (Fig. 2). For example, the growth of lamella ice crystals at moderate freezing rates results in lamellar pore morphology in the final sample, Fig. 2a [67]. On the other hand, TBA crystals grow in a hexagonal prismatic shape and result in hexagonal pore architecture in the final material, Fig. 2b [66]. Whereas camphene solvent results in interconnected circular pores and the impressions of overgrown solid camphene dendrites in the final ice-templated structure as shown in Fig. 2c.

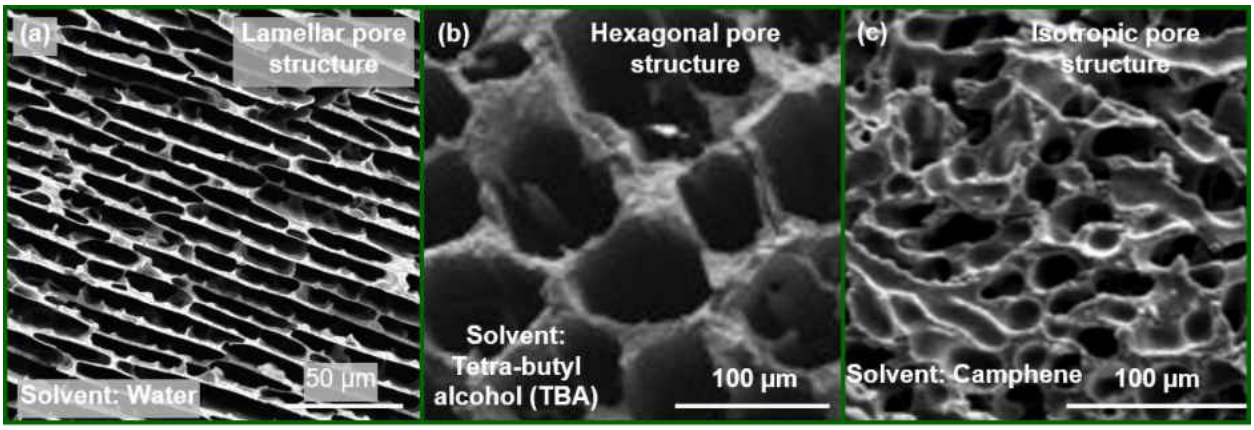

Figure 2: SEM images of freeze-cast ceramics showing (a) lamellar pore structure by using water as a solvent, (b) approximately hexagonal pore structure by using tetra-butyl alcohol (TBA) as a solvent [66], and (c) isotropic pore morphology by using camphene as a solvent [67].

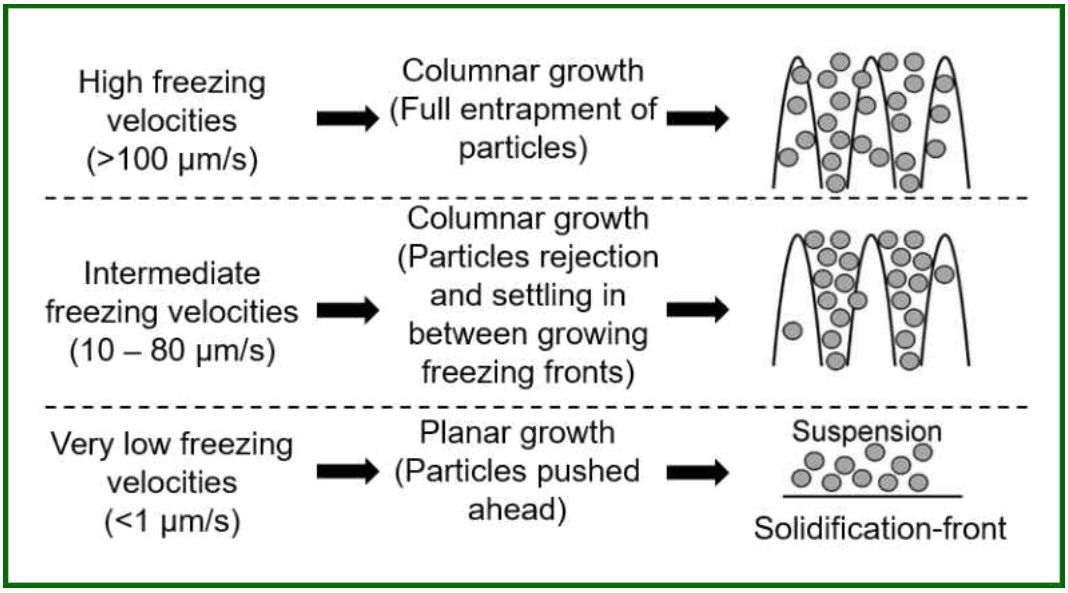

Figure 3: Schematics showing the variation of shape of ice crystals with growth velocity and the effects of the velocity of solidification front on particle rejection vs. particle entrapment by solvent crystals [68].

Water, however, remains as the predominantly employed freezing vehicle because of the abundance and being environment-friendly [10,69]. We commonly refer to freeze-casting as ice-templating when water is the freezing vehicle [10,45,46]. The unique ability of the freeze-casting technique to produce both dense and porous ceramics is inherently rooted in the velocity and stability of advancing freezing front. Figure 3 shows several schematics that depict the variation of shape of ice crystals with growth velocity and the effects of the velocity of freezing-front on particle rejection vs. particle entrapment by solvent crystals. At very low velocity (< 1 μm/s), the ice front moves as a planar front. The planar growth of solvent crystals pushes the particles ahead of the freezing front where the particles accumulate [10]. We can utilize this mechanism of ice growth for the fabrication of dense (non-porous) ceramic materials [70]. As the growth velocity of ice crystals increases (intermediate-range, 10 – 80 μm/s), the thermodynamic equilibrium of a suspension is perturbed. That is, a phenomenon called constitutional supercooling (explained in a later section) of the liquid occurs in front of the freezing front. This phenomenon destabilizes the planar freezing front that finally leads to columnar growth of freezing front [10,68]. As this process continues, it forms alternate layers of ice crystals and ceramics particles. Removal of the solvent crystals later creates a directional porous ceramic structure [10,46,68]. At the very high ice growth velocities, due to the less time available for rejection, the particles are engulfed more in the ice crystals [10,68].

1.3 Ice-templating technique

Figure 4 shows the four principal steps of the ice-templating technique. In this technique, the first step is to prepare a stable aqueous ceramic suspension. Typically, the use of dispersant increases repulsive forces between particles and prevents the settling of particles during the templating process [10]. The use of water-soluble additive enhances the strength of green samples (before sintering) and enables safe handling. The next and most critical step is templating that occurs during unidirectional solidification of suspension. During this stage, the ice crystals grow in the direction of the applied unidirectional temperature gradient. Ceramic particles rejected by the moving ice crystals (also referred to as solidification front) accumulate between growing crystals [68,71]. At the end of the unidirectional freezing process, we obtain a solidified suspension which contains alternate layers of ice crystals and ceramic particles with both oriented in the direction of the applied temperature gradient. In the next step, ice removal from the frozen samples through sublimation (freeze-drying at low pressure and temperature) results in a macroporous green sample. The final porous structure is a replica of ice crystals [10,68,71]. The last step is the sintering of freeze-dried green bodies that imparts strength to the structure but retains pore morphology.

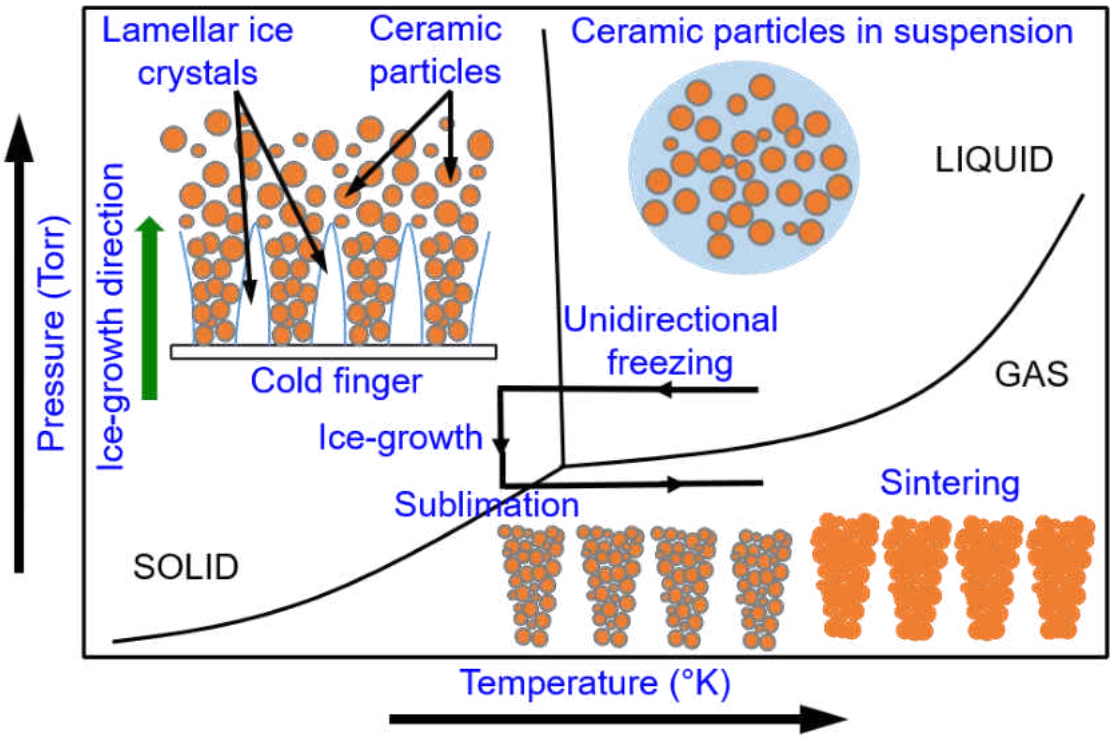

Figure 4: A schematic representation of four principal stages in the ice-templating technique [71].

Here, we briefly discuss the growth characteristics of ice crystals and the origin of the lamellar morphology that typically develops in ice-templated porous ceramics. Figure 5a is a schematic representation of a hexagonal ice crystal and shows the preferred growth direction (along *a*-axis) and limited growth direction (along the *c*-axis). The growth of ice crystals is approximately 10^2 to 10^3 times faster along the crystallographic *a*-axis compared to that along *c*-axis [71,72]. For the growth of ice crystals along the *c*-axis, it requires four molecules from the liquid phase to form six bonds to the growing ice layer along the *c*-axis. On the other hand, it requires only two molecules to form the same bond ratio and attach to the growing ice front along the *a*-axes. Since the probability of the formation of a two-molecular group is energetically more favorable compared to a four-molecular group, the growth rates of ice crystals along the *a*-axes are markedly higher

than along the *c*-axis [72]. As a result, the growth of ice crystals is highly anisotropic, and ice crystals grow in lamellar fashion. By applying a unidirectional temperature gradient, it is possible to align the lamellar ice crystals in the direction of the applied gradient. The preferred growth characteristics of ice crystals and their alignment along an applied temperature gradient form the basis of lamellar morphology that develops in ice-templated porous materials. During unidirectional freezing of aqueous ceramic suspensions, ceramic particles accumulate in between the growing ice lamellae and develop ceramic lamellae. Upon freeze-drying, the spaces occupied by the ice lamellae turn into directional pores and porous ceramic with lamellar morphology results. Figure 5b shows highly lamellar morphology in ice-templated sintered porous Al_2O_3 ceramic in which elongated pores formed due to the rapid growth of ice crystals along the basal plane (*a*-axes). However, with the increase in ice crystal growth velocity, the propensity of entrapment of ceramic particles within the growing ice-crystals also increases. Followed by the sublimation and sintering, the entrapped particles can develop lamellar bridges that connect the adjacent lamella walls in the direction transverse to the growth direction of ice crystals, Fig. 5c [10].

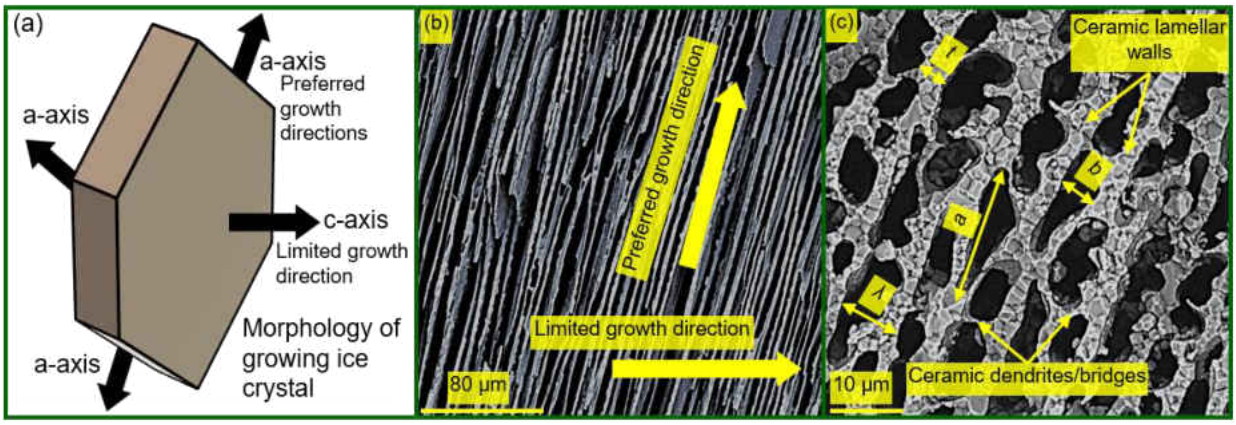

Figure 5: (a) A schematic of a hexagonal ice crystal that shows both preferred growth direction (along *a*-axis) and limited growth direction (along *c*-axis) [71]; (b) A representative SEM image of the vertical cross-section of an ice-templated ceramic revealing highly lamellar morphology in ice-templated sintered porous Al_2O_3 ceramic; (c) A representative SEM micrograph of the horizontal cross-section in an ice-templated sintered porous Al_2O_3 ceramic revealing various microstructural features.

1.4 The physics of ice-templating

As it is discussed in the previous sections, the ice front velocity and the interactions between particle-ice front play a crucial role in the microstructure evolution in ice-templated ceramics. Thus, it is imperative to study the interaction between particle-ice front to understand the role of various parameters to fine-tune the microstructure of these porous materials. The schematic in Fig. 6 shows two spherical particles of radius R suspended in water, and an ice front (also referred to as freezing front or solidification front) that moves at a velocity v (also referred to as freezing front velocity, FFV) from bottom to top (the direction of applied unidirectional temperature gradient). Particle A is far away from the moving ice front to have any interaction with the ice front. Whereas,

particle B is at a distance d (of the order of average intermolecular distance in the liquid film present between the solidification front and particle) to the solidification front that is close enough to have interactions with the solvent crystals [73,74]. For solidification of a liquid containing insoluble foreign particles (such as ceramic particles in water), the interaction between the solidification front and particles can occur in one of three distinct modes: (i) the front may push the particle indefinitely and segregate it in the last-freezing liquid, (ii) the front may engulf a particle instantaneously upon contact, or (iii) the front may engulf the particle after pushing it over some distance. The first scenario corresponds to a very slow freezing front velocity and is useful in the fabrication of dense materials employing the freeze-casting technique [47,68,73]. On the other hand, rejection of particles is desirable in the ice-templating technique to achieve the characteristic directional pore architecture [10,68,73]. However, some level of particle engulfment is necessary as well to allow the formation of lamellar bridges, which aid to enhance the strength of templated porous materials [10,68,69,73]. Therefore, the ice-templating technique encounters both particle rejection and particle entrapment phenomena, and several factors contribute to the underlying mechanisms. Also, note that these are mutually competitive mechanisms since a particle will either be rejected or engulfed. In the following, we will discuss two approaches to understand particle rejection vs. particle entrapment.

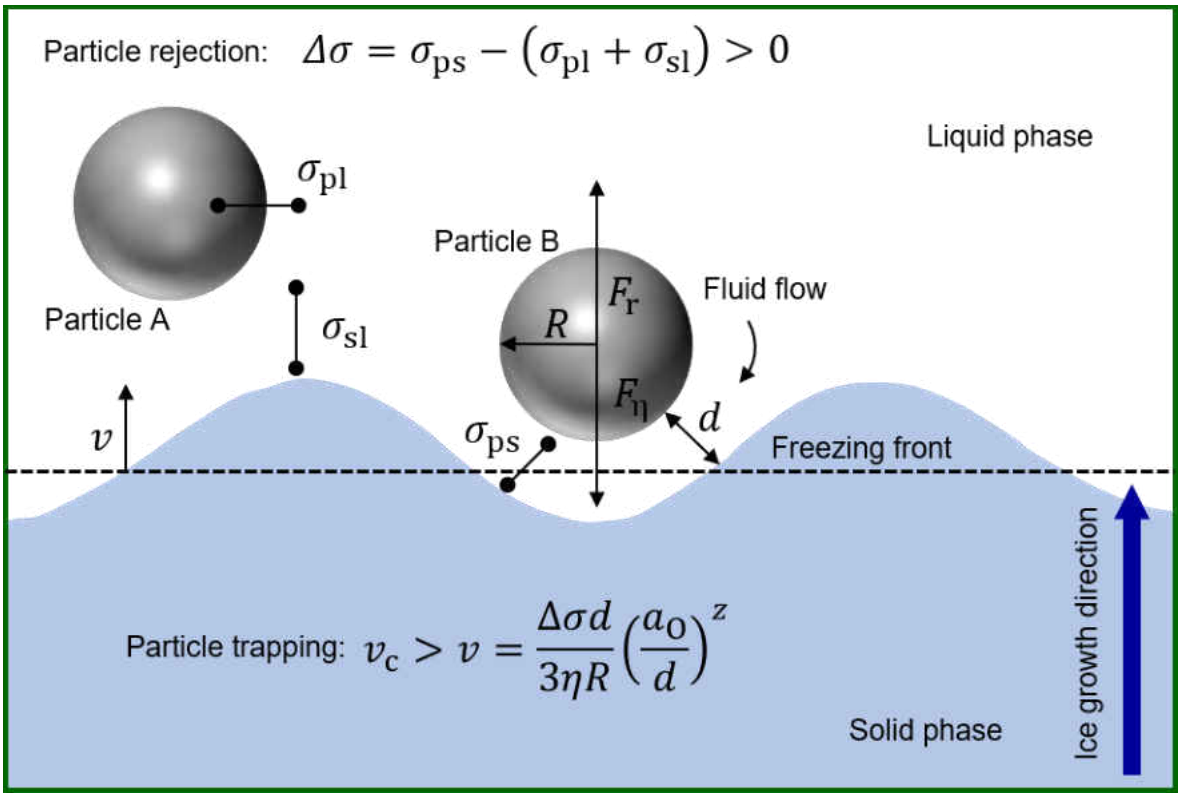

Figure 6: Schematic representation of various interactions that possibly occur between solid-liquid interface and material particle in a suspension during the ice-templating process [74].

First, we try to comprehend the process of particle rejection vs. particle entrapment from a thermodynamic viewpoint (i.e., based on energy balance). As shown in Fig. 6, there are three surface free energy terms (σ_{pl}, σ_{sl}, and σ_{ps}) associated with three interfaces, which are critical in particle-solidification front interactions [68,73,74]. σ_{pl} corresponds to surface energy due to particle-liquid interface in a liquid medium containing particles. σ_{sl} is the surface free energy associated with the solid (ice)-liquid interface that originates during solidification of liquid. The third surface free energy term σ_{ps} is due to the solid (ice)-particle interface and will result only from the engulfment of the particle by the ice crystal. To encapsulate the particle, the solidification

front must bend and create a solid-particle interface at the expense of other interfaces [10,73,74]. Thus, the engulfment of a particle suspended in a liquid by a freezing front requires replacement of two interfaces (particle-liquid and liquid-solid) by a single interface (solid-particle). However, the process of interface substitution must be energetically favorable for the engulfment of particles to be spontaneous [10,68,73,74]. Figure 7 shows a schematic of the anticipated variation in total surface free energy ($\Delta\sigma$) with particle-solid separation distance (d). We can express the variation using a power law form as [73-81]:

$$\Delta\sigma = \Delta\sigma_0 \left(\frac{a_0}{d}\right)^z. \qquad (1)$$

Here, a_0 is the minimum possible separation between particle and solid (average intermolecular distance in the liquid film between the solidification front and particle) and $\Delta\sigma_0$ is surface free energy at this minimum distance, also referred to as the free energy of adhesion [73]. z is a constant and typically can range between 4-5 [74]. It is understandable from equation (1) that change in $\Delta\sigma$ is insignificant at a very large value of d ($\gg a_0$, i.e., no interaction between solidification front and particle). As d decreases $\Delta\sigma$ becomes appreciable and approaches $\Delta\sigma_0$. For the solidification front to push the particle ahead (i.e., particle rejection), a layer of liquid of thickness at least a_0 must always be present between the particle and the advancing ice front [73,74].

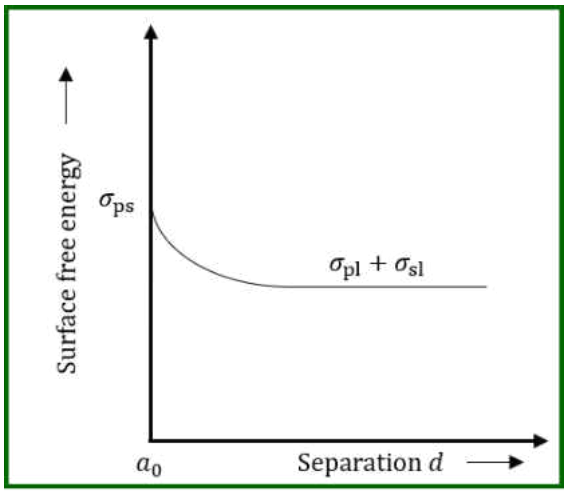

Figure 7: Schematic showing the variation in surface energy with respect to particle-solid separation [73,80].

At any instant, away from the solidification front ($d \gg a_0$,), ($\sigma_{pl} + \sigma_{sl}$) represents the total surface free energy ($\Delta\sigma$) of a liquid medium that contains an insoluble particle (Fig. 7). As we mentioned before, engulfment of a particle by the solidification front (for which particle is at a distance $d \leq a_0$) will result in the formation of a new interface (solid-particle) at the expense of two interfaces (particle-liquid and liquid-solid). However, particle engulfment can only occur if the process is energetically favorable and we can write the necessary thermodynamic condition for engulfment as [73,74,78,79]:

$$\Delta\sigma_0 = \sigma_{ps} - (\sigma_{pl} + \sigma_{sl}) < 0. \qquad (2)$$

Here, we replaced $\Delta\sigma$ by $\Delta\sigma_0$ which is the surface free energy at $d \sim a_0$. Whereas, for $\Delta\sigma_0 > 0$, the solidification front will reject the particle. This thermodynamic model is reasonable for the prediction of critical particle size for rejection vs. entrapment at very low freezing velocities and in the absence of any force being applied to the particle [68]. However, the main shortcoming of

this oversimplified thermodynamic model is the lack of consideration of the forces that act on a particle in liquid during the solidification process [10,73].

Here, we discuss a force criteria-based approach for particle rejection and engulfment, which considers all the forces that act on a particle facing a solidification front. In a simplified approach, there are three forces that act on a particle in front of an advancing solid-liquid interface: thermomolecular force, cryosuction (or drag) force, and gravity force [10]. The thermomolecular force (F_{t} or F_{r}) considers all the potential electromagnetic forces that govern the interactions between the interface and the particle and includes Van der Waals forces as well [73]. F_{r} is generally a repulsive force and, therefore, repels the particle from the solidification front and decreases very rapidly as d increases. The pushing of a particle away from the solidification front by F_{r} arises from the need to maintain a stable liquid film between the particle and solidification front, which will prevent contact with the front and particle engulfment. We can express the repulsive force as [74,75,78,79]:

$$F_{\mathrm{r}} = 2\pi R \Delta\sigma_0 \left(\frac{a_0}{d}\right)^z. \qquad (3)$$

For crystal growth, a constant flux of liquid is necessary to supply solvent molecules from the suspension toward the solid-liquid interface and, particularly, between the particle and the interface [74]. This flux of liquid attracts the particle by generating a viscous drag toward the interface. Thus, the viscous drag by the fluid on a particle during solidification front-particle interactions is an attractive force (F_{η}) that compresses the particle toward the front during growth and favors engulfment [10,73]. Larger particles will experience a greater viscous drag compared to finer particles and hence the propensity for engulfment will increase as particle size increases [73]. Also, with increasing viscosity, viscous drag forces on particles increase [76,78]. For a

particle moving very close to a solidification front, the standard Stokes' equation for the drag force is no longer valid as the solidification front perturbs the flow of liquid [78]. According to Carrier [77], we can express the drag force for the case of a flat interface as:

$$F_{\eta} = \frac{6\pi\eta v R^2}{d}, \qquad (4)$$

where η denotes the viscosity of the suspension. Another force is gravity force (F_{g}); however, F_{g} is negligible with particles in the colloidal size range [10]. Therefore, during the solidification of a liquid containing insoluble particles, the repulsive forces accelerate a particle ahead of the advancing solidification front when the width of the gap between the two becomes comparable to the size of the zone of strong interactions [73]. However, the viscous drag on the particle balances this repulsive interaction. From the balance of the attractive force (F_{η}) and repulsive force (F_{r}), and by neglecting F_{g}, we can derive a critical freezing front velocity (v_{cr}) above which solidification front will completely engulf particles as [74,75,78]:

$$v_{\mathrm{cr}} = \frac{\Delta\sigma_0 d}{3\eta R}\left(\frac{a_0}{d}\right)^{z}. \qquad (5)$$

According to equation (5), v_{cr} is inversely proportional to particle radius. The main problem with equation (5) is the determination of correct values for d and η and the uncertainty of experimental values for $\Delta\sigma_0$ [10]. However, we can use equation (5) to qualitatively describe the role of particle size in particle rejection vs. entrapment. According to equation (5), solvent crystals will completely engulf particles for FFV greater than v_{cr}. We can also state that as FFV increases and approaches v_{cr} of a system, the propensity of particle engulfment will also increase. Whereas, solidification velocity well below of v_{cr} will promote particle rejection. These statements are in excellent agreement with the observation that for an aqueous ceramic suspension of given suspension, ice-

templating at low FFVs results in the formation of a lamellar structure due to favorable conditions for particle rejection [68,82]. Whereas an increase in FFV leads to the development of dendritic structure due to the increased propensity for particle engulfment [68,82]. Rejected particles accumulate between the growing ice crystals and form lamella walls, whereas entrapped particles lead to the formation of lamellar bridges (Fig. 8). Thus, FFV has a dominant role in the evolution of ice-templated microstructure.

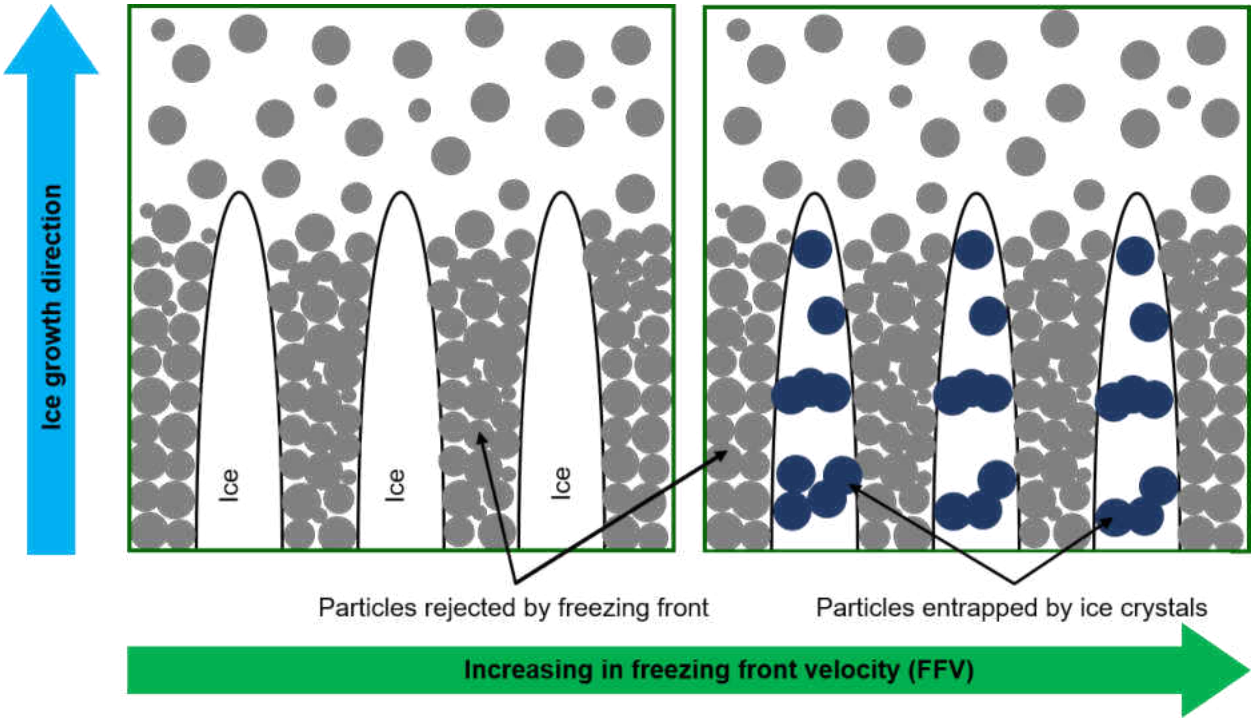

Figure 8: Schematic representation of particle rejection or entrapment within the ice crystals with variation in FFV.

From the above discussion, we can now form a fundamental basis to test particle size effects in the development of ice-templated microstructure, which is the crux of this dissertation. According to

equation (5), v_{cr} is inversely related to R. Thus, the presence of large particles (i.e., large R) in an aqueous ceramic suspension will lower v_{cr} of the system and vice-versa. We can interpret that for the same unidirectional solidification condition applied to ceramic suspensions of different particle size but same concentration, as particle size increases the same FFV will get closer to the v_{cr} of the system. As a result, we can use particle size as a critical tool to tune microstructure, morphology, and macroscopic mechanical properties of ice-templated porous materials. For the same solid loading of ceramic suspensions and applied unidirectional temperature gradient, a decrease and increase in particle size will promote lamellar structure (favorable condition for particle rejection and lamella wall formation) and dendritic structure (favorable condition for particle engulfment and lamellar bridge formation), respectively. In other words, we can utilize particle size effects to tailor lamellar bridge density in ice-templated ceramics. However, it is also important to consider that increase in particle size will reduce particle packing within lamella walls during the templating stage and sinterability, which will have detrimental effects on strength. It is of note that there are studies on the influence of several parameters such as freezing agent, suspension additives, FFV and solids loading on ice-templated microstructure and mechanical properties [10,82,83]. However, the effects of particle size on processing-structure-property relationships are less emphasized.

1.5 Use of ceramic platelets (anisotropic particles) in the development of ice-templated ceramics

Ice-templated ceramics are typically fabricated from aqueous suspensions of fine, equiaxed particles (~ 1 μm) [74]. One advantage of using fine ceramic particles is that they improve the

sinterability of resultant materials [68,82]. We propose a novel approach in which we will replace a small volume fraction of fine, equiaxed ceramic particles in aqueous suspension with large particles. The rationale is that the solidification front will reject small particles and the rejected particles will develop lamella walls. Whereas, larger particles will preferentially be engulfed by the solidification front and result in the formation of lamellar bridges. By varying the ratio of small to large particles, we can further tailor lamellar bridge density in ice-templated ceramics. Another significant advantage is that the preferential presence of finer particles within lamella walls will facilitate sintering in the walls and with the large particles and can offset the potential detrimental effects of large particles on sintering. Before proceeding further with the research hypothesis, in the following paragraph, we discuss the selection of morphology of large ceramic particles.

Ceramic particles are available in various morphologies such as equiaxed (most common), flakes, whiskers, and platelets [10]. Among those, platelets are of a class of anisometric particles which have been extensively used in ceramic processing [84-90]. Figure 9 shows an SEM image, revealing the morphology of Al_2O_3 platelets. Typically, the diameter (or width) of platelets is much greater than the thickness. Production and processing of ceramic platelet particles are relatively simple compared to other types of particle morphologies [91]. Ceramic platelets are crystalline, oxidation resistant, and can be mass-produced with consistent morphologies [91]. Also, the flexural strength of a single platelet particle is substantially greater than the particles of other morphologies such as fibers and whiskers [91]. Platelets have been intensively used for templated grain growth (TGG) in a fine-grain ceramic matrix for texture development and enhancement of stiffness and strength [92-98]. Studies have also shown sintering compatibility between fine ceramic particles and large ceramic platelets [87]. There are few studies that have utilized ceramic platelets in the development of ice-templated porous materials [99-101]. These studies suggest that

during the freezing process platelets can self-assemble within lamella walls [99-101]. However, there is no study on ice-templated ceramics that are processed from the combination of equiaxed and platelet-shaped particles. Therefore, to take advantage of the above-mentioned characteristics and ease of commercial availability, this dissertation selects Al_2O_3 platelets (anisometric particles) as large particles and seeks to understand their role in the synthesis of ice-templated porous ceramics.

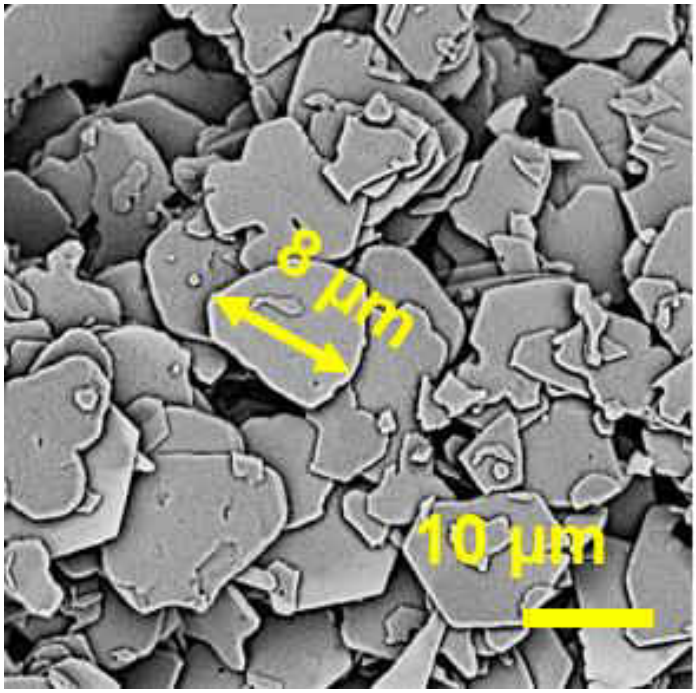

Figure 9: An SEM micrograph revealing the morphology of Al_2O_3 platelets.

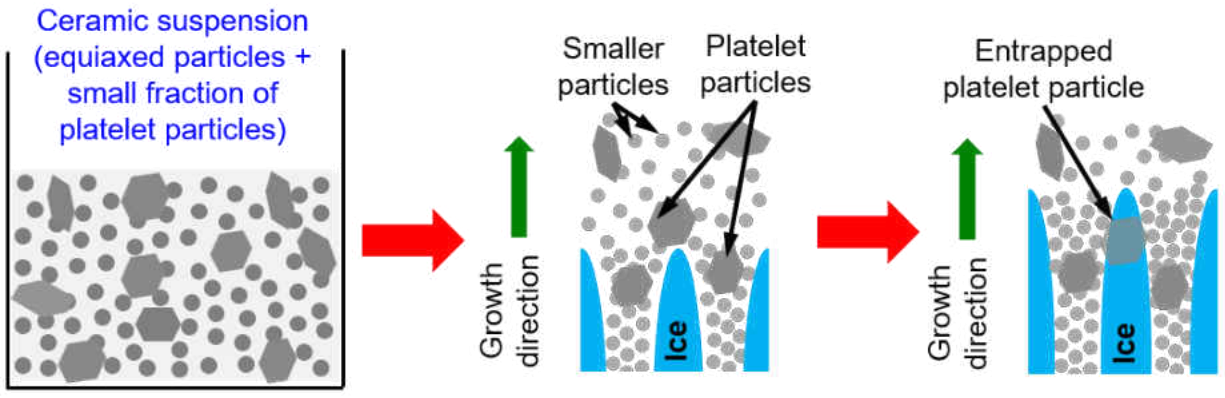

Figure 10: Schematic representation of the role of platelets in microstructural evolution during the ice-templating process.

Figure 10 schematically illustrates the research hypothesis, based on the development of ice-templated porous ceramics using fine ceramic particles and ceramic platelets. This dissertation uses fine, equiaxed Al_2O_3 particles and large Al_2O_3 platelets as model materials; however, the proposed research concept is readily available to other oxide and non-oxide ceramics. Let us consider ice-templating of an aqueous ceramic suspension that contains mainly fine, equiaxed particles and a small volume fraction of platelets (particles. Recall from equation (5) that larger diameter particles are more prone to entrapped by the growing ice crystals. Therefore, based on the previous discussion, during ice-templating, equiaxed particles will exhibit a greater propensity for rejection by the solidification front, whereas ceramic platelets will have a greater propensity for engulfment by the growing ice crystals. Due to the superior mechanical properties of platelets, we anticipate that the trapped platelets can lead to the formation of strong lamellar bridges between the adjacent ceramic walls and enable significant strength enhancement. As mentioned before, the development of ice-templated ceramics from aqueous suspensions containing only platelets revealed that platelet particles self-assemble within lamella walls [99-102]. Therefore, we suggest

that two competing mechanisms can be operative during the ice-templating process: one is the engulfment of platelets by ice crystals that lead to lamellar bridge formation and the other is the self-assembly of platelets within the ceramic matrix of lamella walls. The presence of platelets in the matrix of fine ceramic particles of lamella walls can also enhance the strength of walls and thus of ice-templated ceramics. We hypothesize that by varying the ratio of small particles to platelets and other variables such as FFV and concentration of ceramic suspension, we can control the underlying effects of these two mechanisms on the development of ice-templated ceramics and their macroscopic mechanical properties.

1.6 Research objectives

In this dissertation, we will address the following research questions.

As discussed in the above section, it is important to explore which factor, between platelets self-assembly and entrapment, does dominate during the ice-templating process and how the microstructure develops. It is also known that the FFV significantly influences microstructural evolution in ice-templated ceramics. Therefore, it can be interesting to understand the combined effects of platelets and FFV on the microstructure development and mechanical property relationships in these porous ceramics. A few works of the literature showed that using a larger size, equiaxed ceramic particles in the suspension promotes more particle entrapment that results in dendritic morphology, but micropores also appear in lamella walls due to the poor packing efficiency of larger size particles. Whereas the fine, equiaxed particles are easy to be rejected by growing ice crystals that result in lamellar pore structure with dense lamella walls. Adding platelets to these two ceramic suspensions systems may affect the particle packing during ice-templating

and the densification during sintering. Thus, it can be exciting to study how microstructural development occurs by varying the matrix particle size in the suspension. Another important consideration is that the interactions of these matrix particles with platelets at different sintering temperatures. Since the lamella walls of ice-templated porous ceramics are at micrometer length scales, it is crucial to understand how the temperature effects the lamella wall microstructure, compressive strength and structural stability of these pore architectures. The compressive response of porous materials majorly depends on total porosity, constituent material, pore architecture, and strain rate. Studies revealed that closed-cell aluminum porous materials show strain rate sensitivity but contrastingly, the open cell porous aluminum materials show no rate sensitivity. However, there is no study available on the strain rate sensitivity on porous ceramics. Since ice-templated ceramics can potentially be used in impact protection applications, it is important to study their compressive mechanical behavior at high-strain rate loading regimes and their rate sensitivity. Thus, the research objectives of this dissertation are as follows:

1. Explore the effects of platelets' content and FFV on the microstructural evolution.
2. Investigate the effects of matrix material particle size along with the variation of platelets' content and FFV on the microstructural evolution.
3. Characterize the uniaxial compressive response of these novel porous ceramics both in the quasistatic and dynamic regime of loading conditions.
4. Probe the damage evolution and fracture characteristics in these porous ceramics both in quasistatic and high-strain rate loading regimes of loading.
5. Investigate the effects of temperature on matrix-platelets interactions and the structural stability of these platelets induced porous ceramic materials.
6. Develop structure-property (mechanical) relationships.

The rest of the dissertation is structured as follows. In Chapter 2, investigation of the effects of replacing a small fraction of equiaxed particles with the platelet-shaped particles in the aqueous ceramic suspension and FFV on the microstructural evolution and mechanical properties in ice-templated porous ceramics are presented. Next, the role of the size of equiaxed particles (matrix particles) in the aqueous suspensions containing a mixture of equiaxed particles and platelets are discussed in Chapter 3. Fracture mechanisms within the lamella walls of platelets-induced ice-templated ceramic materials under quasistatic uniaxial compressive loading conditions are discussed in Chapter 4. Then, the effects of strain rate on the uniaxial compressive response of ice-templated porous ceramics containing no platelets and containing platelets are discussed in Chapter 5 and Chapter 6, respectively. Later, the effects of temperature and platelets on the microstructural development and structural stability of ice-templated porous ceramics are discussed in Chapter 7. Finally, in Chapter 8 conclusions and directions for future research are outlined.

CHAPTER 2

INFLUENCE OF ANISOMETRIC PARTICLES (PLATELETS) ON THE MICROSTRUCTURE AND UNIAXIAL COMPRESSIVE RESPONSE OF ICE-TEMPLATED SINTERED ALUMINA CERAMICS

Note: The contents of this chapter have been published in Acta Materialia.

D. Ghosh. H. Kang, M. Banda, V. Kamaha, Influence of anisotropic grains (platelets) on the microstructure and uniaxial compressive response of ice-templated sintered alumina scaffolds, Acta Mater., 125 (2017) 1 – 14.

DOI: https://doi.org/10.1016/j.actamat.2016.11.047

Abstract:

Ice-templated ceramics have unique lamellar pore morphology that offers better compressive mechanical properties in comparison to the typical ceramic foams with isotropic pore morphology. However, for very high-level porosity (>65 vol.%) strength difference diminishes. This investigation reveals that by inducing anisotropic grains within the matrix of a fine-grained ceramic, uniaxial compressive response of the ice-templated sintered scaffolds can be markedly enhanced without causing any considerable modification of the total porosity. To address this innovative materials design strategy, we synthesized a series of microstructures by systematically varying the anisotropic grains content in an aqueous suspension and the freezing kinetics to investigate the process-microstructure correlations and understand the structure-property relationships. Microstructural investigations revealed the unique arrangements of the platelets within and out of the lamella walls, where the upward moving ice fronts aligned the platelets' in-plane direction to the ice-growth direction. In the low freezing front velocity regime, platelets were

observed to be mainly within the lamella walls, whereas platelets started to develop lamellar bridges with the increasing velocity. As a result, a transition of the pore morphology occurred with the increasing platelets content and the freezing front velocity. A novel method based on the rigorous microstructural analysis is developed to estimate the distribution of the platelets within and out of the walls and the variation of the platelets distribution with the composition and freezing front velocity. A drastic improvement of the compressive mechanical properties (stiffness, strength, energy absorption capacity) response was measured due to the platelets' addition, which has been related to the platelets' distribution within and out of the walls and the pore morphology modifications. Results are rationalized based on the role of the platelets during the compressive deformation.

Keywords: Ice-templating, Grain-level anisotropy, Intralamella and interlamellar platelets, Pore morphology, Lamellar bridging, Compressive response, Energy absorption.

2.1 Introduction

Macroporous ceramic scaffolds with an oriented pore morphology and low pore tortuosity are an emerging class of materials that are promising for bone-tissue engineering, solid-state battery electrodes, solid oxide fuel cells, and impact energy-absorption. While the conventional ceramic foaming techniques yield isotropic pore morphology, freeze casting (also called ice-templating) is one technique that can synthesize ceramic scaffolds with oriented pores [7,8,83,102-105]. Structure-property (mechanical in particular) relationships of the ice-templated ceramics are not well understood, however, a limited number of studies suggest that relative density, lamellar bridge density, pore size, and lamella wall thickness are influencing factors to the uniaxial compressive

response [7,8,102,83,104-106]. Relative density (thus total porosity) depends on the solids loading of a suspension, whereas the bridge density, pore size and wall thickness can be manipulated by exploiting the solids loading and the unidirectional freezing kinetics. Very little, however, is known about the influence of the anisotropic grains (e.g., ceramic platelets) on the compressive response of the ice-templated sintered ceramic scaffolds. Hunger et al. [99,107] showed that presence of large spherical or platelet Al_2O_3 particles in chitosan-alumina (Al_2O_3) freeze-cast porous composites reduced the lamella wall porosity and thereby improved the overall mechanical performance. However, there is no study that addresses the grain anisotropy effects on the mechanical response of the ice-templated sintered scaffolds containing only the ceramic phase. To that end, the authors recently reported that Al_2O_3 platelets (diameter ~8 μm thickness ~400 nm) drastically improved compressive stiffness and fracture strength of the ice-templated highly porous (~80 vol.%) sintered Al_2O_3 scaffolds that were mainly comprised of the equiaxed fine grains (1-3 μm) [108]. However, to develop the process-structure-property (mechanical) correlations of the newly developed novel platelets-reinforced ice-templated sintered porous scaffolds, it is imperative to conduct a study that systematically investigates the combined effects of the platelets content and the freezing kinetics, and addresses the interlinks in between the microstructural parameters and the mechanical response.

During an ice-templating process, particles are ejected by the upward moving ice fronts (under the influence of a unidirectional temperature gradient) and accumulate in between the growing ice lamellae [8]. Presence of large anisotropic platelets in an aqueous suspension containing mainly equiaxed fine particles and variation of the platelets fraction are expected to affect the particle packing during the freeze casting and the densification during sintering. This is because while a small amount of platelets in a matrix of equiaxed fine particles can improve the packing fraction

and densification, both may deteriorate with the increasing platelets concentration. It is thus possible that strength of the sintered scaffolds may go through a maximum. Another consideration is that pore morphology of the ice-templated scaffolds gradually transitions from lamellar to dendritic to isotropic structure with the increasing particle size [68,82]. Since, lamellar bridge density and pore size increases and decreases, respectively, with the transition of the pore architecture from lamellar to dendritic to isotropic, strength of the scaffolds is expected to increase with the increasing particle size [82]. Therefore, increasing the fraction of the large platelets in a suspension containing fine equiaxed particles may cause a pore morphology transition from lamellar to dendritic/isotropic, resulting in a strength improvement. Moreover, freezing kinetics significantly influence the microstructure and mechanical response of the ice-templated scaffolds. Therefore, there could be competing factors that evolve with the change of the anisotropic grains (platelets) concentration and freezing kinetics and can influence the compressive response.

Therefore, this work synthesized ice-templated sintered porous Al_2O_3 scaffolds from the equiaxed fine particles as well as from the mixtures of the equiaxed fine and large platelet particles. Microstructural evolution was characterized as a function of the anisotropic grains content and the freezing front velocity (FFV). And the observed changes of the relative density and microstructure were linked to the measured uniaxial compressive mechanical response to understand the effects of the grain-level anisotropy on the structure-property (mechanical) relationships.

2.2 Experimental

2.2.1 Materials and aqueous ceramic suspension preparation

Ice-templated scaffolds were processed from the commercially available fine equiaxed Al_2O_3 powder (~0.9 μm, Alfa Aesar, Ward Hill, MA) and large Al_2O_3 platelets (diameter ~8 μm and

thickness ~400 nm, Alusion^{TM}, Antaria Ltd., Bentley, Western Australia); referred to here as SA and PA, respectively. All the scaffolds were processed from aqueous suspensions with 15 vol.% Al_2O_3 content. However, within the 15 vol.% of total Al_2O_3 content, proportion of the SA and PA was varied and scaffolds were synthesized from five different compositions: (i) SA (0 vol.% PA), (ii) SA-2.5PA (2.5 vol.% PA), (iii) SA-5PA (5 vol.% PA), (iv) SA-10PA (10 vol.% PA), and (v) SA-20PA (20 vol.% PA). Here, PA content is presented with respect to the total Al_2O_3 content.

2.2.2 Unidirectional freeze casting and sintering

A custom-made device was employed to conduct the unidirectional ice-templating experiments [82]. In this device, by adjusting the gap in between the cold-finger and the liquid N_2 (L-N_2) surface unidirectional thermal gradient and thus the FFV are controlled, where the FFV increases with the decreasing gap. Distance in between the cold finger and the L-N_2 surface was kept fixed during a freeze casting experiment. However, the gap was varied from scaffold to scaffold to change the average FFV. Minimum and maximum gaps used were 1 mm and 30 mm, respectively. Ice-templated Al_2O_3 scaffolds were processed within an FFV (average) range of ~10-35 $\mu m/s$. For each experiment, an average FFV is estimated by dividing the height of a frozen sample with the time required for completion of solidification of the suspension. Samples were next freeze-dried at a low pressure 0.014 mbar and temperature -50°C for 96 hours and sintered at 1550°C for 4 h.

2.2.3 Microstructure characterization, density measurements and uniaxial compression testing

Although the sintered scaffolds were about 16.5 mm in diameter and of 39 mm height, a small sample was extracted from each scaffold (Fig. S1) for the microstructural characterization, density

measurement, and compression test. For the microstructural characterization, a transverse plane (top plane) of each specimen was utilized (Fig. S1). Sintered density of each specimen (ρ^*) was determined from the mass and dimensions. Relative density (ρ_r) was estimated using $\rho_r = \rho^*/\rho_s$, where ρ_s is the bulk density of α-Al_2O_3 (3.96 g/cm^3). Total porosity was estimated using $p_t = (1 - \rho_r) \times 100$. A Tinius Olsen (model 10ST) mechanical testing machine equipped with a 5 kN load cell was employed to conduct the uniaxial compression experiments using a displacement rate of 0.5 mm/min. More details of the experiments are available in the Supplementary material.

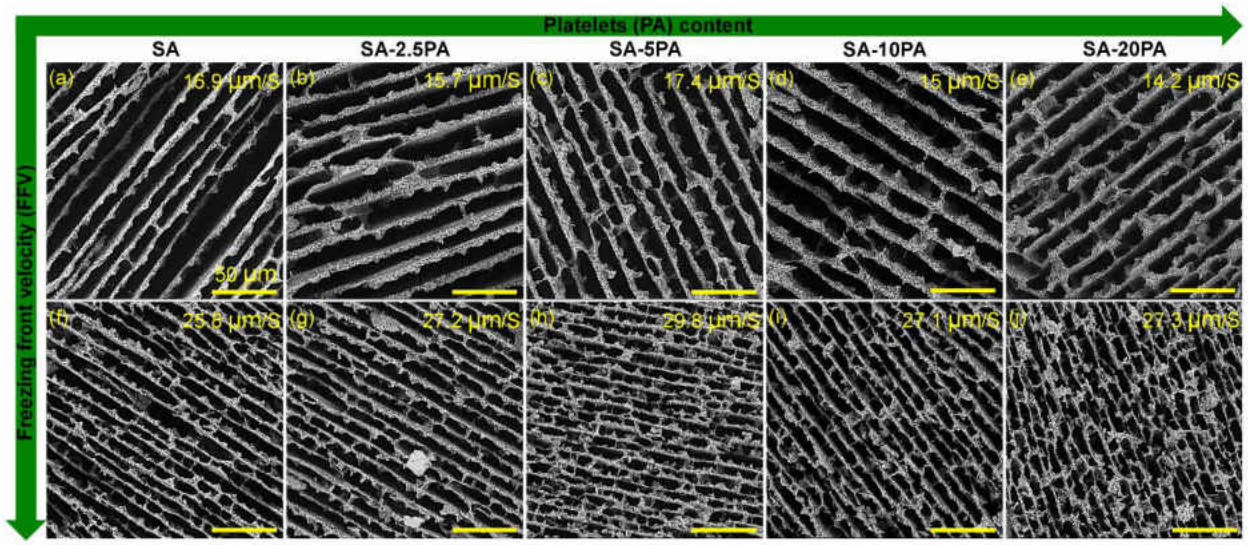

Figure 1: SEM micrographs revealing microstructures of the ice-templated sintered Al2O3 scaffolds without (SA) and with (SA-2.5PA, SA-5PA, SA-10PA, SA-20PA) platelets at relatively low FFV (a through e) and relatively high FFV (f through j). Length of the scale bar is 50 µm and ice growth direction is out of the page.

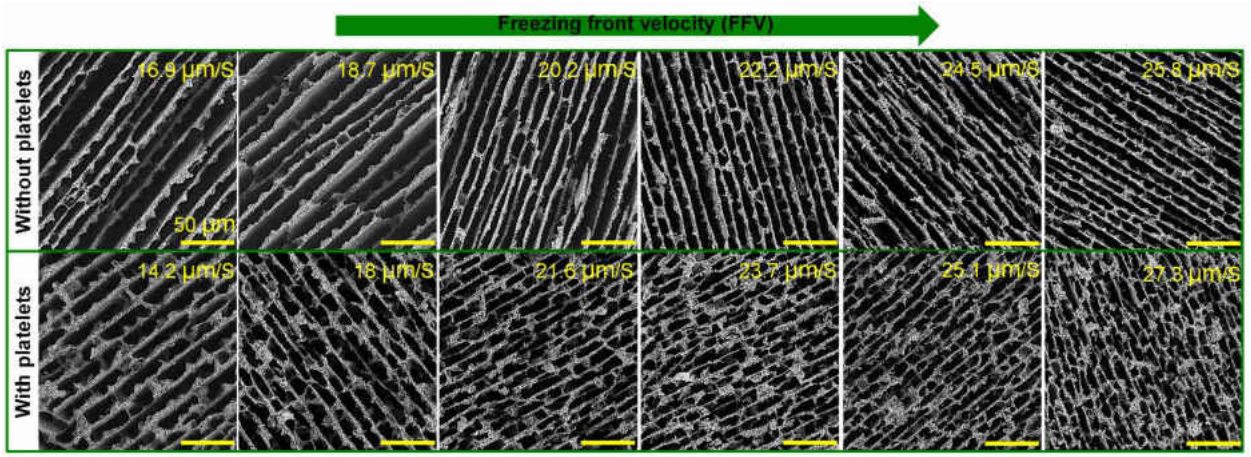

Figure 2: Progressive microstructure evolution with the increasing FFV of the SA (top SEM micrographs) and SA-20PA scaffolds (bottom SEM micrographs). Length of the scale bar is 50 µm and ice growth direction is out of the page.

2.3 Results

2.3.1 Microstructure evolution with platelets content and freezing front velocity

Figure 1 shows the representative microstructures of all the sintered porous scaffolds at relatively low and high FFVs, where each SEM micrograph corresponds to the transverse plane (top plane) located at a height of 9 mm from the bottom of a sintered cylindrical scaffold (Fig. S1). Figure S2a and S2b reveal microstructures of the top plane (located at 9 mm from the bottom) and bottom plane (located at 5 mm from the bottom), respectively, of a specimen extracted from the sintered SA scaffold processed at a relatively low FFV (16.9 µm/s). Both planes exhibit comparable microstructures, suggesting negligible microstructural variations within a distance of 4 mm along the ice-growth direction. Therefore, the SEM micrographs corresponding to the top planes (Fig. 1) can be considered as the representative of the overall microstructures of the small rectangular specimens, utilized for the density measurements and uniaxial compression tests. For all the

compositions, pore morphology of the sintered scaffolds at low FFVs could be considered as lamellar. However, at high FFVs pore morphology of the scaffolds appears to be dendritic due to the increased lamellar bridges. Moreover, extent of the lamellar bridging at high FFVs also appears to increase with the PA content. Figures 2a and 2b show the microstructural variations of the SA and SA-20PA, respectively, with the FFV. Progressive increase of the lamellar bridging with the increasing FFV can be observed. Furthermore, Fig. 2 reveals that at a comparable FFV pore morphology of the SA-20PA appears to be less lamellar in comparison to the SA. Figure 2 thus supports that with the increasing FFV, pore morphology transitions from lamellar to dendritic and lamellar bridging is enhanced to a greater extent due to the platelets. Similar changes with the FFV are also observed for other scaffolds compositions (not shown here).

High magnification SEM micrographs (Fig. 3) reveal several interesting microstructural features that are observed only for the scaffolds containing the platelets. For the SA-2.5PA (Figs. 3a and 3b) processed at a relatively high FFV (27.2 μm/s), platelets are distinctly visible in between the lamellae (i.e., interlamella platelets shown by the orange arrows) forming the lamellar bridges. Platelets within lamellae (i.e., intralamella platelets shown by the green arrows) can also be observed for both the SA-2.5PA (Figs. 3a and 3b) and SA-10PA scaffolds (Fig. 3c, 17.5 μm/s). Therefore, lamellar bridges of the SA scaffolds developed through the equiaxed grains, whereas for the other scaffolds (SA-2.5PA, SA-5PA, SA-10PA and SA-20PA) a fraction of the bridges formed through the large anisotropic grains (i.e., interlamella platelets) and usually a single platelet connected the adjacent lamellae. In the relatively low FFV regime platelets are observed to be located primarily within the lamellae (Fig. 3c). While the majority of the intralamella platelets and interlamella platelets are observed to be mutually perpendicular, overall platelets' in-plane direction is observed to be orientated parallel to the ice-growth direction. It is known that

unidirectional ice-templating process can self-assemble large anisotropic particles and orient those particles along the crystal growth direction [99,100]. Therefore, during ice-templating Al_2O_3 platelets ejected by the advancing ice fronts accumulated in between the ice (lamellae) crystals and were aligned by the growing ice crystals, resulting in intralamella platelets' in-plane direction almost parallel to the walls. Whereas, some platelets probably were trapped within the ice crystals, where the mechanism of ice tip-splitting and subsequent tip-healing [7] resulted in the bridge formation through the interlamella platelets. More specifically, an upward moving ice front can come across a platelet in the suspension and the platelet can get trapped, rather than being ejected, within the ice crystal by an ice-tip splitting process [7]. Moreover, splitted ice fronts continue to grow upward on both sides of the entrapped platelet and can orient the platelet's in-plane direction to the ice-growth direction. The splitted ice-fronts eventually cross the length of the platelet and combine together to a single ice front, which is referred here as the ice-tip healing. As a result, the interlamella platelets' in-plane direction became almost vertical with respect to the adjacent lamellae. As the freezing kinetics slowed down, frequency of platelets ejection by the ice fronts increases and more platelets accumulated in between the growing ice (lamellae) crystals. Moreover, with the decreasing FFV lamellae spacing became greater that the platelet diameter and thus at lower FFVs bridge formation through the platelets was negligible.

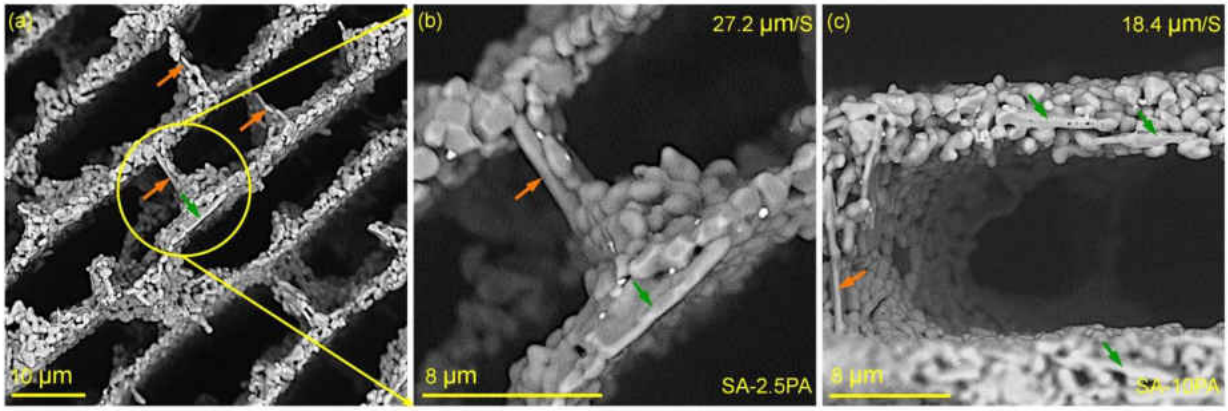

Figure 3: Microstructure investigation at higher magnification reveals (a – b) interlamella platelets (indicated by orange arrows) in a SA-2.5PA scaffold processed at a relatively high FFV (27.2 µm/s) and (c) intralamella platelets (indicated by green arrows) in a SA-10PA scaffold processed at a relatively low FFV (18.4 µm/s). Ice growth direction is out of the page. (For interpretation of the references to color in this figure legend, the reader is referred to the web version of this article).

2.3.2 Variation of relative density and lamella thickness and interlamellae spacing

Figure 4a shows variation of the ρ_r of the sintered scaffolds with the FFV. Dotted lines in Fig. 4a and in all other plots only represent the apparent trends, but not the actual trend lines. Due to a significant scatter of the ρ_r values of the SA scaffolds it is difficult to predict a trend, although the ρ_r values are observed to be higher in the high FFV regime relative to the low FFV regime. Interestingly, for the other compositions scatter of the ρ_r is marginal and trends are relatively apparent, however, a caution is to be made due to the limited number of the data. Both the SA-2.5PA and SA-5PA exhibit an approximate linear increase of the ρ_r with the increasing FFV, whereas ρ_r of the SA-10PA and SA-20PA remains almost unchanged. Figure 4a also indicates that ρ_r of the scaffolds increases with the PA content up to 5 vol.%, but further increase of the platelets

causes a decrease of the ρ_r. To better reveal the composition dependence of ρ_r, Fig. 4b presents variation of the average relative density ($\rho_{r(avg)}$) and average total porosity ($p_{t(avg)}$) with the PA content. Here, $\rho_{r(avg)}$ and $p_{t(avg)}$ of each composition were estimated from all the ρ_r and p_t values, respectively, over the entire range of the FFV of that specific composition. For the SA scaffolds, the $\rho_{r(avg)}$ and $p_{t(avg)}$ are approximately 0.19 and 81 vol.%, respectively. Interestingly, $\rho_{r(avg)}$ and $p_{t(avg)}$ increase and decrease, respectively, with the increasing PA content and reach a maximum and minimum, respectively, at 5 vol.% PA. With a further increase of the PA content, $\rho_{r(avg)}$ and $p_{t(avg)}$ start to decrease and increase, respectively. For the SA-20PA, $\rho_{r(avg)}$ and $p_{t(avg)}$ are observed to be slightly lower and higher in comparison to that of the SA scaffolds. Nevertheless, variation of both the $\rho_{r(avg)}$ and $p_{t(avg)}$ as a function of the platelets concentration is not drastic, and $p_{t(avg)}$ values of the sintered scaffolds are observed to be within a narrow range of ~79-82 vol.%.

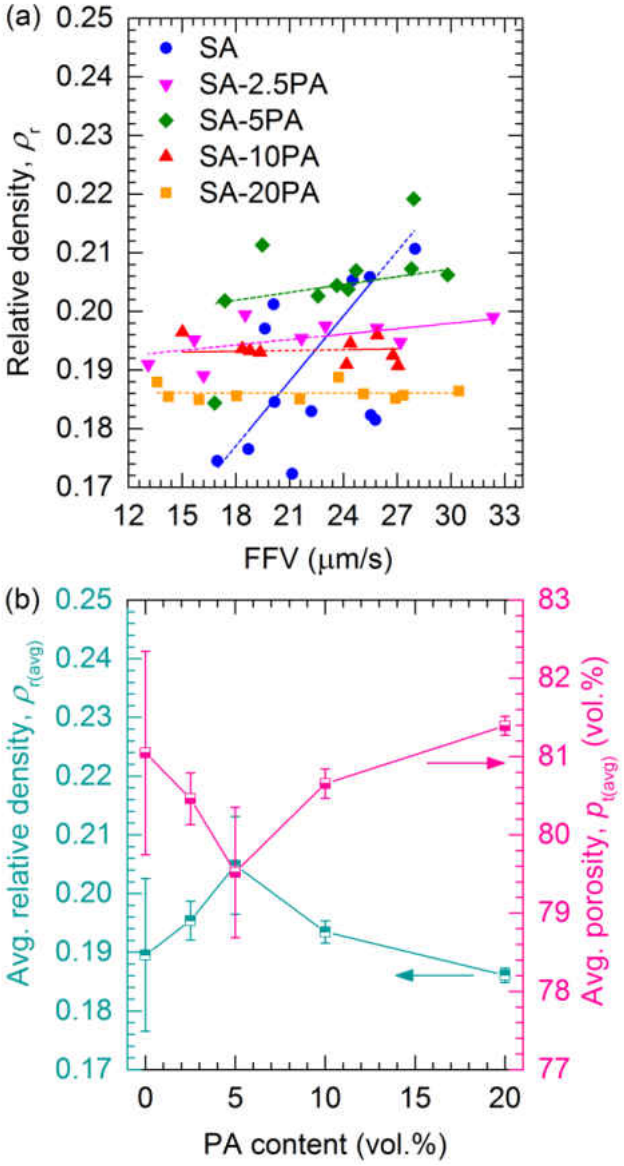

Figure 4: Variation of (a) relative density (ρ_r) with FFV and (b) average relative density ($\rho_{r(avg)}$) and average total porosity ($p_{t(avg)}$) with platelets (PA) content.

In general, increase of the ρ_r with the FFV of the SA, SA-2.5PA and SA-5PA scaffolds can be attributed to the increase of the lamellar bridges with the FFV [82,103]. Mass transport during sintering is influenced by the radius of curvature of the solid-vapor interface and density of the sintered porous scaffolds increases with a decrease of the pore radius of curvature [103,109]. As

mentioned previously, pore morphology tends to transition from lamellar to dendritic with the increasing FFV. Since, dendritic pores have a relatively smaller radius of curvature in comparison to the lamellar pores, density of the sintered SA, SA-2.5PA and SA-5PA scaffolds increases with the increasing FFV. As will be shown latter (Fig. 6), at comparable FFVs bridge density increases from SA to SA-2.5PA to SA-5. Due to the increasing bridging, pore morphology becomes increasingly less lamellar, which can cause an increase of the ρ_{r} and $\rho_{\mathrm{r(avg)}}$ from SA to SA-2.5PA to SA-5PA. Interestingly, for the SA-10PA and SA-20PA scaffolds ρ_{r} remains almost unchanged over the entire range of the FFV (Fig. 4a), although microstructural observations indicate significant transition of the pore morphology. Also, as mentioned previously, both the ρ_{r} and $\rho_{\mathrm{r(avg)}}$ values are observed to decrease from SA-5PA to SA-10PA to SA-20PA. It is possible that there are competing factors that govern the ρ_{r}, particularly at higher FFV. With a continuing increase of the extent of the lamellar bridging with the increasing PA content and FFV, pore morphology becomes progressively more dendritic from SA-5PA to SA-10PA to SA-20PA. While this would tend to increase the ρ_{r} with the FFV and PA content, particle packing fraction can deteriorate due to the increasing platelets content, which would tend to decrease the ρ_{r}. It is, therefore, possible that due to these competing factors ρ_{r} probably did not change with FFV for the SA-10PA and SA-20PA. Observed decrease of ρ_{r} and $\rho_{\mathrm{r(avg)}}$ from SA-10PA to SA-20PA could be due to the continued deterioration of the particle packing fraction with the increasing PA content.

Figures 5a and 5b show variation of the t and λ with the FFV (for clarity error bars are not shown), whereas Fig. 5c shows variation of the t_{avg} and λ_{avg} (for each composition averaged over the entire range of the FFV) with the PA content. Both the t and μ decrease with the increasing FFV.

However, for a given FFV t and λ values are observed to be comparable for all the compositions. Figure 5c also shows that the t_{avg} and λ_{avg} values of all the compositions are comparable.

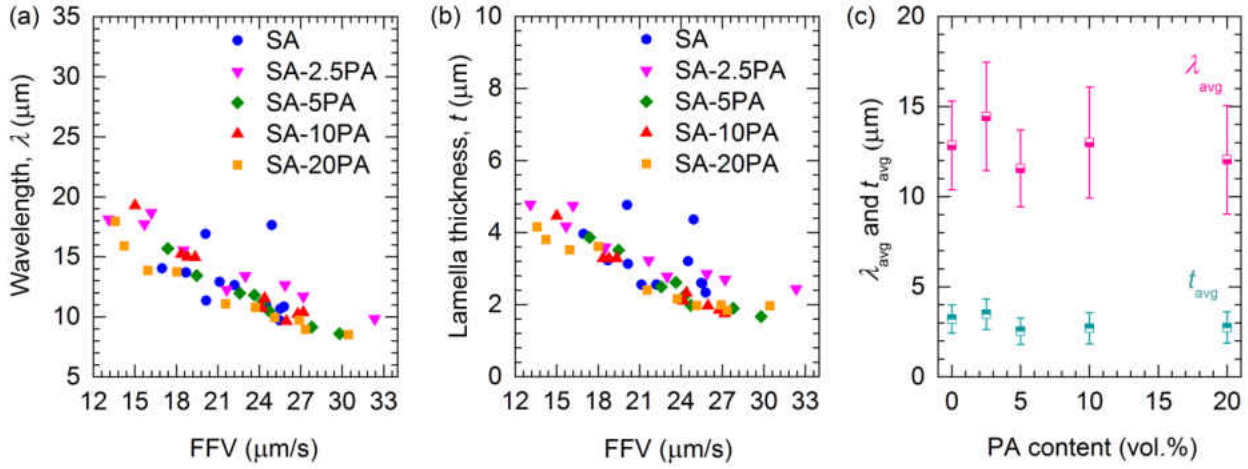

Figure 5: Variation of the (a) wavelength (λ) with FFV, (b) lamella thickness (t) with FFV, and (c) average wavelength (λ_{avg}) and average thickness (t_{avg}) with platelets (PA) content of the ice-templated Al_2O_3 scaffolds.

2.3.3 Estimation of bridge density and ratio of interlamella vs. intralamella platelets

Bridge density (ρ_b) is defined as the number of bridges present in between the adjacent lamellae walls per unit area [5,14]. Since, lamellar spacing is inversely related to the FFV, number of the bridges within a given area will inevitably increase with the increasing FFV and may cause an overestimation of the ρ_b. Naglieri et al. [103] defined a dimensionless morphological parameter (m)

$$m = \frac{1}{\rho_b \lambda^2} \quad (1)$$

to describe the pore morphology of the freeze-cast sintered silicon carbide (SiC) ceramic scaffolds, where m gradually decreases with a pore morphology transition from lamellar to dendritic to isotropic structures. Due to normalized by λ^2, variation of m may be considered as a better representative of the structural modifications. Nevertheless, we have utilized here both ρ_b and m to characterize the microstructural evolution. For all the compositions ρ_b increases exponentially with the FFV (Fig. 6a). It can be observed that within a comparable range of FFV, both the SA and SA-2.5PA scaffolds exhibit similar ρ_b values as a function of the FFV. ρ_b of the SA-5PA and SA-10PA scaffolds as a function of the FFV is also observed to be comparable, however, moderately greater relative to that of the SA and SA-2.5PA. With a further increase of the PA content to 20 vol.%, ρ_b of the SA-20PA scaffolds exhibits a considerable increase in the low FFV regime, however, in the high FFV regime ρ_b approaches that of the SA-5PA and SA-10PA. Overall, ρ_b increased exponentially from low FFV regime to high FFV regime by about 5 times or higher depending on the composition and also increased with the increasing PA content.

Figure 6b reveals that the morphological parameter m decreases gradually with both the FFV and PA content. However, m values for all the compositions tend to converge in the high FFV regime. Moreover, except SA-20PA, all other compositions exhibit a significant decrease of the m with the increasing FFV. Naglieri et al. [103] suggested that for freeze-cast sintered SiC scaffolds pore morphology is lamellar for $m > 5$, dendritic for $1 < m < 5$, and isotropic for $m < 1$. Ice-templating is a physical process and variation of the ceramic systems (e.g., SiC vs. Al_2O_3) is expected to have limited impact on the overall pore morphology. Therefore, Fig. 6b supports the microstructural observations that with the increasing FFV and PA content pore morphology progressively transitions from lamellar to dendritic structure. Also, at comparable FFVs pore morphology becomes progressively less lamellar with the increasing PA content. As a result, extent of the

structural modifications, in terms of the pore morphology transition, becomes less drastic as the PA content increased. For example, for the SA scaffolds m decreased from about 13 to 4, which suggests pore morphology transitioned from highly lamellar in the low FFV regime to dendritic structure in the high FFV regime. In contrast, a decrease of the m from 5 to 3 for the SA-20PA scaffolds indicates that pore architecture remained primarily dendritic over the entire FFV range, however, dendritic nature perhaps increased to some extent with the increasing FFV.

FFV is one factor that influences the lamellar bridge formation phenomenon, because increase of the FFV promotes particles entrapment within the ice crystals and thus lamellar bridging [82,83,103,105]. As a result, ρ_{b} and m typically increases and decreases, respectively, with the increasing FFV, which is also observed in Fig. 6. However, gradual increase and decrease of the ρ_{b} and m, respectively, with the increasing PA content also suggest a governing role of the platelets in the bridge development. Recall that Fig. 3 provides an evidence of the lamellar bridging through the platelets and a possible mechanism is discussed in Section 3.1. Governing role of the platelets in the bridge formation can be addressed based on the particle size effects. There exists a critical FFV (v_{c}) above which particles get engulfed by the ice crystals and is expressed as [74,103]

$$v_{\mathrm{c}} = \frac{\Delta\sigma d}{3\eta R}\left(\frac{a_{\mathrm{O}}}{d}\right)^{z}, \tag{2}$$

where $\Delta\sigma$ is the mean free energy of a particle, a_{O} is the average intermolecular distance in the liquid film between the particle and the solid front, d is the overall thickness of this film, η is the slurry viscosity, R is the particle radius, and z is an exponent that can vary from 1 to 5. Since, magnitude of v_{c} decreases with an increasing R, at comparable FFVs increase of the particle size promotes particle engulfment and lamellar bridging. As a result, for a comparable suspension concentration and FFV, ρ_{b} and m are expected to gradually increase and decrease, respectively,

with the increasing particle size and/or with the increasing fraction of the large particles in a suspension [82], which is also observed in Fig. 6.

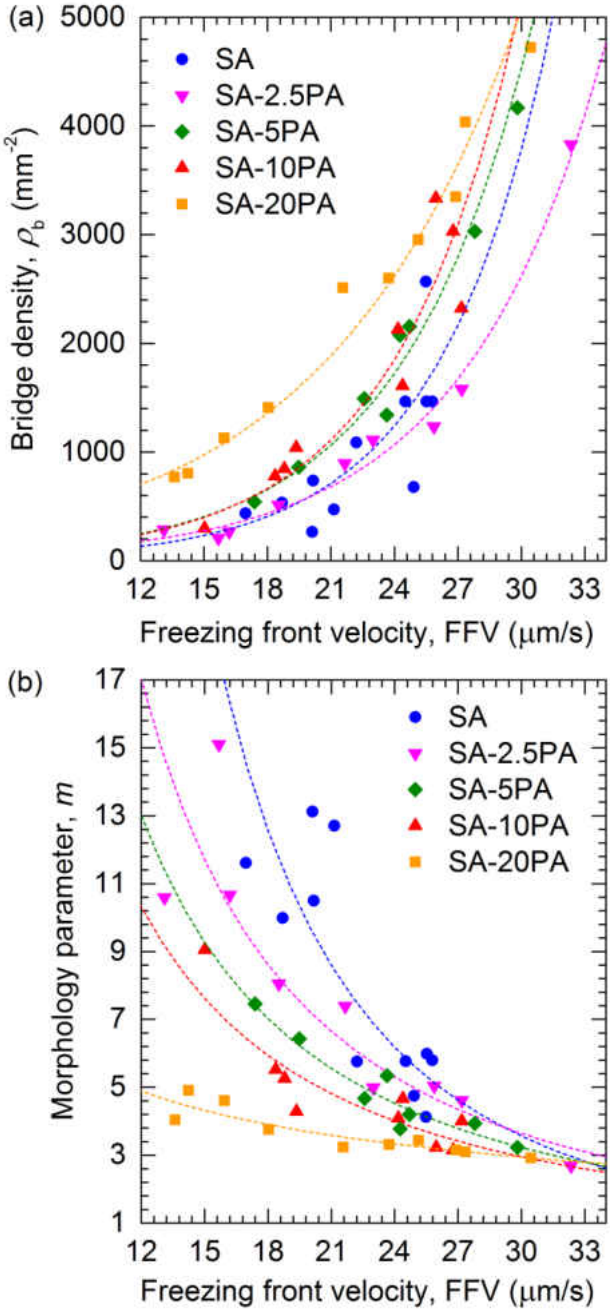

Figure 6: Variation of (a) lamellar bridge density (ρ_b) and (b) morphological parameter (m) of the ice-templated Al_2O_3 scaffolds with FFV.

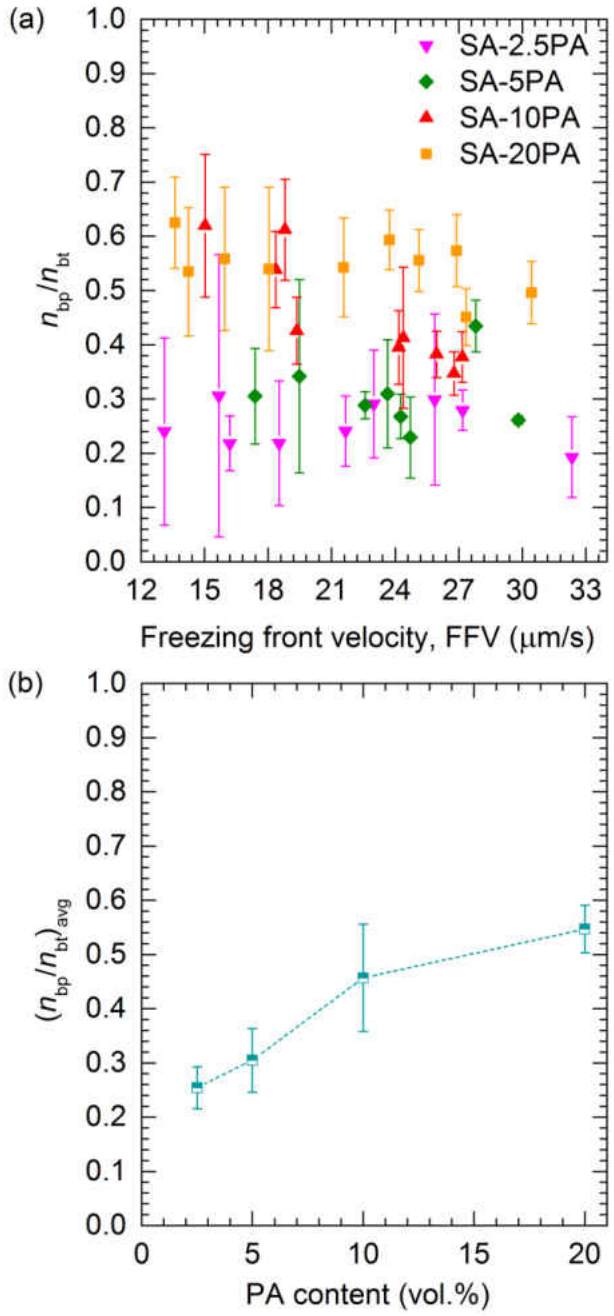

Figure 7: Variation of (a) $n_{\mathrm{bp}}/n_{\mathrm{bt}}$ with FFV and (b) $(n_{\mathrm{bp}}/n_{\mathrm{bt}})_{\mathrm{avg}}$ with platelets (PA) content.

To further understand the role of the platelets in the lamellar bridge formation, we next delve into the microstructural characteristics of the bridges. Lamellar bridges of the SA scaffolds developed solely through the equiaxed SA grains, whereas for the other compositions both the anisotropic

grains (platelets) and equiaxed fine grains participated in the bridge formation. Since, in the SEM micrographs platelets are usually visible within the bridges, we made an attempt to approximately estimate the ratio of the number of lamellar bridges containing platelets (n_{bp}) to the total number bridges (n_{bt}) as a function of the FFV and PA content. Figure 7a shows variation of the $n_{\mathrm{bp}}/n_{\mathrm{bt}}$ as a function of the FFV, whereas variation of the $(n_{\mathrm{bp}}/n_{\mathrm{bt}})_{\mathrm{avg}}$ (for each composition averaged over the entire range of the FFV) is shown in Fig. 7b. In spite of the considerable scatter of the data, Fig. 7 sheds some light into the microstructural characteristics of the bridges. Figure 7a does not indicate any considerable variation of the $n_{\mathrm{bp}}/n_{\mathrm{bt}}$ with FFV. Recall from Fig. 6a that for a given composition ρ_{b} increases with the increasing FFV. Therefore, one rationalization is that both n_{bp} and n_{bt} for a given composition possibly increase almost in same proportion with the increasing FFV and as result, the $n_{\mathrm{bp}}/n_{\mathrm{bt}}$ remains comparable over the entire range of the FFV. In contrast, within the entire range of the FFV Fig. 7a suggests a moderate increase of the $n_{\mathrm{bp}}/n_{\mathrm{bt}}$ as the PA content increased from 2.5 to 20 vol.%. In other words, increase of the PA concentration increases the fraction of bridges that contains anisotropic grains. For example, for the SA-2.5PA scaffolds $n_{\mathrm{bp}}/n_{\mathrm{bt}}$ is observed to be below 0.3, whereas almost about 0.6 for the SA-20PA scaffolds. This is also supported by Fig. 7b, which reveals a considerable increase of $(n_{\mathrm{bp}}/n_{\mathrm{bt}})_{\mathrm{avg}}$ with the increasing PA content. Based on these observations, it can be stated that increase of the $n_{\mathrm{bp}}/n_{\mathrm{bt}}$ with the PA content perhaps also contributed to the observed increase of the ρ_{b} from SA to SA-20PA and to the corresponding microstructural modifications.

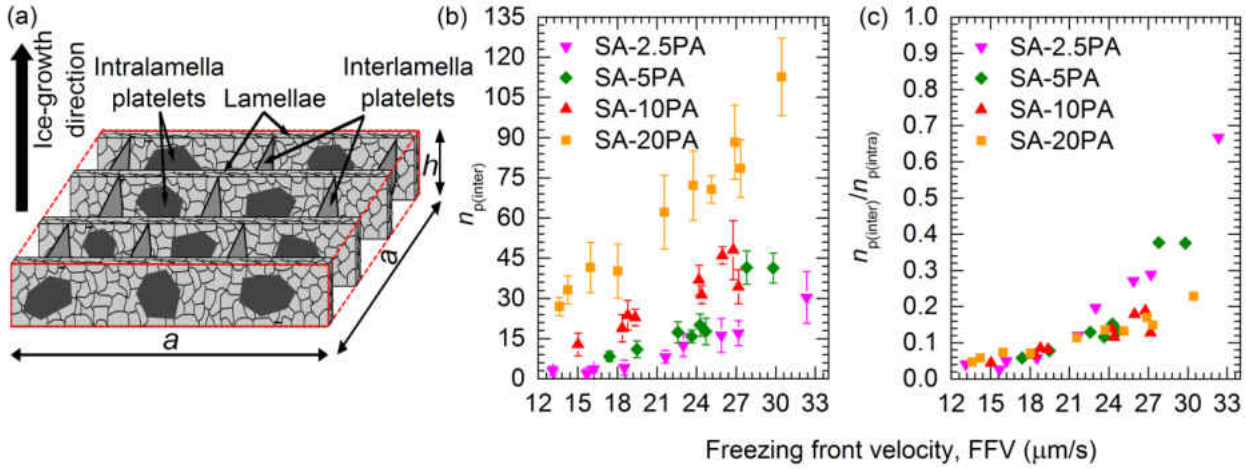

Figure 8: (a) A schematic of a representative volume element (RVE) that is used to estimate the distribution of the intralamella and interlamellar platelets. Changes of (b) $n_{\mathrm{p(inter)}}$ and (c) $n_{\mathrm{p(inter)}}/n_{\mathrm{p(intra)}}$ with FFV of the ice-templated Al_2O_3 scaffolds.

Finally, in this section, we describe a method that is developed to determine the approximate ratio of the number of the intralamella platelets ($n_{\mathrm{p(intra)}}$) and interlamella platelets ($n_{\mathrm{p(inter)}}$) to understand the distribution of the anisotropic grains within and in between the lamella walls as a function of the FFV and PA content. Figure 8a shows a simplified schematic of a representative volume element (RVE, $a \times a \times h$) illustrating locations of the intralamella and interlamella platelets, depicted using two different colors to distinguish in between them. Red dotted lines are drawn to simply show the boundary of the RVE. Although locations of the majority of the platelets are similar to those shown in Fig. 8a, microstructural investigations also revealed platelets protruding out of the lamellae walls that did not completely develop the bridges. For the simplicity of the calculations, platelets protruding out of the lamellae walls were also considered as the interlamella platelets. Dimensions of the representative volume element (RVE) were chosen based on the SEM micrographs and observations made from therein. Details on the dimensions of the

RVE, and estimation of total number platelets within a RVE as well as $n_{\mathrm{p(intra)}}$ and $n_{\mathrm{p(inter)}}$ are provided in the supplementary material. Figure 8b shows that $n_{\mathrm{p(inter)}}$ of the SA-2.5PA, SA-5PA, SA-10PA and SA-20PA increases gradually with the FFV. While the differences are not significant, Fig. 8b also indicates that at a comparable FFV $n_{\mathrm{p(inter)}}$ exhibits an increasing trend with the PA content and $n_{\mathrm{p(inter)}}$ of SA-20PA is observed to be considerably greater relative to the other compositions. Figure 8b thus suggests an increase of the number of the platelets within the bridges with the increasing FFV and PA content. Based on the dimensions of the RVE and suspension composition, total number of the platelets within the RVE is estimated to be approximately 75 for SA-2.5PA, 150 for SA-5PA, 300 for SA-10PA, and 600 for SA-20PA. Therefore, it can be stated that magnitude of the $n_{\mathrm{p(inter)}}$ increases with the FFV and PA content, but a large fraction of the platelets still remains within the walls as the intralamella platelets. It is of note that estimation of the $n_{\mathrm{p(inter)}}$ becomes relatively difficult in the higher FFV regime and an underestimation is possible particularly for the SA-10PA and SA-20PA scaffolds. Finally, Fig. 8c reveals the variation of the $n_{\mathrm{p(inter)}}/n_{\mathrm{p(intra)}}$ with the FFV. For each of the four compositions, $n_{\mathrm{p(inter)}}/n_{\mathrm{p(intra)}}$ remains very small (~0.05) at lower FFVs and gradually reaches to about 0.2 or even greater in the high FFV regime. This further supports that in spite of an increase of the $n_{\mathrm{p(inter)}}/n_{\mathrm{p(intra)}}$ with the FFV, majority of the platelets remain within the walls as intralamella platelets. It is also interesting to note that in spite of a variation of the PA content from 2.5 to 20 vol.% in the aqueous suspensions, $n_{\mathrm{p(inter)}}/n_{\mathrm{p(intra)}}$ of all the compositions remains almost comparable as a function of the FFV. Figure 8c further suggests an abrupt increase of the $n_{\mathrm{p(inter)}}/n_{\mathrm{p(intra)}}$ at higher FFVs, however, more data are required to establish the trend for the high FFV regime. Some differences of the $n_{\mathrm{p(inter)}}/n_{\mathrm{p(intra)}}$ among the four compositions can be

observed above 27 μm/s. This is perhaps related to the increasing difficulty of counting $n_{\mathrm{p(inter)}}$ for the compositions with the higher PA content at high FFVs. Nevertheless, the proposed method is able to approximately estimate the distribution of the intralamella and interlamella platelets, and provides insights into the variation of the distribution of the anisotropic grains as a function of the FFV and PA content. Therefore, microstructural investigations revealed the unique arrangements of the platelets within the scaffolds, whereas the proposed innovative method is utilized to quantify the platelets-induced microstructural modifications over multiple length-scales, critical to address the structure-property relationships in this class of novel ceramics.

2.3.4 Effects of platelets on uniaxial compressive response and energy absorption

Figures 9a and 9b show the representative uniaxial compressive stress-strain response of the ice-templated sintered scaffolds at relatively low and high FFVs, respectively. In each stress-strain curve, three distinct zones can be noticed: (i) an elastic regime where stress increases almost linearly with strain to a maximum (peak stress, σ_{p}), (ii) a stress plateau regime where stress exhibits a gradual decrease with increasing strain over a large range of strain, and (iii) finally a densification stage where steep rise of stress is observed with small increase of strain. In cellular ceramics, peak stress (i.e., compressive strength) is a measure of the resistance to inelastic deformation and corresponds to a stress level where brittle failure initiates [110]. In the plateau regime stress decreases gradually due to the continuous brittle crushing of the cell walls, which results in the energy-absorption [110]. At both low and high FFVs, compressive strength of the SA scaffolds is observed to be lower relative to the other scaffold compositions. However, SA scaffolds exhibit a substantial increase of compressive strength from low FFV to high FFV. It is interesting that in the low FFV regime, strength increases significantly with the increasing PA content. Whereas in

the high FFV regime, strength increases significantly up to 5 vol.% PA, but further increase of the PA concentration leads to a decrease of the strength. Also, for each composition strength is observed to be greater at high FFV in comparison to low FFV. Figure 9 thus reveals a marked improvement of the uniaxial compressive response of the ice-templated sintered scaffolds in presence of the platelets.

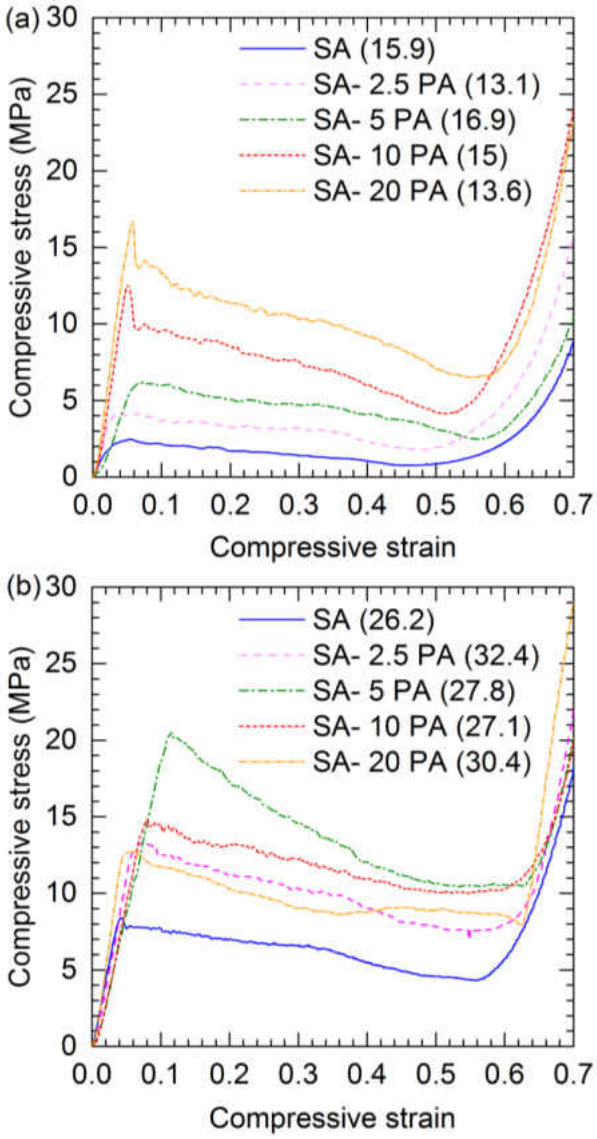

Figure 9: Representative uniaxial compressive stress-strain curves of the ice-templated Al_2O_3 scaffolds at relatively (a) low and (b) high FFVs.

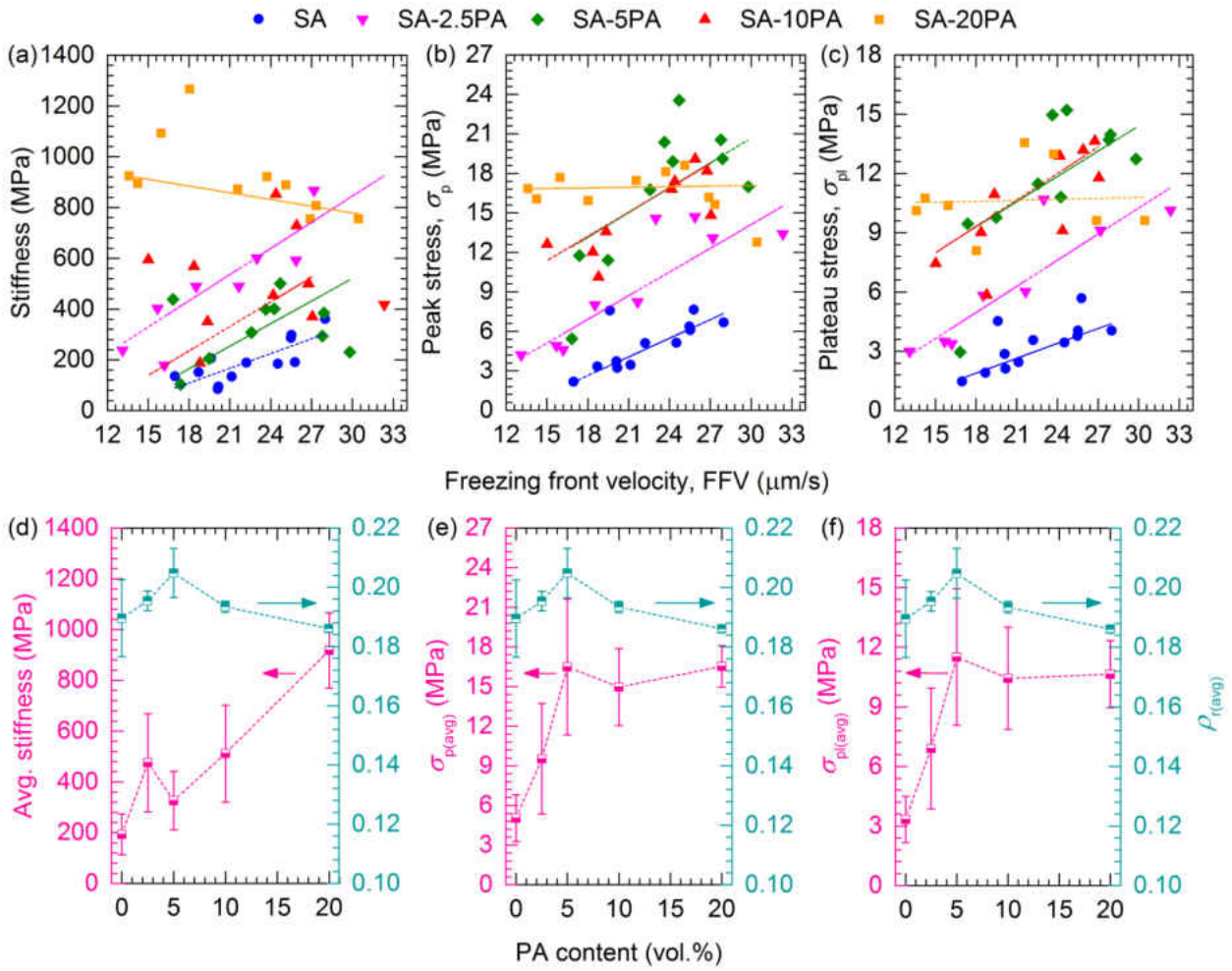

Figure 10: Changes of (a) stiffness, (b) peak stress (σ_p) and (c) plateau stress (σ_{pl}) with FFV and (d) average stiffness, (e) average peak stress ($\sigma_{p(avg)}$) and (f) average plateau stress ($\sigma_{pl(avg)}$) with platelets (PA) content of the ice-templated Al_2O_3 scaffolds.

Figure 10 shows variation of the stiffness (Fig. 10a), σ_p (Fig. 10b), and plateau stress (σ_{pl}, Fig. 10c) with the FFV as well as variation of the average stiffness (Fig. 10d), average σ_p ($\sigma_{p(avg)}$, Fig. 10e) and average σ_{pl} ($\sigma_{pl(avg)}$, Fig. 10f) with the PA vol.%. Variation of the $\rho_{r(avg)}$ with the PA content is also shown in Figs. 10d-f. For each composition, average values were determined over the entire range of the FFV. Stiffness values were estimated from the slope of the linear part of the

uniaxial compressive stress-strain curves. Due to a gradual decrease of the stress with the increasing strain in the plateau regime, σ_{pl} was determined as follows [111,112]:

$$\sigma_{\mathrm{pl}} = \frac{\int_{\varepsilon_{\mathrm{a}}}^{\varepsilon_{\mathrm{cd}}} \sigma d\varepsilon}{\varepsilon_{\mathrm{cd}} - \varepsilon_{\mathrm{a}}}, \quad (3)$$

where ε_{a} is the strain at the initial fracture point corresponding to the first peak of the crushing stress and $\varepsilon_{\mathrm{cd}}$ is the onset densification strain that is correlated to the initiation of cell wall interactions [111]. From a plot of the energy absorption efficiency parameter (e) vs. strain, $\varepsilon_{\mathrm{cd}}$ is determined as the strain level where e reaches a global maximum [111,112]. An example plot is shown in Fig. S3. e is defined as the ratio of the energy absorption up to a strain level ε divided by the σ at that strain level as follows [111,112]:

$$e = \frac{1}{\sigma}\int_0^{\varepsilon} \sigma d\varepsilon. \quad (4)$$

Due to the scatter of the data exact trends of the stiffness vs. FFV (Fig. 10a) is not discernable. However, platelets considerably reinforced the sintered scaffolds and the effects become more prominent at higher PA vol.%. Average stiffness values of the platelets-reinforced scaffolds are about 2-4 times greater in comparison to that of the SA scaffolds. In spite of some scatter of the data, trends of the σ_{p} vs. FFV (Fig. 10b) and $\sigma_{\mathrm{p(avg)}}$ vs. PA vol.% (Fig. 10e) are rather apparent and a significant improvement due to the platelets addition is evident, further supporting the platelets-induced reinforcement of the scaffolds. In general, σ_{p} exhibits an approximate linear increase with the FFV for all the compositions, except the SA-20PA for which σ_{p} seems to remain comparable over the entire FFV range. However, Fig. 10b also indicates that in the high FFV regime σ_{p} probably starts to decrease slightly with the increasing FFV particularly for the high PA vol.%. Nevertheless, a drastic improvement of σ_{p} of the scaffolds due to platelets addition is distinctly evident. $\sigma_{\mathrm{p(avg)}}$ of the SA scaffolds is 5$\pm$1.8 MPa and increases markedly to 16.5$\pm$5.1

MPa at 5 vol.% PA. With a further increase of PA content $\sigma_{p(avg)}$ remains almost unchanged; 15±2.9 MPa and 16.5±1.6 MPa for the SA-10PA and SA-20PA, respectively. Similar trend is also observed for the plateau stress that increases with both the FFV (Fig. 10c) and PA vol.% (Fig. 10f), except for the SA-20PA composition that exhibits an almost unchanged σ_{pl} over the entire FFV range. $\sigma_{pl(avg)}$ of the SA scaffolds is observed to be 3.3±1.2 MPa, but increased to 11.5±3.4 MPa at 5 vol.% PA. Similar to the peak stress, in the high FFV regimes a decrease of the σ_{pl} with the FFV is observed and higher PA content does not seem to modify the plateau stress any further. SA-10PA and SA-20PA scaffolds exhibit $\sigma_{pl(avg)}$ of 10.4±2.6 MPa and 10.6±1.7 MPa, respectively (Fig. 10f).

Total energy absorption per unit volume (U_v) is estimated from the area under the stress-strain (σ-ε) curve up to the ε_{cd} and is expressed as [110-112]

$$U_v = \int_0^{\varepsilon_{cd}} \sigma \, d\varepsilon. \quad (5)$$

Whereas the energy absorption per unit mass i.e., specific energy absorption capacity (U_m) is calculated as

$$U_m = U_v/\rho^*, \quad (6)$$

where ρ^* is the density of the foam. Figure 11 shows variation of the ε_{cd} (Fig. 11a), U_v (Fig. 11b) and U_m (Fig. 11c) with the FFV as well as variation of the average ε_{cd} ($\varepsilon_{cd(avg)}$, Fig. 10d), average U_v ($U_{v(avg)}$, Fig. 11e) and average U_m ($U_{m(avg)}$, Fig. 11f) with the PA vol.%. Additionally, variation of the $\rho_{r(avg)}$ with the PA content is shown in Figs. 11d-f. For each composition, $\varepsilon_{cd(avg)}$, $U_{v(avg)}$ and $U_{m(avg)}$ values were determined over the entire range of the FFV. Although a significant scatter of the ε_{cd} values is observed, ε_{cd} exhibits an increasing trend with both the FFV and PA vol.%. It is observed that $\varepsilon_{cd(avg)}$ of the SA scaffolds is 0.5±0.03 and increases to a

maximum of 0.58±0.02 for the SA-5PA scaffolds. With a further increase of the PA content, $\varepsilon_{cd(avg)}$ values remain comparable; 0.56±0.05 and 0.55±0.04 for the SA-10PA and SA-20PA, respectively. Similar trends are also observed for the U_v and U_m, where both are observed to increase significantly with the FFV and PA vol.%, however, SA-20PA exhibits less variation of the energy absorption capacity with FFV. Similar to σ_p and σ_{pl}, energy absorption capacity in the high FFV regime (>24 μm/s) also seems to decrease with the increasing FFV. $U_{v(avg)}$ and $U_{m(avg)}$ of the SA scaffolds are observed to be 1.7±0.7 MJ/m^3 and 2.2±0.9 kJ/kg, respectively, and increase to 6.5±2.0 MJ/m^3 and 8.0±2.3 kJ/kg, respectively, for the SA-5PA scaffolds. For the SA-10PA scaffolds $U_{v(avg)}$ and $U_{m(avg)}$ are observed to be 5.9±1.7 MJ/m^3 and 7.7±2.3 kJ/kg, respectively, whereas 6.0±1.2 MJ/m^3 and 8.2±1.6 kJ/kg, respectively, for the SA-20PA.

Therefore, influence of the Al_2O_3 platelets on the uniaxial compressive response of the ice-templated sintered Al_2O_3 scaffolds is observed to be significant. Figure 12 summarizes percent changes of the $\sigma_{p(avg)}$, $\sigma_{pl(avg)}$, $U_{v(avg)}$ and $U_{m(avg)}$ of the platelets-reinforced scaffolds relative to those of the SA scaffolds. It can be observed that for the SA-2.5PA scaffolds average increase of the $\sigma_{p(avg)}$, $\sigma_{pl(avg)}$, $U_{v(avg)}$ and $U_{m(avg)}$ is about 100%, whereas $\rho_{r(avg)}$ changes by only 3%. With the increase of the PA content to 5 vol.%, $\sigma_{p(avg)}$, $\sigma_{pl(avg)}$, $U_{v(avg)}$ and $U_{m(avg)}$ of the SA-5PA scaffolds exhibit an average increase of about 200-250%, but $\rho_{r(avg)}$ changes by only 8%. For the SA-10PA and SA-20PA scaffolds changes of the $\sigma_{p(avg)}$, $\sigma_{pl(avg)}$, $U_{v(avg)}$ and $U_{m(avg)}$ are observed to be comparable to that of the SA-5PA, whereas percent change of the $\rho_{r(avg)}$ gradually decreases with the increasing PA content from 5 to 20 vol.% and $\rho_{r(avg)}$ approaches to that of the SA scaffolds. Overall, this investigation reveals that presence of the large anisotropic grains can markedly improve the uniaxial compressive mechanical properties of the ice-templated sintered Al_2O_3 scaffolds, however, without significantly altering the total porosity.

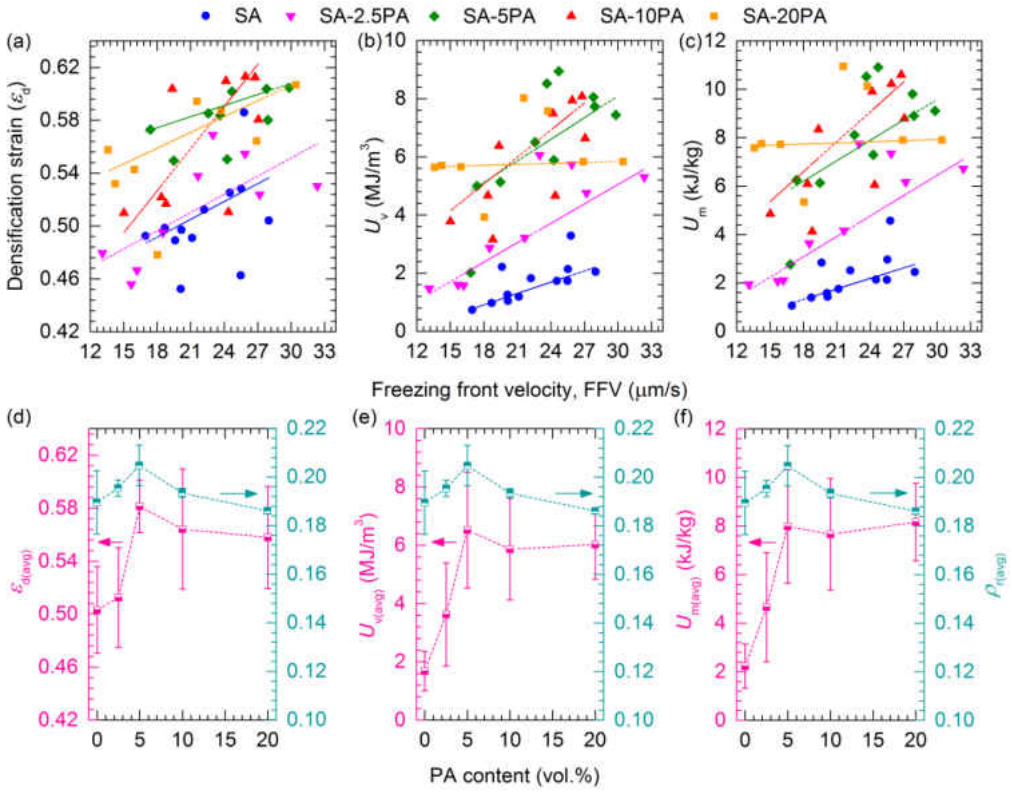

Figure 11: Changes of (a) densification strain (ε_{cd}), (b) volume based total energy absorption capacity (U_v) and (c) mass based total energy absorption (U_m) with FFV and (d) average densification strain ($\varepsilon_{cd(avg)}$), (e) volume based average total energy absorption capacity ($U_{v(avg)}$) and (f) mass based average total energy absorption capacity ($U_{m(avg)}$) with platelets (PA) content of the ice-templated Al_2O_3 scaffolds.

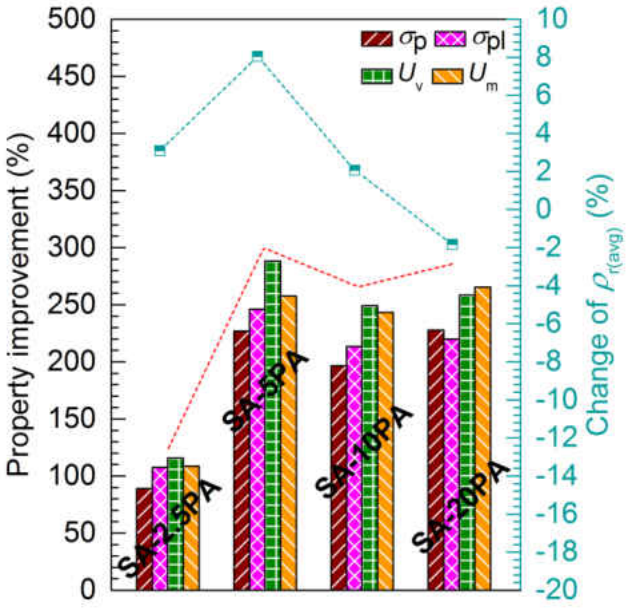

Figure 12: Percent changes of the $\sigma_{p(avg)}$, $\sigma_{pl(avg)}$, $U_{v(avg)}$ and $U_{m(avg)}$ of the platelets-reinforced scaffolds relative to those of the SA scaffolds.

2.4 Structure-property (mechanical) relationships

ρ_r is one prime factor that influences the mechanical properties of the cellular solids. Figures 10-12, however, suggest that variation of the strength and the energy absorption capacity with the PA content do not completely follow the trend observed for the $\rho_{r(avg)}$. This is because $\rho_{r(avg)}$ initially increased with the increasing PA content up to 5 vol.%. However, a decrease is observed with the further increase of the PA content to 20 vol.% and $\rho_{r(avg)}$ values of the SA and SA-20PA are observed to be comparable. $\sigma_{p(avg)}$, $\sigma_{pl(avg)}$, $U_{v(avg)}$, and $U_{m(avg)}$ also increased up to 5 vol.% PA content, but unlike $\rho_{r(avg)}$ do not exhibit any considerable decrease in the range of 5-20 vol.% PA. $\rho_{r(avg)}$ of the SA-5PA is only about 8% greater relative to the SA, whereas $\sigma_{p(avg)}$, $\sigma_{pl(avg)}$, $U_{v(avg)}$ and $U_{m(avg)}$ of the former are enhanced by more than 200% relative to those of the latter. Also, in

the range of 5-20 vol.% PA, $\sigma_{\mathrm{p(avg)}}$, $\sigma_{\mathrm{pl(avg)}}$, $U_{\mathrm{v(avg)}}$, and $U_{\mathrm{m(avg)}}$ of the SA-10PA and SA-20PA scaffolds remain comparable to those of the SA-5PA scaffolds and thus significantly greater in comparison to those of the SA scaffolds. According to Gibson and Ashby models [110], compressive strength (σ) of brittle cellular solids is related to ρ_{r} as

$$\frac{\sigma}{\sigma_{\mathrm{s}}} \propto \rho_{\mathrm{r}} \text{ (for closed-cell),} \tag{7}$$

$$\frac{\sigma}{\sigma_{\mathrm{s}}} \propto (\rho_{\mathrm{r}})^{1.5} \text{ (for open-cell),} \tag{8}$$

and

$$\frac{\sigma}{E_{\mathrm{s}}} \propto (\rho_{\mathrm{r}})^{3} \text{ (honeycomb, out-of-plane),} \tag{9}$$

where σ_{s} and E_{s} are compressive fracture strength and Young's modulus, respectively, of the cell wall bulk material. Both $\sigma_{\mathrm{p(avg)}}$ and $\sigma_{\mathrm{pl(avg)}}$ are observed to be maximum and minimum for the SA-5PA and SA scaffolds, respectively. Utilizing equations (7)-(9), ratio of the compressive strength of the SA-5PA ($\sigma_{\mathrm{SA-5PA}}$) to that of the SA (σ_{SA}) can be expressed as

$$\frac{\sigma_{\mathrm{SA-5PA}}}{\sigma_{\mathrm{SA}}} = \left(\frac{\rho_{\mathrm{r(SA-5PA)}}}{\rho_{\mathrm{r(SA)}}}\right)\left(\frac{\sigma_{\mathrm{SA-5PA}}}{\sigma_{\mathrm{SA}}}\right) = 1.08\left(\frac{\sigma_{\mathrm{SA-5PA}}}{\sigma_{\mathrm{SA}}}\right) \text{ (for closed-cell),} \tag{10}$$

$$\frac{\sigma_{\mathrm{SA-5PA}}}{\sigma_{\mathrm{SA}}} = \left(\frac{\rho_{\mathrm{r(SA-5PA)}}}{\rho_{\mathrm{r(SA)}}}\right)^{1.5}\left(\frac{\sigma_{\mathrm{SA-5PA}}}{\sigma_{\mathrm{SA}}}\right) = 1.12\left(\frac{\sigma_{\mathrm{SA-5PA}}}{\sigma_{\mathrm{SA}}}\right) \text{ (for open-cell),} \tag{11}$$

and

$$\frac{\sigma_{\mathrm{SA-5PA}}}{\sigma_{\mathrm{SA}}} = \left(\frac{\rho_{\mathrm{r(SA-5PA)}}}{\rho_{\mathrm{r(SA)}}}\right)^{3}\left(\frac{E_{\mathrm{SA-5PA}}}{E_{\mathrm{SA}}}\right) = 1.3\left(\frac{E_{\mathrm{SA-5PA}}}{E_{\mathrm{SA}}}\right) \text{ (honeycomb, out-of-plane),} \tag{12}$$

where $\rho_{\mathrm{r(SA-5PA)}}/\rho_{\mathrm{r(SA)}}$ is 1.08 (utilizing the $\rho_{\mathrm{r(avg)}}$ values). Therefore, equations (10)-(12) further support that moderate increase of the ρ_{r} from SA to SA-5PA alone may not attribute to the observed strength improvement of the SA-5PA scaffolds by more than 3 times relative to the SA

scaffolds. Elastic and fracture properties of cell wall material also significantly influence mechanical response of cellular solids, which is evident from equations (10)-(12). An increase of about 25% of the Young's modulus and fracture strength has been reported for sintered fine-grain dense Al_2O_3 ceramics reinforced with platelets [113]. Therefore, in addition to the ρ_r, we need to consider the influence of the grain-level anisotropy on the cell wall material properties and the corresponding effects on the macroscopic response of the scaffolds. Moreover, the microstructural modifications and changes of the ρ_b and bridge characteristics due to the anisotropic grains might have also contributed to the measured property improvement.

For this purpose, we first address the microstructural differences of the SA-5PA and SA scaffolds, because measured properties maximize at 5 vol.% PA. Both the t and λ of the SA-5PA and SA are observed to be comparable (Fig. 5), whereas ρ_b of the former is moderately greater than the later (Fig. 6a). As a result, except in the high FFV regime, at all other FFVs pore morphology of the SA-5PA scaffolds is less lamellar relative to that of the SA scaffolds (Fig. 6b). Although not measured, evolution of the dendritic morphology is known to reduce the pore size [82,83,103]. Therefore, we suggest that increase of the ρ_b and the corresponding decrease of the pore size due to the anisotropic grains-induced microstructural modifications contributed to the strength enhancement of the SA-5PA scaffolds in comparison to the SA scaffolds. This is because increase of lamellar bridging and decrease of pore size enhance the resistance of the lamellae walls of the ice-templated ceramics to compressive deformation [82,83]. However, it is interesting to observe that m values of the SA-5PA and SA scaffolds converge with the increasing FFV, whereas throughout the FFV range both the strength (Fig. 10) and the energy absorption capacity (Fig. 11) of the former remain significantly greater than the latter. Moreover, gap of the strength (or energy absorption capacity) values in between the SA-5PA and SA scaffolds remains comparable

throughout the FFV range. Also, while the ρ_b of the SA scaffolds in the high FFV regime is observed to be greater than that of the SA-5PA scaffolds in the low FFV regime, strength of the former at high FFVs still remains significantly lower in comparison to that of the latter at low FFVs. Thus, there are possibly other factors also that contributed to the measured property enhancement.

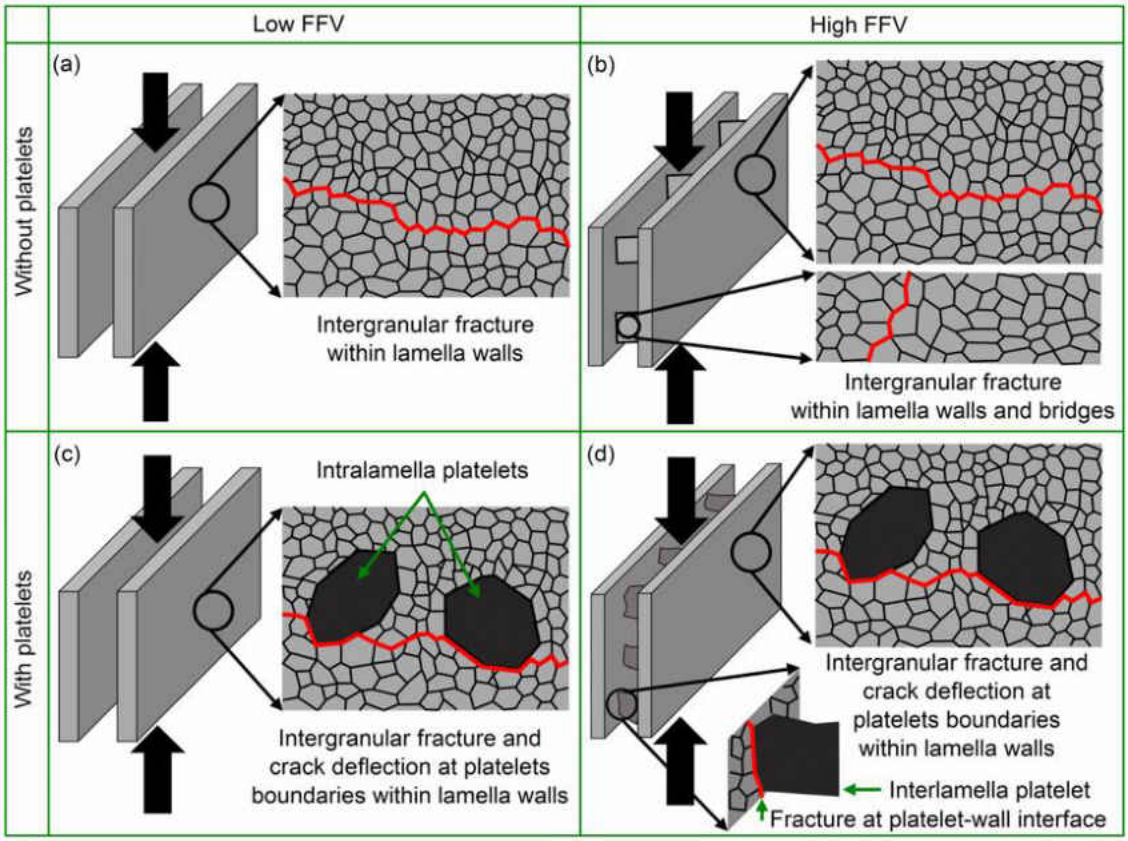

Figure 13: Schematic representation of the possible fracture modes of the lamella walls and lamellar bridges under compressive loading at a (a) low FFV of scaffolds without platelets, (b) high FFV of scaffolds without platelets, (c) low FFV of scaffolds with platelets, and (d) high FFV of scaffolds with platelets. Due to the fine-grained microstructures of the processed scaffolds (Fig. 3), crack propagation mechanism is considered as intergranular (grain-boundary), which is shown by the red lines.

One key difference in between the SA-5PA scaffolds and SA scaffolds is the presence of the large anisotropic grains (i.e., platelets) within the lamellae walls and bridges of the former. In Fig. 13, we present schematics of four different scenarios to understand the possible response of the cell walls and bridges with and without the anisotropic grains (platelets) to compressive deformation. For each case, we have shown only two ceramic walls and illustrated crack propagation within the wall as well as within the bridge. At a low FFV ceramic lamellae are relatively thicker and lamellar bridging is assumed to be negligible (no bridges are shown), whereas at a high FFV lamellae are relatively thinner and connected through the bridges. A generalized failure scenario is that under uniaxial compressive loading along the ice-growth direction (i.e., parallel to lamellae) polycrystalline ceramic walls are subjected to bending forces [83]. This will lead to separation of the lamellae causing crack propagation through the walls and brittle fracture of individual lamella. Due to the fine-grain microstructure (1-2 μm) of the lamellae walls (Fig. 3), intergranular (grain-boundary) crack propagation is expected to be the dominant fracture mechanism that is commonly observed in the fine-grain (few μm) Al_2O_3 ceramics [114]. At a low FFV and without the PA (Fig. 13a), resistance to compressive loading of the highly porous (~80 vol.%) ice-templated Al_2O_3 is not expected to be significant and is supported by the measured low strength values (Fig. 10). In presence of the platelets and at a low FFV (Fig. 13c), magnitude of the ρ_b is not affected considerably. However, microstructure of the lamellae is modified due to the presence of the anisotropic grains (i.e., intralamella platelets) within the matrix of the fine Al_2O_3 grains. Young's modulus of Al_2O_3 single crystals (425-460 GPa) [115] is greater than that of the fine-grained Al_2O_3 ceramics (393 GPa) [116]. Therefore, during the compressive loading relatively stiffer (intralamella) platelets can enhance the bending/buckling resistance of the walls and, thereby,

improve the stiffness of the scaffolds. This is supported by the measured results. Similarly, intralamella platelets are also expected to influence the strength and fracture characteristics of the lamellae walls. Microstructural investigation (not shown here) of the deformed scaffolds did not reveal fracture of the individual platelets, which can be attributed to the significantly high strength (~2 GPa) of the Al_2O_3 platelets [117]. Flexural strength of the fine-grained polycrystalline Al_2O_3 ceramics is about 500 MPa [118]. Therefore, high-strength intralamella platelets is expected to enhance the compressive fracture strength of the lamellae walls and, thereby, overall strength of the scaffolds. While the individual lamella will fracture through intergranular crack propagation, large anisotropic grains (intralamella platelets) can result in crack deflection (Fig. 13c) and extrinsically toughen the walls [119]. This may attribute to additional fracture resistance to the cell walls and further improve the compressive response of the scaffolds. Overall, in the low FFV regime, grain-level anisotropy within the lamellae walls of the SA-5PA scaffolds in the form of the intralamella platelets is a possible governing factor that improves the compressive mechanical properties in comparison to those of the SA scaffolds.

In the high FFV regime, increase of the ρ_{b} enhances the stiffness, strength, and energy absorption capacity of the SA scaffolds. Both the ceramic walls and bridges will exhibit intergranular fracture (Fig. 13b). As mentioned earlier, in spite of the comparable pore morphology at high FFVs mechanical properties of the SA-5PA scaffolds remain superior in comparison to those of the SA scaffolds. For the SA-5PA scaffolds at a high FFV platelets are present both in the walls and in the bridges, and the interlamella platelets evolve at the expense of the intralamella platelets. Figure 8c shows that $n_{\mathrm{p(inter)}}/n_{\mathrm{p(intra)}}$ is about 0.05 in the low FFV regime and increases to above 0.2 in the high FFV regime. Decrease of the fraction of the intralamella platelets with the increasing FFV may cause weakening of the walls, however, is probably compensated by other strength

enhancing factor(s). One possibility is the presence of the interlamella platelets. Under the compressive loading, ceramic walls will exhibit intergranular fracture and the platelets-induced crack deflection (extrinsic toughening) could be operative (Fig. 13d). However, for the bridges with interlamella platelets, platelet fracture is highly unlikely due to the high fracture strength. Microstructural investigations of the deformed scaffolds also did not reveal any evidence of interlamella platelets fracture. Figure 14 shows representative SEM micrographs of a partially deformed (~10% engineering strain) SA-20PA scaffold that was processed in the high FFV regime (25.1 μm/s). Limited separation of the lamellae walls can be observed (Fig. 14a). It can also be observed that a lamellar bridge without interlamella platelet exhibited intergranular fracture (Fig. 14b), whereas a lamellar bridge containing an interlamella platelet does not exhibit any evidence of platelet fracture (Fig. 14c). Therefore, bridges with the interlamella platelets can enhance the fracture resistance of the scaffolds. Bridge fracture can occur at the platelet-interlamella interfaces (Fig. 13d). Fine Al_2O_3 grains are observed to be well bonded to the Al_2O_3 platelet (Fig. 3b) and such interfaces may also contribute to enhance the resistance of the SA-5PA scaffolds under the compressive loading conditions. It is of note that for the SA-5PA composition, at any FFV almost 30% of the bridges contain interlamella platelets (Fig. 7). However, $n_{\mathrm{p(inter)}}$ is negligible at a low FFV (Fig. 8b) due to very low ρ_{b}. With the increasing FFV, $n_{\mathrm{p(inter)}}$ also increased and thus their contribution to the properties. Overall, in the high FFV regime, greater ρ_{b} and grain-level anisotropy present both within the lamellae walls in the form of the intralamella platelets and in the lamellar bridges in the form of interlamella platelets in the SA-5PA scaffolds are the critical factors that improved the compressive response relative to the SA scaffolds. Above discussion thus sheds light into the origin of the superior properties of the scaffolds containing platelets in terms

of the role of the intralamella and interlamella platelets. Measured results well support the rationalization presented here.

Finally, we briefly address the origin of the observed compressive response characteristics of the SA-5PA, SA-10PA, and SA-20PA scaffolds. Increase of the average stiffness with the increasing PA content can be attributed to the increasing ρ_{b} as well as to the increasing fraction of the stiffer anisotropic grains within the lamellae walls and in the bridges. Note that both the $(n_{\mathrm{bp}}/n_{\mathrm{bt}})_{\mathrm{avg}}$ and $n_{\mathrm{p(intra)}}$ increase with the increasing PA content. Stiffer Al_2O_3 platelets would exhibit a greater resistance to elastic deformation and, therefore, increase of the fraction of the platelets within a matrix of the fine-grain Al_2O_3 could enhance the overall stiffness of the matrix. Similar behavior has been observed for ceramics reinforced with Al_2O_3 platelets [120]. On the other hand, it is interesting that $\sigma_{\mathrm{p(avg)}}$, $\sigma_{\mathrm{pl(avg)}}$, $U_{\mathrm{v(avg)}}$, and $U_{\mathrm{m(avg)}}$ of the SA-5PA, SA-10PA and SA-20PA scaffolds remain comparable. We argue that decrease of the $\rho_{\mathrm{r(avg)}}$ in the 5-20 vol.% range of the anisotropic grains will tend to reduce the strength and thus energy absorption capacity. This is probably compensated by the increase of the $(n_{\mathrm{bp}}/n_{\mathrm{bt}})_{\mathrm{avg}}$ and $n_{\mathrm{p(inter)}}$ with the increasing PA content, as both are considered as the strength enhancing factors. However, it is possible that with a significant increase of the PA content in the matrix, properties of the scaffolds can start to deteriorate. This is because for a significantly higher PA content platelets will start to come in direct contact to each other, which will considerably lower the particle packing fraction and densification. Although outside the scope of this study, our preliminary work showed that ice-templated scaffolds processed primarily from the Al_2O_3 platelets have significantly lower strength in comparison to the platelets containing scaffolds investigated here.

While the scaffolds were tested under the compressive loading conditions, results can also be applicable to the other loading conditions. This is because irrespective of the loading type

(compression, tension or bending) and associated the stress field, lamellae walls and bridges will ultimately fracture through the brittle crack propagation. Moreover, even under uniaxial compressive loading the lamellae walls are subjected to bending forces prior to fracture. Therefore, all the length-scale features of the hierarchical microstructures and the mechanisms that resist the deformation and failure of the platelets-reinforced scaffolds under the compressive loading conditions may also contribute to enhance the mechanical properties under other loading conditions.

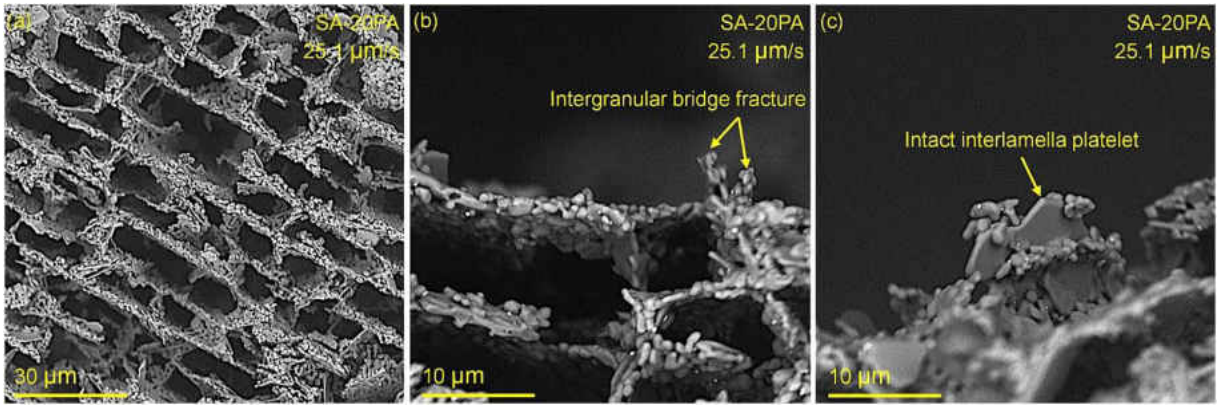

Figure 14: SEM micrographs of a partially deformed (~10% engineering strain) SA-20PA scaffold that was processed in the high FFV regime. (a) Loading surface of the specimen revealing limited separation of the lamellae walls. (b) Intergranular fracture of a lamellar bridge without an interlamella platelet. (c) Intact interlamella platelet on the deformed scaffold surface.

Ice-templated multilayered porous ceramic scaffolds are an emerging class of bioinspired materials, which can be employed directly or can be infiltrated with a polymer/metal to develop hybrid composites. Therefore, compressive strength of the ice-templated sintered porous ceramic structures is critical for the end applications. For a given aqueous ceramic suspension concentration, increase of the unidirectional freezing kinetics increases the ρ_b and decreases the

pore size, which can improve the compressive response of the scaffolds. However, our investigation reveals that in the high porosity regime (~80 vol.%), increase of the FFV did not cause adequate strength enhancement of the SA scaffolds. Moreover, a drastic increase of the FFV can result in a loss of the characteristic multilayered anisotropic pore morphology of the ice-templated ceramics, which may not be desirable. Utilizing Al_2O_3 as a model material system, here we have demonstrated that grain-level anisotropy is one key length-scale parameter that can be uniquely employed to markedly enhance the compressive response of the highly porous ice-templated sintered ceramics scaffolds without decreasing the porosity. Our investigation revealed that moderate vol.% of the large anisotropic grains present in the lamella walls (intralamella platelets) and lamellar bridges (interlamella platelets) is critical to drastically improve the compressive response of the scaffolds. Therefore, anisotropic grain content and FFV can be coupled uniquely to systematically modify the grain-level microstructure and pore morphology to tailor the scaffolds properties, however, without causing considerable variation of the porosity. Platelets-reinforced scaffolds can be infiltrated with another phase to develop novel hybrid materials with the improved mechanical properties. We believe that this investigation provides significant insights into an innovative strategy that can be implemented to the bioinspired materials design and development. Currently, high-strain rate characterization of the uniaxial compressive response of the scaffolds is in progress.

2.5 Conclusions

1) Highly porous (~80 vol.%) ice-templated Al_2O_3 scaffolds were processed from the fine equiaxed (~0.9 μm) particles and from the mixtures of the fine equiaxed and platelet particles (diameter ~8 μm and thickness ~400 nm). A series of microstructures were synthesized to

investigate the combined effects of the anisotropic grains (platelets) content and freezing front velocity (FFV) on the microstructure and uniaxial compressive mechanical properties, and develop the structure-property relationships.

2) It is observed that in the low FFV regime, platelets are mainly present within the lamella walls (intralamella platelets), whereas with the increasing FFV more platelets can be found in between the walls (interlamella platelets) that developed lamellar bridges.
3) This investigation reveals that for a given suspension concentration, not only the FFV but also the platelets content can induce significant microstructural modifications, which can be systematically controlled. Under the comparable ice-templating conditions, pore morphology of the scaffolds gradually transitioned from lamellar to dendritic structure with the increasing platelets content. The observed microstructural modifications are characterized in terms of the lamellar bridge density (ρ_b) and morphological parameter (m).
4) Microstructural investigations further revealed that fraction of the lamellar bridges that contain platelets increased substantially with the increasing platelets content. Based on the rigorous microstructural analysis, an innovative method is proposed that can determine the distribution of the intralamella and interlamella platelets as well as can capture the variation of the distribution as a function of the composition and FFV.
5) Uniaxial compression experiments revealed a marked improvement of the stiffness, peak stress, plateau stress, and energy absorption capacity of the scaffolds in presence of the anisotropic grains (platelets). For an addition of only 5 vol.% platelets (with respect to the total Al_2O_3 content), property improvements over 200% were measured.
6) Finally, an attempt has been made to develop the structure-property (mechanical) relationships to shed light into the origin of the measured compressive property improvement. It is suggested

that anisotropic grains present within the lamella walls and in the bridges attribute to the measured drastic property enhancement, which is rationalized based on the better elastic and fracture properties of the Al_2O_3 platelets relative to the fine-grained Al_2O_3 matrix and role of the platelets during compressive deformation. Overall, this investigation reveals an unique strategy that can be implemented to stiffen and strengthen highly porous ice-templated sintered ceramics for bioinspired materials design and development.

Acknowledgements

We thank the Applied Research Center (ARC) of College of William and Mary for providing the access to the desktop SEM and Prof. Xiaoyu Zhang (Mechanical and Aerospace Engineering, Old Dominion University) for providing access to the high temperature furnace. DG acknowledges the Summer Research Fellowship Program (SRFP 2015), Office of Research, Old Dominion University. DG and HK also acknowledge the support of the Honors College and Office of Research, Old Dominion University, under the Program for the Undergraduate Research and Scholarship (PURS). Finally, we also thank Mr. Nikhil Dhavale (former graduate student at ODU) for his assistance during freeze casting.

2.6 Supporting information

2.6.1 Preparation of aqueous alumina (Al_2O_3) suspensions and freeze casting and sintering

In this work, commercially available Al_2O_3 powders were utilized (0.9 μm, Alfa Aesar, Ward Hill, MA; platelets, Alusion^{TM}, Antaria Ltd., Bentley, Western Australia). For each aqueous suspension, required amount of the Al_2O_3 powder(s) and small amount (0.5 wt.% of the powder) of ammonium polymethacrylate anionic dispersant (Darvan C, R.T. Vanderbilt Co., Norwalk, CT) were first

mixed in deionized water, and milled for 24 hours. Next, an organic binder poly(2-ethyl-2-oxazoline) was added to the slurry (5 wt.% of the powder) and mixed for another hour. Afterwards, the ZrO_2 spheres were separated from the slurry and de-aired for 30 min. Freeze casting was conducted using a custom-made set up. In this set up, a Teflon tube is placed on the top of a thin (0.5 mm) steel plate, partially filled with Al_2O_3 slurry, and the whole assembly is inserted inside a liquid nitrogen (N_2) Dewar. Ice nucleation and growth start at the bottom of the suspension in contact with the cold-finger, and the ice crystals propagate upwards under the influence of the applied temperature gradient. The Teflon tube is radially insulated to ensure that the suspension is frozen only under unidirectional (vertical) thermal gradient. Top of the mold is kept open and is at room temperature at the beginning of the freezing process. By adjusting the distance between the steel plate and liquid N_2, freezing front velocity (FFV) was controlled. Temperature changes of the cold-finger during the unidirectional freeze casting are measured through a thermocouple attached on the top of the cold-finger. For each experiment, an average FFV is estimated by dividing the height of a frozen sample with the time required for completion of solidification of the suspension. In this investigation, ice-templated Al_2O_3 samples were processed within an average FFV range of ~10 - 35 μm/s. Freeze-cast frozen samples (approximately 19 mm in diameter and 45 mm in height) were freeze-dried at a low pressure (0.014 mbar) and temperature (-50°C) for 96 hours using a freeze dryer (2.5L, Labconco, Kansas City, MI). Sintering of the dried samples was conducted in a box furnace (KSL-1700X, MTI Corporation, Richmond, CA) in air atmosphere and the following time-temperature schedule was employed: (i) room temperature to 450°C at a rate of 3°C/min and binder burnout at 450°C for 4 hours, (ii) 450°C to 1550°C at a rate of 5°C/min and sintering at 1550°C for 4 hours, and (iii) finally 1550°C to room temperature at a rate of 5°C/min.

2.6.2 Microstructure characterization and uniaxial compression testing

Dimensions of the cylindrical sintered porous Al_2O_3 scaffolds were approximately 16.5 mm in diameter and 39 mm in height. Although large samples were processed in this study, the current investigation focused to a small region within each sintered sample for the microstructural characterization, density measurements, and uniaxial compressive response measurements. Figure S1 shows a schematic of the sintered sample to illustrate the location of the transverse plane (to the ice growth direction) that was utilized for the microstructural measurements from each sample. Similarly, location of a rectangular specimen of 8 mm × 8 mm × 4 mm dimensions is also shown that was extracted from each sintered scaffold using a low-speed diamond saw for the density measurements and uniaxial compression tests. As shown in Fig. S1, the 8 mm × 8 mm × 4 mm specimen is located at a height of 5 mm from the bottom of the sintered cylindrical sample and location of the transverse plane (i.e., top of the small specimen) is at 9 mm from the bottom of the sample. For A desktop Phenom SEM was employed for the microstructural characterization from the transverse plane. Uniaxial compression tests were conducted along the ice growth direction where the 8 mm × 8 mm cross-section was the loading surface.

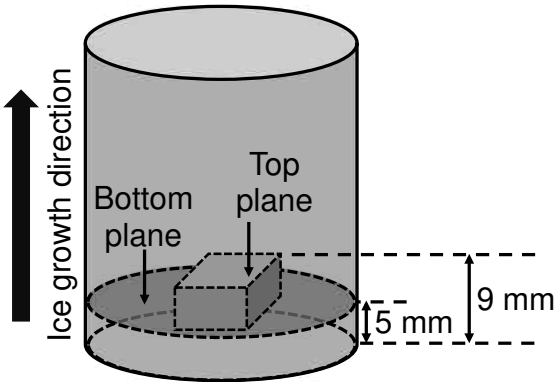

Figure S1: A schematic of the sintered ice-templated scaffold sample illustrating location of the specimen extracted for density measurement, microstructural characterization, and compression test. Locations of the top and bottom of the specimen are also shown. (Not to scale)

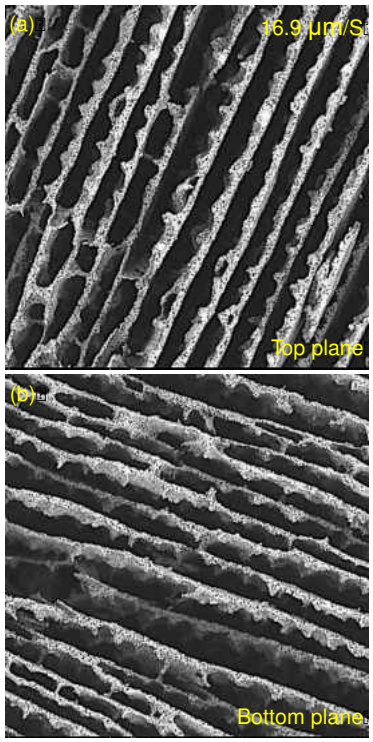

Figure S2: SEM micrographs of top (a) and (b) bottom planes of a porous SA scaffold specimen, revealing comparable microstructures.

2.6.3 Estimation of bridge density and fraction of interlamella vs. intralamella platelets

For each composition and FFV, ρ_b and m were estimated from the average of the ρ_b and λ values measured from six SEM micrographs (1500x magnification). For the estimation of the ρ_b values the only bridges that completely connected the adjacent lamellae walls were accounted. Area (a × a) of the RVE was set as the area of an SEM micrograph at 1500x (0.03 mm^2). Observations made from the SEM micrographs suggested that all the platelets are oriented in the direction of the ice growth and are thus observed to be perpendicular to the plane of the SEM micrographs. Based on this observation, height (h) of the RVE was considered to be the average diameter of the platelets (~8 μm). For each composition and at a FFV, 6 SEM micrographs (1500x) were utilized to estimate an average of the number/volume fractions of the intralamella and interlamella platelets. Considering negligible settling of the platelets, it was assumed that composition of a suspension contained within any representative volume during ice-templating remained same as that of the original suspension. From the knowledge of the average diameter (~8 μm) and thickness (~400 nm) of a single PA particle and volume concentration of a suspension, total number of the platelets (n_{pt}) within the RVE (Fig. 8a) was estimated. Since the sintered scaffolds exhibit an approximate 29% volume shrinkage, a correction factor was used in the estimation of the volume of the RVE. Next from the set of the 6 SEM micrographs (1500x), total number of the interlamella platelets was counted and then an average of the interlamella platelets within a RVE ($n_{p(\mathrm{inter})}$) was estimated. Finally, number of the intralamella platelets within a RVE ($n_{p(\mathrm{intra})}$) was estimated from the difference of the ($n_{\mathrm{pt}} - n_{\mathrm{p(inter)}}$) and number/volume fraction of the interlamella to intralamella platelets was determined from the ratio $n_{\mathrm{p(inter)}}/n_{\mathrm{p(intra)}}$.

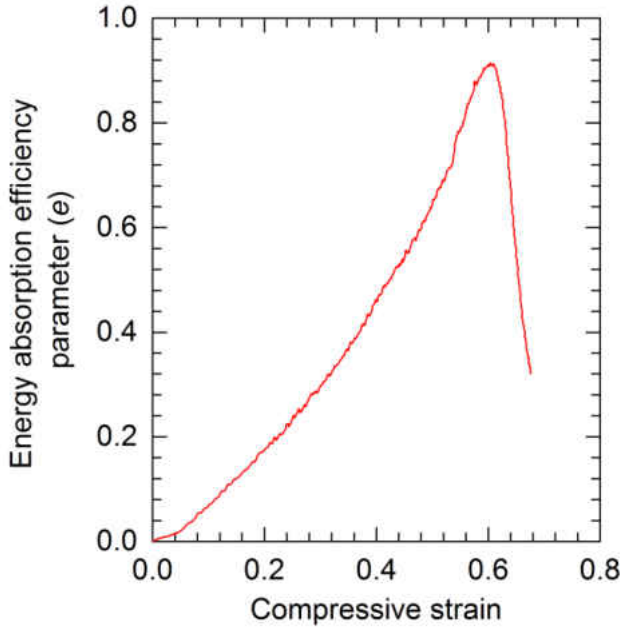

Figure S3: A sample plot variation of the energy absorption parameter (*e*) with compressive strain.

CHAPTER 3

PLATELETS-INDUCED STIFFENING AND STRENGTHENING OF ICE-TEMPLATED HIGHLY POROUS ALUMINA SCAFFOLDS

Note: The contents of this chapter have been published in Scripta Materialia

D. Ghosh, M. Banda, H. Kang, N. Dhavale, Platelets-induced stiffening and strengthening of ice-templated highly porous alumina scaffolds, Scripta Mater., 125 (2016) 29 – 33.

DOI: https://doi.org/10.1016/j.scriptamat.2016.07.030

Abstract

This paper describes the effects of the grain-level anisotropy on the microstructure and uniaxial compressive response of the ice-templated alumina scaffolds. Highly porous (~80 vol.%) scaffolds were fabricated from alumina powders of equiaxed morphology as well as from powder mixtures containing equiaxed and small amount of platelet particles. Presence of the platelets (diameter 8 μm and thickness 400 nm) led to the formation of the interlamellae bridges, and significantly enhanced the stiffness and compressive strength of the scaffolds. Measured improvement of the mechanical response is rationalized based on the stiffening and strengthening effects exhibited by the intralamella and interlamella platelets.

Keywords: Grain morphology; freeze casting; porosity; interlamellae bridging; compressive strength.

3.1 Introduction

Ice-templated anisotropic porous scaffolds can exhibit greater compressive strength relative to the isotropic cellular solids; however, the strength becomes comparable for porosity above 75 vol.%) [7,105]. For the ice-templated scaffolds, rate of freezing, suspension viscosity and pH can be varied to increase the interlamellae bridge density and decrease the pore size for the strength enhancement [9,83,102,105,106,121]. However, such modifications exploiting the above processing variables may not result in an adequate strength improvement for porosity beyond 75 vol.%. Therefore, it is of significant interests to explore the effects of other variables such as the powder particle morphology on the compressive response of ice-templated anisotropic porous ceramics. It may be possible to improve the mechanical response by incorporating grains of anisotropic morphology within the ice-templated porous ceramic scaffold that primarily consist of the equiaxed grains. To this end, we processed ice-templated alumina (Al_2O_3) scaffolds from the equiaxed powder particles as well as from the mixtures of the equiaxed and platelet-shaped particles, and investigated the effects of the induced grain-level anisotropy through platelets addition on the uniaxial compressive response. Overall this manuscript aims to shed light on the effects of the grain morphology on the structure-property (mechanical) relationships of the highly porous (~80 vol.%) ice-templated sintered ceramic scaffolds.

3.2 Materials and experimental approach

Al_2O_3 powders of equiaxed morphology of two different sizes (0.3 and 0.9 μm) and of platelet morphology (diameter ~8 μm and thickness ~400 nm) were utilized; referred to here as NA (nano Al_2O_3) for the 0.3 μm particle size, SA (submicron Al_2O_3) for the 0.9 μm powder particle size, and PA for the Al_2O_3 platelets. Scaffolds were processed from the aqueous suspensions of: (i) NA, (ii)

SA, (iii) 90-10 vol.% mixture of NA and PA, and (iv) 90-10 vol.% mixture of SA and PA. For each suspension, total Al_2O_3 content was 15 vol.% (details of suspension preparation in Supplementary material). Employing a custom-made freeze casting device, Al_2O_3 ceramics were processed within a freezing front velocity (FFV) range of 10 - 35 μm/s. Frozen samples were freeze-dried at 0.014 mbar pressure and -50°C for 96 hours, and sintered at 1550°C for 4 hours. Microstructures of the porous ceramics were characterized from two different planes located at 5 mm (referred to as bottom plane) and 30 mm (referred to as top plane) heights from the bottom of a sample (Fig. S1a). For each sintered scaffold three specimens were extracted from three specific heights (referred to as #1, #2 and #3, Fig. S1b) and uniaxially compressed in the direction of ice growth at a displacement rate of 0.5 mm/min (Tinius Olsen, 10ST). Specimen dimensions of 8 mm × 8 mm × 4 mm were utilized with 8 mm × 8 mm being the loading surface. Sintered density (ρ^*) was determined from the mass and dimensions, and relative density (ρ_r) was estimated using $\rho_r = \rho^*/\rho_s$, where ρ_s is the bulk density of α-Al_2O_3 (3.96 g/cm^3).

3.3 Results and discussion

Figure 1 shows representative SEM micrographs of both the top and bottom planes of the SA, NA, SA-10PA, and NA-10PA porous (sintered) scaffolds processed at relatively low and high FFVs. Pore morphology of the scaffolds is observed to be primarily lamellar; however, some differences are observed in terms of the extent of the interlamellae bridging. Both the SA (Fig. 1a) and NA (Fig. 1c) porous scaffolds exhibit negligible bridging at low FFVs but an increase of the bridge density is observed at relatively high FFVs (Figs. 1e and 1g). Both the SA-10PA and NA-10PA scaffolds exhibit relatively higher bridge density both at the relatively low (Figs. 1b and 1d) and high (Figs. 1f and 1h) FFVs relative to the SA and NA, respectively. However, the interlamellae

bridging is observed to be negligible on the top planes at low FFVs for all the scaffolds compositions. Overall, it can be stated that the bridge density decreased progressively along the ice growth direction (bottom to top). Although not measured but qualitatively for a given composition and FFV, lamella thickness (t) and wavelength (μ) increased gradually along the ice growth direction (Fig. 1). The observed progressive microstructural variations along the ice growth direction are typical of the ice-templated scaffolds and are attributed to the difficulty of maintaining a constant FFV over long distance (cm) [8,9,105,106,121]. Note that the distance in between the bottom and top planes is 2.5 cm (Fig. S1b). Microstructural investigation of all the scaffold compositions at all the FFVs is beyond the scope of this manuscript; however, Fig. 1 indicates that for a given composition the lamellae bridge density increased gradually with the FFV.

Microstructural observations made from Fig. 1 for the SA-10PA and NA-10PA porous scaffolds suggest a governing role of the Al_2O_3 platelets in the interlamellae bridge formation. For the SA-10PA (Fig. 2a), platelets are readily visible in between the lamellae (referred to as interlamella platelets, indicated by green arrows) and within the lamella walls (referred to as intralamella platelets, indicated by yellow arrows). Although most of the intralamella and interlamella platelets are observed to be mutually perpendicular, overall they are orientated in the direction of the ice growth. For both the SA-10PA (Fig. 2a) and NA-10PA (Fig. 2b) scaffolds, the interlamella platelets are observed to form majority of the bridges and a single platelet directly connects the adjacent lamellae for most of the bridges. Growth of the ice crystals during the unidirectional freezing can self-assemble large anisotropic particles and orient those particles along the crystal growth direction [99,100]. Thus, during unidirectional freezing some of the Al_2O_3 platelets ejected by the advancing ice fronts accumulated in between the ice lamellae and were aligned by the

growing ice crystals. As a result, the intralamella platelets are observed to be almost parallel to the lamella walls. On the other hand, lamellae bridges that formed through the interlamella platelets possibly resulted by a different mechanism. As the advancing ice crystals encountered with the Al_2O_3 platelets, some of the platelets were trapped within the crystals by tip-splitting and subsequent healing that led to the bridge formation (Fig. 2c) [7]. The splitted ice fronts moving upward on both sides of the platelet probably oriented the platelet in the direction of the ice crystal growth, resulting the interlamella platelets to be oriented almost vertically with respect to the adjacent lamellae. For simplicity, here, we have shown the interaction of an advancing ice crystal with a single platelet only that after drying and sintering forms a bridge. Another observation is that for the SA-10PA and NA-10PA processed at low FFVs (Fig. 1b and 1d), lamellae bridging through the interlamella platelets is almost absent, although platelets protruding out of the lamella walls can be found (not shown). Although not measured, qualitatively SEM micrographs presented in Fig. 1 suggest that the interlamellae spacing of the porous scaffolds in the relatively low FFV regime is greater than 15 μm. Therefore, it is argued that since the spacing between the adjacent lamellae becomes greater than the platelet diameter (8 μm) towards the top of the samples particularly at the low FFVs, bridging through a single platelet becomes unlikely.

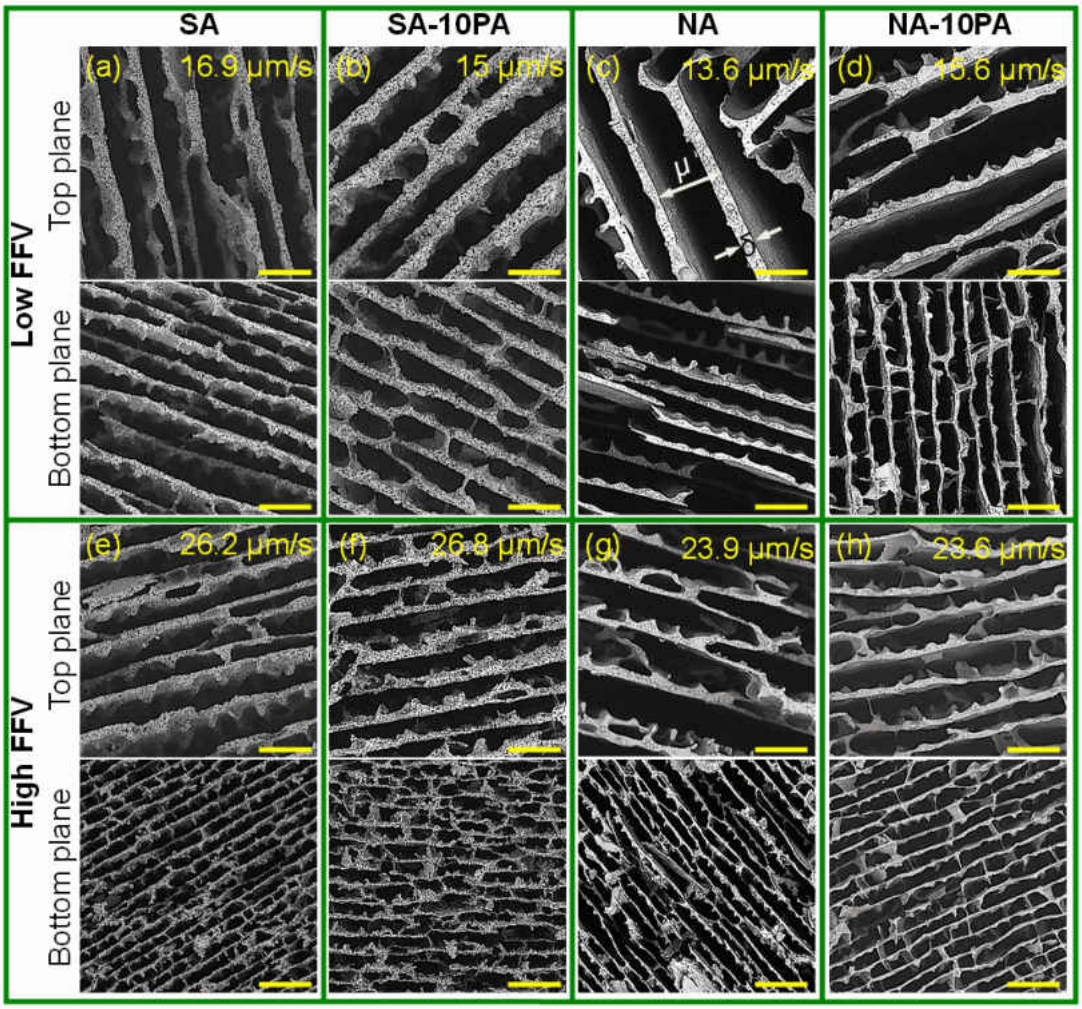

Figure 1: SEM micrographs of the top and bottom planes of the ice-templated porous Al_2O_3 scaffolds processed at relatively low and high freezing front velocities (FFVs). Ice growth direction is out of the page and length of the scale bar is 30 µm.

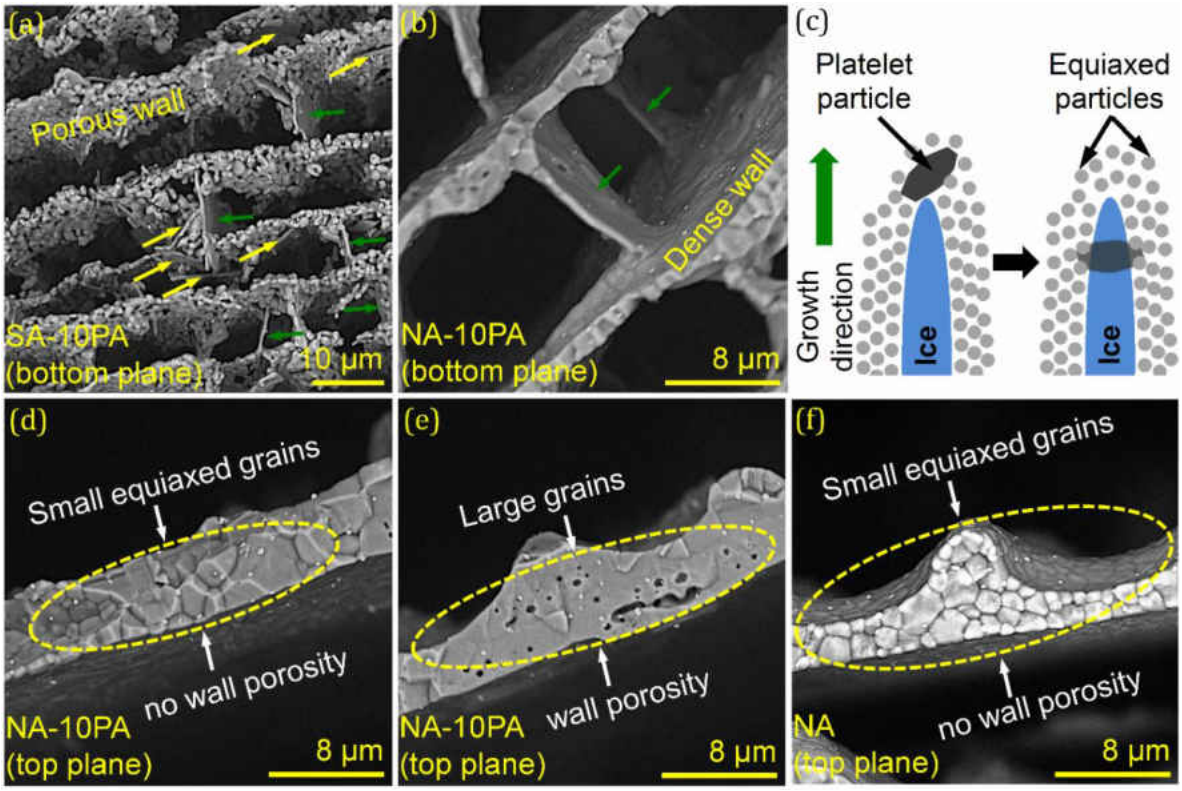

Figure 2: High magnification SEM micrographs revealing (a) intralamella platelets (indicated by yellow arrows) and interlamella platelets (indicated by green arrows) in the SA-10PA, and (b) interlamella platelets (indicated by green arrows) in the NA-10PA. (c) A simplified schematic of the mechanism of interlamellae bridge formation through an interlamella platelet is shown. High magnification SEM micrographs further revealing (d) a dense lamella wall with equiaxed fine-grained microstructure of the NA-10PA, (e) micropores within the lamellae walls of the NA-10PA, and (f) dense and equiaxed fine-grained microstructure of the NA. For all the SEM micrographs ice growth direction is out of the page.

Furthermore, lamellae of the SA-10PA are observed to be significantly more porous than those of the NA-10PA, and the interlamella platelets are well bonded to the lamellae of the NA-10PA (Fig. 2b) in comparison to those of the SA-10PA (Fig. 2a). Decrease of the ceramic particle size

enhances densification during sintering [122]. Additionally, smaller particles can pack better in between the ice lamella [123]. Therefore, greater sinterability and better particle packing of the relatively finer NA particles (0.3 μm) in comparison to the relatively coarser SA particles (0.9 μm) resulted in the greater densification of the NA-10PA scaffolds in comparison to the SA-10PA scaffolds; also supported by the higher ρ_r of the former relative to the later (Fig. 3a). Another observation is that the platelets are not readily visible within the lamellae walls of the NA-10PA unlike that of the SA-10PA. A closer view of the lamellae cross-sections of the NA-10PA revealed that most of the regions are dense with no visible porosity and contain small equiaxed grains (Fig. 2d); however, there are areas that contain micropores and absence of the equiaxed fine grains can be noticed (Fig. 2e). Since the NA scaffolds (i.e., without platelets) exhibit a fine-grained microstructure without any visible microporosity (Fig. 2f), we argue that localized templated grain growth (TGG) might have occurred in the NA-10PA leading to the absence of the fine-grained microstructure and development of the microporosity at some areas within the lamellae walls [101]. Although no glassy phase that aids the TGG was utilized here, finer NA particles probably facilitated the TGG. Overall, it can be stated that the lamellae walls of both the SA-10PA and NA-10PA porous scaffolds contain anisotropic Al_2O_3 grains dispersed within the matrix of equiaxed Al_2O_3 grains, and are connected through the interlamella platelets. Therefore, utilizing powder particles of the platelet morphology, it is possible to make microstructural modifications at multiple length-scales, induce a grain-level anisotropy, and develop interlamellae bridges in the ice-templated scaffolds.

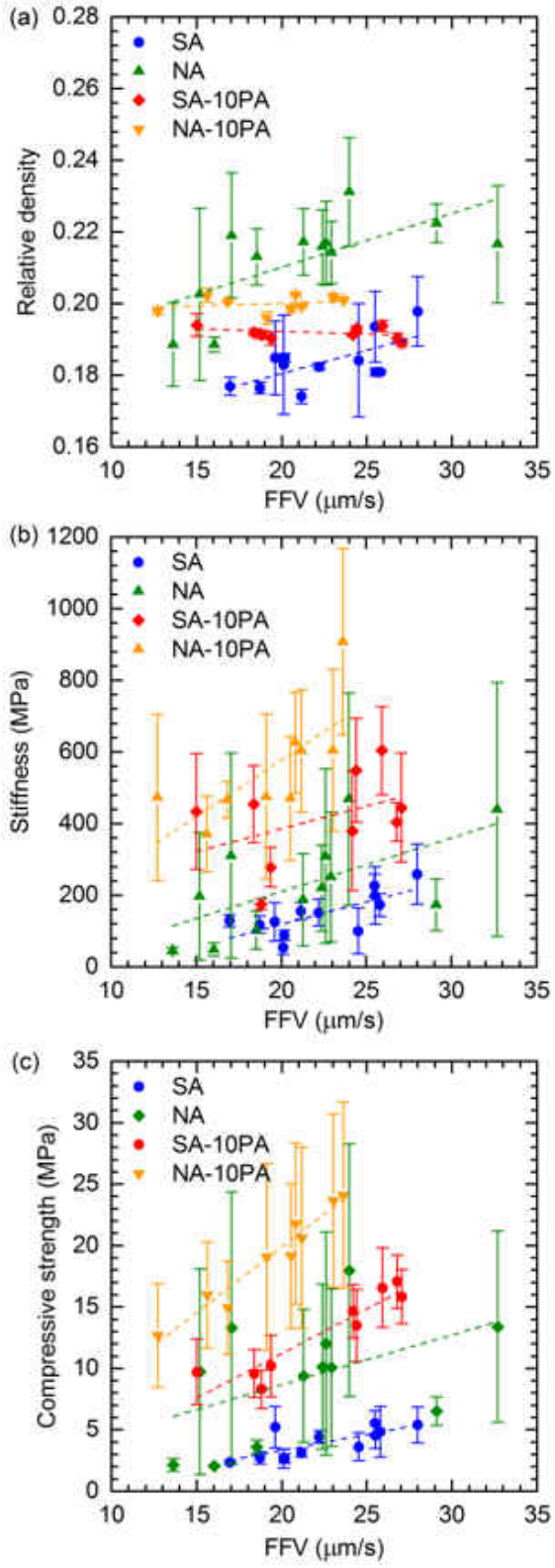

Figure 3: Variation of the (a) relative density, (b) stiffness, and (c) compressive strength with freezing front velocity (FFV) of the NA, SA, SA-10PA, and NA-10PA scaffolds.

Figure 3 shows variation of the ρ_r (Fig. 3a), stiffness (Fig. 3b), and compressive strength (Fig. 3c) with the FFV. For each composition and FFV, average and standard deviation of ρ_r, stiffness and compressive strength were estimated from the corresponding values of the #1, #2 and #3 specimens. Dotted lines shown in Fig. 3 are provided to simply to show the apparent trends of the data and do not necessarily present the actual trend lines. Total porosity ((1-ρ_r)*100) of all the scaffolds is observed to be within the range of 77-83 vol.%. ρ_r of both the NA and SA increases almost linearly with the increasing FFV; however, over the entire range of FFV, ρ_r of the former (ranges from 0.19-0.23) is observed to be greater relative to that of the later (ranges from 0.17-0.2). Although the SA and NA scaffolds were processed from the suspensions of the same concentration, the final ceramic content is influenced by both the powder particle size and FFV. Higher ρ_r of the NA relative to the SA is attributed to both the better particle packing in between the ice lamellae and sinterability of the relatively finer NA powder. Increase of the ρ_r with the FFV is rationalized based on the pore curvature [103]. Mass transport during densification is enhanced by a decrease of the radius of curvature of the solid-vapor interface and sintered density thus increases with the decrease of the pore curvature. Since the interlamellae bridge density of both the NA and SA increases with the FFV, pores become more dendritic and the pore curvature decreases, resulting in an increase of the density with the FFV [103]. ρ_r of both the SA-10PA and NA-10PA, however, remains almost constant over the entire range of FFV, although ρ_r of the former is observed to be slightly lower relative to that of the later. Also, while the ρ_r of the SA-10PA remains relatively higher in comparison to the SA except at the high FFVs, ρ_r of the NA-10PA is observed to be lower relative to that of the NA. The observed trend of ρ_r of the SA-10PA and NA-10PA scaffolds is not well understood and requires further microstructural investigation. However, one possible explanation is that the smallest dimension of the platelets (thickness 0.4

μm) is smaller than the characteristic size of the SA particles (0.9 μm) but larger than the characteristic size of the NA particles (0.3 μm). This could result in a better packing fraction for SA-10PA compared to SA but a worse packing fraction for NA-10PA compared to NA. The observed decrease of the ρ_r of the NA-10PA relative to the NA is attributed to the micropores present within the lamellae walls of the former as a result of the TGG.

Stiffness of the ice-templated sintered scaffolds was estimated from the slope of the linear part of the uniaxial compressive stress-strain curves. In spite of the considerable scatter in the data, stiffness of all the Al_2O_3 scaffolds seems to exhibit an almost linearly increase with the FFV (Fig. 3b). Slightly higher stiffness of the NA relative to the SA is attributed to the higher ρ_r of the former than the later. On the other hand, considerably greater stiffness of both the NA-10PA and SA-10PA relative to the SA and NA, respectively, is attributed to the platelets-induced stiffening effects due to presence of the intralamella platelets and interlamella platelets (forming interlamellae bridges). Similar to the stiffness, in spite of the significant scatter of the data uniaxial compressive strength of the scaffolds also increases almost linearly with the FFV (Fig. 3c). Greater compressive strength of the NA in comparison to the SA is attributed to the higher ρ_r of the former relative to the later. On the other hand, significant increase of the strength of the SA-10PA and NA-10PA scaffolds relative to the SA and NA scaffolds, respectively, is attributed to the platelets-induced strengthening effects, similar to the platelets-induced stiffening. Increase of the stiffness and compressive strength with the FFV is, in general, a result of the gradual increase of the interlamellae bridge density with the FFV (Fig. 1) [103,105].

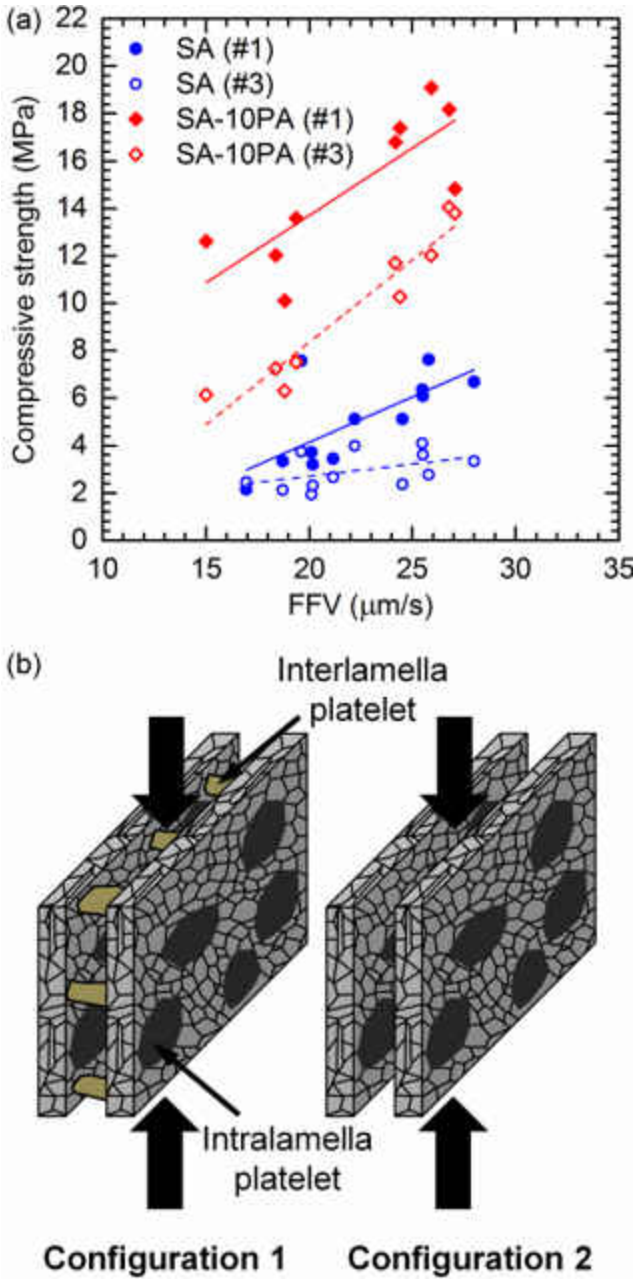

Figure 4: (a) Variation of the compressive strength of the #1 and #3 specimens of the SA and SA-10PA scaffolds with the FFV, and (b) schematics to describe the uniaxial compressive response of the lamellae walls with both the intralamella platelets and interlamella platelets (*Configuration 1*), and with only the intralamella platelets (*Configuration 2*).

To further embark on the platelets-induced strengthening mechanism, we show in Fig. 4a the variation of the compressive strength of the #1 and #3 specimens with FFV of the SA and SA-10PA scaffolds. Over the entire range of FFV, strength of the #1 and #3 specimens of the SA-10PA is observed to be consistently greater in comparison to that of the SA, which is attributed to the platelets-induced strengthening effects. However, since the strength of the #1 specimens is consistently greater than that of the #3 specimens of the SA-10PA, we argue that this difference may be due to the variation of the contribution of the platelets-induced strengthening effects in between the #1 and #3 specimens. Since ρ_r of the #1 specimens is only slightly higher in comparison to that of the #3 specimens of the SA-10PA scaffolds (Fig. S2, Supplementary material), this marginal difference of ρ_r may not account for the considerable strength difference that is observed in between the #1 and #3 specimens. Recall from Figs. 1 and 2 that both the intralamella platelets and interlamella platelets (forming interlamellae bridges) are observed on the bottom plane both at the relatively low and high FFVs. On the top plane, both the intralamella platelets and interlamella platelets (forming bridges) are observed at the relatively high FFV, but mainly the intralamella platelets are present at the relatively low FFV. Therefore, it can be stated that for the #1 specimens platelets are present at both the intralamella and interlamella locations, and the bridge density increases gradually with the FFV. On the other hand, for the #3 specimens in the low FFV regime, platelets are present primarily within the lamellae walls and the interlamellae bridges through the interlamella platelets probably started to develop only in the high FFV regime. We schematically present these two specific scenarios in Fig. 4b, where both the intralamella platelets and interlamella platelets (forming bridges) are present for the *Configuration 1*, whereas only the intralamella platelets are present for the *Configuration 2*. Under the uniaxial compressive loading of the *Configuration 1*, both the intralamella platelets and bridge forming

interlamella platelets will resist the Euler buckling of the lamellae, and prevent the crack propagation through the parallel lamellae walls as well as brittle fracture of the individual lamella walls. On the other hand, for the *Configuration 2*, only the intralamella platelets will resist the Euler buckling and fracture of the individual lamella walls. Therefore, ice-templated sintered porous scaffolds with the *Configuration 1* can exhibit better mechanical properties in comparison to the scaffolds with the *Configuration 2*, as is observed in Fig. 4a.

3.4 Conclusions

This study reveals the effects of the grain morphology on the uniaxial compressive response of the ice-templated sintered porous Al_2O_3 scaffolds. It is shown that by incorporating grains of platelet morphology within the scaffolds that mainly consist of the equiaxed grains, both the stiffness and strength under uniaxial compressive loading conditions can be significantly improved. The observed platelets-induced stiffening and strengthening of the porous scaffolds are attributed to the reinforcement effects due to presence of the platelets within the lamellae walls (intralamella platelets) and in between the lamellae walls (interlamella platelets). Furthermore, this study reveals the advantage of using finer powder particles to enhance the strength of the ice-templated sintered porous scaffolds. This study thus presents a novel approach to significantly improve the compressive response of the ice-templated porous sintered ceramics by inducing grain-level anisotropy, however, without modifying the overall materials composition and porosity. Such grain-level anisotropy can also be employed to modify the functional properties of freeze-cast materials. Overall, results presented here are expected to provide significant insights to design bio-inspired hierarchical materials for structural, biomedical and energy storage applications.

Acknowledgements

The authors thank the Applied Research Center (ARC) of College of William and Mary for providing the access to the desktop SEM and Prof. Xiaoyu Zhang (Mechanical and Aerospace Engineering, Old Dominion University) for providing access to the high temperature furnace. DG acknowledges the Summer Research Fellowship Program (SRFP 2015), Office of Research, Old Dominion University. DG and HK also acknowledge the support of the Honors College and Office of Research, Old Dominion University, under the Program for the Undergraduate Research and Scholarship (PURS).

3.5 Supporting information

Preparation of aqueous alumina (Al_2O_3) suspensions and freeze casting

In this work, commercially available Al_2O_3 powders were utilized (0.3 μm, APA-0.5, Sasol, Tuscan, AZ; 0.9 μm, Alfa Aesar, Ward Hill, MA; platelets, Alusion^{TM}, Antaria Ltd., Bentley, Western Australia). For each suspension, required amount of the Al_2O_3 powder(s) and small amount (0.5 wt.% of the powder) of ammonium polymethacrylate anionic dispersant (Darvan C, R.T. Vanderbilt Co., Norwalk, CT) were first mixed in deionized water, and milled for 24 hours. Next, an organic binder poly(2-ethyl-2-oxazoline) was added to the slurry (5 wt.% of the powder) and mixed for another hour. Afterwards, the ZrO_2 spheres were separated from the slurry and de-aired for 30 min.

Freeze casting was conducted using a custom-made set up. In this set up, a Teflon tube is placed on the top of a thin (0.5 mm) steel plate, partially filled with Al_2O_3 slurry, and the whole assembly is inserted inside a liquid nitrogen (N_2) Dewar. By adjusting the distance between the steel plate and liquid N_2, freezing front velocity (FFV) was controlled. Average FFV was estimated by

dividing the frozen sample height with the total time required for freezing of the sample. All the materials were processed within a FFV range of 10 - 35 μm/s.

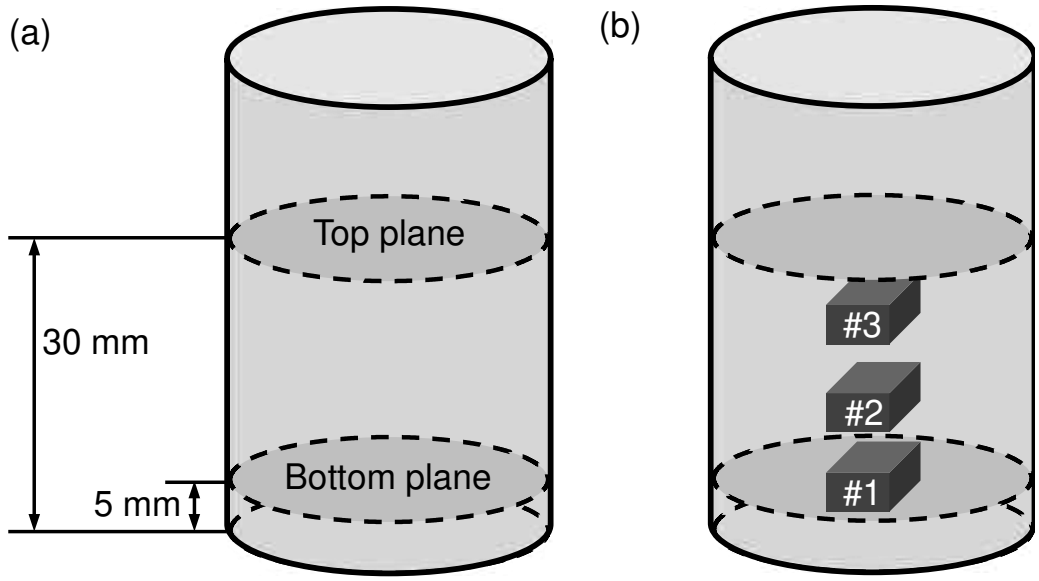

Figure S1: Schematic presentation of the locations of the (a) top and bottom planes, and (b) #1, #2 and #3 compression tests specimens.

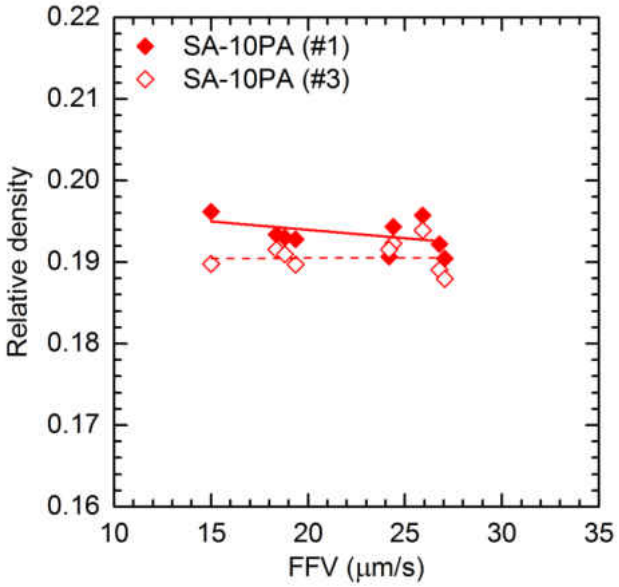

Figure S2: Variation of the relative density of the #1 and #3 specimens of the SA-10PA scaffolds with the FFV.

CHAPTER 4

ON THE BRITTLE FRACTURE CHARACTERISTICS OF LAMELLA WALLS OF ICE-TEMPLATED SINTERED ALUMINA SCAFFOLDS AND EFFECTS OF PLATELETS

Note: The contents of this chapter have been published in Scripta Materialia

D. Ghosh, M. Banda, S. Akurati, H. Kang, V. O. Fakharizadeh, On the brittle fracture characteristics of lamlella walls of ice-templated sintered alumina sacffolds and effects of platelets, 138 (2017) 139 – 144.

DOI: http://dx.doi.org/10.1016/j.scriptamat.2017.05.049

Abstract

We attempted to develop a phenomenological understanding of the evolution of the fracture events within fine-grained lamella walls of partially deformed ice-templated sintered Al_2O_3 scaffolds and revealed the effects of the platelets on the crack propagation characteristics. Detailed microstructural analyses suggest that intergranular cracks within the walls evolved at two orientations, parallel and perpendicular to the loading direction. We proposed probable mechanisms including one based on the so-called wing-crack model to rationalize the observed crack orientations. We presented crack propagation behavior in lamella walls in presence of the platelets and discussed the effects in terms of the crack deflection mechanism.

Keywords: Ice-templating; polycrystalline lamella walls; intergranular fracture; platelets; crack deflection.

4.1 Introduction

Uniaxial compressive stress-strain response of ice-templated sintered ceramic scaffolds is akin to that of the cellular ceramics that features a linear elastic regime, a stress plateau part with a gradual decrease of stress with increasing strain, and a densification stage with a sharp rise of stress with a small increase of strain [9,103,112]. A general understanding is that inelastic deformation of ice-templated ceramics in the stress plateau regime proceeds through the brittle crushing of the polycrystalline lamella walls [104-106]. There is, however, no detailed study on the fracture characteristics of the lamella walls, which is essential to model the underlying damage-mechanics. It is also important to investigate the effects of the microstructural modifications of the lamella walls on the fracture characteristics, such that their relation to the macroscopic mechanical behavior of the ice-templated ceramics can be understood. The authors have recently investigated the influence of the anisotropic grains (platelets: diameter ~8 μm and thickness ~400 nm) on the microstructure and uniaxial compressive response of highly porous (~80 vol.%) ice-templated sintered alumina (Al_2O_3) scaffolds, where the scaffolds were mainly fabricated from the submicrometer equiaxed particles and from the mixtures of the submicrometer equiaxed particles and the platelets [108,124]. Findings of the investigation revealed an unprecedented improvement of the compressive response of the scaffolds containing small volume fraction of platelets relative to the scaffolds without the platelets. In that context, aim of the current study is twofold: (i) shed light into the fracture mechanisms that evolve under the influence of the compressive loading within the polycrystalline lamella walls of ice-templated sintered Al_2O_3 scaffolds containing fine equiaxed grains (~2 μm) and (ii) reveal the influence of the platelets (i.e., the anisotropic grains) present within the lamella walls on the crack propagation characteristics.

4.2 Experimental approach

A custom-made device was employed to synthesize the ice-templated Al_2O_3 scaffolds, which were processed from the aqueous suspensions containing (a) fine equiaxed Al_2O_3 powder (average diameter 300 nm, referred to here as NA and corresponding scaffolds as NA-scaffolds) and (b) 80-20 vol.% mixture of the NA powder and the Al_2O_3 platelets (referred to here as PA and corresponding scaffolds as NA20PA-scaffolds). For each suspension, total Al_2O_3 content was 15 vol.%. All the scaffolds were unidirectionally solidified, and average freezing front velocity (FFV) was 30.6 ± 1.8 μm/s and 30.6 ± 1.5 μm/s for the NA-scaffolds and NA20PA-scaffolds, respectively. Frozen scaffolds were freeze-dried at 0.014 mbar pressure and -50°C for 96 hours, and sintered at 1550°C for 4 hours. From each sintered scaffold, a 6 mm × 6 mm × 3 mm specimen was extracted for density measurements, microstructural characterization, and uniaxial compression tests. Sintered specimens were compressed beyond the densification stage to capture the complete uniaxial stress-strain response. However, one specimen from each composition was compressed up to 15% strain and the obtained fragments were analyzed using an SEM to reveal the fracture characteristics within the polycrystalline lamella walls. Further experimental details are provided in the Supplementary Material.

4.3 Results and discussion

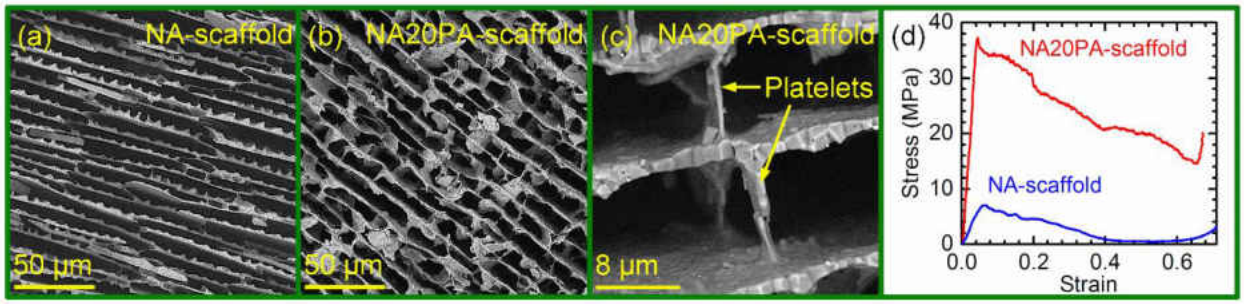

Figure 1: SEM micrographs reveal (a) lamellar pore morphology of the NA-scaffold and (b) dendritic pore morphology of the NA20PA-scaffold, and (c) high magnification SEM micrograph shows lamellar bridge formation through the platelets (ice-growth direction is out of the page). (d) Comparison of uniaxial compressive response of the NA-scaffold and the NA20PA-scaffold.

Figures 1a and 1b show the representative SEM micrographs of the top plane of a NA-scaffold and a NA20PA-scaffold, respectively. Pore morphology of the NA-scaffold appears lamellar, whereas the extent of the bridging is observed to have increased significantly in the NA20PA-scaffold and resulted in a dendritic pore architecture. Figure 1c shows a representative high magnification SEM micrograph of the NA20PA-scaffold that reveals the formation of the lamellar bridges through the platelets. A significant fraction of the bridges of the NA20PA-scaffolds formed through the platelets, usually a single platelet connected the adjacent lamella walls, and an increase of the bridge density is attributed to the additional bridge formation through the platelets. Lamella walls of the NA-scaffolds are observed to be dense, whereas some micropores can be noticed within the walls of the NA20PA-scaffolds. Average relative density ($\rho_r = \rho^*/\rho_s$, where ρ_s is the bulk density of α-Al_2O_3, 3.96 g/cm^3) values of the NA-scaffolds and NA20PA-scaffolds are measured to be 0.23 and 0.19, respectively. Thus, the total average porosity ((1-ρ_r)*100) values

of the NA-scaffolds and the NA20PA-scaffolds are found to be 77% and 81%, respectively. We attribute the increased porosity in the NA20PA-scaffolds to the micropores present within the polycrystalline lamella walls. Figure 1d shows representative uniaxial compressive stress-strain curves of NA-scaffolds and NA20PA-scaffolds. NA20PA-scaffolds exhibit a marked improvement of the compressive response in comparison to that of the NA-scaffolds, suggesting a dramatic influence of the platelets on the compressive mechanical properties.

Figures 2a and 2b show microstructure of the lamella wall of the NA-scaffold and the NA20PA-scaffold, respectively. For the NA-scaffold, a fine-grained homogeneous microstructure can be observed, and the lamella wall appears dense. Lamella wall of the NA20PA-scaffold also exhibits similar microstructural features such as the fine Al_2O_3 grains. However, the presence of the relatively larger grains within the lamella wall of the NA20PA-scaffold can also be observed. Another distinct difference is the presence of the micropores in the lamella wall of NA20PA-scaffold, and it is interesting to observe that the micropores are predominantly present inside the large grains, Fig. 2b. We suggest that majority of the large grains (indicated by the yellow arrows in Fig. 2b) are actually the Al_2O_3 platelets. Since the micropores in the NA20PA-scaffolds are observed only within the regions containing the large grains and not in the NA-scaffold, we conjecture that origin of the microporosity is related to the Al_2O_3 platelets. One possibility is that localized templated grain growth (TGG) [101] probably occurred in the NA20PA-scaffolds, where the fine NA-powder particles (300 nm) might have facilitated the TGG and led to the development of the micropores.

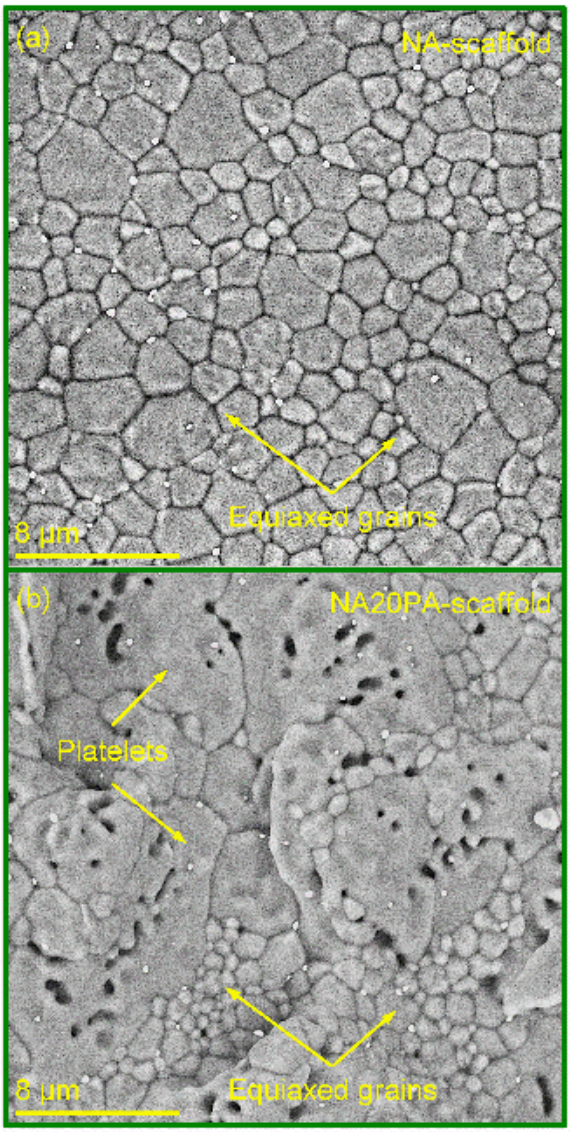

Figure 2: Polycrystalline microstructure of the lamella wall of the sintered (a) NA-scaffold and (b) NA20PA-scaffold.

Figure 3a shows a low magnification SEM micrograph of the fractured lamella walls within a fragment, which corresponds to the NA-scaffold that was deformed up to a strain of 15%. Significant damage is evident and brittle fracture of the individual lamella walls occurred mainly in two orientations, parallel and perpendicular to the applied loading direction, which is also the ice-growth direction (shown by the solid block arrow). While the microstructural analysis revealed

mainly the presence of large size fragments of the walls, there are also regions where the walls are observed to be extensively fractured resulting in the formation of finer fragments as indicated by the dotted white square in Fig. 3a. Therefore, it can be stated that in the plateau regime, with the increasing deformation extensive fragmentation of the walls will continue to occur up to the densification stage. A closer observation of the fragmented walls revealed intergranular (grain boundary) cracking as the mode of brittle fracture. Figure 3b shows an intergranular crack within the lamella wall, where the crack propagated almost perpendicular to the loading direction. Similarly, Fig. 3c reveals another intergranular crack within the wall that propagated in between two ridges (which developed during the ice-growth and are parallel to the growth direction) and almost parallel to the loading direction. It is of note that the lamella walls shown in Figs. 3b and 3c were still attached to the other walls, observed to be only partially cracked, and, therefore, are useful to gain insights into the micromechanisms of brittle fracture within the walls. In sintered dense Al_2O_3 ceramic, cracks typically propagate transgranularly (i.e., intragranular fracture mode) for the coarse-grained microstructure and switches to the intergranular fracture mode as the grain size is reduced [114]. Therefore, the observed intergranular crack propagation within the lamella walls is attributed to the fine-grained Al_2O_3 microstructure.

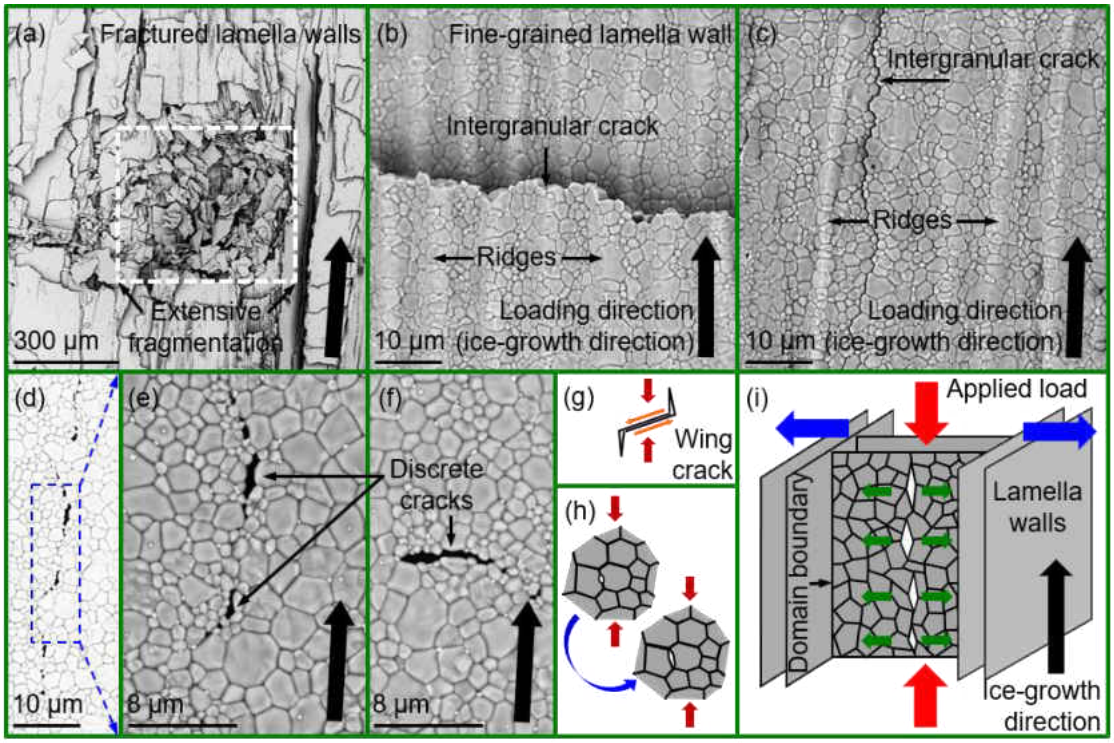

Figure 3: (a) Fragmented lamella walls of the NA-scaffold deformed up to a strain of 0.15 and a region of extensive fragmentation is indicated by a white dotted box. Intergranular crack propagation within the lamella walls of the partially deformed NA-scaffold, where the cracks are oriented (b) perpendicular and (c) parallel to the loading direction. (d) A region within the lamella wall of the NA-scaffold exhibits discrete mesocracks oriented towards the loading direction and (e) a high magnification SEM micrograph reveals the formation of the discrete cracks by the separation of the grains (microvoids along the grain boundaries). (f) Formation of a mesocrack oriented almost perpendicular to the loading direction. Schematic representations (g) of the so-called wing crack model and (h) a probable mechanism of a mesocrack development at the grain boundary that can lead to the intergranular cracks oriented towards the loading direction. (i) Another possible mechanism for the formation of intergranular cracks parallel to the loading direction (schematics not to scale). The solid block arrow indicates ice-growth direction.

Formation of the intergranular cracks in the orientations parallel and perpendicular to the loading direction suggests that they were probably formed under the influence of different stress states or by different mechanisms. However, without any modeling effort, it is challenging to predict the stress fields that actually evolve in the ice-templated ceramic scaffolds under the uniaxial compressive loading conditions. Nevertheless, here we made an attempt to develop a phenomenological understanding of the governing stress fields or the mechanisms that might have led to the observed crack propagation orientations with respect to the loading direction. To that end, we conducted more rigorous microstructural analysis to decipher any evidence that may help to understand the fracture events within the polycrystalline lamella walls of the sintered Al_2O_3 scaffolds under the compressive loading conditions. Figure 3d (intentionally brightened to make the discontinuity of the crack path distinctively visible) shows a region within a lamella wall where a series of discrete small cracks (mesocracks) are observed to be oriented towards the loading direction. It can be envisioned that although the cracks are not connected, further extension of the crack tips probably would have caused them to grow and coalesce into a single large crack. Therefore, it can be stated that Fig. 3d probably represents a region within the lamella wall that is at the onset of fracture. We have also made similar observations within many other lamella walls. A closer look at these discrete mesocracks revealed that they are the microvoids that developed due to the separation of the grains and are oriented towards the loading direction, Fig. 3e. Additionally, we observed similar microvoids within the lamella walls that are oriented away from the loading direction (almost perpendicular to the loading direction), Fig. 3f. It is of note that the lamella walls of the sintered NA-scaffolds appear to be fully dense and microstructural analysis did not reveal any presence of the microvoids within the walls of the undeformed scaffolds. Therefore, when an ice-templated sintered ceramic scaffold is subjected to uniaxial compression

load, it is possible that primarily two sets of mesocracks develop intergranularly within the lamella walls. Cracks in one set are oriented towards the loading direction, whereas in the other set away from the loading direction. The growth of the mesocracks leading to their coalescence and formation of a large single crack that can ultimately cause rupture of the walls will be governed by the stress concentration at the crack tips.

We will now attempt to understand the origin of the observed crack propagation orientations within the lamella walls with respect to the loading direction. Under uniaxial compression tall, slender, brittle lamella walls of the ice-templated sintered Al_2O_3 scaffolds can be considered to be subjected to bending/Euler buckling [83,124]. Therefore, it can be envisioned that at a critical stress level, isolated intergranular mesocracks oriented (almost) perpendicularly to the loading direction start to develop (Fig. 3f), which can continue to grow to coalesce and eventually cause rupture of the lamella walls (Fig. 3b). On the other hand, origin of the cracks oriented towards the loading direction is perhaps more challenging to understand. Since the lamella walls are dense, we draw a parallel in between the dense polycrystalline walls of the ice-templated sintered Al_2O_3 scaffolds and the dense polycrystalline ceramics to rationalize the origin of the intergranular cracks being oriented towards the applied load. In dense ceramics, under uniaxial compression cracks grow in an orientation that is (almost) parallel to the loading direction and brittle failure occurs by the axial splitting [125,126]. Compressive failure characteristics of dense polycrystalline ceramics has been rationalized by the so-called wing crack model (Fig. 3g) [125-127]. According to this model, under the uniaxial compressive loading conditions each individual sliding microcrack nucleates tensile wing cracks and upon reaching a critical stress intensity factor (mode I stress intensity factor, K_I) the wing cracks start to grow in a stable manner in the direction of compression. A number of microcracks can grow until they interact, coalesce, and cause eventual failure in ceramics by the

axial splitting. For the dense polycrystalline lamella walls of the ice-templated scaffolds, one possibility is that under compressive loading separation of the Al_2O_3 grains results in the formation of the microvoids and each microvoid can occupy the entire straight segment of the grain boundaries, i.e., the formation of a mesocrack (Fig. 3h) [128]. Next, the mesocracks can nucleate tension cracks (wing cracks), which will continue to grow until they coalesce, form a large single crack, and eventually cause failure of the lamella walls. This process can result in the formation of the intergranular cracks within the lamella walls to be oriented towards the loading direction, Fig. 3c. Another possibility is depicted using a simplified schematic in Fig. 3i, where three sets of lamella walls are subjected to uniaxial compression. Since the lamella walls are randomly oriented on the plane perpendicular to the ice-growth direction, each set of parallel walls is connected with the other sets of the parallel walls along the domain boundaries. For the sake of simplicity, polycrystalline microstructure is only shown for the front wall. It is typical for the ice-templated sintered ceramics scaffolds subjected to uniaxial compression that the walls tend to split apart along the domain boundaries and spread out laterally in a mushroom-like structure [104-106], which was also observed for the NA-scaffolds (not shown here). Therefore, under uniaxial compression, as the walls on the left and right hand sides (Fig. 3i) tend to separate along the domain boundaries they can create tensile stress in the middle set of walls acting approximately perpendicular to the loading direction, Fig. 3i. This mechanism may also nucleate mesocracks oriented towards the loading direction (Fig. 3d) and ultimately can result in the development of the intergranular cracks parallel to the loading direction (Fig. 3b).

Finally, we present the fracture characteristics of the lamella walls of the NA20PA-scaffold that contains Al_2O_3 platelets and was deformed up to a strain of 0.15 under the compressive loading conditions. Figures 4a and 4b reveal the crack propagation characteristics within the lamella walls

at two different locations, where similar features can be observed in both the regions. Therefore, microstructural analysis of the lamella walls of the partially deformed NA20PA-scaffold suggests that brittle fracture of the lamella walls occurred through the intergranular crack propagation, which is similar to that observed for the walls of the NA-scaffolds. An interesting observation is that within the walls of the NA20PA-scaffold cracks not only propagated through the boundaries of the fine equiaxed grains but also through the interface areas between the equiaxed grains and the platelets. Also, the microstructural analysis, in general, indicates that the Al_2O_3 platelets remain intact. A general scenario can thus be envisioned that as a crack encountered a platelet with the lamella wall of the NA20PA-scaffold, the crack was deflected towards the interface of the fine equiaxed grain and the platelet, rather than propagating transgranularly through the platelet as illustrated schematically in Fig. 4c. Lack of fracture of the platelets within the lamella walls can be attributed to the significantly greater fracture strength of the individual platelets [91]. Therefore, it can be stated that the Al_2O_3 platelets triggered a crack deflection mechanism within the lamella walls, which can be considered to attribute extrinsic toughening [119] to the walls. As a result, lamella walls of the NA20PA-scaffolds can exhibit additional resistance to the inelastic deformation.

There are multiple factors that might have led to the drastic improvement of the stiffness, peak stress and plateau stress of the NA20PA-scaffolds in comparison to the NA-scaffolds. Addition of the platelets enhances the extent of the lamellar bridging and induces a grain-level anisotropy within the polycrystalline microstructure of the lamella walls. Increase of the stiffness of the NA20PA-scaffolds can be attributed to both the enhanced lamellar bridge density and the induced grain-level anisotropy. Lamellar bridges help to hold together the lamella walls such that the walls do not separate and spread out laterally under compression. Therefore, an increase of the bridge

density will enhance the overall structural rigidity of the NA20PA-scaffolds and, thereby, the compressive stiffness. Simultaneously, microstructural modifications of the bridges and the lamella walls due to the presence of the platelets can also contribute to enhancing the stiffness. This is because Young's modulus of the Al_2O_3 single crystals (425–460 GPa) [115] is greater than that of the fine-grained Al_2O_3 ceramics (393 GPa) [116]. Therefore, during the compressive loading relatively stiffer platelets can enhance the bending/buckling resistance of the walls and, thereby, the stiffness of the NA20PA-scaffolds. On the other hand, compressive crushing of the ceramic scaffolds will be influenced by the fracture characteristics of the lamella walls. Strength of the platelets (>2GPa) [91] is significantly greater in comparison to the flexural strength of fine-grained polycrystalline Al_2O_3 ceramics (~500 MPa) [118]. Therefore, presence of the high-strength platelets within the lamella walls of the NA20PA-scaffolds will invariably enhance the compressive fracture strength of the walls and, thereby, of the scaffolds. While the individual lamella walls will fail through the intergranular mode of fracture, crack deflection at the interface areas of the fine equiaxed grains and the platelets (Fig. 4) will further enhance the crack propagation resistance of the walls and improve the compressive response of the NA20PA-scaffolds (Fig. 1d). Therefore, the detailed investigations of the microstructural mechanisms of fracture within the lamella walls and the associated phenomenological rationale of the fracture events provide a necessary foundation to thoroughly comprehend the role of the platelets leading to the measured marked improvements of the compressive response of the NA20PA-scaffolds over the NA-scaffolds.

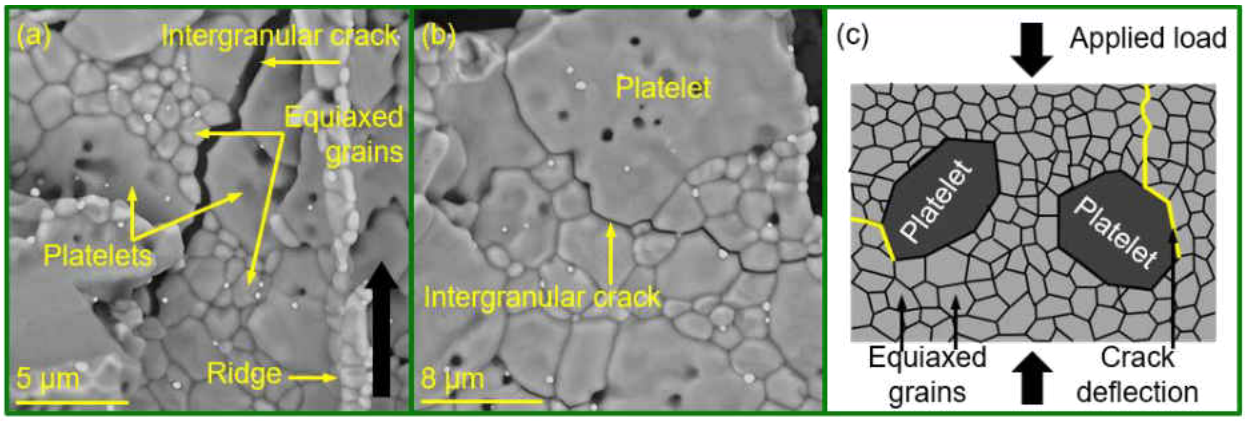

Figure 4: (a) and (b): Crack propagation characteristics within the lamella walls of the partially deformed (0.15 strain under compression) NA20PA-scaffold. (c) A schematic representation of crack deflection at the interface areas in between the equiaxed grains and the platelets (not to scale).

4.4 Conclusions

In summary, this study reveals the fracture mechanisms within the polycrystalline lamella walls of ice-templated sintered Al_2O_3 scaffolds, which were fabricated from equiaxed submicrometer powder and from the mixture of equiaxed submicrometer powder and platelets. Uniaxial compressive response measurements showed a marked improvement for the scaffolds containing platelets relative to the scaffolds without the platelets. To understand the fracture events within the lamella walls, some of the scaffolds were deformed only up to a strain level of 0.15 and the obtained fragments were analyzed in an SEM. Intergranular cracking was identified as the dominant brittle fracture mechanism within the lamella walls. Based on the rigorous microstructural analyses of the partially fractured regions of the lamella walls, we suggest that intergranular cracks evolved mainly in two orientations, parallel and perpendicular to the compressive loading direction. We attempted to develop a phenomenological understanding of the

evolution of the fracture events within the lamella walls under the uniaxial compressive loading conditions and proposed probable mechanisms to rationalize the microstructural observations of the crack propagation orientations. For the scaffolds containing the platelets, intergranular cracking remained the dominant fracture mechanism and crack deflection at the interface of fine equiaxed grain and platelet is noticed. We conjecture that crack deflection at the interface of fine equiaxed grain and platelet can lead to an extrinsic toughening of the lamella walls and might have contributed to the measured markedly improved compressive response of the NA20PA-scaffolds. We emphasize that insights into the fundamental brittle fracture mechanisms within the polycrystalline lamella walls of the ice-templated ceramics is essential to understand the structure-property relationships and design mechanically robust lightweight materials.

Acknowledgements

The authors thank the Applied Research Center (ARC) of College of William and Mary for providing access to the desktop SEM. DG and HK also acknowledge the support of the Honors College and Office of Research, Old Dominion University, under the Program for the Undergraduate Research and Scholarship (PURS).

4.5 Supporting information

Preparation of aqueous alumina (Al_2O_3) suspensions, freeze casting and characterization

In this work, commercially available Al_2O_3 powders were utilized (0.3 μm and equiaxed morphology, APA-0.5, Sasol, Tuscan, AZ; platelets, Alusion^{TM}, Antaria Ltd., Bentley, Western Australia). For each suspension, required amount of the Al_2O_3 powder(s) and small amount (0.5

wt.% of the powder) of ammonium polymethacrylate anionic dispersant (Darvan C, R.T. Vanderbilt Co., Norwalk, CT) were first mixed in deionized water, and milled for 24 hours. Next, an organic binder poly(2-ethyl-2-oxazoline) was added to the slurry (5 wt.% of the powder) and mixed for another hour. Afterwards, the ZrO_2 spheres were separated from the slurry and de-aired for 30 min.

Freeze casting was conducted using a custom-made set up. In this set up, a Teflon tube is placed on the top of a thin (0.5 mm) steel plate, partially filled with Al_2O_3 slurry, and the whole assembly is inserted inside a liquid nitrogen (N_2) Dewar. By adjusting the distance between the steel plate and liquid N_2, freezing front velocity (FFV) was controlled. In this study, all the scaffolds were processed at a fixed gap between the liquid N_2 and steel plate. Average FFV was estimated by dividing the frozen sample height with the total time required for freezing of the sample.

Sintered density (ρ^*) of each extracted specimen was estimated from the measurements of mass and dimensions and relative density (ρ_r) was determined using $\rho_r = \rho^*/\rho_s$, where ρ_s is the bulk density of α-Al_2O_3 (3.96 g/cm^3). Top surface (also referred to as top plane, Fig. S1) of each specimen was utilized for microstructural characterization. Each specimen was compressed uniaxially along the ice-growth direction at a displacement rate of 0.5 mm/min (Tinius Olsen. 10ST), 6mm × 6mm being the loading surface.

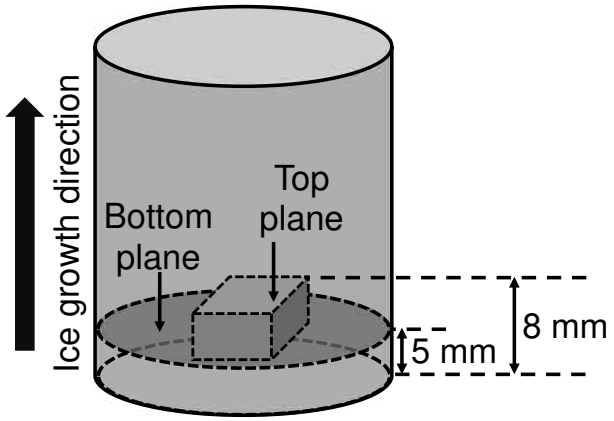

Figure S1: A schematic of the sintered ice-templated scaffold sample illustrating location of the specimen extracted for density measurement, microstructural characterization, and compression test. Locations of the top and bottom of the specimen are also shown. (Not to scale)

CHAPTER 5

EFFECTS OF POROSITY AND STRAIN RATE ON THE UNIAXIAL COMPRESSIVE RESPONSE OF ICE-TEMPLATED SINTERED MACROPOROUS ALUMINA

Note: The contents of this chapter have been published in Acta Materialia

M. Banda and D. Ghosh, Effects of porosity and strain rate on the uniaxial compressive response of ice-templated microporous alumina, Acta Mater., 149 (2018) 179 – 192.

DOI: https://doi.org/10.1016/j.actamat.2018.02.027

Abstract

We investigated and thoroughly analyzed compressive response of ice-templated ceramics in quasistatic and dynamic regimes of strain rate. In the high pore volume regime, sintered scaffolds exhibited highly lamellar pore morphology and pore architecture transitioned to dendritic with the decreasing pore volume. Mechanical property measurements in the quasistatic regime of strain rate revealed that with increasing density, compressive response transitioned from a damageable, cellular-like failure to a brittle-like failure. We rationalized the measured results in terms of the propensity of the lamella walls to undergo buckling. Our conjecture is that in the high pore volume regime, lamella walls of the scaffolds are prone to buckling-induced elastic instability, which leads to a compressive response that manifests a gradual decrease of stress beyond peak stress. In contrast, we suggest that in the low pore volume regime thick lamella walls and extensive transverse bridging exhibit marked resistance to buckling-induced instability and scaffolds undergo a global failure, which is manifested in the measured quasistatic compressive response as a sharp drop of stress beyond peak stress. Dynamic compressive response of the scaffolds exhibited

measurable differences relative to the quasistatic compressive response. Scaffolds exhibited a relatively gradual decrease of dynamic compressive stress beyond peak stress, and an overall improvement of compressive response and energy absorption capacity was measured under the dynamic loading conditions. We rationalized the measured differences in between the strain rate regimes in terms of the micro-inertia and other effects. This study is of critical significance for applications of ice-templated structures in dynamic environments.

Keywords: Ice-templating; compressive response; high-strain rate; buckling; energy absorption.

5.1 Introduction

Ice-templated sintered ceramics due to hierarchical microstructure and directional porosity have drawn significant attention with the possibilities of being applicable to a number of engineering endeavors [7,10,71,74,83,105,129-131]. There has been, however, little emphasis on the mechanical characterization and structure-property relationships, which are crucial for mechanical reliability and performance of ice-templated macroporous components. Uniaxial compressive response of ice-templated sintered ceramics exhibits an approximate linear stress-strain regime up to maximum compressive stress (peak stress), a plateau regime up to a large inelastic strain ($\geq$0.4) in which stress decreases gradually with increasing strain, and a densification stage where stress rises sharply with a slight increase of strain [124]. Compressive response of cellular and porous solids is affected by a number of variables such as the relative density, constituent material, type of porosity, and pore size [110]. Among these variables, increase of relative density not only increases fracture strength, but also can result in a change in the characteristic compressive response from graceful progressive failure to brittle-like failure [132]. In applications where

porous components are subjected to compressive loading conditions, mechanical reliability and thereby performance of ice-templated macroporous sintered ceramics will depend on the compressive fracture strength as well as on the post-fracture inelastic deformation and energy absorption characteristics. Therefore, it is imperative that we systematically investigate uniaxial compressive response of ice-templated ceramic materials over a spectrum of porosity and characterize material performance with respect to the overall compressive deformation behavior.

Another important consideration is to understand the effects of strain rate on compressive mechanical properties, which would be deemed necessary to implement ice-templated sintered macroporous ceramic structures in the dynamic environments where materials are subjected to high-strain rate ($\geq 10^2$ s^{-1}) loading conditions. Uniaxial compressive response measured in the quasistatic regime of strain rate ($\sim 10^{-3}$ s^{-1}) does not truly represent the compressive response of materials corresponding to high-strain rates [112,133,134]. It is also of note that while much work has been done on the combined effects of porosity and strain rate on compressive deformation response of metallic and polymeric foams, such studies do not necessarily exist in the open literature for cellular and porous ceramic materials.

In the present investigation, we will study uniaxial compressive response of ice-templated sintered ceramic materials over a porosity range of 50 – 70 vol.%. Compressive deformation behavior will be characterized both in quasistatic (10^{-3} s^{-1}) and dynamic ($\geq 10^2$ s^{-1}) regimes of strain rate. We will investigate ice-templated sintered macroporous alumina (Al_2O_3) materials, which will be templated from aqueous suspensions of three different solids loadings (20, 25 and 30 vol.%); however, at comparable freezing-front velocities, FFVs. Investigation of uniaxial compressive response of the synthesized sintered ceramic scaffolds will not only allow to probe into the effects of porosity on compressive mechanical properties but also can provide insights into the effects of

microstructure on the measured macroscopic response. By conducting both the uniaxial quasistatic and dynamic compression experiments, we may be able to unravel the effects of porosity and length scale features of ice-templated sintered hierarchical microstructure on the material response at two widely different strain rate regimes.

5.2 Experimental

5.2.1 Materials, aqueous ceramic suspension preparation, ice-templating, and sintering

Ice-templated scaffolds were developed from aqueous suspensions of fine, equiaxed Al_2O_3 powder (d_{50}=300 nm, APA-0.5, Sasol, Tuscan, AZ) of three different solids (Al_2O_3) loadings: 20, 25 and 30 vol.%. For each suspension, required amount of Al_2O_3 powder and 1 wt.% (of powder) of ammonium polymethacrylate anionic dispersant (Darvan C, R.T. Vanderbilt Co., Norwalk, CT) were mixed in deionized water and milled for 24 hours using zirconia (ZrO_2) spheres. Next, an organic binder poly(2-ethyl-2-oxazoline) was added (5 wt.% of powder) and further mixed for an hour. Afterwards, ZrO_2 spheres were separated and the suspension was de-aired for 30 min. All the Al_2O_3 suspensions were prepared following the above-mentioned steps. A custom-made ice-templating device (details in Supplementary Material) was employed to synthesize Al_2O_3 scaffolds. For each experiment, an average FFV was determined by dividing the height of a frozen sample with the time required for completion of solidification of a suspension. Ice-templated frozen samples were freeze-dried at a pressure of 0.014 mbar and temperature of -50°C for a duration of 96 hours inside a freeze dryer (2.5L, Labconco, Kansas City, MI). Sintering of the dried samples was conducted in a box furnace (KSL-1700X, MTI Corporation, Richmond, CA) in an air atmosphere at 1550°C for 4 hours.

5.2.2 Estimation of relative density and porosity and microstructure characterization

From each sintered scaffold cylinder (approximately 16.9 mm in diameter and 15.6 mm in height) a specimen of dimensions 6mm×6mm×3mm was extracted (Fig. S1, Supplementary Material), which was utilized for density measurement, microstructural characterization, and compression tests. Sintered density (ρ^*) of each extracted specimen was determined from the measurements of mass and dimensions. Relative density (ρ_r) was estimated using $\rho_r=\rho^*/\rho_s$, where ρ_s is the bulk density of α-Al_2O_3 (taken here as 3.96 g/cm^3), and total porosity was calculated using $p_t=(1-\rho_r)\times100$. For each composition, two sintered Al_2O_3 scaffolds were randomly selected for microstructural analyses and top surface of extracted specimen (Fig. S1) was utilized for microstructural analyses employing a Phenom ProX Tabletop scanning electron microscope (SEM). Each SEM micrograph was analyzed to determine lamella wall thickness (δ) and spacing (i.e., wavelength, λ), pore (usually elliptical) major axis (a), minor axis (b) and aspect ratio ($\chi = a/b$), lamellar bridge density (ρ_b), and pore morphology (m). ρ_b is defined as the number of bridges present in between the adjacent lamellae walls per unit area [103,124]. Pore morphology can be defined using a dimensionless morphological parameter (m) defined as [103]

$$m = \frac{1}{\rho_b \lambda^2}, \quad (1)$$

where according to Naglieri et al. [103] pore architecture can be described as lamellar for $m>5$, dendritic for $1<m<5$, and isotropic for $m<1$. Since the scaffolds were processed at comparable freezing conditions, it can be assumed that the results of microstructural analyses corresponding to two scaffolds will be a representative of all the scaffolds for the respective composition.

5.2.3 Characterization of uniaxial compressive response at quasistatic and dynamic regimes

Uniaxial compression experiments were conducted both at low- (10^{-3} s^{-1}) and high-strain rates ($\geq 10^2$ s^{-1}). For each extracted rectangular specimen compressive load was applied on the 6mm×6mm surface, i.e., compressed parallel to the ice-growth direction. Quasistatic compression experiments were conducted using a mechanical testing machine (MTS, ALLIANCE RF/300) at a displacement rate of 0.5 mm/min. For the high-strain rate compression experiments, a split Hopkinson pressure bar (SHPB) setup was employed, which consists of a solid striker bar of length 330.2 mm, a solid incident bar of length 1524 mm, and a solid transmission bar of length 914.4 mm; all the bars have a common diameter of 12.7 mm and are made out of a high-strength aluminum (Al) alloy. Details of working principle are discussed in the supplementary material. Stress in a specimen is estimated as [135]

$$\sigma(t) = E\varepsilon_{\mathrm{T}}(t)\frac{A_{\mathrm{t}}}{A_{\mathrm{s}}}, \tag{2}$$

where E is Young's modulus of the bar material, $\varepsilon_{\mathrm{T}}(t)$ is the time-resolved axial strain in the transmission bar, and A_{T} and A_{S} are the cross-sectional areas of the transmission bar and sample, respectively. Similarly, strain rate in a specimen is calculated as [135]

$$\dot{\varepsilon}(t) = -\frac{2c_{\mathrm{o}}}{l_{\mathrm{S}}}\varepsilon_{\mathrm{R}}(t), \tag{3}$$

where c_{o} is the wave velocity of the bar material, l_{S} is the original length of the specimen, $\varepsilon_{\mathrm{R}}(t)$ is the time-resolved axial strain of the reflected pulse in the incident bar. Finally, strain in a homogeneous specimen is calculated as [135]

$$\varepsilon(t) = \int_0^{\mathrm{t}} \dot{\varepsilon}_{\mathrm{R}}(t). \tag{4}$$

5.3 Results

5.3.1 Morphology of ice-templated sintered macroporous alumina, relative density, and porosity

Table 1: Variation of lamella wall thickness (δ), wavelength (λ), pore major axis (a), pore minor axis (b), pore aspect ratio (χ), bridge density (ρ_b), and pore morphology parameter (m) of NA20-scaffolds, NA25-scffolds and NA30-scaffolds.

Scaffold ID	δ (µm)	λ (µm)	a	b	χ (a/b)	ρ_b (mm^{-2})	m
NA20	3.9 ± 0.9	13.3 ± 3.1	82.4 ± 54.1	9.3 ± 2.4	8.8 ± 6.2	143.5 ± 20.5	39.4
NA25	4.8 ± 1.3	14.5 ± 3.4	57.1 ± 38.1	9.7 ± 3.6	5.9 ± 4.5	413.3 ± 136.8	11.51
NA30	7.2 ± 2.5	14.4 ± 3.5	40.3 ± 34.8	7.2 ± 4.3	5.6 ± 5.9	1533.7 ± 163.5	3.1

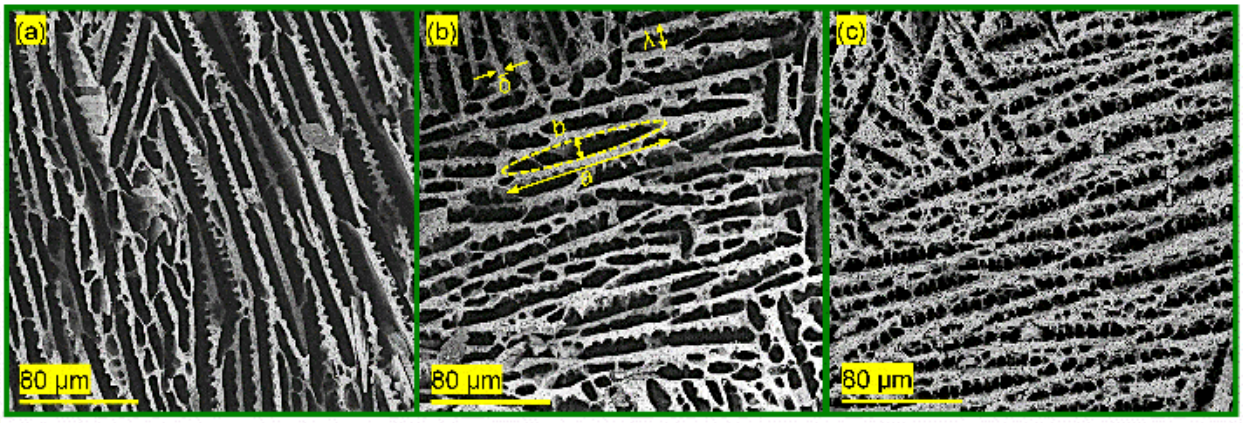

Figure 1: Representative SEM micrographs of the (a) NA20-scaffold, (b) NA25-scaffold, and (c) NA30-scaffold, revealing transition of pore morphology from highly lamellar in the NA20-scaffold (high porosity) to highly dendritic in the NA30-scaffold (low porosity). For all the SEM micrographs, ice-growth direction is out of the page.

Figure 1 shows representative SEM micrographs of NA20-scaffold (Fig. 1a), NA25-scaffold (Fig. 1b), and NA30-scaffold (Fig. 1c), which reveal microstructural features such as parallel ceramic (lamella) walls and elongated pores. Note that these scaffolds were processed at comparable high FFV (NA20-scaffolds: 32.1 ± 1.1 μm/s; NA25-scaffolds: 33.0 ± 1.3 μm/s; NA30-scaffolds: 35.3 ± 1.3 μm/s, Table 2). For the NA20-scaffold (Fig. 1a) lamellar bridging is minimal, long elongated pores are observed, and pore morphology can be considered as lamellar. The extent of lamellar bridging increased considerably from NA20-scaffold (Fig. 1a) to NA25-scaffold (Fig. 1b) to NA30-scaffold (Fig. 1c), and pore architecture appears dendritic particularly for the NA30-scaffold. As a result, pore size and aspect ratio also decreased from the NA20-scaffolds to the NA30-scaffolds. Table 1 shows the variations of lamella wall thickness (δ) and spacing (i.e., wavelength, λ), pore major axis (a), pore minor axis (b), pore aspect ratio (χ), lamellar bridge density (ρ_b), and pore morphology parameter (m) across the scaffold compositions. From the NA20-scaffold to NA25-scaffold to NA30-scaffold, δ increased from 3.9 ± 0.9 μm to 4.8 ± 1.3 μm to 7.2 ± 2.5 μm, respectively, whereas λ is observed to remain comparable across the scaffold compositions (~14 μm). Also, from the NA20-scaffold to NA25-scaffold to NA30-scaffold, a decreased from 82.4 ± 54.1 μm to 57.1 ± 38.1 μm to 40.3 ± 34.8 μm, respectively, whereas b changed from 9.3 ± 2.4 μm to 9.7 ± 3.6 μm to 7.2 ± 4.3 μm, respectively. As a result, from the NA20-scaffold to NA25-scaffold to NA30-scaffold χ decreased from 8.8 ± 6.2 to 5.9 ± 4.5 to 5.6 ± 5.9, respectively. Further, from the NA20-scaffold to NA25-scaffold to NA30-scaffold, ρ_b increased markedly from 143 ± 23.5 mm^{-2} to 413.3 ± 136.8 mm^{-2} to 1533.7 ± 163.5 mm^{-2}, respectively. Results of these measurements are consistent with the observations made from the representative SEM micrographs presented in Fig. 1. This is further supported from the estimation of m, which is 39.4 for the NA20-scaffold, 11.5 for the NA25-scaffold, and 3.1 for the NA30-

scaffold. Recall that according to Naglieri et al. [103] pore morphology can be described as lamellar for $m>5$, dendritic for $1<m<5$, and isotropic for $m<1$. Therefore, pore architecture of the NA20-scaffolds is highly lamellar, becomes significantly less lamellar for the NA25-scaffolds, and transitions to dendritic for the NA30-scaffolds. Figure 2 shows variation of average relative density (ρ_r) and porosity (p_t) with the solids loading of aqueous suspensions; average values are also provided in Table 2. Additionally, Table 2 shows average FFV values. From NA20-scaffolds to NA30-scaffolds, average ρ_r increased from 0.30 ± 0.01 to 0.46 ± 0.01 and average p_t (%) decreased from 70.0 ± 0.9 to 54.0 ± 1.5.

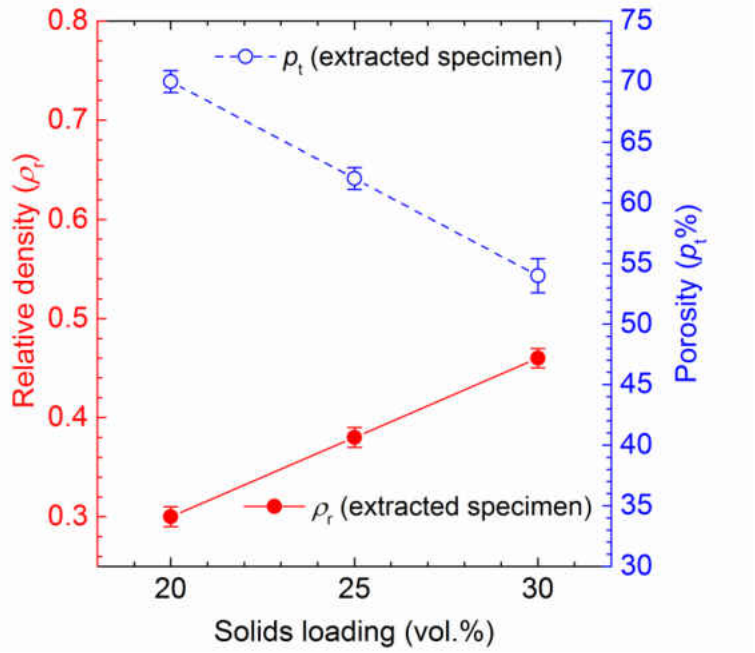

Figure 2: Variation of average relative density (ρ_r) and average total porosity (p_t) of the extracted specimens from the sintered scaffolds as a function of solids loadings of suspensions.

Table 2: Variation in FFV, sintered density (ρ^*), relative density (ρ_r), and total porosity (p_t) of NA20-scaffolds, NA25-scaffolds, and NA30-scaffolds.

Scaffold ID	**Avg. FFV (µm/s)**	**Extracted specimens**		
		ρ^* **(gm/cm^3)**	ρ_r	p_t **(%)**
NA20	32.1 ± 1.1	1.2 ± 0.03	0.30 ± 0.01	70 ± 0.9
NA25	33.0 ± 1.3	1.5 ± 0.04	0.38 ± 0.01	62 ± 0.9
NA30	35.3 ± 1.3	1.8 ± 0.05	0.46 ± 0.01	54 ± 1.5

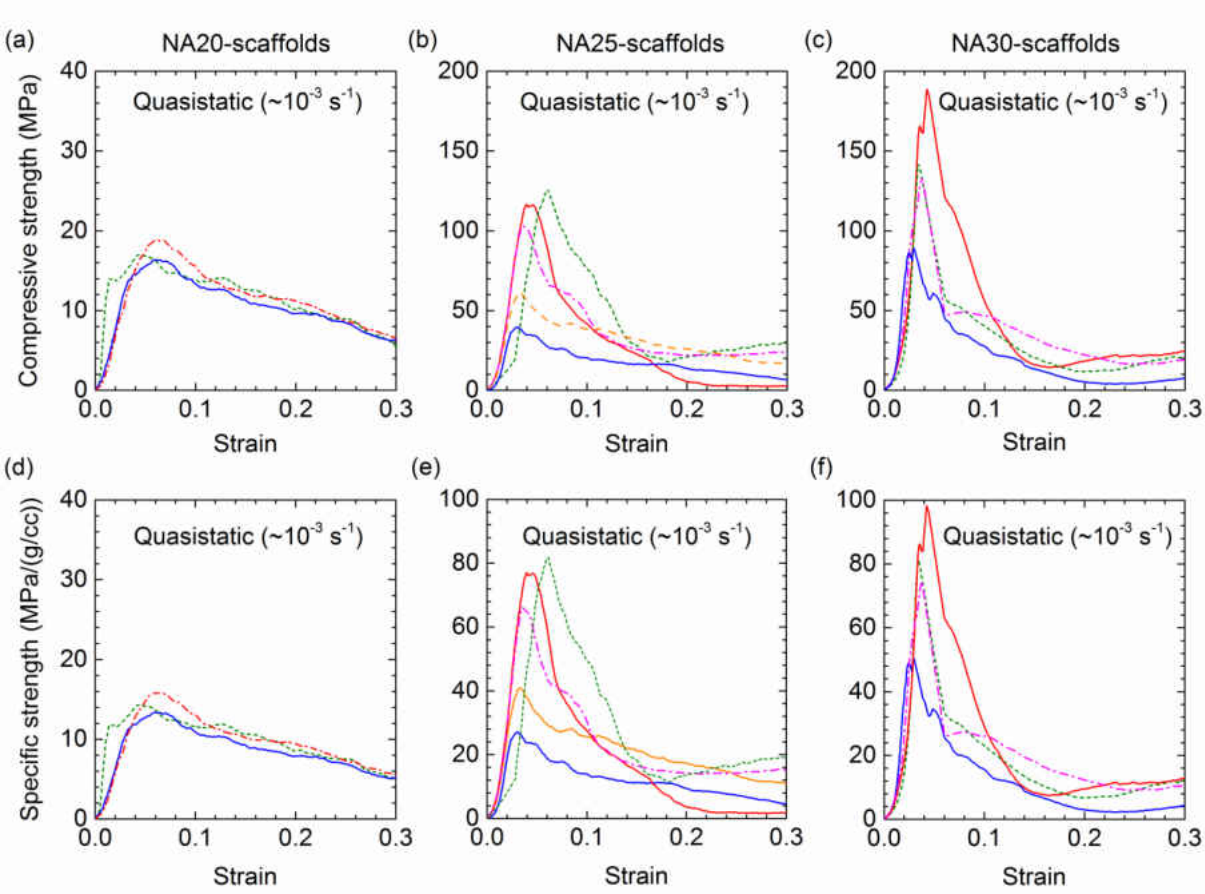

Figure 3: Quasistatic uniaxial compressive stress-strain curves of the (a) NA20-scaffolds, (b) NA25-scaffolds, (c) NA30-scaffolds; and quasistatic uniaxial specific compressive stress vs. strain curves of the (d) NA20-scaffolds, (e) NA25-scaffolds, (f) NA30-scaffolds.

5.3.2 Quasistatic uniaxial compressive response

Figure 3 shows quasistatic (strain rate ~10^{-3} s^{-1}) uniaxial compressive stress-strain curves, shown up to 0.3 strain, for the NA20-scaffolds (Fig. 3a), NA25-scaffolds (Fig. 3b), and NA30-scaffolds (Fig. 3c). Measured response for all the compositions exhibits an increase of stress almost linearly with strain, attains maximum (peak stress, σ_p), and further increase of strain leads to a decrease of stress. σ_p is observed to increase significantly from NA20-scaffolds to NA25-scaffolds to NA30-scaffolds, which is attributed to increase in strength with decreasing porosity. For the NA20-

scaffolds, compressive response exhibits graceful progressive failure, all the stress-strain curves are observed to be almost identical, and σ_p values are found to be within a narrow range of 16-19 MPa. In contrast, for the measured number of specimens NA25-scaffolds exhibit a wide variation of σ_p (39 MPa-126 MPa) and similar observation is also made for the NA30-scaffolds (89 MPa-188 MPa). Moreover, for the NA25-scaffolds there is also a noticeable difference in the regime beyond σ_p across the samples. For the compressive stress-strain curves that exhibit σ_p values above 90 MPa stress drops sharply beyond σ_p, which suggest brittle-like failure and a loss of load-bearing capacity. Whereas, for the compressive stress-strain curves that exhibit σ_p values below 60 MPa stress rather decreases gradually with the increasing strain (i.e., graceful progressive failure). For the NA30-scaffolds, all the stress-strain curves beyond σ_p rather exhibit a sharp drop of stress with the increasing strain, i.e., brittle-like failure response. For each composition, all the scaffolds were processed at comparable freezing conditions; however, a slight variation of ρ_r across the scaffolds was measured. To account for this, Fig. 3 also shows quasistatic specific compressive stress vs. strain curves for the NA20-scaffolds (Fig. 3d), NA25-scaffolds (Fig. 3e), and NA30-scaffolds (Fig. 3f). For each curve, stress values were divided by the sintered density (ρ^*) of the respective scaffold. For the NA20-scaffolds, all the specific stress vs. strain curves remain comparable. Whereas, the NA25-scaffolds exhibited a significant difference (55 MPa/g/cc) in between the maximum (82 MPa/g/cc) and minimum (27 MPa/g/cc) specific strength values. Similarly, the NA30-scaffolds also exhibit a significant difference (48 MPa/g/cc) in between the maximum (98 MPa/g/cc) and minimum (50 MPa/g/cc) specific strength values. Therefore, we suggest that for both the NA25-scaffolds and NA30-scaffolds the observed considerable scatter of the strength values could be related to the microstructural variation rather than the ρ_r variation.

The majority of studies on ice-templated ceramics have been carried out in the high porosity regime, and overall compressive response is rarely addressed. Our previous work [9,124,136] revealed that for ice-templated Al_2O_3 scaffolds of p_t 80 vol.% and greater, uniaxial compressive response beyond σ_p exhibits a prominent plateau regime where stress decreases gradually with the increasing strain (i.e., graceful progressive failure). Therefore, with decreasing porosity, uniaxial compressive deformation of ice-templated sintered Al_2O_3 materials transitions from damageable, cellular-like failure behavior to a brittle-like failure response. For porous Al_2O_3 with isotropic pore morphology, Meille et al., [132] reported a similar transition of compressive response from high pore volume regime (70%) to low pore volume regime (40%). For brittle solids in the low pore volume regime, isolated pores tend to govern the mechanical properties, and tensile cracks originate from the largest pores (i.e., largest flaws). With an increasing compressive stress most favorably oriented (toward the applied load) individual tensile cracks propagate in a stable manner, leading to crack-crack interaction, and ultimately causing failure by the axial splitting. As a result, compressive load-bearing capacity is diminished abruptly beyond peak stress. On the other hand, for highly porous brittle solids that exhibit a damageable, cellular-like behavior distribution of the solid phase tends to govern the compressive mechanical response. Under compression, cracks originate within the solid walls in between the pores; however, due to the large separation in between the walls and lack of the continuous and relatively straight segments of the solid phase (parallel to the loading direction), probability of stable crack propagation leading to crack-crack interaction and formation of macroscopic crack remains unlikely. As a result, under uniaxial compressive loading highly porous brittle solids rather exhibit a progressive failure mode. This rationale could be also applicable to the ice-templated anisotropic Al_2O_3 scaffolds. However, for cellular ceramics buckling as well as bending of the cell walls and struts have a governing role on

compressive response [110]. In ice-templated materials, it is expected that upon compression lamella walls will experience the applied load, whereas lamellar bridges will provide mechanical support to the walls. Initiation of the separation and/or fracture of the ceramic walls can be considered to set the limit for the maximum compressive load-bearing capacity. In ice-templated ceramics, primary structural component is tall, slender lamella walls, which can be treated as shell elements. And lamellar bridges anchor together the shell elements, which tend to give rise to structural mechanical stability to ice-templated sintered ceramics subjected to compression. Elastic instability of shell elements arises from buckling, which is characterized by a sudden sideways failure of a structural member subjected to uniaxial compressive stress. Therefore, mechanical stability of ceramic lamella walls will depend more on their elastic stability to buckling/bending in comparison to compressive strength of the individual elements. Toward this end, it is important to provide insights into the measured compressive response of ice-templated ceramics of different pore volumes in relation to the probability of the lamella walls to undergo buckling.

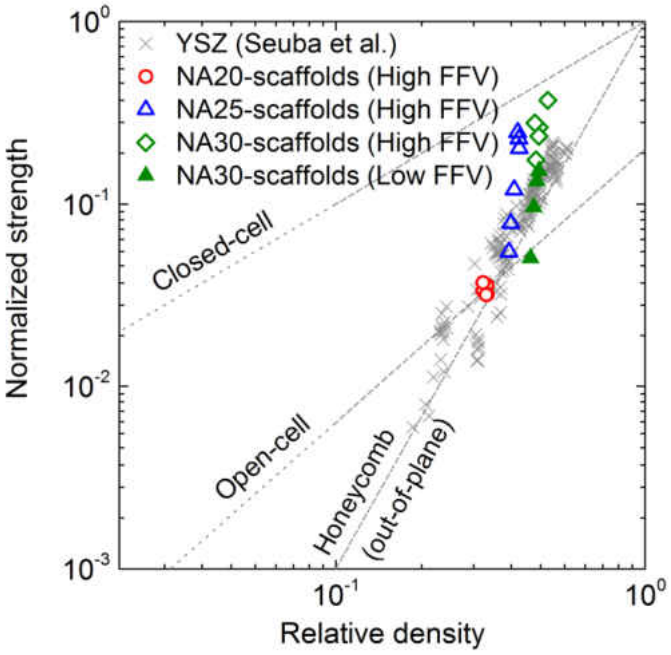

Figure 4: Variation of the normalized quasistatic compressive strength with relative density of the NA20-scaffolds, NA25-scaffolds and NA30-scaffolds. The dotted lines represent the model predictions of compressive strength by Gibson and Ashby for closed-cell, open cell, and honeycomb (out-of-plane deformation) foams. Also, included data for ice-templated sintered ZrO2 from the work of Seuba et al. [106].

According to Gibson and Ashby models [110], compressive strength (σ) of brittle cellular solids is related to ρ_r as

$$\frac{\sigma}{\sigma_s} \propto \rho_r \text{ (for closed-cell)}, \quad (5)$$

$$\frac{\sigma}{\sigma_s} \propto (\rho_r)^{1.5} \text{ (for open-cell)}, \quad (6)$$

and

$$\frac{\sigma}{E_s} \propto (\rho_r)^3 \text{ (for honeycomb, out-of-plane deformation)}, \quad (7)$$

where σ_s and E_s are compressive strength and Young's modulus, respectively, of cell wall material. The semi-empirical analytical Gibson and Ashby models relate to the deformation mechanisms of cell walls and edges. Under compression, in the elastic deformation regime cell walls of open cell foam bend at low ρ_r and with increasing ρ_r (>0.1) contribution of the compression of cell walls become more significant [110]. For closed-cell foams, under compression cell edges both bend and contract, while membranes that form cell faces stretch [110]. For out-of-plane compressive deformation of honeycombs, axial compression of cell walls is the dominant elastic deformation mechanism and brittle fracture can result from the elastic instability (i.e., buckling) of the walls [110]. Therefore, a comparison of the experimentally measured data with the model predictions can provide some insights into the compressive deformation behavior of ice-templated ceramics. While Gibson and Ashby models for open- and closed-cell foams have been attempted for ice-templated materials [74,107,137,138], Seuba et al. [106] recently suggested that compressive strength of ice-templated sintered ZrO_2 is in a better agreement with the model prediction for out-of-plane compression of honeycomb morphology.

In Fig. 4 we compared the variation of σ_p (normalize by the flexural strength of sintered, dense Al_2O_3, 510 MPa) of the NA20-scaffolds, NA25-scaffolds, and NA30-scaffolds with ρ_r to the model predictions (dotted lines) for the closed-cell, open-cell, and honeycomb architectures. Note that these ice-templated Al_2O_3 materials were processed at relatively high FFVs (32-35 μm/s, Table 2). In Fig. 4, we also incorporated the normalized compressive strength values corresponding to the NA30-scaffolds processed at relatively low FFV (21 μm/s) in this work as well as of the ice-templated sintered ZrO_2 from the work of Seuba et al. [106]. As suggested by Seuba et al. [106], compressive strength of ice-templated ZrO_2 is reasonably well predicted by the honeycomb model for out-of-plane deformation [10]. The normalized strength values of the NA20-scaffolds and

NA25-scaffolds (with relatively low σ_p, <60 MPa) are observed to reside within the same band of data for ice-templated sintered ZrO_2 [106]. However, normalized strength values of the NA25-scaffolds with relatively high σ_p (>90 MPa) and NA30-scaffolds are observed to be well outside and above the prediction made by the honeycomb model for out-of-plane compression. Interestingly, normalized compressive strength values of the NA30-scaffols, processed at relatively low FFV (21 μm/s) and exhibited σ_p <60 MPa, also reside within the same band of the data for the ice-templated sintered ZrO_2 [106]. In our previous study [9,108,124], we have shown that compressive strength of ice-templated sintered Al_2O_3 materials can substantially increase with increasing FFV. Therefore, although the porosity values of the NA30-scaffolds processed at relatively high and low FFVs are comparable, significant difference in compressive strength could be associated with a change in the deformation behavior. An agreement with the honeycomb model suggests that compressive deformation response of the NA20-scaffolds, NA25-scaffolds (with relatively low σ_p, <60 MPa), and NA30-scaffolds (processed at low FFV and with relatively low σ_p, <60 MPa) could be similar to that of the out-of-plane deformation of honeycomb morphology. Therefore, for these three sets of Al_2O_3 scaffolds, it is possible that buckling-induced elastic instability of lamella walls might have led to brittle fracture and set the limit for compressive strength (σ_p). In contrast, a considerable deviation of normalized strength values of the NA25 scaffolds (with relatively high σ_p, >90 MPa) and NA30-scaffolds (processed at high FFV) from the model prediction for out-of-plane deformation of honeycomb could be associated with a change in deformation mechanism. Overall, Fig. 4 suggests that compressive strength of ice-templated sintered Al_2O_3 materials with low σ_p (<60 MPa) is in a reasonable agreement with the model prediction for out-of-plane compressive deformation of honeycomb. Whereas, normalized strength values of the Al_2O_3 scaffolds corresponding to high σ_p (>90 MPa) deviated considerably

from the model prediction for out-of-plane deformation of honeycomb. Seuba et al. [106] also made the similar observation. In the absence of computational modeling or in situ investigation, which is beyond the scope of this work, we suggest that compressive stress-strain characteristics could shed some light into the possible changes of deformation mechanism. Toward this end, we compressed few NA20-scaffold and NA30-scaffold and interrupted the experiments in the vicinity of peak stress.

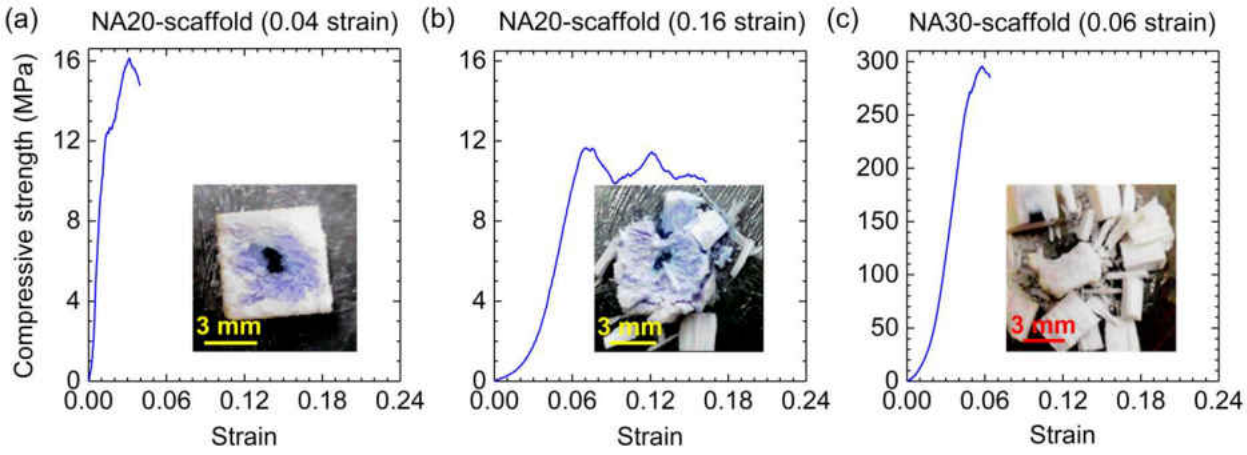

Figure 5: Quasistatic compressive stress-strain curves and corresponding optical images of the ice-templated sintered Al_2O_3 scaffolds deformed up to different strain levels: (a) NA20-scaffold up to 0.04 strain, (b) NA20-scaffold up to 0.16 strain, and (c) NA30-scaffold up to 0.06 strain.

Figure 5a shows stress-strain response of a NA20-scaffold compressed up to 0.04 strain and optical image (inset) of the deformed specimen reveals that the scaffold remained almost intact. The recovered specimen was lightly tapped with a small wooden stick, which further confirmed the overall intactness of the specimen and suggested occurrence of only localized damage. As a result, beyond peak stress NA20-scaffolds exhibit graceful progressive failure response (Fig. 3a). Another

NA20-scaffold was compressed up to 0.16 strain (Fig. 5b). The recovered sample appeared intact and light tapping with a wooden stick caused the structure to laterally separate into multiple large fragments, although a major portion of the specimen still remained intact (inset, Fig. 5b), which supports that in the NA20-scaffolds graceful progressive failure (i.e., localized damage) continues with further compression beyond compression. A NA30-scaffold specimen was compressed up to 0.06 strain (Fig. 5c). The recovered specimen appeared intact but light tapping with a wooden stick caused lateral collapse into numerous fragments (inset, Fig. 5c), which supports that in low pore volume regime ice-templated sintered Al_2O_3 materials exhibit brittle-like failure response and thus a sudden drop in compressive load-bearing ability is observed (Fig. 3b). Next, we measured axial length of the fragments corresponding to the partially deformed NA20-scaffold (0.16 strain) and NA30-scaffold (0.06 strain). For the NA20-scaffold undeformed specimen was 3.1 mm long and average length of the fragments was 2.4 mm. Length of the undeformed NA30-scaffold was 3.15 mm and average length of the fragments was 2.9 mm. The NA20-scaffold was deformed up to 0.16 strain and length measurement of the fragments indicates 0.22 strain, which is not significantly different. Similarly, the NA30-scaffold was deformed up to about 0.06 strain and length measurement of the fragments indicates 0.08 strain. We argue that these measurements could provide further insight into the uniaxial compressive deformation behavior of ice-templated sintered Al_2O_3 materials.

In NA20-scaffolds, beyond peak stress gradual decrease of stress and accumulation of strain can be attributed to progressive fracture of lamella walls. Each wall is akin to dense ceramic that can accumulate ~1% elastic strain. Thus, measured decrease of length of the fragments corresponding to partially deformed NA20-scaffold and associated large inelastic strain can be accounted by considering lamella wall fracture approximately perpendicular to the direction of compression,

possibly resulting from elastic instability (i.e., buckling) of the walls. Recall from Table 1 that NA20-scaffold contains long elongated pores (a = 82.4 ± 54.1 μm), thin walls (thickness = 3.9 ± 0.9 μm), and lamellar bridge density is negligible (143.5 ± 20.5 mm^{-2}), which could make the walls prone to buckling and resulting brittle fracture of the walls would cause a shortening of the axial length. Therefore, measured strength values of NA20-scaffolds are in a reasonable agreement with the honeycomb model prediction for out-of-plane deformation (Fig. 4). For NA30-scaffolds, pore length (a = 40.3 ± 34.8 μm) is considerably smaller in comparison to that of NA20-scaffolds. Additionally, lamella walls are considerably thicker (7.2 ± 2.5 μm) and bridge density (1533.7 ± 163.5 mm^{-2}) is significantly greater for NA30-scaffolds in comparison to those of NA20-scaffolds. Thick lamella walls and high bridge density in NA30-scaffolds could make the walls resistant to buckling. Comparable values of the length of undeformed NA30-scaffold and length of axially splitted fragments after deformation (0.06 strain) perhaps support that buckling-induced failure of lamella walls could be less prevalent in NA30-scaffolds (high FFV). Thus, NA30-scaffolds corresponding to high FFV exhibited strength well above that predicted by the honeycomb model for out-of-plane deformation.

To further substantiate, we utilized critical buckling load (P_{crit}) derived for elastic buckling of honeycombs (out-of-plane deformation) to evaluate the buckling stability of lamella walls. P_{crit} is related to wall width (l) and wall thickness (δ) as follows [110]:

$$P_{\text{crit}} \propto \frac{\delta^3}{l}. \tag{8}$$

For ice-templated structure, we can assume that major axis (a) of an ellipsoidal pore is equivalent to l and rewrite equation (8) as

$$P_{\text{crit}} \propto \frac{\delta^3}{a} \tag{9}$$

Next, we determined the ratio of P_{crit} for NA25-scaffold to NA20-scaffold, NA30-scaffold to NA20-scaffold, and NA30-scaffold to NA25-scaffold. Thus, using equation (9) we can write

$$(P_{\mathrm{crit}})_{\mathrm{NA25}}/(P_{\mathrm{crit}})_{\mathrm{NA20}} = \left(\frac{\delta^3}{a}\right)_{\mathrm{NA25}}/\left(\frac{\delta^3}{a}\right)_{\mathrm{NA20}} \quad (10)$$

$$(P_{\mathrm{crit}})_{\mathrm{NA30}}/(P_{\mathrm{crit}})_{\mathrm{NA20}} = \left(\frac{\delta^3}{a}\right)_{\mathrm{NA30}}/\left(\frac{\delta^3}{a}\right)_{\mathrm{NA20}} \quad (11)$$

and

$$(P_{\mathrm{crit}})_{\mathrm{NA30}}/(P_{\mathrm{crit}})_{\mathrm{NA25}} = \left(\frac{\delta^3}{a}\right)_{\mathrm{NA30}}/\left(\frac{\delta^3}{a}\right)_{\mathrm{NA25}} \quad (12)$$

Using the values of a and δ from Table 1, we estimated $(P_{crit})_{NA25}/(P_{crit})_{NA20}$ as 2.7, $(P_{crit})_{NA30}/(P_{crit})_{NA20}$ as 12.9, and $(P_{crit})_{NA30}/(P_{crit})_{NA25}$ as 4.8. All the estimated ratios are greater than 1, suggesting an increase of resistance to buckling of the lamella walls from NA20-scaffolds to NA25-scaffolds and NA30-scaffolds. Here, we mainly considered $(P_{crit})_{NA30}/(P_{crit})_{NA20}$ to further relate the buckling stability of the walls to the observed damageable, cellular-like and brittle-like compressive response of the NA20-scaffolds and NA30-scaffolds, respectively. The high value of $(P_{crit})_{NA30}/(P_{crit})_{NA20}$ suggests a marked increase in resistance to elastic buckling of lamella walls of NA30-scaffolds relative to NA20-scaffolds. Thus, buckling-induced failure may not be dominant in NA30-scaffolds, which we also inferred based on the observations made from Fig. 5. We argue that with increasing solids loading ice-templated pore architecture may still resemble to honeycomb morphology; however, a significant increase in lamellar bridge density (at high FFV) enhance the stability of the walls to elastic buckling. As a result, measured strength values of NA30-scaffolds deviated from the model prediction for honeycomb.

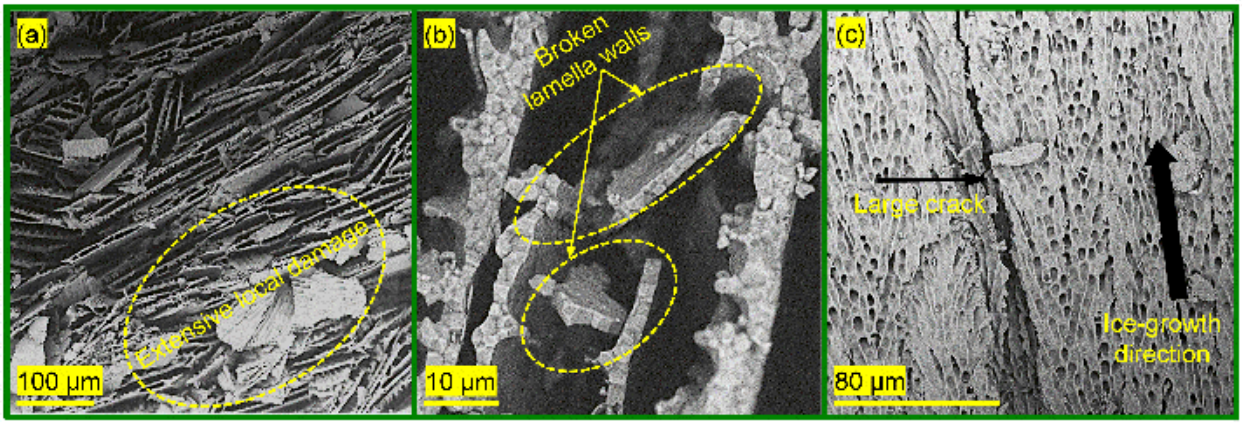

Figure 6: SEM micrographs of one of the loading surfaces of the NA20-scaffold deformed up to 0.04 strain at (a) low- and (b) high-magnification, which reveal evidence of local damage due to fracture of lamella walls. (c) Large crack propagation (in the direction of ice-growth) within the lamella walls in the NA30-scaffold, which was deformed up to 0.06 strain.

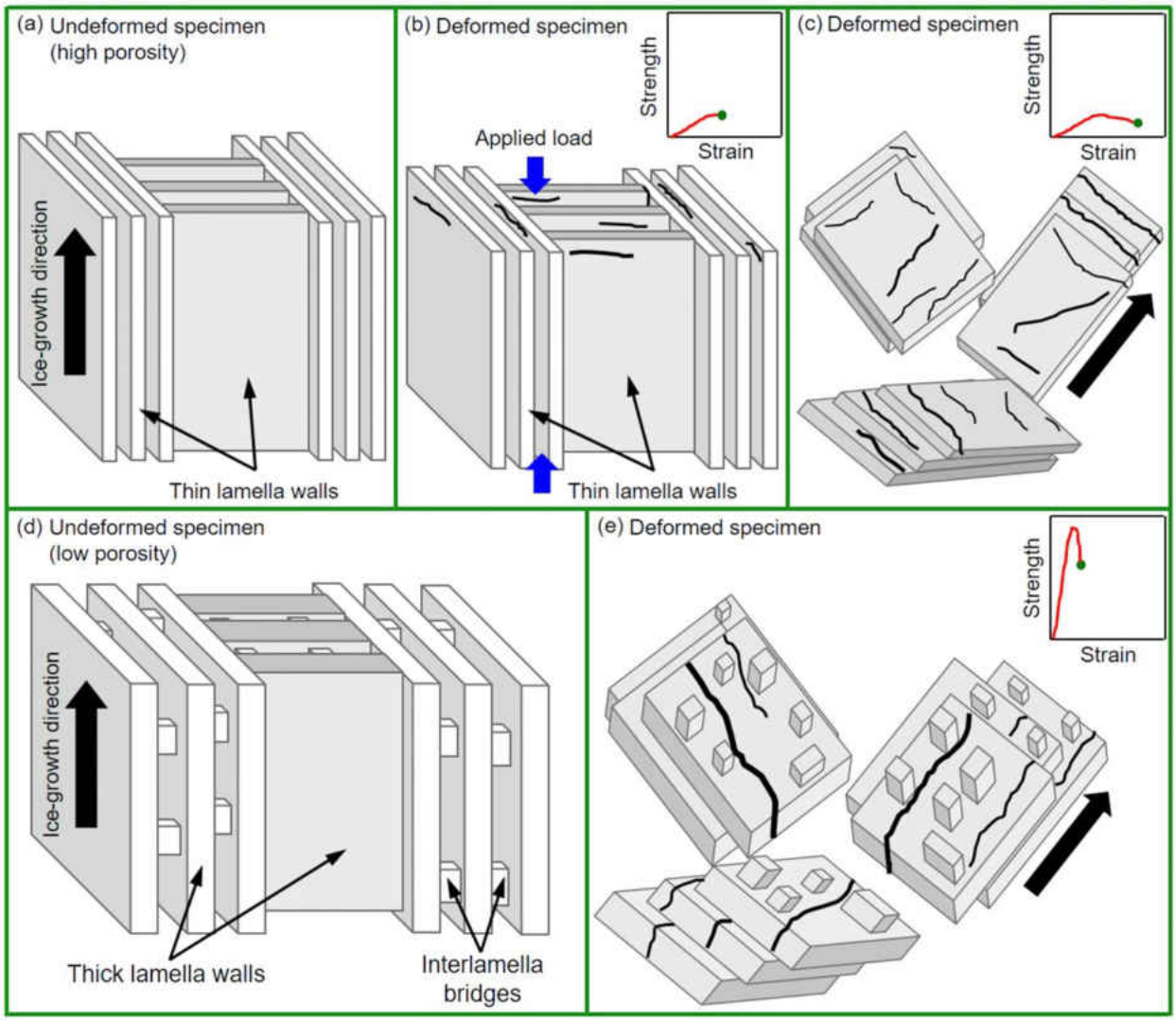

Figure 7: Schematics of proposed sequence of failure events in NA20-scaffold and NA30-scaffold during uniaxial compression. (a) Undeformed NA20-scaffold, (b) almost intact NA20-scaffold at peak stress, (c) collapsed walls of NA20-scaffold loaded to up to a reasonably higher level of strain in the inelastic regime, (d) undeformed NA30-scaffold, and (e) collapsed lamella walls of NA30-scaffold with cracks parallel to the loading direction at peak stress.

For additional evidence, we analyzed the partially deformed NA20-scaffold and NA30-scaffold specimens in SEM. Figure 6a shows low-magnification SEM image of compression loading

surface of NA20-scaffold (0.04 strain), revealing evidence of localized brittle fracture. Figure 6b also reveals localized brittle fracture within lamella walls. We conjecture that such local damage occurred throughout the NA20-scaffold structure. Microscopic evidence of fragmentation of lamella walls further supports localized elastic instability (buckling) within the walls, while at a macroscopic level macroporous structure remains almost intact. Thus, lamella walls of NA20-scaffolds are prone to localized brittle failure through buckling, which sets the limit for compressive strength. Upon further compression, lamella walls continue to undergo localized failure and inelastic strain accumulation causes in a plateau regime with a gradual decrease of stress, resulting in a damageable, cellular-like compressive response. In contrast, lamella walls of NA30-scaffolds could exhibit significant resistance to buckling and with increasing compressive load brittle fracture can initiate within the lamellar bridges. Additionally, mesocracks oriented toward the applied load can develop within the walls and favorably oriented cracks can grow and coalesce to form large macroscopic cracks, leading to the axial splitting of the walls. Therefore, upon reaching the peak stress, the corresponding applied compressive load level could be high enough to cause fracture of the bridges throughout the structure and perhaps simultaneously results macroscopic crack propagation (parallel to the direction of applied load) within the lamella walls, leading to almost complete separation of the walls (or segments of the walls); this behavior is manifested as a sharp drop of compressive load-bearing capacity beyond peak stress, i.e., a brittle-like compressive failure response. Figure 6c shows an evidence of macroscopic crack propagation, toward the applied load, within lamella walls of partially deformed NA30-scaffold (0.06 strain). Therefore, the observed transition from damageable, cellular-like compressive behavior in NA20-scaffolds to brittle-like behavior in NA30-scaffolds could be attributed to stability of lamella walls to elastic buckling. In Fig. 7, we schematically depicted deformation and failure mechanisms in

NA20-scaffold and NA30-scaffold, which we discussed above and rationalized through a series of evidences.

5.3.3 Dynamic compressive response

Figure 8 shows uniaxial dynamic (strain rate ~350-1800 s^{-1}) compressive response of NA20-scaffolds (Fig. 8a), NA25-scaffolds (Fig. 8b), and NA30-scaffolds (Fig. 8c). For the SHPB experimental conditions used in this study, we achieved compressive strain in the range of 0.15-0.2. Therefore, stress-strain curves are shown up to 0.16 strain. For each composition two representative quasistatic stress-strain curves are also shown for comparison purpose, which present upper and lower bounds of the measured quasistatic compressive response. Similar to quasistatic regime, dynamic compressive strength, in general, is also observed to increase significantly from NA20-scaffolds to NA30-scaffolds, i.e., with increasing ρ_r. For NA20-scaffolds, overall signature of stress-strain curves remains similar in between the two strain rate regimes. Within the measured high-strain rate range, stress-strain curves for NA20-scaffolds do not exhibit any particular trend. However, dynamic compressive response suggests considerable stiffening in NA20-scaffolds in comparison to quasistatic loading. Similarly, dynamic σ_p values of NA20-scaffolds (23-27 MPa) are observed to be considerably greater (~43%) in comparison to quasistatic σ_p values (16-19 MPa). Figure 8a further shows that under dynamic loading there is an increase of compressive stress in the plateau regime in comparison to quasistatic loading. As a result, area of dynamic stress-strain curves is observed to be greater in comparison to that of quasistatic stress-strain curves. Thus, NA20-scaffolds exhibited a measurable and considerable enhancement of uniaxial compressive mechanical properties in the dynamic regime of strain rate in comparison to the quasistatic regime of strain rate.

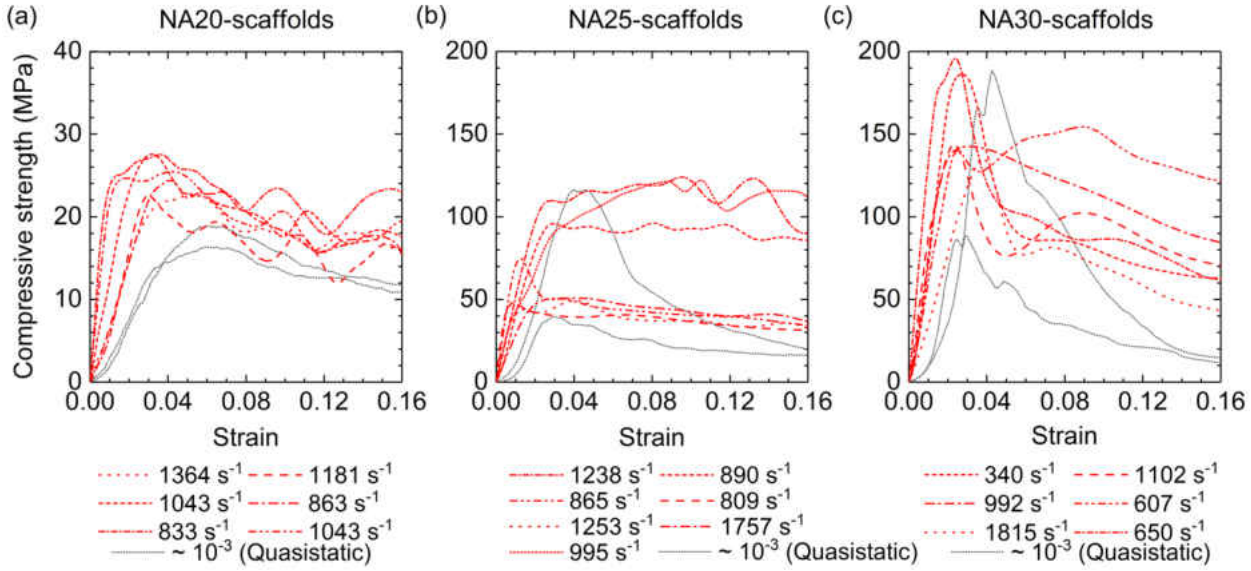

Figure 8: Uniaxial high-strain rate compressive stress-strain curves of the (a) NA20-scaffolds, (b) NA25-scaffolds, and (c) NA30-scaffolds. For each composition, two representative stress-strain curves that represent the upper and lower bounds of quasistatic compressive are also shown for the comparison purpose.

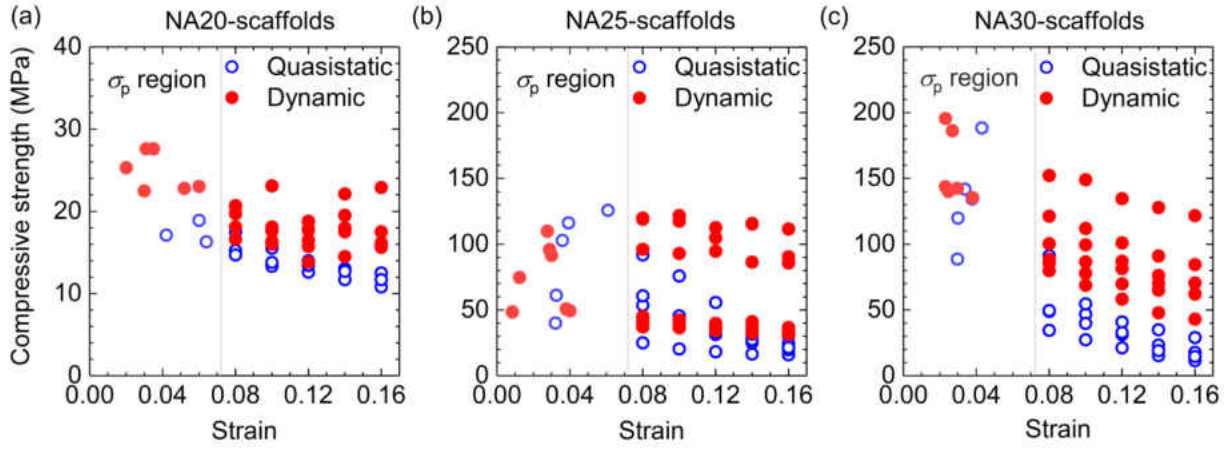

Figure 9: Dynamic and quasistatic compressive strength values of the (a) NA20-scaffolds, (b) NA25-scaffolds and (c) NA30-scaffolds at selected strains.

For NA25-scaffolds (Fig. 8b), a considerable scatter of dynamic σ_p values (50-110 MPa) is observed and σ_p values across the strain rate regimes are found to be within a comparable range. However, in between the strain rate regimes, NA25-scaffolds do exhibit a striking difference in compressive response beyond peak stress. Recall that for quasistatic stress-strain curves with σ_p values above 90 MPa stress drops abruptly beyond σ_p with increasing strain, whereas for σ_p values below 60 MPa a gradual decrease of stress with increasing strain is observed. Interestingly, all the measured dynamic compressive stress-strain curves exhibit a gradual decrease of stress (or almost constant stress) beyond peak stress. Therefore, for comparable dynamic and quasistatic σ_p, area for dynamic stress-strain curve is observed to be greater in comparison to that in quasistatic regime. For NA30-scaffolds (Fig. 8c), considerable scatter of dynamic σ_p values (135-196 MPa) is also noticed as well as measured values do not indicate any significant variation of strength in between the strain rate regimes. Under dynamic loading, NA30-scaffolds exhibit a gradual decrease of stress beyond peak stress as opposed to quasistatic regime where stress drops abruptly beyond peak stress. As a result, for stress-strain curves of comparable σ_p, area for dynamic stress-strain curve is also observed to be greater than that for quasistatic stress-strain curve. Therefore, in quasistatic regime with decreasing porosity compressive response transitioned from progressive failure to brittle-like failure behavior. In dynamic regime, however, all the materials exhibited cellular-like progressive failure.

To further illustrate the differences of compressive response, Fig. 9 shows dynamic and quasistatic compressive strength values of NA20-scaffolds (Fig. 9a), NA25-scaffolds (Fig. 9b), and NA30-scaffolds (Fig. 9c) at selected strain values. For each composition, compressive strength values measured at 10^3 s^{-1} and 10^{-3} s^{-1} strain rates are referred to as dynamic and quasistatic, respectively. In each figure, dynamic and quasistatic σ_p values are shown in the shaded area. Figure 9a clearly

shows increase of σ_p for NA20-scaffolds in dynamic regime in comparison to quasistatic regime, whereas Figs. 9b and 9c suggest that for both NA25-scaffolds and NA30-scaffolds, respectively, respective σ_p values remain comparable across the strain rate regimes. Figure 9 is further useful to illustrate the variation of plateau stress with strain rate. For a compressive stress-strain response in which stress in plateau regime remains constant or exhibits a gradual increase or decreases, an average plateau stress can be conveniently estimated. This is in contrast to quasistatic compressive response of NA25-scaffolds and NA30-scaffolds, where an abrupt drop of stress is observed beyond peak stress. To that end, in Fig. 9 we plotted variation of stress in the post peak stress regime at selected strain values, in the range of 0.08 to 0.16 with a strain interval of 0.02. In this strain range, for any selected strain level, irrespective of composition dynamic stress is observed to be consistently greater in comparison to quasistatic stress. Also, in this strain range for both NA25-scaffolds and NA30-scaffolds, difference of fracture stress in between dynamic and quasistatic regimes increased with increasing strain. Therefore, irrespective of pore volume, in comparison to quasistatic regime ice-templated Al_2O_3 materials under dynamic loading conditions exhibited an overall enhancement of uniaxial compressive response and a prominent stress plateau regime, and thereby maintained the compressive load-bearing capacity during inelastic deformation in the plateau regime.

Strain rate effects in ice-templated ceramics can emerge from inherent rate-sensitivity of the constituent material and micro-inertia effects [112,133,134,139-144]. Micromechanical models also suggest that relative density can strongly influence dynamic compressive response of cellular solids. Mechanical properties of sintered Al_2O_3 are moderately rate-sensitive [145,146]. Therefore, not only compressive mechanical response of ice-templated macroporous Al_2O_3 materials are expected to exhibit a strain rate-sensitivity but also the difference of compressive strength in

between dynamic and quasistatic strain rate regimes is expected to increase with increasing ρ_r from NA20-scaffolds to NA30-scaffolds (i.e., with increasing Al_2O_3 content). While NA20-scaffolds do exhibit a moderate increase of maximum uniaxial compressive strength (σ_p) from quasistatic regime to dynamic regime, NA25-scaffolds and NA30-scaffolds do not exhibit any considerable increase of σ_p from quasistatic regime to dynamic regime. Similar behavior has been also observed for some other cellular solid materials, in which maximum uniaxial compressive strength did not exhibit any measurable strain rate-sensitivity. Cellular solids, which exhibit such behavior, include open-cell and closed-cell aluminum (Al) foams, Al alloy/silicon carbide (SiC) hollow sphere syntactic foams, cp-Al/cenosphere syntactic foams, and amorphous metal foam [134,147-149]. Strain rate-insensitive compressive response of Al-based foams is largely attributed to rate-independent mechanical response of Al and Al alloys. While compressive fracture strength of dense Al_2O_3 is moderately rate-sensitive, one possibility is that over the porosity range of 54-70 vol.% Al_2O_3 volume fractions perhaps did not attribute any significant rate-sensitivity to compressive strength of ice-templated sintered Al_2O_3 materials. Therefore, we may not attribute inherent rate-sensitivity of the constituent material (i.e., Al_2O_3) to the measured differences of dynamic and quasistatic response, which otherwise would have increased the difference of dynamic and quasistatic maximum compressive strength with increasing relative density of ice-templated Al_2O_3 materials.

However, the overall improvement of dynamic compressive response of ice-templated sintered Al_2O_3 materials in comparison to quasistatic compressive response is, in general, consistent to that observed for cellular solids under dynamic and shock loading conditions [112,133,134,139,150-156]. In the dynamic regime of strain rate, the influence of loading rate on the macroscopic response of cellular solids can also arise from the local dynamic effects induced by the rapid

crushing of cell walls, which is referred to as micro-inertia effects [112,157-160]. Micro-inertia effects of cellular solids are related to lateral and rotational inertia of the rapidly displacing cell walls subjected to high-rate loading conditions [134,160,161] and become dominant during the collapse of cell walls at the onset of compressive fracture as well as during the progressive deformation in stress plateau regime, leading to a stress enhancement for failure initiation (peak stress) and/or propagation (plateau stress) under dynamic loading conditions. In cellular solids, inelastic deformation is associated with microstructural mechanisms such as microbuckling of struts, microyielding of constituent material, and microfracture of cell walls, which in dynamic regime are affected by micro-inertia effects [112,139]. Therefore, next we evaluate the probable role of the micro-inertia effects in relation to the measured dynamic response of ice-templated Al_2O_3 materials.

In Section 3.2, we suggested that localized brittle fracture of lamella walls in NA20-scaffolds (Fig. 6a and Fig. 6b) probably resulted from the elastic instability due to buckling. Dynamic compressive stress enhancement due to micro-inertia effects can become particularly significant when asymmetric modes of deformation such as buckling or kink band formation is associated with the initial stress peak in the measured stress-strain response of cellular solids [139,162]. As a result, under high-strain rate loading conditions, lateral inertia of cell walls tends to suppress or retard the more compliant asymmetric modes of cell deformation and a dynamic stress enhancement is measured due to continued axial compression of cell walls (i.e., a macroscopic increase of compressive load) before the asymmetric mode of deformation is triggered [139]. Therefore, under dynamic loading micro-inertia effects probably delayed the initiation of elastic instability within lamella walls of NA20-scaffolds and, in turn, increased maximum uniaxial compressive strength (σ_p) relative to quasistatic regime (Fig. 8a). Recall that quasistatic σ_p values

of NA20-scaffolds are reasonably well predicted by the honeycomb model for out-of-plane compressive deformation (Fig. 4). Since dynamic σ_p values are considerably greater in comparison to quasistatic σ_p values, dynamic strength values would deviate from the model prediction for out-of-plane compressive deformation of honeycomb, which would suggest an enhanced resistance of lamella walls to elastic buckling. Similarly, under dynamic loading conditions, micro-inertia effects can also delay the buckling-induced localized fracture of lamella walls during cellular-like progressive failure stage and thereby enhance compressive stress in the plateau regime. On the other hand, according to our discussion in Section 3.2, axial splitting of lamella walls in NA30-scaffolds is considered to have resulted from macroscopic crack propagation (Fig. 6c). Therefore, for low porosity ice-templated Al_2O_3 materials, fracture of lamellar bridges and perhaps simultaneous axial splitting of lamella walls probably set the limit for maximum compressive strength, caused almost complete separation of the walls (or segments of the walls), and thereby an abrupt drop of compressive stress beyond peak stress was measured. We suggest that within the investigated range of high-strain rate and volume fraction of the solid phase, mechanisms that set the limit for compressive strength in low porosity ice-templated Al_2O_3 materials are probably less strain rate-sensitive. As a result, respective maximum uniaxial compressive strength values (σ_p) of NA25-scaffolds as well as NA30-scaffolds are observed to be comparable across the strain rate regimes.

A more challenging task is to rationalize the dynamic deformation behavior of NA25-scaffolds and NA30-scaffolds in the regime beyond peak stress. This is because NA25-scaffolds and NA30-scaffolds did not exhibit any considerable increase of maximum dynamic strength in comparison to their respective maximum quasistatic strength; however, under dynamic loading conditions an enhancement of compressive stress in the plateau regime is observed relative to quasistatic loading.

It is of note that literature on dynamic compressive behavior of cellular and porous ceramics is non-existent. Assuming negligible contribution from the inherent rate-sensitivity of the constituent material(s), a close relationship exists between the cellular topology and micro-inertial dynamic strength enhancement. While the cellular solids with periodic topology (e.g., honeycombs) are prone to dynamic strength enhancement in the longitudinal direction [163-165], those with stochastic topology (e.g., foams) remain insensitive to loading rate [134,166-168]. Therefore, irrespective of the contribution from the constituent Al_2O_3 phase, anisotropic hierarchical structure ice-templated materials is expected to impose a strain rate-dependence to compressive mechanical properties, which is clearly supported by the results shown in Fig. 8. Several studies [169-174] suggested that cellular structures with strain-softening quasistatic compressive response (referred to as Type II structures) are much more susceptible to micro-inertia based dynamic strength enhancement relative to structures with a flat topped stress-strain curve in plateau regime (referred to as Type I structures). Investigations on strain-softening characteristics during quasistatic deformation (Type II structures) and dynamic strength enhancement have been mainly studied for metallic honeycombs. For example, Al honeycombs compressed in the out-of-plane direction behave as Type-II structure and dynamic strength enhancement was measured including in the intermediate stress plateau regime [165]. For Type II structures, under dynamic loading conditions, micro-inertial effects can result in a symmetric rather than asymmetric mode of deformation in the plateau regime, thereby substantially increasing the stress requirement for deformation to proceed in the intermediate phase and resulting in dynamic stress enhancement.

We can also categorize ice-templated Al_2O_3 materials as Type II structures, because of the apparent strain-softening in quasistatic compressive response beyond peak stress, i.e., decrease of stress with increasing strain (Fig. 3) and due to the dynamic strength enhancement in the stress plateau

regime (Fig. 8). Although the inelastic deformation mechanisms are different for metallic and ceramic cellular solids, we can compare dynamic compressive behavior of Type II cellular solid structures and ice-templated Al_2O_3 materials to gain some insights into the origin of dynamic strength enhancement in the plateau regime for the latter materials. Among the Al_2O_3 materials, NA25-scaffolds (with high peak stress values) and NA30-scaffolds exhibited maximum strain-softening in the quasistatic compressive response (Fig. 3). The apparent quasistatic strain-softening behavior is considered to stem from brittle-like failure and due to increased resistance to elastic buckling (an asymmetric mode of deformation) of lamella walls. Recall from Fig. 5a that in NA30-scaffold upon reaching maximum quasistatic compressive strength, the entire structure axially splitted into almost equal size fragments. We can consider axial splitting as a symmetric mode of deformation that resulted global failure under quasistatic loading conditions in ice-templated Al_2O_3 materials with low porosity and having high peak stress. In the dynamic regime of loading, upon damage initiation in the ice-templated structures of higher ceramic volume fractions, it is possible that damage evolution is of localized nature due to lateral inertia and damage progressively propagates through the structure. As a result, compressive load-bearing capacity in NA25-scaffolds and NA30-scaffolds is maintained to an extent beyond peak stress. Therefore, beyond peak stress dynamic compressive response of NA25-scaffolds and NA30-scaffolds exhibited a gradual decrease of stress with the increasing strain as opposed to quasistatic compressive response where stress drops abruptly.

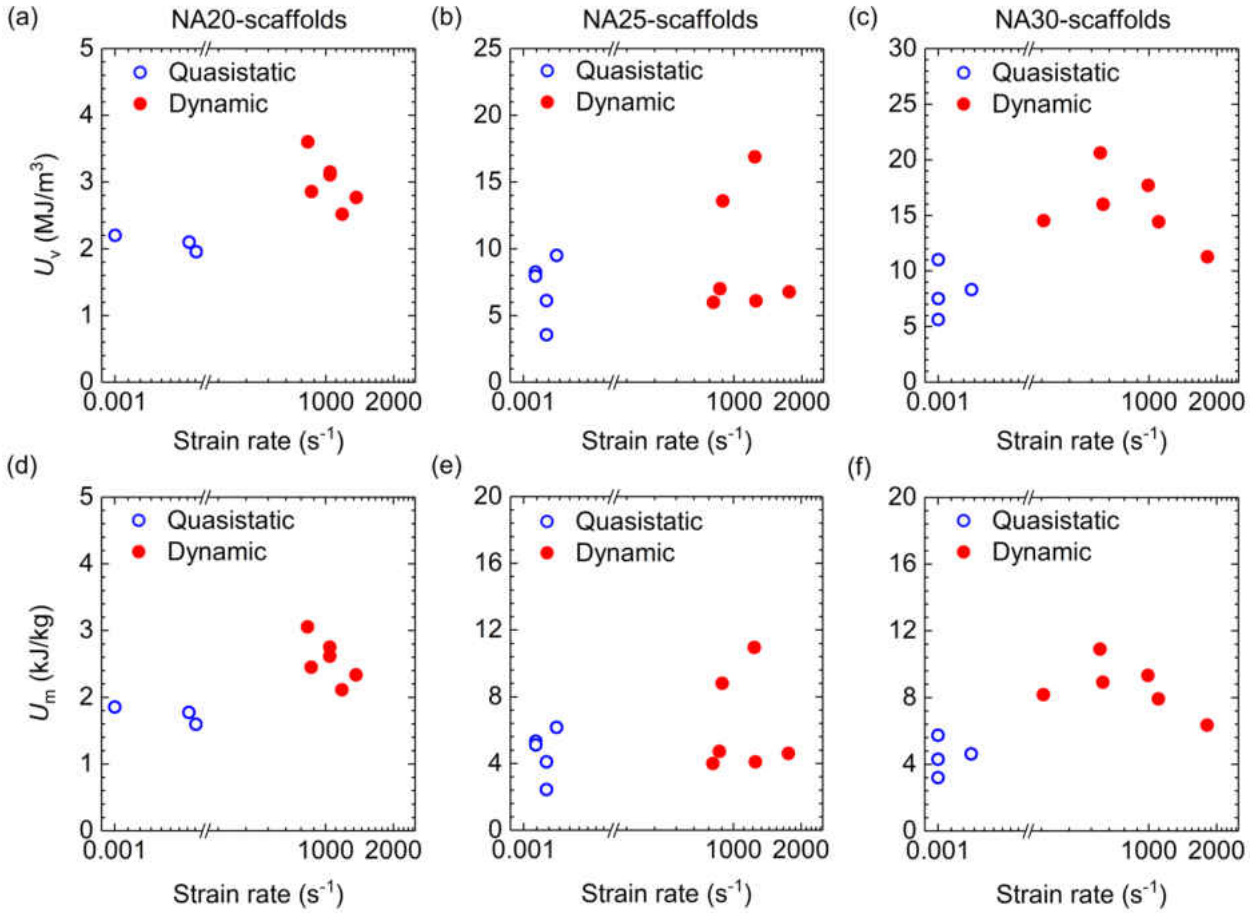

Figure 10: Variation of volume-based energy absorption U_v (up to 0.16 strain) of the (a) NA20-scaffolds, (b) NA25-scaffolds, and (c) NA30-scaffolds under dynamic and quasistatic loading conditions. Also, variation of mass-based energy absorption U_m (up to 0.16 strain) of the (d) NA20-scaffolds, (e) NA25-scaffolds, and (f) NA30-scaffolds.

5.3.4 Energy absorption and efficiency

The area under a compressive stress-strain curve is a measure of the energy absorption ability of a material, which is an important consideration to design materials and structures for applications where graceful progressive failure is desired. Energy absorption capacity per unit volume (U_v) is calculated as [112]

$$U_v = \int_0^{\varepsilon} \sigma \, d\varepsilon. \quad (13)$$

Whereas, energy absorption capacity per unit mass (U_m) can be estimated as

$$U_m = U_v/\rho^*, \quad (14)$$

where ρ^* is the density of the foam. Here, for each compressive stress-strain curve U_v and U_m values were calculated up to a strain (ε) value of 0.16. Figure 10 shows variations of U_v and U_m with strain rate for NA20-scaffolds (Figs. 10a and 10d), NA25-scaffolds (Figs. 10b and 10e), and NA30-scaffolds (Figs. 10c and 10f). Since U_v and U_m values are only calculated up to 0.16 strain, the estimated values should not be compared directly to those of the other materials where energy absorption is usually calculated up to densification strain [112]. Rather, the purpose of Fig. 10 is to make relative comparisons of U_v and U_m values across the compositions and in between the strain rate regimes. For NA20-scaffolds both U_v and U_m values are observed to be considerably lower relative to those of NA25-scaffolds and NA30-scaffolds, which is attributed to low compressive strength of NA20-scaffolds. However, a moderate increase of energy absorption is observed from quasistatic regime to dynamic regime and is attributed to dynamic strength enhancement. For both NA25-scaffolds and NA30-scaffolds, irrespective of the differences of ρ_r and σ_p, U_v and U_m values are observed to be comparable in quasistatic regime. In dynamic regime, both NA25-scaffolds and NA30-scaffolds exhibited an increase of energy absorption relative to that in quasistatic regime. Overall, under dynamic loading, NA30-scaffolds exhibited highest U_v and U_m values among all the materials. Figure 11 shows the percentage of improvement of energy absorption capacity of ice-templated Al_2O_3 materials from quasistatic regime to dynamic regime. For each scaffold composition, all the U_v and U_m values measured at quasistatic loading conditions were utilized to estimate average quasistatic U_v and U_m and corresponding standard deviations. Similarly, for each scaffold composition, all the U_v and U_m values measured in the dynamic regime

were utilized to estimate average dynamic U_v and U_m and corresponding standard deviations. Figure 11 suggests that for all the ice-templated Al_2O_3 materials, energy absorption capacity improved from quasistatic regime to dynamic regime. While NA20-scaffolds and NA25-scaffolds exhibited improvement in the range of 30-40%, NA30-scaffolds exhibited over 90% improvement in energy absorption capacity.

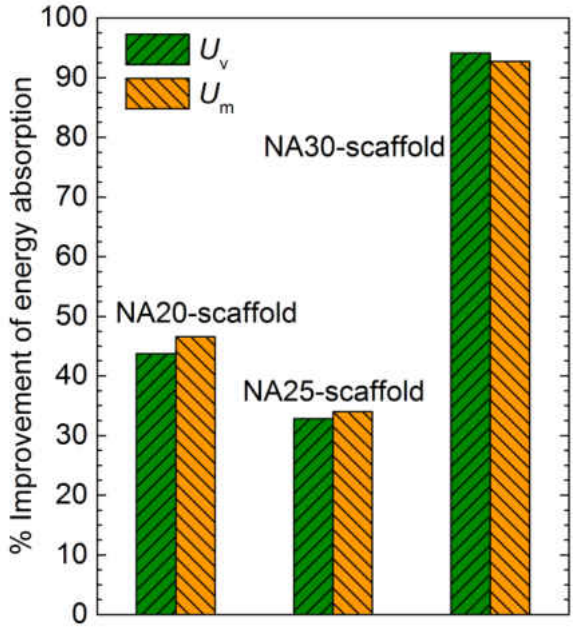

Figure 11: The percentage improvement in energy absorption (U_v and U_m) from quasistatic regime to dynamic regime of strain rate for the NA20-scaffolds, NA25-scaffolds, and NA30-scaffolds.

In addition to energy absorption, further insights can be obtained from the energy absorption efficiency parameter (e), where e is defined as the ratio of the energy absorption up to a strain (ε) divided by the stress (σ) at that strain level as follows [112]:

$$e = \frac{1}{\sigma}\int_0^{\varepsilon} \sigma d\varepsilon. \qquad (15)$$

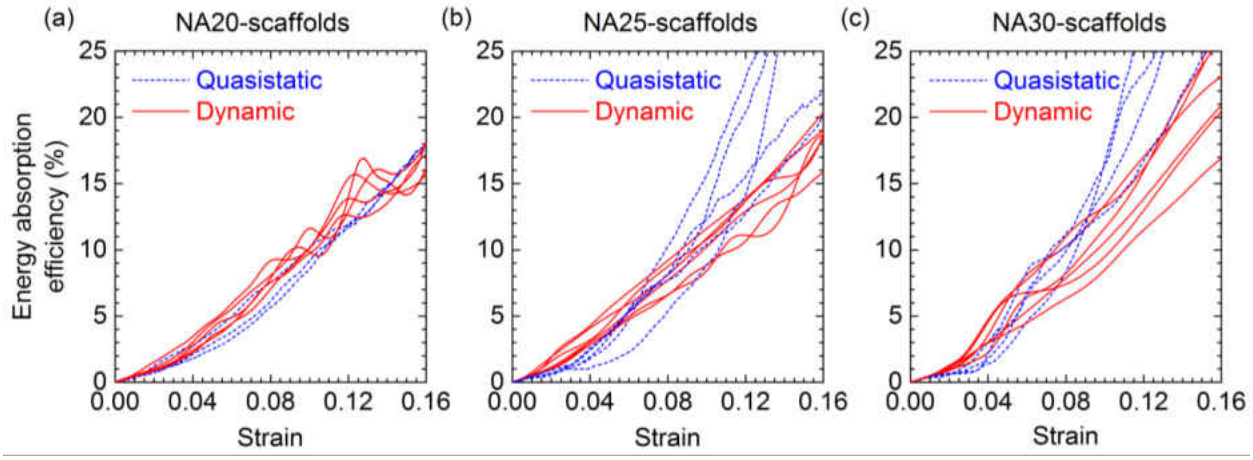

Figure 12: Variation of energy absorption efficiency parameter (%) as a function of strain under dynamic and quasistatic loading conditions for the (a) NA20-scaffolds, (b) NA25-scaffolds, and (c) NA30-scaffolds.

Figure 12 compares variations of e(%) with ε for NA20-scaffolds, NA25-scaffolds, and NA30-scaffolds in between the quasistatic and dynamic regimes. For all the scaffolds within the ε range of 0-0.16 e is observed to vary almost linearly with increasing ε. For NA25-scaffolds (Fig. 12b) and NA30-scaffolds (Fig. 12c), some of the quasistatic data show a sudden increase of e beyond about 0.1 ε, which is attributed to the abrupt drop of σ beyond peak stress. For those data, the apparent increase of e beyond 0.1 ε does not necessarily mean an increase in the energy absorption efficiency of the corresponding scaffolds at relatively higher strain levels. In general, Fig. 12 does not indicate any significant differences across the scaffold compositions and strain rate regimes, and within the ε range of 0-0.16 e increases almost linearly and reaches about 15-20%. Therefore, in spite of a considerable variation of total energy absorption capacity across the scaffold compositions and strain rate regimes, effects of changes of pore volume, pore morphology, microstructural features such as lamella wall thickness and lamellar bridge density, and strain rate on the energy absorption efficiency is observed to be insignificant.

5.4 Concluding remarks

We investigated effects of porosity and strain rate on the uniaxial compressive response of ice-templated sintered Al_2O_3 materials. In high porosity regime (70 vol%) quasistatic compressive response exhibited damageable, cellular-like failure and transitioned to brittle-like failure behavior in low porosity regime (54 vol.%). For NA20-scaffolds (porosity 70 vol.%) having highly lamellar structure with thin ceramic walls and minimal lamellar bridging, we conjecture that the limit of maximum uniaxial compressive strength (i.e., peak stress) is set by the buckling-induced elastic instability in the walls. Due to limited resistance to buckling lamella walls of NA20-scaffolds undergo localized failure, whereas macroporous structure remains almost intact at macroscopic level. Upon further compression beyond peak stress, structure continues to undergo localized failure through the fracture of the walls dominantly in a direction almost perpendicular to the applied loading direction (parallel to the walls) and the measured quasistatic compressive response proceeds through a prominent plateau regime where stress decreases progressively with increasing strain. On the other hand, we suggest that due to thick lamella walls and extensive lamellar bridging, lamella walls of NA30-scaffolds exhibited marked resistance to buckling-induced instability. In the vicinity of peak stress, the applied compressive load could be sufficient enough to cause a failure of the bridges and perhaps simultaneous axial splitting of the walls throughout the structure. Thus, NA30-scaffolds exhibited global failure, which is manifested by an abrupt drop of compressive stress beyond peak stress.

Dynamic compressive response of ice-templated Al_2O_3 materials exhibited measurable and interesting differences relative to quasistatic response. In the dynamic regime, NA20-scaffolds exhibited an overall improvement of compressive response in comparison to quasistatic regime. For NA25-scaffolds and NA30-scaffolds, respective maximum compressive strength values were

observed to be comparable between the strain rate regimes; however, in the dynamic regime beyond peak stress, compressive response exhibited a gradual decrease of stress that is in sharp contrast to the abrupt decrease of stress measured in the quasistatic regime. We suggested that inherent strain rate-sensitivity of Al_2O_3 might not have influenced the dynamic behavior of ice-templated Al2O3 materials. We rationalized the overall improvement in dynamic compressive response in terms of micro-inertia and other effects. Overall, in the dynamic regime of strain rate, all the ice-templated Al_2O_3 materials exhibited an improvement of compressive response and energy-absorbing ability in comparison to quasistatic loading conditions. Among all the compositions and across the strain rate regimes, energy absorption capacity was observed to be highest for NA30-scaffolds under dynamic loading conditions. However, energy absorption efficiency remained comparable across the compositions and strain rate regimes. The measured results of uniaxial compressive response and the rationalization presented here can have a critical significance toward the applications of ice-templated macroporous ceramic structures in high-strain rate (dynamic) loading environments.

Acknowledgements

We thank the Applied Research Center (ARC) of College of William and Mary for providing the access to the desktop SEM and Prof. Xiaoyu Zhang (Mechanical and Aerospace Engineering, Old Dominion University) for providing access to the high temperature furnace.

5.5 Supplementary information

5.5.1 Ice-templating using a custom-made device

Freeze casting was conducted using a custom-made set up. In this set up, a Teflon tube is placed on the top of a thin (0.5 mm) steel plate, partially filled with Al_2O_3 slurry, and the whole assembly is inserted inside a liquid nitrogen (N_2) Dewar. The Teflon tube is kept radially insulated to ensure that the suspension is frozen only under the influence of unidirectional (vertical) thermal gradient. By adjusting the distance between the steel plate and liquid N_2, freezing front velocity (FFV) was controlled. In this study, all the scaffolds were processed at a fixed gap (1 mm) between the liquid N_2 and steel plate. Average FFV was estimated by dividing the frozen sample height with the total time required for freezing of the sample. Temperature changes of cold-finger during unidirectional freeze casting were measured through a thermocouple attached on the top of the cold-finger.

From each sintered scaffold cylinder (approximately 16.9 mm in diameter and 15.6 mm in height), a small specimen of dimensions 6mm × 6mm × 3mm was extracted (Fig. S1).

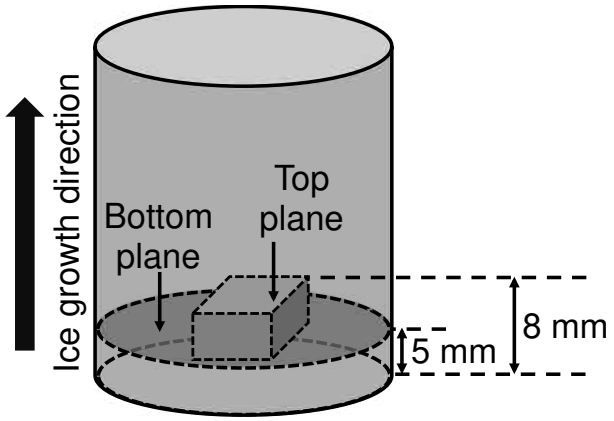

Figure S1: A schematic of the sintered ice-templated scaffold sample illustrating location of the specimen extracted for density measurement, microstructural characterization, and compression test. Locations of the top and bottom of the specimen are also shown. (Not to scale)

5.5.2 SHPB testing

Upon impact by the striker bar, a compressive stress pulse is produced in the incident bar, travels through the bar and loads the sample in compression. A part of the pulse is transmitted through the specimen to the transmission bar while the rest is reflected back to the incident bar. These stress pulses were utilized to determine the stress-strain response of the glass foams. A copper (Cu) pulse shaper was placed at the striker bar-incident bar interface to substantially increase the rise time of the loading pulse and to filter out the high-frequency components from the elastic stress waveform. Stress pulses were measured through the strain gages (mounted in the middle of the incident and transmission bars) using a signal conditioning amplifier (2310B, Vishay) and a high-speed digitizer (NI PCI-5105, National Instrument).

CHAPTER 6

DYNAMIC STRENGTH ENHANCEMENT AND STRAIN RATE SENSITIVITY IN ICE-TEMPLATED CERAMICS PROCESSED WITH AND WITHOUT ANISOMETRIC PARTICLES

Note: The contents of this chapter have been published in Scripta Materialia.

D. Ghosh, M. Banda, J. E. John, D. A. Terrones, Dynamic strength enhancement and strain rate sensitivity in ice-templated ceramics processed with and without anisometric particles, Scripta Mater., 154 (2018) 236 – 240.

DOI: https://doi.org/10.1016/j.scriptamat.2018.06.006

Abstract:

We investigated the effects of platelets and strain rate on the compressive response of ice-templated porous alumina, processed from ultrafine, equiaxed particles and from a mixture of ultrafine, equiaxed and large platelet particles. Results revealed a remarkable enhancement of the quasistatic and dynamic compressive mechanical properties of the templated ceramics in the presence of platelets. Specific compressive mechanical properties of the ice-templated alumina containing platelets are superior in comparison to those of the various metallic, syntactic and natural cellular solids. In the presence of platelets, compressive strength exhibited contrasting strain rate sensitivity between the elastic and inelastic stages of deformation.

Keywords: Ice-templating; platelets; compressive response; strain rate; strain rate sensitivity.

6.1 Introduction

Significant interest in ice-templated macroporous ceramic materials has arisen primarily from their inherent hierarchical, anisotropic microstructure, directional porosity and low pore tortuosity (i.e., high pore connectivity), which are deemed suitable to enhance the performance of porous materials in biomedical, defense, energy, filtration, and other engineering applications [7,10,46,83,105]. In these engineering endeavors, compressive mechanical properties are of major significance to ensure the mechanical reliability of ice-templated macroporous ceramic components. Compressive response of ice-templated sintered macroporous ceramic materials features an approximately linear increase of stress with strain up to a maximum compressive stress (referred to as peak stress) and exhibits a graceful progressive failure beyond maximum compressive stress, as such further compression leads to a gradual decrease of stress with increasing strain [9,105,106]. At a specific level of porosity (i.e., material density) processing mechanisms capable of enhancing compressive mechanical properties of ice-templated ceramic materials are of great interest. Ice-templated ceramics are typically processed from aqueous suspensions containing fine, equiaxed ceramic particles [7,9,46,83,105,106]. In our recent studies [108,124,136], we revealed that inclusion of small fraction of large anisometric alumina (Al_2O_3) particles of platelet morphology in aqueous suspension that mainly consisted of fine, equiaxed Al_2O_3 particles led to two-fold unique microstructural effects in the templated sintered Al_2O_3 materials: substantial increase of lamellar bridge density and modification of lamella wall microstructure. The resulted sintered ceramic materials exhibited an unprecedented enhancement of uniaxial compressive strength, plateau stress, and energy absorption capacity (area under the stress-strain curve). To utilize platelets-reinforced ice-templated hierarchical lightweight ceramics in dynamic environments in which materials are subjected to mechanical forces in tens of microseconds (μs), it is necessary to

investigate compressive mechanical properties in the high-strain rate regime of $\geq 10^2$ s^{-1} that is drastically greater relative to that encountered under quasistatic loading conditions, strain rate ~10^{-3} s^{-1}. Due to the significant strain rate difference, compressive deformation response of cellular and porous solids measured in the quasistatic strain rate regime does not truly represent the material behavior in the dynamic loading regime [112,139]. In a recent study [175], we showed that compressive mechanical properties of ice-templated Al_2O_3 materials are considerably strain rate sensitive. In this letter, we report on the dynamic strength enhancement, progressive deformation characteristics, energy absorption, and strain rate sensitivity of ice-templated Al_2O_3 materials processed with and without anisometric platelet particles.

6.2 Materials used and experimental approach

In this study, we synthesized ice-templated Al_2O_3 materials from aqueous suspensions containing (a) ultrafine, equiaxed Al_2O_3 (UA) powder particles (d_{50} = 300 nm) and (b) 80-20 vol.% mixture of UA particles and large Al_2O_3 platelets (PA, diameter ~8 μm and thickness ~400 nm); however, total Al_2O_3 content in all the suspensions was same, 20 vol.%. Ceramic suspensions were unidirectionally solidified at comparable freezing conditions and resulted average freezing-front velocity (FFV) was 38.9 ± 1.5 μm/s and 38.2 ± 1.5 μm/s for ice-templated UA materials and UA-PA materials, respectively. Templated materials were freeze-dried at 0.014 mbar pressure and -50°C for 96 hours and sintered at 1550°C for 4 hours. All the sintered materials were of cylindrical geometry (diameter ~10 mm and height ~18 mm). From each sintered material, a thin disk (2 mm) was extracted using a diamond saw and utilized for density measurement and uniaxial compression test. Quasistatic compression tests over a strain rate range of 10^{-4} – 10^{-1} s^{-1} were conducted in mechanical testing machines (MTS Alliance RF/300 and Tinius Olsen 10ST), whereas a modified

split-Hopkinson pressure bar (SHPB) was employed to perform dynamic compression experiments (strain rate $\geq 10^2$ s^{-1}). For both dynamic and quasistatic tests, compressive load was applied parallel to the growth direction of ice crystals. SHPB set up and working principles and other experimental details are provided in the Supplementary Material.

6.3 Results and discussion

Average relative density (ρ_r) of ice-templated sintered UA material was found to be 0.3 (i.e., 70 vol.% porosity), whereas ice-templated sintered UA-PA material exhibited an average density of 0.25 (i.e., 75 vol.% porosity). While the average relative density difference is not drastic, results of density measurements suggest that presence of a small fraction of platelets increased porosity to an extent relative to the templated materials processed without platelets. Our earlier work on ice-templated Al_2O_3 materials [108,124,136] showed that large platelet particles formed lamellar bridges between adjacent ceramic lamella walls and significantly enhanced lamellar bridge density in comparison to Al_2O_3 materials processed without the platelets. Additionally, the presence of platelets increased porosity to an extent. In this study, we investigated the effects of anisometric platelet particles on both the uniaxial dynamic and quasistatic compressive response of ice-templated sintered Al_2O_3 materials.

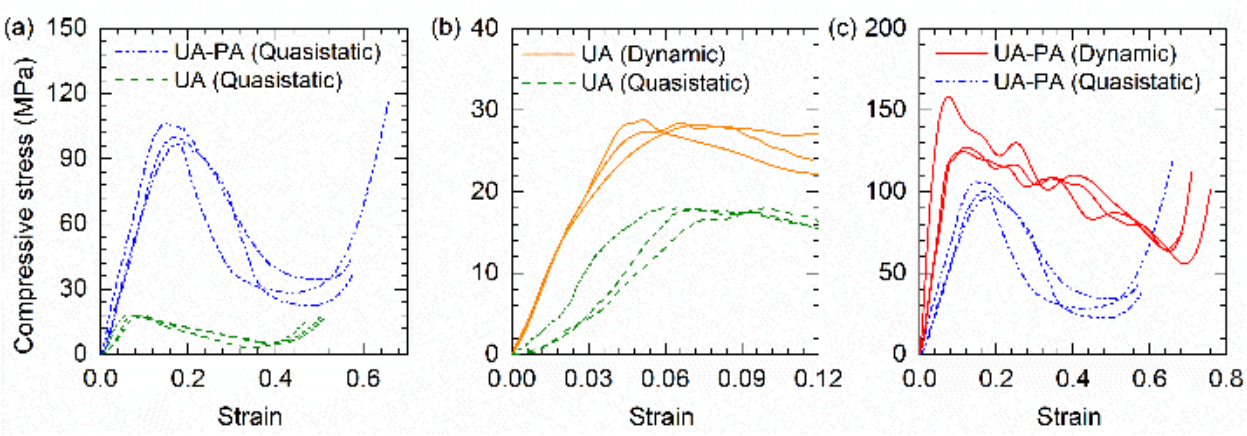

Figure 1: Representative uniaxial compressive stress-strain curves of (a) UA material and UA-PA material in quasistatic regime of strain rate, (b) UA material both in quasistatic and dynamic regime of strain rate (~730-2200 s^{-1}), and (c) UA-PA material both in quasistatic and dynamic regime of strain rate (~1700-3200 s^{-1}). For both materials strain rate in quasistatic regime is ~0.002 s^{-1}.

Figure 1a shows representative uniaxial quasistatic (strain rate ~0.002 s^{-1}) compressive response of ice-templated UA and UA-PA materials. For both UA and UA-PA, the compressive response shows approximately a linear increase of stress with strain and beyond peak stress (i.e., maximum compressive stress, σ_p) a decrease of stress with increasing strain, followed by a densification stage. At a strain rate level of 0.002 s^{-1}, UA-PA exhibited a drastic enhancement of σ_p relative to UA. As a result area under stress-strain curve up to densification strain, which is a measure of total energy absorption capacity, is also observed to be significantly greater for UA-PA relative to UA. Therefore, while relatively greater porosity of UA-PA in comparison to UA is expected to cause a decrease of strength for the former materials in comparison to the latter materials, the addition of small amount of anisometric PA particles resulted in a marked enhancement of compressive mechanical properties. While UA-PA exhibited a distinct strength advantage over UA, the addition

of anisometric particles also resulted in an observable difference in the overall signature of compressive response in between two materials. Beyond peak stress, further uniaxial compression resulted in a gradual decrease of stress with increasing strain for UA, whereas UA-PA exhibited a drastic decrease of stress with increasing strain. However, at any strain level, compressive strength of UA-PA remained significantly greater in comparison to UA. The uniaxial compressive response of UA-PA (porosity 75 vol.%) can be considered as a brittle-like failure behavior as opposed to the graceful progressive failure that is observed in UA (porosity 70 vol.%). For ice-templated sintered Al_2O_3 materials with a porosity of 70 vol.% and greater, the uniaxial compressive response has been observed to be of progressive failure type [9,105,106,112,124]. According to Gibson and Ashby [110], brittle materials with relative density ≤0.3 (i.e., porosity ≥70 vol.%) are considered as cellular solids, which exhibit a damageable, cellular-like compressive response. Therefore, it is interesting that small fraction of anisometric particles caused an apparent change in the compressive deformation behavior in ice-templated sintered Al_2O_3 materials despite of having porosity above 70 vol.%.

Figures 1b and 1c show representative uniaxial dynamic compressive stress-strain response of ice-templated sintered UA in the strain rate range of 730-2200 s^{-1} and UA-PA in the strain rate range of 1700-3200 s^{-1}. For the purpose of comparison, representative quasistatic stress-strain curves (strain rate ~0.002 s^{-1}) are also shown. For the applied SHPB experimental conditions, about 0.12 strain was achieved in UA, whereas densification strain was achieved in UA-PA. For UA material, the overall signature of stress-strain curves is observed to be comparable in between the dynamic and quasistatic strain rate regimes. The dynamic compressive response suggests a considerable stiffening in UA material in comparison to quasistatic loading. Similarly, dynamic σ_p of UA is observed to be considerably greater in comparison to quasistatic σ_p. Figure 1b further shows that

under dynamic loading conditions there is an increase of compressive stress in the plateau regime in comparison to quasistatic loading conditions. As a result, the area of dynamic stress-strain curves is observed to be greater in comparison to that of quasistatic stress-strain curves, indicating an increase of energy absorption capacity in the dynamic regime relative to the quasistatic regime of strain rate. Therefore, for UA material with increasing strain rate, we measured a considerable enhancement of compressive mechanical properties. Similarly, UA-PA material also exhibited significant strain rate sensitivity (Fig. 1c). The high-strain rate measurements for UA-PA revealed significant stiffening as well as enhancement of σ_p and plateau stress in comparison to quasistatic strain rate regime. Under dynamic loading conditions, an increase of area under stress-strain curves also suggests an increase of energy absorption capacity relative to that under the quasistatic loading conditions. Moreover, in the dynamic regime, UA-PA exhibited considerably greater densification strain in comparison to that of UA. For UA-PA, another major noticeable difference between the dynamic and quasistatic strain rate regimes is observed in the compressive failure response beyond peak stress. Under the quasistatic loading, beyond peak stress, compressive stress is observed to decrease sharply with increasing strain, which resemblances to brittle-like failure behavior. Whereas, in the dynamic regime UA-PA exhibited a prominent plateau regime in which compressive stress decreased gradually with increasing strain, which represents a cellular-like progressive failure response. As a result, in the plateau regime at any strain level not only the dynamic compressive strength is observed to be significantly greater in comparison to the quasistatic compressive strength but also the difference in between the dynamic and quasistatic strength increased gradually with increasing strain, i.e., with continued compressive deformation.

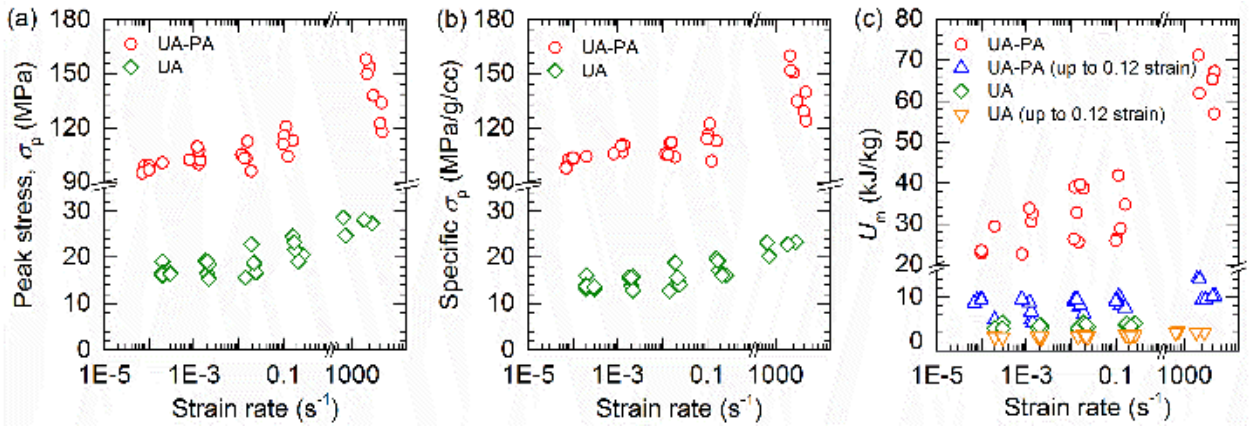

Figure 2: Variation in (a) peak stress, (b) specific peak stress, and (c) mass based energy absorption capacity with strain rate for UA and UA-PA materials.

Figure 2a shows a variation of σ_p as a function of strain rate, whereas to account for density variation among the specimens we also plotted specific σ_p (=σ_p/density) with strain rate in Fig. 2b. While the overall trend did not necessarily change, a slight decrease in the scatter of data can be observed. Over the entire strain rate range of 10^{-4} – 3200 s^{-1}, σ_p of UA-PA is consistently observed to be markedly greater in comparison to that of UA. It is interesting that both the materials also exhibited strain rate sensitivity in the quasistatic strain rate regime. At strain rate of 10^{-4} s^{-1}, average σ_p of UA is 16.8 ± 1 MPa (average specific σ_p = 14 ± 1 MPa/g/cm^3), whereas in the dynamic strain rate regime average σ_p of UA is 27.2 ± 1.5 MPa (average specific σ_p = 22.3 ± 1.2 MPa/g/cm^3). Similarly, for UA-PA average σ_p is 98.2 ± 2 MPa (average specific σ_p = 102.2 ± 2.3 MPa/g/cm^3) at strain rate of 10^{-4} s^{-1} and 139.2 ± 14.3 MPa (average specific σ_p = 141.5 ± 12.2 MPa/g/cm^3) in the dynamic strain rate regime. Therefore, we can state that a combination of anisometric platelet particles and dynamic loading resulted in an unprecedented enhancement of compressive strength of ice-templated sintered Al_2O_3 materials from 16.8 ± 1 MPa (specific σ_p = 14 ± 1 MPa/g/cm^3) to 139.2 ± 14.3 MPa (specific σ_p = 141.5 ± 12.2 MPa/g/cm^3). Figure 2c shows a variation of mass-

based energy absorption capacity (U_m) of UA and UA-PA materials with strain rate. For UA U_m was calculated up to densification strain for quasistatic strain rate range; however, was also estimated up to 0.12 strain for the entire strain rate range, since we achieved only 0.12 strain in UA under dynamic loading conditions. For UA-PA, U_m was calculated up to densification strain as well as up to 0.12 strain for the purpose of comparison with UA. Figure 2c shows that in the quasistatic strain rate range U_m of UA-PA is markedly greater relative to that of UA. Also for estimation up to 0.12 strain, over the entire strain rate range U_m of UA-PA is observed to be significantly greater in comparison to that of UA. U_m of UA-PA shows a considerable increase with increasing strain rate and U_m values in the dynamic loading regime are observed to be markedly greater in comparison to that in the quasistatic regime as well as compared to UA. Overall, Fig. 2 reveals that in presence of small quantity of platelet particles both the dynamic compressive strength and energy absorption capacity of ice-templated sintered Al_2O_3 materials enhanced markedly. We attribute the measured drastic enhancement of dynamic energy absorption capacity of UA-PA to the increase in peak stress and plateau stress as well as to densification strain under high-strain rate loading conditions.

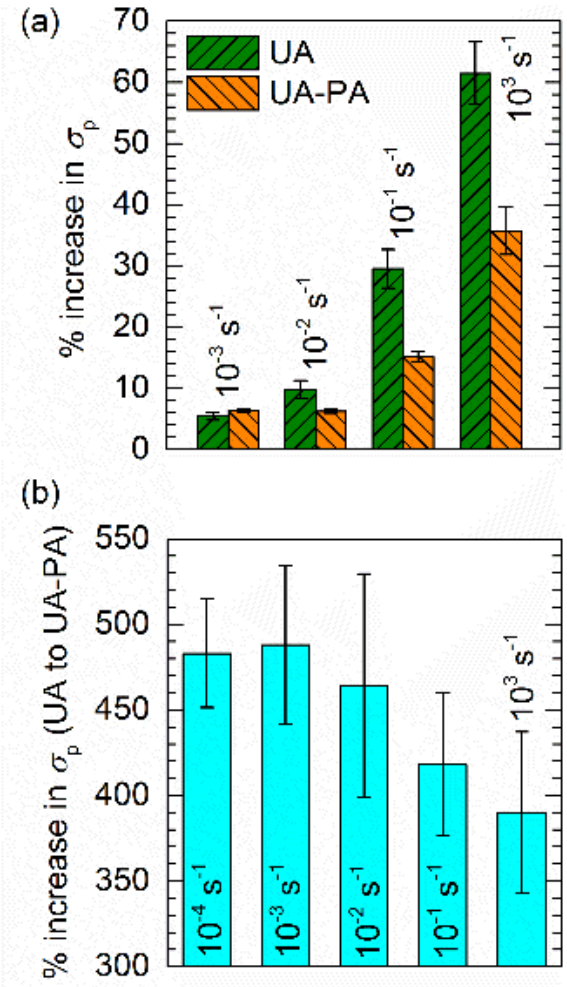

Figure 3: (a) The percentage change in peak stress of UA and UA-PA materials with an increase in strain rate. For each material, average peak stress at a strain rate of 10^{-4} s^{-1} is taken as a reference value and average peak stress values at higher strain rates of 10^{-3} s^{-1}, 10^{-2} s^{-1}, 10^{-1} s^{-1} and 10^{3} s^{-1} are utilized to estimate the % change with respect to the reference peak stress. (b) The percentage change in the average peak stress in between UA-PA and UA at different strain rates.

We compared the uniaxial compressive mechanical properties of UA-PA material to those of the commonly investigated metallic, syntactic and natural cellular solids. For steel based composite metal foams, corresponding to a material density range of 2-3 g/cm^3 quasistatic specific yield strength values have been reported in the range of 41-44 MPa/g/cm^3 [176]. In contrast, for ice-

templated UA-PA we measured quasistatic specific compressive strength (σ_p) in the range of 96-122 MPa/g/cm^3 (Fig. 2b) for material density ≤1 g/cm^3. For Al and Al alloy foams, high-strain rate U_m values have been found to be on the order of 5 kJ/kg [177-181], whereas for various syntactic foams dynamic U_m values fall in the range of 25-40 kJ/kg [182-184]. For steel and composite metal foams dynamic U_m has been reported in the range of 15-40 kJ/kg [176,185-187] and natural cellular solids such as balsa wood exhibited U_m of about 60 kJ/kg under high-strain rate loading conditions [139]. As can be observed in Fig. 2c measured dynamic U_m values of UA-PA material are in the range of 56-72 kJ/kg. Therefore, our results suggest that in presence of small quantity of platelet particles ice-templated UA-PA material exhibited specific compressive mechanical properties that are superior in comparison to those of the various metallic, syntactic and natural cellular solids.

We also attempted to understand the effects of anisometric platelet particles on the strain rate sensitivity of uniaxial compressive response of ice-templated sintered Al_2O_3 materials. Figure 3a shows percent (%) change in σ_p for both materials with increasing strain rate. For each material, average σ_p at a strain rate of 10^{-4} s^{-1} is taken as a reference value and average σ_p values at higher strain rates of 10^{-3} s^{-1}, 10^{-2} s^{-1}, 10^{-1} s^{-1} and 10^{3} s^{-1} are utilized to estimate the % change with respect to the reference σ_p. In the dynamic regime of strain rate, for each material we estimated average dynamic σ_p value over the entire high-strain rate range, 730-2200 s^{-1} for UA and 1700-3200 s^{-1} for UA-PA. While the increase of % change in σ_p with increasing strain rate further supports rate sensitivity of maximum compressive strength in both the materials, at a comparable level of strain rate greater % change in σ_p for UA in comparison to that for UA-PA indicates toward a decrease in rate sensitivity in ice-templated sintered Al_2O_3 containing platelets. In Fig. 3b we plotted % change of σ_p in between UA-PA and UA materials at different strain rates. A decrease in % change of σ_p with increasing strain rate from 483% at 10^{-4} s^{-1} to 390% at 10^{3} s^{-1} further supports a possible

reduction of strain rate sensitivity of maximum compressive strength in ice-templated Al_2O_3 materials containing platelet particles.

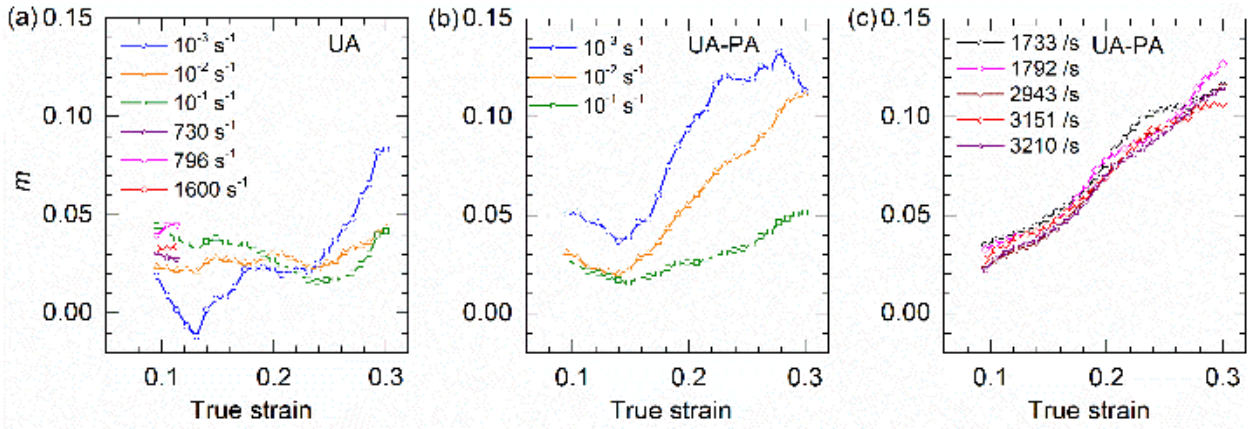

Figure 4: Variation in strain rate sensitivity parameter (m) with true strain for (a) UA material in both strain rate regimes, (b) UA-PA material in quasistatic strain rate regime, and (c) UA-PA material in dynamic strain rate regime.

To further understand the effects of platelets on the strain rate sensitivity of compressive response, we next evaluated rate sensitivity of compressive strength of both UA and UA-PA materials beyond peak stress, i.e., in the inelastic deformation stage. Toward this end, we estimated a strain rate sensitivity parameter 'm' for both materials, which is defined as [177]

$$m = \left(\frac{\partial log\sigma_t}{\partial log\dot{\varepsilon}}\right) = \frac{log(\sigma_{2t}/\sigma_{1t})}{log(\dot{\varepsilon}_2/\dot{\varepsilon}_1)}, \quad (1)$$

where σ_{1t} and σ_{2t} are true stresses at strain rates $\dot{\varepsilon}_1$ and $\dot{\varepsilon}_2$, respectively for a prescribed value of strain (ε). For each material, true stress values beyond peak stress corresponding to a strain rate of 10^{-4} s^{-1} ($\dot{\varepsilon}_1$) at selected ε levels were taken as σ_{1t} values and true stress values beyond peak stress corresponding to higher strain rate ($\dot{\varepsilon}_2$, 10^{-3} s^{-1}, 10^{-2} s^{-1}, 10^{-1} s^{-1} or 10^{3} s^{-1}) at the same ε levels were taken as σ_{2t} values, which were utilized to calculate m. It is to be noted that σ_p values for both the

materials at various strain rates appeared at different strains and, therefore, *m* was not estimated corresponding to σ_p. Figure 4 shows a variation of *m* within the true strain (ε_t) range of 0.09-0.3 for UA and UA-PA materials, respectively. For each curve indicated strain rate corresponds to $\dot{\varepsilon}_2$. According to Fig. 4a, UA material does not exhibit any particular trend in *m* with the variation of true strain and strain rate and *m* values are found to be in the range of 0.02 to 0.04. Therefore, it may be inferred that in the inelastic deformation stage, strain rate sensitivity of compressive response of UA remained unchanged. Figures 4b and 4c, on the other hand, reveal an almost linear increase in *m* from 0.03 to 0.13 with increasing strain both in the quasistatic and dynamic strain rate regimes, respectively, which suggests an increase in rate sensitivity for UA-PA material during inelastic compressive deformation. However, in the quasistatic strain rate regime with increasing strain *m* of UA-PA material is observed to decrease as the strain rate increased from 10^{-3} s^{-1} to 10^{-1} s^{-1} (Fig. 4b), which indicates a decrease of strain rate sensitivity during inelastic deformation with increasing strain rate in the quasistatic regime. In the dynamic regime of strain rate (Fig. 4c), UA-PA does not exhibit any particular trend with changes in strain rate. It is to be noted that in the higher strain level *m* of UA-PA material is observed to be considerably greater in comparison to that of UA material. Although Figs. 3 and 4 suggest a contrasting trend in strain rate sensitivity of uniaxial compressive response in between UA and UA-PA materials, it should be taken into account that the presented results correspond to two different stages of compressive deformation, elastic (Fig. 3) and inelastic (Fig. 4). Therefore, in the elastic deformation stage, it appears that platelets caused in a reduction of strain rate sensitivity of ice-templated Al_2O_3 materials, whereas UA-PA exhibited an increase of rate sensitivity over UA during inelastic deformation.

6.4 Conclusions

Results of the current study revealed a remarkable influence of anisometric Al_2O_3 platelet particles on the quasistatic and dynamic compressive mechanical properties as well as shows that platelets differently impacted strain rate sensitivity of compressive response depending on elastic deformation vs. inelastic deformation. It may, however, be nontrivial to pinpoint the exact origin of the platelets-induced effects on the observed dynamic compressive mechanical properties and strain rate sensitivity. A comparison of the dynamic response of UA-PA and UA materials as well as of dynamic and quasistatic response of UA-PA material is insufficient to deconvolute the effects of platelets and the associated underlying microstructural changes on the measured properties at different strain rates. Toward this end, our future work will concentrate on the through microstructure analysis of UA and UA-PA materials to understand how the inherent microstructural length scale features contribute to compressive mechanical properties both in the dynamic and quasistatic strain rate regimes.

6.5 Supplementary information

6.5.1 Ice-templating using a custom-made device

Freeze casting was conducted using a custom-made setup. In this setup, a Teflon tube is placed on the top of a thin (0.5 mm) steel plate, partially filled with Al_2O_3 slurry, and the whole assembly is inserted inside a liquid nitrogen (N_2) Dewar. The Teflon tube is kept radially insulated to ensure that the suspension is frozen only under the influence of unidirectional (vertical) thermal gradient. By adjusting the distance between the steel plate and liquid N_2, freezing front velocity (FFV) was controlled. In this study, all the scaffolds were processed at a fixed gap (1 mm) between the liquid

N_2 and steel plate. Average FFV was estimated by dividing the frozen sample height with the total time required for the freezing of the sample.

6.5.2 SHPB testing

Upon impact by the striker bar, a compressive stress pulse is produced in the incident bar, travels through the bar and loads the sample in compression. A part of the pulse is transmitted through the specimen to the transmission bar while the rest is reflected back to the incident bar. These stress pulses were utilized to determine the stress-strain response of the glass foams. A copper (Cu) pulse shaper was placed at the striker bar-incident bar interface to substantially increase the rise time of the loading pulse and to filter out the high-frequency components from the elastic stress waveform. Stress pulses were measured through the strain gages (mounted in the middle of the incident and transmission bars) using a signal conditioning amplifier (2310B, Vishay) and a high-speed digitizer (NI PCI-5105, National Instrument).

CHAPTER 7

EFFECTS OF TEMPERATURE AND PLATELETS ON LAMELLA WALL MICROSTRUCTURE, STRUCTURAL STABILITY, AND COMPRESSIVE STRENGTH IN ICE-TEMPLATED CERAMICS

Note: The contents of this chapter have been published in Materialia

M. Banda and D. Ghosh, Effects of temperature and platelets on lamella wall microstructure, structural stability, and compressive strength in ice-templated ceramics, Materialia, 9 (2020) 100537.

DOI: https://doi.org/10.1016/j.mtla.2019.100537

Abstract:

The current investigation provides insights into microstructure development as a function of sintering temperature within lamella walls of ice-templated ceramics, effects of ceramic platelets on wall microstructure, and the influence of those developments on the compressive mechanical response. The results revealed a profound influence of both on the several aspects of ice-templated ceramics, enabling an improved understanding of the structure-mechanical property relationships in these materials and limitations in the development of the ice-templated ceramic structure. In the materials without platelets, at low-temperature walls were highly porous, at intermediate temperature a pore-free lamella wall with fine-grained microstructure developed, and at high-temperature along with grain growth significant abnormal grain growth occurred as well. More dramatic was the combined effects of temperature and platelets. The effects of platelets were realized at two length scales. Some of the platelets developed lamellar bridges, whereas the platelets that became part of the lamella walls remarkably impacted wall microstructure. The

current results strongly suggest that there are significant structural and mechanical strength advantages in the incorporation of large anisometric particles in ice-templated ceramics. The addition of large platelets resulted in a marked increase of compressive strength. A significant structural advantage is that the materials containing platelets exhibited improved stability to structural deformation at higher temperatures compared to the materials without the platelets. Thus, this study shows the importance of deeply probing into the structure-mechanical property relationships of ice-templated ceramics as a function of temperature and composition, providing valuable guidance into the microstructure design of these materials.

Keywords: Ice-templating; platelets; sintering temperature; lamella wall microstructure; structural stability; compressive strength.

7.1 Introduction

Ice-templated directionally porous ceramics can be employed in a number of engineering endeavors, such as bone-tissue engineering, filtration, lithium-ion battery electrode, solid-oxide fuel cell, and energy-absorbing structure [7,10,83,105]. The current literature is significantly invested in understanding the effects of process and material variables on the templated structure but to a lesser extent on mechanical properties. Prior studies have revealed that changes in process variables such as freezing front velocity (growth velocity of ice crystals) [8,68,103], solvent [51,55,189], and additive [190-192] allow modifying the templated structure from lamellar with negligible lamellar bridges to dendritic with a significantly increased bridging between the adjacent lamella walls [9,68,83,103,105,123,124,193,194]. Lamellar bridges are the dendritic arms that connect the adjacent lamella walls and result from the particles that get entrapped within the ice crystals during the templating step [9]. The majority of the studies characterized the mechanical

response of ice-templated ceramics under uniaxial compressive loading condition and the increase in lamellar bridge density (defined as the number of bridges present in between the adjacent lamellae walls per unit area [103]) is shown to be accompanied by an increase of strength [9,83,108,124,136,195].

Particle size plays a critical role in tailoring the templated structure and lamellar bridge density [9]. While ice-templated ceramics are typically fabricated from fine, equiaxed particles (~1 μm), we revealed that significant gain in compressive strength can be achieved by incorporating a small volume fraction of large platelets (i.e., anisometric particles) in templated structure [108,124,136,195]. We synthesized ice-templated porous alumina (Al_2O_3) materials from aqueous suspensions containing mainly fine, equiaxed Al_2O_3 particles and a small volume fraction of large Al_2O_3 platelets. After ice-templating and freeze-drying, porous materials were sintered at 1550 °C. Microstructure analysis revealed the formation of lamellar bridges through platelet particles as well as their presence in the lamella walls, which provided a significant reinforcement to the materials to deformation under uniaxial compressive loading.

In the prior studies on the Al_2O_3 platelets-based ice-templated ceramics, we specifically investigated platelets-induced strengthening [108], influence of the ratio of platelets to fine ceramic particles on microstructure and compressive response [124], effects of platelets on the brittle fracture characteristics of lamella walls [136], and compressive response under high-strain rate (dynamic) loading condition [195]. None of these studies, however, addressed the temperature dependence of microstructure development and structure-mechanical property relationships in ice-templated ceramics. Understanding the mechanical behavior of these materials can be significantly improved by probing into the developments of lamella wall microstructure and changes in macroscopic compressive response as a function of sintering temperature and directly comparing

for the material compositions with and without platelets. The knowledge of temperature dependence of microstructure development is currently lacking since there is no study that systematically addressed the evolution of microstructure in ice-templated ceramics with sintering temperature and composition. Another important aspect of this work is investigating the self-stability of ice-templated porous ceramic structures at elevated temperatures (>1550 °C) and the effects of platelets on structural stability.

The aims of this study are thus three-fold: (i) investigation of temperature dependence of microstructure development in ice-templated porous Al_2O_3 materials synthesized from equiaxed, ultrafine particles, (ii) investigation of temperature dependence of microstructure evolution in ice-templated porous Al_2O_3 materials synthesized from mixture of ultrafine, equiaxed particles and large platelets, and (iii) investigation of mechanical response of the resultant materials under uniaxial compressive loading condition. All the materials were synthesized from aqueous suspensions containing 15 vol.% Al_2O_3 particles and developed from two different compositions. One composition contained only ultrafine, equiaxed Al_2O_3 particles. Whereas, for the composition containing large Al_2O_3 platelets, of the 15 vol.% total ceramic content in aqueous suspensions, the mass ratio of ultrafine, equiaxed Al_2O_3 particles and platelets was maintained at 9:1. All the materials were ice-templated at comparable freezing front velocity (FFV). Materials were sintered in the temperature range of 1200–1700 °C, microstructure analysis was conducted using a scanning electron microscope (SEM), and the compressive mechanical response was characterized under uniaxial loading condition.

7.2 Experimental

7.2.1 Materials and preparation of aqueous alumina ceramic suspensions

Ultrafine, equiaxed Al_2O_3 powder (d_{50} = 300 nm, APA-0.5, Sasol, Tuscan, Arizona, referred to here as UA) and large Al_2O_3 platelets (diameter ~8 μm and thickness ~400 nm, Alusion™, Antaria Ltd., Bentley, Australia, referred to here as PA) were used to process ice-templated porous ceramics. Figures 1a and 1b show SEM images of the as-received UA and PA powders, respectively. The following procedure was utilized to prepare aqueous ceramic suspensions. First, the required amount of deionized water and ammonium polymethacrylate anionic dispersant (Darvan C, R.T. Vanderbilt Co., Norwalk, CT, 1 wt.% of Al_2O_3 powder) were taken into a Nalgene bottle; then, a measured amount of Al_2O_3 powder was added to the bottle. Next, zirconia (ZrO_2) spheres were added to the aqueous suspension and milled for 24 hrs. An organic binder solution of poly(2-ethyl-2-oxazoline) was next added to the suspension (5 wt.% of powder) and the suspension was further mixed for an hour. Next, the ZrO_2 spheres were separated from the suspension and the suspension was de-aired for 30 minutes.

7.2.2 Ice-templating of porous alumina ceramic materials

A custom-made ice-templating device was employed to solidify aqueous suspensions of Al_2O_3 under the influence of unidirectional temperature gradient [9]. In this device, a thin steel plate (referred to as “Cold-finger”) containing a hollow Teflon tube filled with aqueous ceramic suspension is placed inside liquid nitrogen (L-N_2) Dewar to conduct unidirectional solidification of the suspension. As the temperature of the Cold-finger reaches below 0 °C, ice nucleation and growth start at the bottom of the suspension in contact with the Cold-finger and the ice crystals propagate upward under the influence of unidirectional temperature gradient. During each

experiment, the top of the mold was kept open and exposed to room temperature. In this study, all the materials were processed at a fixed gap (1 mm) in between the Cold-finger and L-N_2, which resulted in a comparable FFV across all the samples. For each experiment, an average FFV was determined by dividing the height of a frozen sample with the time required for the completion of the solidification of the suspension. Frozen samples were freeze-dried at low pressure (0.014 mbar) and temperature (-50 °C) for 96 hours inside a freeze dryer (2.5L, Labconco, Kansas City, MI).

7.2.3 Study of microstructure evolution in ice-templated ceramics with sintering temperature

Aqueous ceramic suspensions of two different compositions were prepared: suspensions containing 15 vol.% UA particles and suspensions containing 15 vol.% UA and PA particles in the mass ration of 9:1; ice-templated materials developed from the former and latter compositions are referred to here as UA-15 and UA-10PA-15 materials, respectively. The ice-templated and freeze-dried materials were sintered in the temperature range of 1200–1700 °C in air atmosphere using a tube furnace (GSL-1800X, MTI Corporation, Richmond, CA), and the following sintering cycle was employed. Materials were heated from (i) room temperature to 450 °C at a rate of 3 °C/min and held for 4 hours for binder burnout, (ii) 450 °C to the selected sintering temperature at a rate of 5 °C/min and held at that temperature for 4 hours, and (iii) cooled from the sintering temperature to room temperature at a rate of 5 °C/min. To study the sintering behavior of UA powder, we prepared Al_2O_3 pellets by compacting the powder using a benchtop hydraulic press (Carver 3851) and the green pellets were sintered in the temperature range of 1200–1700 °C in air atmosphere using the same sintering cycle used for ice-templated materials.

7.2.4 Characterization of porosity, microstructure, and uniaxial compressive mechanical response

All the materials were of cylinder form, and the sintered samples were approximately 10 mm in diameter and 18 mm in height. From each sintered cylinder sample, two thin disks (each 10 mm in diameter and 3 mm in thickness) were extracted which were utilized for the characterization of porosity, microstructure, and mechanical response under uniaxial compression. Density (ρ^*) of the sintered materials was estimated from the measurements of mass and dimensions. Relative density (ρ_r) was estimated as $\rho_r = \rho^*/\rho_s$, where ρ_s is the bulk density of α-Al_2O_3 (taken here as 3.96 g/cm^3 for both UA and PA). Total porosity was estimated as $p_t = (1 - \rho_r) \times 100$. The relative density of the cylinder samples was also computed prior to sintering which is referred to here as relative green density (ρ_g). The microstructure of the sintered materials was characterized using a desktop Phenom SEM. A Fiji ImageJ software was used for the estimation of pore major axis (a), pore minor axis (b), lamella wall thickness (t_l), and grain size. For the estimation of a and b, a "Trainable Weka Segmentation" command was used which allows the user to train the software to distinguish between the lamella wall and pore. Next, a "Fit ellipse" command was used to fit ellipses in the pores and obtained the values for a and b. A similar procedure was also followed for the SEM images of the lamella walls to distinguish between grain boundaries and grains for obtaining grain area measurements. Grain size values were obtained by equating each grain area value to the area of a circle. Similarly, for the measurements of t_l, the lamella wall regions in the processed SEM image were divided into several small segments by using a "Watershed" command. After that, ellipses were fit into those regions and the average of the minor axes values were utilized as t_l. Uniaxial compressive response of ice-templated sintered materials was characterized under a quasistatic (low-strain rate, ~10^{-3} s^{-1}) loading condition using a mechanical

testing machine (Tinius Olsen 10ST) and the compressive load was applied parallel to the ice-growth direction. Compression test specimens were 10 mm in diameter and 3 mm in thickness, and for each condition (composition/temperature) 2 specimens were tested.

7.3 Results and discussion

7.3.1 Effects of sintering temperature and alumina platelets on relative density

Figure 1c shows the variations of relative density (ρ_r) and porosity (p_t) of the ice-templated materials with sintering temperature between 1200–1700 °C. Relative green densities (ρ_g) of the materials (indicated by the horizontal dotted green lines) are also included. The values of ρ_g, ρ_r, and p_t are provided in Table 1. In the presence of platelets, particle packing is deteriorated as ρ_g decreased from 0.149 in UA-15 materials to 0.143 in UA-10PA-15 materials, a reduction by about 4%. During the templating process, ultrafine, equiaxed particles would pack more efficiently between the growing ice-crystals than the mixture of ultrafine, equiaxed particles and large anisometric particles, which in turn would result in a reduction of ρ_g in the latter materials. This is consistent with that the presence of anisometric particles which are considerably larger in one dimension with respect to the other dimensions perturbs the packing efficiency in a green ceramic matrix consisted of fine, equiaxed particles [84,124].

Table 1: Variation of relative density (ρ_r) and total porosity (p_t) with sintering temperature.

Composition	**Temperature (°C)**	$\boldsymbol{\rho_r}$	**Total porosity ($\boldsymbol{p_t}$) (vol.%)**
UA-15 (ρ_g = 0.149 ± 0.003)	1200	0.149 ± 0.01	85.1 ± 1.04
	1300	0.169 ± 0.019	83.1 ± 1.94
	1400	0.218 ± 0.013	78.2 ± 1.29
	1450	0.223 ± 0.011	77.7 ± 1.085
	1500	0.235 ± 0.015	76.5 ± 1.505
	1550	0.23 ± 0.003	77 ± 0.956
	1600	0.253 ± 0.008	74.7 ± 0.79
	1650	0.264 ± 0.012	73.6 ± 1.22
	1700	0.309 ± 0	69.1 ± 0
UA-10PA-15 (ρ_g = 0.143 ± 0.002)	1200	0.143 ± 0.0006	85.7 ± 0.055
	1300	0.154 ± 0.0045	84.6 ± 0.445
	1400	0.184 ± 0.0047	81.6 ± 0.465
	1450	0.193 ± 0.005	80.7 ± 0.5
	1500	0.195 ± 0.0016	80.5 ± 0.16
	1550	0.198 ± 0.0068	80.2± 0.685
	1600	0.215 ± 0.0029	78.5 ± 0.29
	1650	0.23 ± 0.0077	77.0 ± 0.775
	1700	0.257 ± 0.0196	74.3 ± 1.995

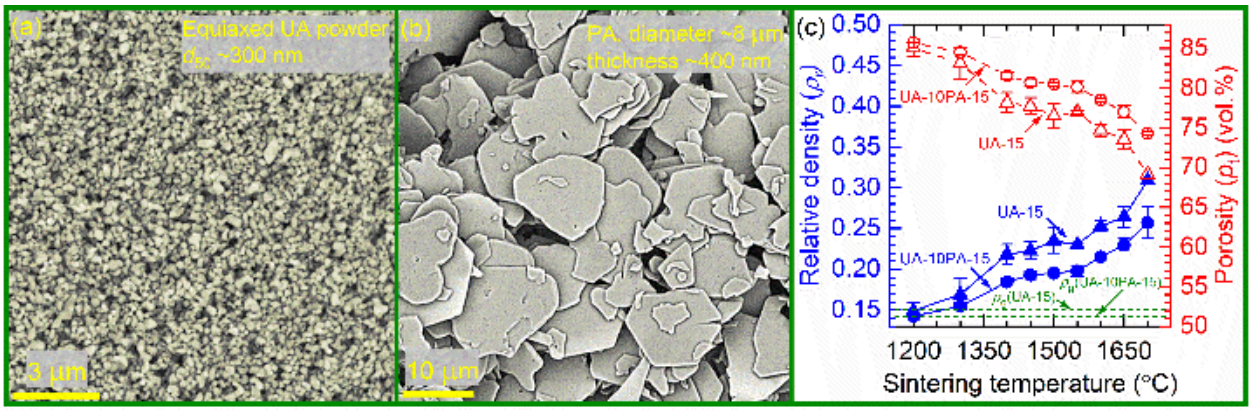

Figure 1: SEM images of as-received alumina (Al_2O_3) powders revealing (a) equiaxed morphology in ultrafine Al_2O_3 particles (referred to as UA powder) and (b) platelet morphology in large Al_2O_3 particles (referred to as PA powder). A comparison of the variations of (c) relative density (ρ_r) and porosity (p_t) of the UA-15 and UA-10PA-15 materials with sintering temperature in the range of 1200–1700 °C. In Fig. 1c, two horizontal dotted green lines represent ρ_g (prior to sintering) of the UA-15 and UA-10PA-15 materials.

ρ_r for each composition at 1200 °C is observed to be comparable to that of the ρ_g of the respective composition (Fig. 1c), suggesting negligible sintering at this temperature. Materials from both the compositions exhibited an increase of ρ_r with temperature; however, ρ_r of the UA-15 materials remained consistently greater in comparison to that of the UA-10PA-15 materials. In between 1200–1400 °C, materials from both the compositions exhibited a steep rise in ρ_r, whereas the change is observed to be moderate between 1400–1550 °C. ρ_r increased again considerably between 1550–1700 °C. The observed similarities in the trends of change in ρ_r with temperature in between the two compositions suggest that sintering kinetics was dominated by the densification behavior of UA particles. Figure 1c revealed that between 1200–1700 °C there is a significant decrease of porosity in the templated materials for both the compositions. At 1200 °C, the porosity

of the UA-15 and UA-10PA-15 materials are and 85.7 vol.%, respectively. Whereas, at 1700 °C, the UA-15 and UA-10PA-15 materials exhibited porosity of 69.1 and 74.3 vol.%, respectively.

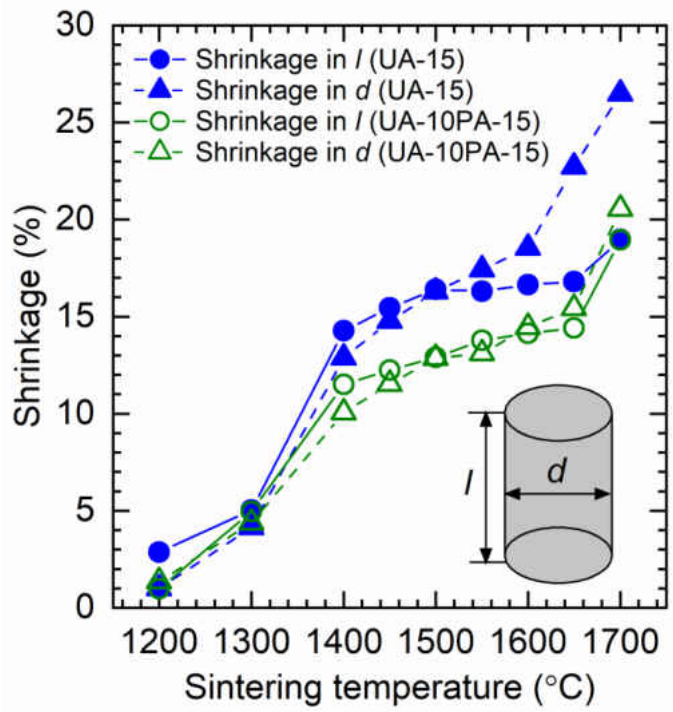

Figure 2: Variations of linear shrinkage of diameter (*d*) and length (*l*) of the UA-15 and UA-10PA-15 samples of cylinder geometry with sintering temperature in the range of 1200–1700 °C.

To further probe into the sintering behavior of the templated materials, in Fig. 2, we show the variation of % change of diameter (*d*), i.e., radial shrinkage, and length (*l*), i.e., axial shrinkage, in the UA-15 and UA-10PA-15 samples, with respect to the dimensions of the green specimens (i.e, prior sintering), as a function of temperature. The UA-15 materials exhibited dissimilar trends between the radial shrinkage and axial shrinkage of the sintered cylindrical specimens. The sintered specimens exhibited a steep but comparable increase of radial and axial shrinkage up to temperature 1400 °C. In between 1400–1650 °C, the axial shrinkage exhibited a plateau but

increased to an extent as the temperature increased to 1700 °C. Whereas radial shrinkage continued to increase but at a reduced rate up to 1600 °C and exhibited a drastic increase as the temperature increased above 1600 °C. The UA-10PA-15 materials also exhibited a steep and comparable increase of both radial and axial shrinkage up to 1400 °C. The % shrinkage for both the dimensions exhibited a plateau between 1400–1650 °C. Above 1650 °C, radial and axial shrinkage increased sharply. However, unlike in the UA-15 materials, both radial and axial shrinkage in the UA-10PA-15 materials were almost similar at each temperature. While the materials from both the compositions exhibited comparable axial shrinkage at 1700 °C, the radial shrinkage for the UA-15 material is observed to be significantly greater compared to that of the UA-10PA-15 material. Therefore, while Fig. 1c suggests that the presence of platelets increased porosity in the templated materials, Fig. 2 revealed that materials with platelets exhibited relatively uniform shrinkage in parallel and perpendicular to the growth direction of ice crystals.

To understand the densification behavior of the UA powder relative to the ice-templated materials, we also sintered compacted UA powder at different temperatures. Figure 3 shows the variation of relative density (ρ_{rp}) of Al_2O_3 pellets as a function of sintering temperature between 1200–1700 °C. The relative green density (ρ_{gp}) of the pressed pellets was about 0.6. At 1200 °C, density change was only marginal but ρ_{rp} increased steadily with the increasing temperature. ρ_{rp} started to plateau above 1400 °C, the sintered material reached about 97% of bulk density of Al_2O_3 (3.96 g/cm^3) at 1550 °C, and a further increase of temperature did not cause any considerable change in the density. Therefore, the UA powder reached close to its bulk density at about 1550 °C. Whereas the density of the templated materials continued to increase beyond this temperature, which strongly suggests the role of the templated structure in the variation of density with the temperature above 1550 °C. We find the observations interesting and will address further in the latter sections.

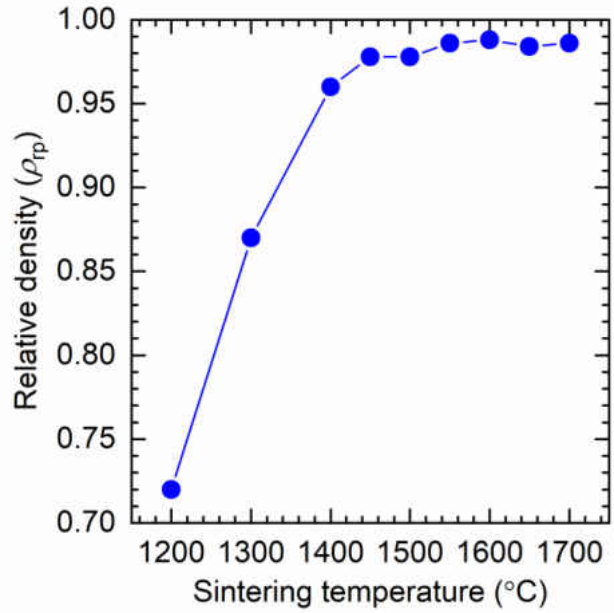

Figure 3: Variation of relative density (ρ_{rp}) of Al_2O_3 disks, prepared from the UA powder using a benchtop hydraulic press, as a function of sintering temperature in the range of 1200–1700 °C.

7.3.2 Effects of sintering temperature and alumina platelets on lamella wall microstructure

SEM images in Fig. 4 and Fig. 6 reveal the temperature dependence of microstructure development in the UA-15 and UA-10PA-15 materials, respectively. Each SEM image in column 1 and column 3 shows the cross-section region (perpendicular to the growth direction of ice crystals) of lamella walls. Whereas, each SEM image in column 2 and column 4 reveals the region within a lamella wall that is parallel to the growth direction of ice crystals; these SEM images were collected from the fragments of the lamella walls. Figures 5 and 7 show additional SEM images for the temperature range of 1550–1700 °C where significant grain growth occurred. A comparison of Figs. 4 and 6 suggests that the morphology of the UA-15 materials is lamellar, whereas the UA-10PA-15 materials exhibited dendritic morphology due to the formation of lamellar bridges mainly through the platelets.

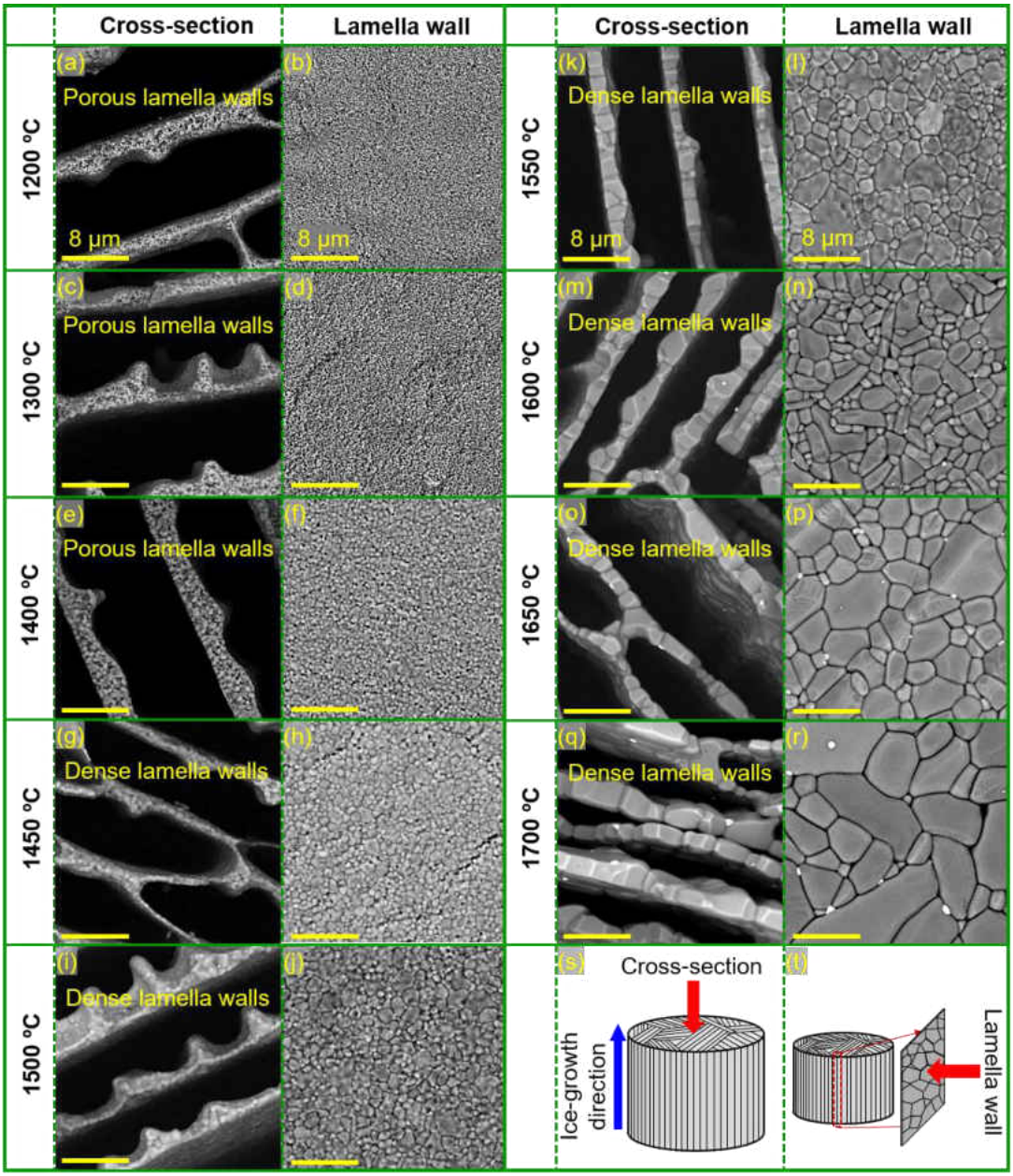

Figure 4: (a)–(r) SEM images of cross-section regions (perpendicular to ice-growth direction) and lamella walls (parallel to ice-growth direction) of the UA-15 materials, revealing development of microstructure with increasing sintering temperature in the range of 1200–1700 °C. (s) and (t) Showing schematic representations of the locations in the sintered samples from where SEM images were captured.

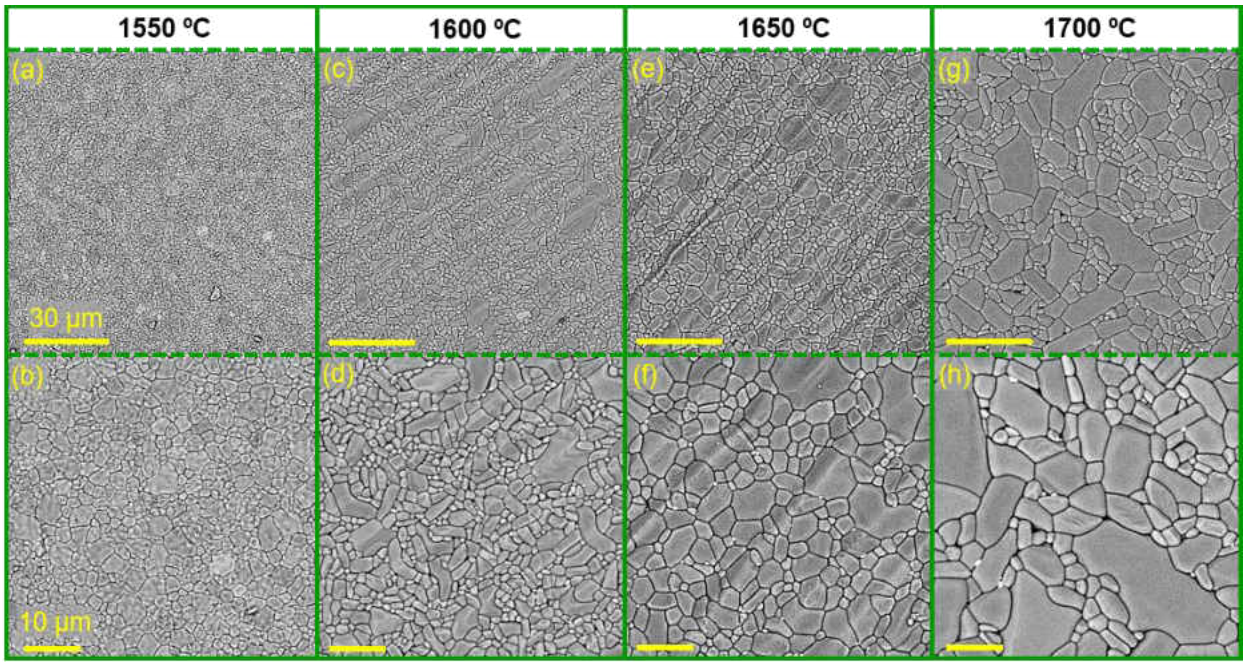

Figure 5: Relatively low- and high-magnification SEM images of polycrystalline lamella walls (parallel to ice-growth direction) of sintered UA-15 materials revealing microstructure evolution within the walls with increasing sintering temperature in the range of 1550–1700 °C. Images in each column belong to the same sintering temperature but captured at two different magnifications.

In the UA-15 materials, at the early stages of sintering (1200–1400 °C), the lamella walls were highly porous and the size of the ceramic grains observed to be similar to the particle size in the as-received UA powder. With the increase of temperature, as the density of the materials increased porosity within the lamella walls also reduced and grain growth resulted. By 1550 °C (Figs. 4k and 4l), the lamella walls became almost pore-free and a fine, equiaxed microstructure evolved, which is also prominent from Figs. 5a and 5b. With the further temperature increase, mainly two changes occurred in the lamella walls. Grain size continued to increase with the increasing temperature and grain morphology changed. At 1550 °C the lamella walls consisted of fine, equiaxed grains (grain dimensions almost same on the plane of the lamella walls). Whereas, above

1550 °C, due to abnormal grain growth elongated grains developed within the walls (elongated on the plane of the walls) and the volume fraction of these grains increased with temperature, Figs. 5c–5h. The microstructural analysis thus revealed profound abnormal grain growth which typically occurs in Al_2O_3 at elevated temperatures [196-199]. Abnormal grain growth in Al_2O_3 is the result of a much faster growth rate of some of the large grains relative to the surrounding fine-grained matrix. At 1700 °C, highly anisotropic grains about 30-50 μm long (with a plate-like morphology) can be observed within the lamella walls of the UA-15 materials. At the early stages of sintering, lamella walls contained several layers of the UA particles, whereas between 1550–1700 °C the walls consisted of a single layer of grains only.

Lamella walls in the UA-10PA-15 materials were also highly porous at the early stages of sintering and large platelet particles within the walls can be easily identified. Figure 6a shows the formation of lamellar bridges through platelets. The formation of lamellar bridges through the large platelet particles was governed by the greater propensity of platelets for entrapment by ice crystals compared to the UA particles. Critical freezing front velocity (v_c) above which particles get entrapped within the solvent crystals can be expressed as [74,103]

$$v_c = \frac{\Delta\sigma d}{3\eta R}\left(\frac{a_0}{d}\right)^z \quad (1)$$

where $\Delta\sigma$ is the mean free energy of the particle, a_0 is the average intermolecular distance in the liquid film between the particle and the solid front, d is the overall thickness of this film, η is the slurry viscosity, R is the particle radius, and z is an exponent that can vary from 1 to 5. Equation (1) suggests that as v_c decreases with the increase of R, an increase in particle size will promote particle entrapment within solvent crystals and lead to the formation of lamellar bridges [9]. Therefore, due to the large size, platelet particles are more prone to be entrapped by the growing

ice crystals compared to the UA particles and as a result a significant amount of lamellar bridges developed in the UA-10PA-15 materials through the platelets. Large particles in suspension can settle during ice-templating and affect lamellar bridge formation. However, in the previous studies we have shown that lamellar bridges are present throughout the structure and bridge formation by platelets can be controlled by the variation of processing variables [124], thus suggesting that bridge formation is not necessarily due to the settling of platelet particles.

Significant microstructural changes occurred as temperature increased to 1400 °C. Figure 6e indicates a substantial decrease of porosity within the lamella walls and Fig. 6f reveals enhanced sinterability between the UA and PA particles and thus an increased diffusion of the UA particles into the platelets. Additionally, Fig. 6f shows the formation of micropores on the surfaces of the platelets. The SEM images corresponding to 1400 °C revealed a substantial change in the shape of the PA particles as well. By 1450 °C, the interactions between the UA and PA particles enhanced significantly and grain growth occurred. At this temperature, micropores within the walls are observed to be mainly present in the regions containing the large grains.

Figure 6j (sintering temperature 1500 °C) revealed the development of a unique microstructure in the lamella wall in which an Al_2O_3 grain (presumably resulting from the lateral growth of a platelet particle) is observed to be embedded within a matrix of fine-grained Al_2O_3, where the fine-grained microstructure resulted from the densification and grain growth of the UA particles. By this temperature, microporosity within the lamella walls decreased significantly and micropores are observed to mainly reside within the large grains. The similar microstructural features are also observed at 1550 °C (Figs. 6k, 6l, 7a, 7b). One notable feature in Fig. 6k is the presence of large grains having thickness same as that of the lamella walls (≥ 2 μm) and few micropores within the regions containing the large grains. Figures 6m and 6n reveal the microstructure of the UA-10PA-

15 material corresponding to 1600 °C. By this temperature, each lamella wall became consisted of a single layer of grains. Figure 6n reveals that with the increasing temperature microstructure development and grain growth within the lamella walls continued. With the further increase of sintering temperature, the lamella walls continued to become pore-free and grain growth proceeded (Figs. 6o, 6p, 6q, 6r). This is also evident from the SEM images shown in Figs. 7e, 7f (1650 °C) and Figs. 7g, 7h (1700 °C). The microstructural analysis of the lamella walls corresponding to the temperature of 1700 °C did not indicate the presence of any micropores within the lamella walls. Figure 8 shows more of the high-magnification SEM images of the cross-section regions in the UA-10PA-15 materials, further comparing the microstructural features of the materials sintered at 1600 °C (Fig. 8a) and 1700 °C (Figs. 8b, 8c). Figure 8 shows that along the thickness direction the lamella walls are consisted of a single layer of grains, unlike the templated materials and at the early stages of sintering. There are regions within the lamella walls at both the temperatures revealing the presence of significantly large grains (diameter >10 μm), but the large grains are observed to be pore-free at 1700 °C. Figure 8c also reveals the presence of equiaxed small grains within the lamella walls.

From Figs. 4-7, it can be seen that lamella walls in the ice-templated materials from both the compositions were almost pore-free at 1550 °C, particularly in UA-15, and thus can be assumed that the walls to achieving close to the bulk density of Al_2O_3. Therefore, beyond this temperature, any significant change in density is not expected in the templated materials with a further increase in temperature. However, contrasting results were obtained from density measurements, further indicating a strong role of ice-templated structure in the densification behavior of the materials above 1550 °C. The possible origin of this discrepancy is discussed in Section 3.4 based on temperature-induced structural instability in the templated materials.

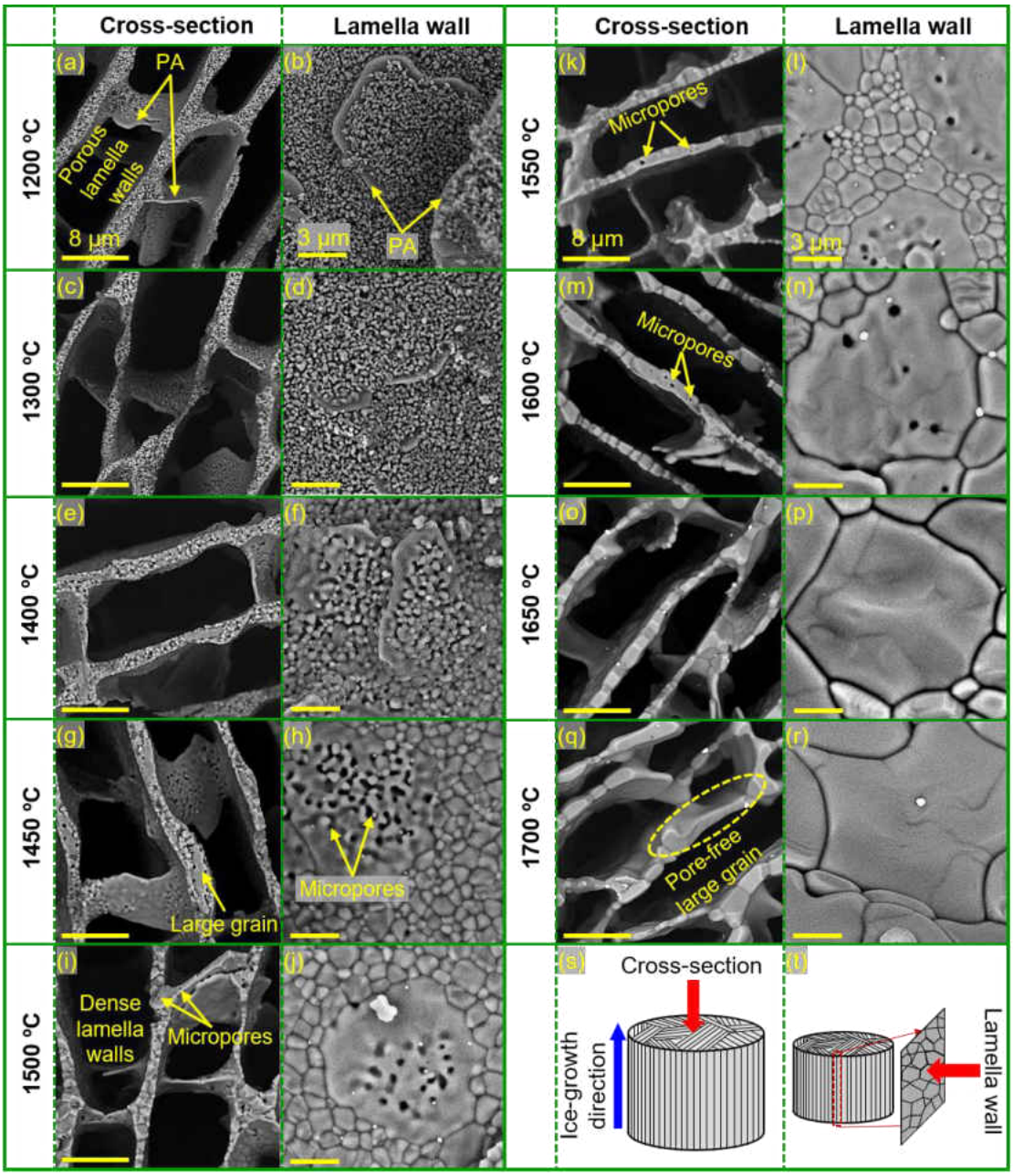

Figure 6: (a)–(r) SEM images of cross-section regions (perpendicular to ice-growth direction) and lamella walls (parallel to ice-growth direction) of the UA-10PA-15 materials, revealing development of microstructure with increasing sintering temperature in the range of 1200–1700 °C. (s) and (t) Showing schematic representations of the locations in the sintered samples from where SEM images were captured.

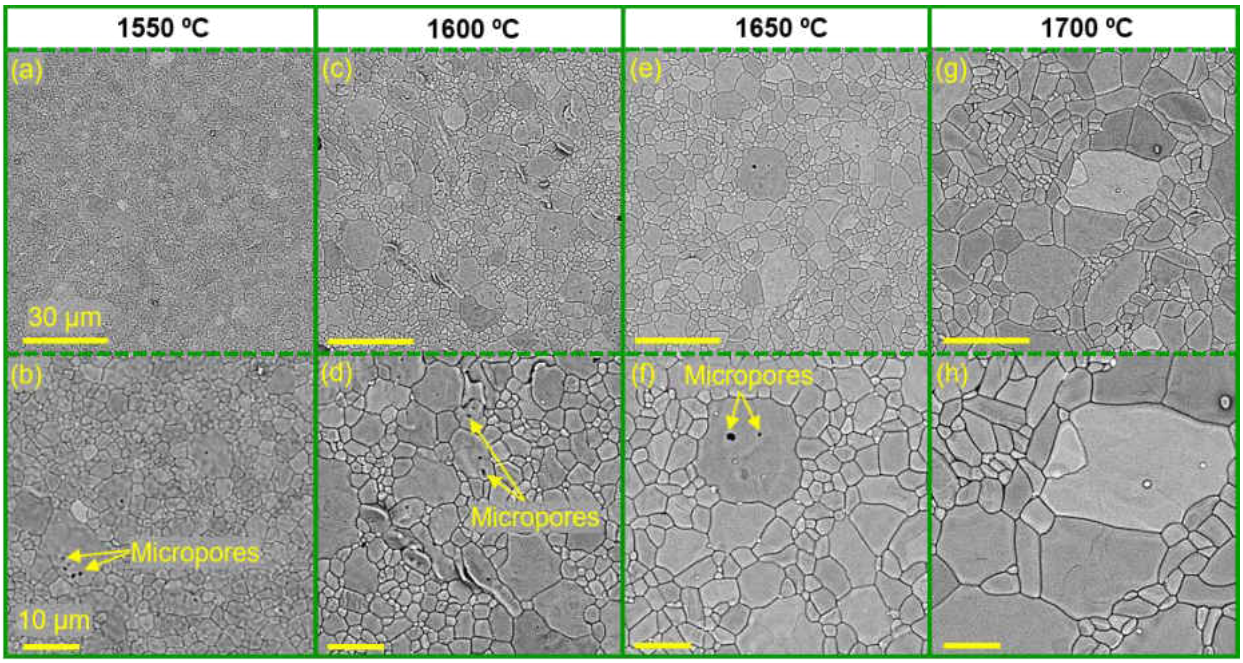

Figure 7: Relatively low- and high-magnification SEM images of lamella walls (parallel to ice-growth direction) in the sintered UA-10PA-15 materials revealing microstructure evolution within the walls with increasing sintering temperature, in the range of 1550–1700 °C. Images in each column belong to the same sintering temperature but captured at two different magnifications.

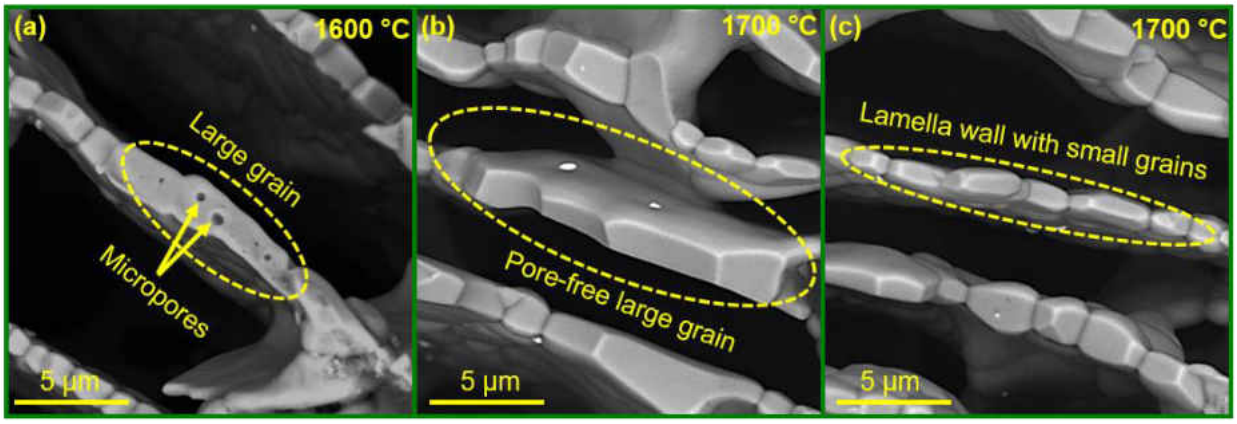

Figure 8: High-magnification SEM images of cross-section regions (perpendicular to ice-growth direction) of the UA-10PA-15 materials, revealing lamella wall microstructure at sintering temperature of 1600 °C and 1700 °C. SEM image in (a) shows a region in the lamella wall corresponding to 1600 °C containing a large grain with micropores present within the grain, (b) reveals a pore-free large grain at 1700 °C, and (c) shows relatively small grains in the wall.

The microstructural analysis suggests that large Al_2O_3 platelets strongly impacted the process of microstructure development in lamella walls as well as the microstructural characteristics of the walls. By 1700 °C, mainly two types of regions emerged in the lamella walls of UA-10PA-15 materials: the regions with a fine-grained, pore-free microstructure and the regions in which large Al_2O_3 grains (pore-free) are embedded within the fine-grained Al_2O_3 matrix. This is in sharp contrast to the polycrystalline microstructure that evolved in the lamella walls of the UA-15 materials. A comparison of Figs. 5 and 7 suggests some additional influence of the platelets on the wall microstructure, particularly on the grain morphology. In the UA-15 materials, at 1700 °C due to abnormal grain growth large, elongated grains developed within the lamella walls with a significant volume fraction present in the walls. Whereas, for the UA-10PA-15 materials, at 1700 °C lamella walls primarily contained small and large equiaxed grains, with a lesser development

of elongated grains compared to UA-15. The results suggest that the presence of platelets within the matrix of UA particles reduced the propensity for abnormal grain growth; however, the overall grain growth was significant. Since larger particles have lower specific surface energy than smaller particles, during sintering platelets grew at the expense of the adjacent smaller grains which developed from the UA particles. Abnormal grain growth in the matrix of fine ceramic particles is impaired by the presence of larger particles from the same or different phases [122]. In fact, the growth of platelets is similar to that observed for the growth of relatively large single crystal Al_2O_3 grain in a fine-grained Al_2O_3 matrix [122]. Due to the presence of large platelets in the matrix of UA particles, the probability of the smaller, equiaxed grains (resulting from the UA particles) undergoing abnormal growth might have been reduced. As a result, the extent of abnormal grain growth is observed to be reduced in UA-10PA-15 compared to that in UA-15. Instead, a significant fraction of the large grains in the lamella walls of UA-10PA-15 materials is observed to be equiaxed on the plane of the walls, which we suggest that they resulted from the radial growth of the platelets at the expense of surrounding small grains.

Table 2: Values of d_{10}, d_{50}, d_{90} (from grain size distribution), and average lamella wall thickness (t_l) for the UA-15 and UA-10PA-15 materials sintered at 1550, 1600, 1650, and 1700 ℃.

Composition	Temperature (°C)	d_{10} (μm)	d_{50} (μm)	d_{90} (μm)	t_l (μm)
UA-15	1550	0.97	1.63	3	2.56 ± 0.84
	1600	0.99	1.74	3.17	2.50 ± 0.75
	1650	1.24	2.45	4.85	2.40 ± 0.52
	1700	1.38	2.97	5.94	2.66 ± 0.78
UA-10PA-15	1550	1.07	1.84	3.36	1.81 ± 0.46
	1600	1.1	2.05	3.99	1.74 ± 0.42
	1650	1.29	2.65	5.29	1.67 ± 0.41
	1700	1.35	2.98	6.70	1.84 ± 0.52

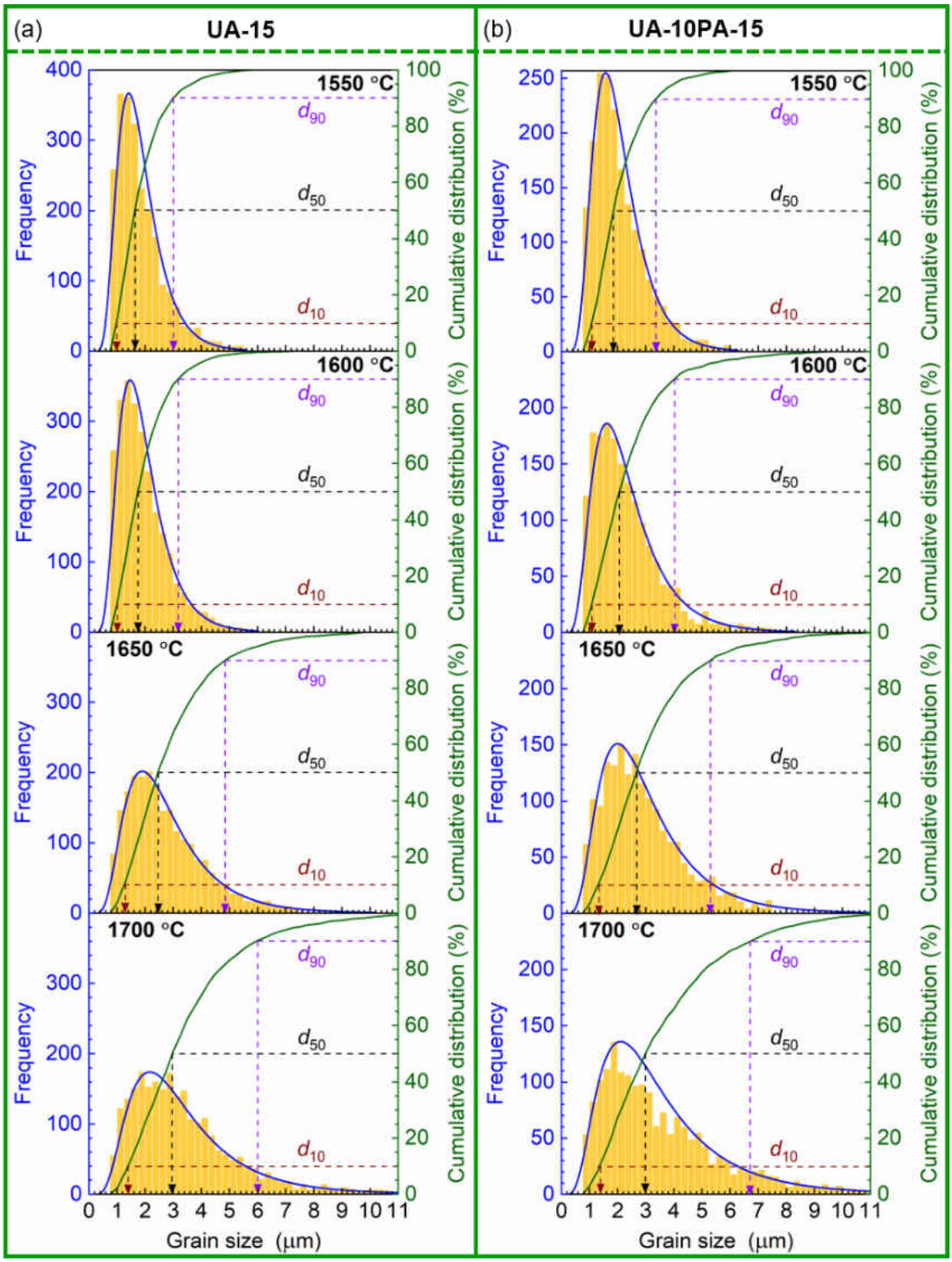

Figure 9: A comparison of grain size distribution in the (a) UA-15 and (b) UA-10PA-15 materials sintered at 1550, 1600, 1650, and 1700 ℃.

7.3.3 Effects of temperature and platelets on grain size and grain size distribution in lamella walls

Figure 9 shows grain size distribution in the lamella walls of the (a) UA-15 and (b) UA-10PA-15 materials, which were sintered between 1550–1700 °C. d_{10} represents that 10% of the grains are smaller than the value indicated by the vertical arrow. d_{50} represents that 50% of the grains are smaller than and 50% of the grains are larger than the value indicated by the vertical arrow. d_{90} represents that 90% of the grains are larger than the value indicated by the vertical arrow. These values and the values of the average lamella wall thickness (t_l) are provided in Table 2. In the UA-15 materials, above 1600 °C, grain size distribution changed considerably with the increasing sintering temperature. Grain size distribution became increasingly asymmetric and the distribution plots corresponding to 1650 °C and 1700 °C show that the fraction of relatively large grains increased. Although, the grain size in the plane of lamella walls is observed to increase with the increasing sintering temperature, the change in t_l with temperature was minimal. In the UA-10PA-15 materials also, grain size and grain size distribution changed considerably and grain size distribution became increasingly asymmetric with the increasing temperature. Figure 9 suggests that at each of sintering temperatures, grain size distribution in the lamella walls is relatively broader in the UA-10PA-15 materials compared to the UA-15 materials, which could be attributed to the development of larger grains from the radial growth of platelets in the former materials. Similar to the UA-15 materials, the change in lamella wall thickness was minimal in the UA-10PA-15 materials. For both the compositions, between 1550–1700 °C, the lamella walls are observed to have a single layer of grains and therefore the grain thickness can be expressed in term of t_l. The comparison of d_{10}, d_{50}, d_{90}, and t_l suggests that grain size increase occurred in the

plane of lamella walls, whereas the grain thickness which is along the direction of wall thickness remained comparable.

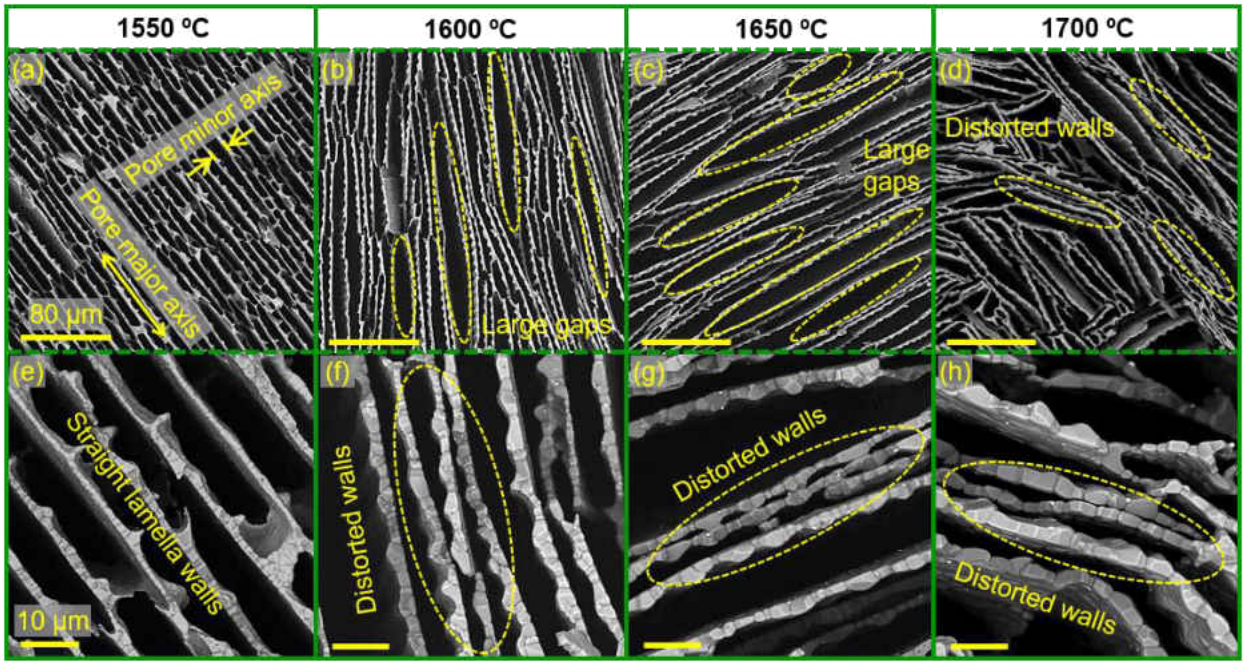

Figure 10: Relatively low- and high-magnification SEM images of the cross-section regions (perpendicular to the ice-growth direction) of the UA-15 materials revealing distortion (bending) of lamella walls with the increasing sintering temperature in the range of 1550–1700 °C. Images in each column belong to the same sintering temperature but captured at two different magnifications.

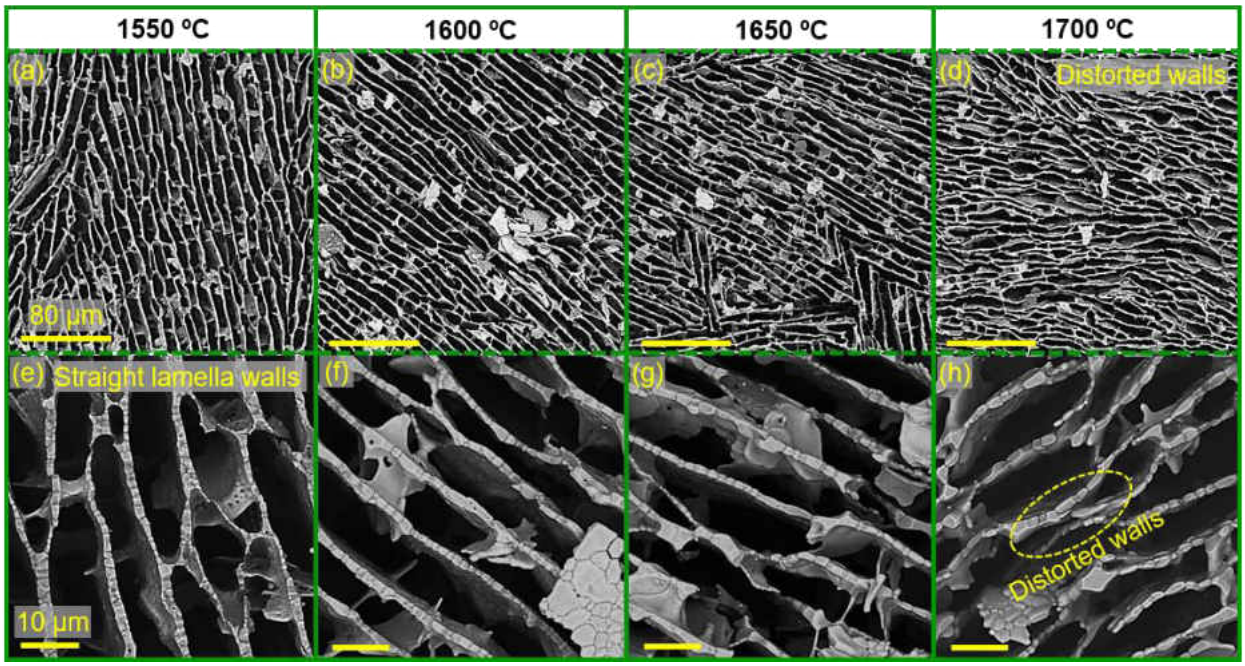

Figure 11: Relatively, low- and high-magnification SEM images of the cross-section regions (perpendicular to the ice-growth direction) in the UA-10PA-15 materials revealing distortion (bending) of lamella walls with the increasing sintering temperature in the range of 1550–1700 °C. Images in each column belong to the same sintering temperature but captured at two different magnifications.

7.3.4 Effects of temperature and platelets on structural instability

Figures 10 and 11 reveal the cross-section regions (perpendicular to the growth direction of ice crystals) of the UA-15 and UA-10PA-15 materials, respectively, sintered at and above 1550 °C. In the UA-15 materials, at 1550 °C, the adjacent lamella walls were straight and parallel. With the increase of temperature, due to the bending of walls the parallelism of the adjacent walls deteriorated and the deterioration became significant at 1700 °C (Fig. 10d, 10h), thus suggesting temperature-induced structural instability which is here referred to as the loss of the straightness and parallelism of the ceramic lamella walls due to the bending of the walls. Many regions can be

seen where significant bending of the lamella walls caused some of the adjacent lamella walls to have joined together and resulted in the formation of regions with large voids. Figure 12a shows a high-magnification SEM image corresponding to 1700 °C, which revealed sintering in between the adjacent lamella walls that underwent excessive bending. Such structural distortion at elevated temperatures will inevitably affect the characteristic pore directionality in ice-templated ceramics and increase pore tortuosity.

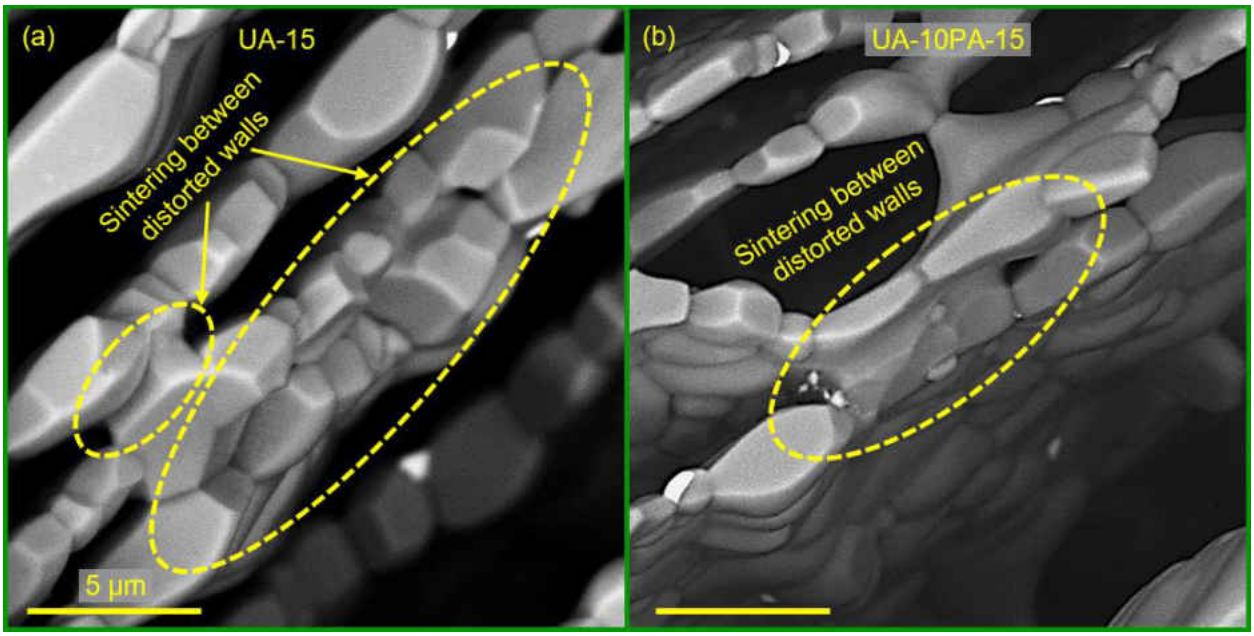

Figure 12: High-magnification SEM images of the cross-section region (perpendicular to ice-growth direction) in the (a) UA-15 material and (b) UA-10PA-15 material sintered at 1700 °C, revealing sintering between adjacent lamella walls.

The lamella walls in the UA-10PA-15 materials are, however, seen to remain relatively straight and parallel up to 1650 °C and structural distortion occurred mainly at 1700 °C. A direct comparison of Fig. 11d and Fig. 10d strongly suggests that the extent of structural distortion was

less in UA-10PA-15 compared to that in UA-15. Figure 12b shows a high-magnification SEM image for sintering temperature of 1700 °C, which revealed sintering in between the adjacent lamella walls that underwent excessive bending. Figure 13 compares microstructures of the UA-15 (a, b) and UA-10PA-15 (c, d) materials along the ice-growth direction which were sintered at 1550 °C and 1700 °C. For both compositions, distortion of the walls at higher sintering temperature is clearly visible. Thus, the bending of the lamella walls occurred both along parallel and perpendicular to the ice-growth direction. However, temperature-induced distortion of the lamella walls is observed to be significantly reduced in the UA-10PA-15 compared to that in the UA-15. The exact origin of structural distortion in ice-templated Al_2O_3 at elevated temperatures is not well understood. This will require an in-depth investigation addressing the effects of various other parameters such as sintering time, heating and cooling rate during sintering, staring powder particle size, and lamella wall thickness, which is beyond the scope of this study and will be addressed in a separate study. However, this investigation revealed two important insights: (i) thin ceramic lamella walls with a single layer of grains are observed to be highly susceptible to distortion (bending) at elevated temperatures and (ii) presence of lamellar bridges (through platelets) significantly enhanced the resistance of the walls to temperature-induced distortion. The UA-15 materials contain tall, slender lamella walls with negligible lamellar bridges. There is thus little mechanical self-support for the lamella walls in ice-templated porous structure of the UA-15 materials. As a result, at higher temperatures the lack of mechanical support to the walls allowed the walls to distort significantly. On the other hand, in the UA-10PA-15 materials, the presence of lamellar bridges which formed through the platelets in between the lamella walls provided greater structural rigidity and significantly limited the distortion of the walls.

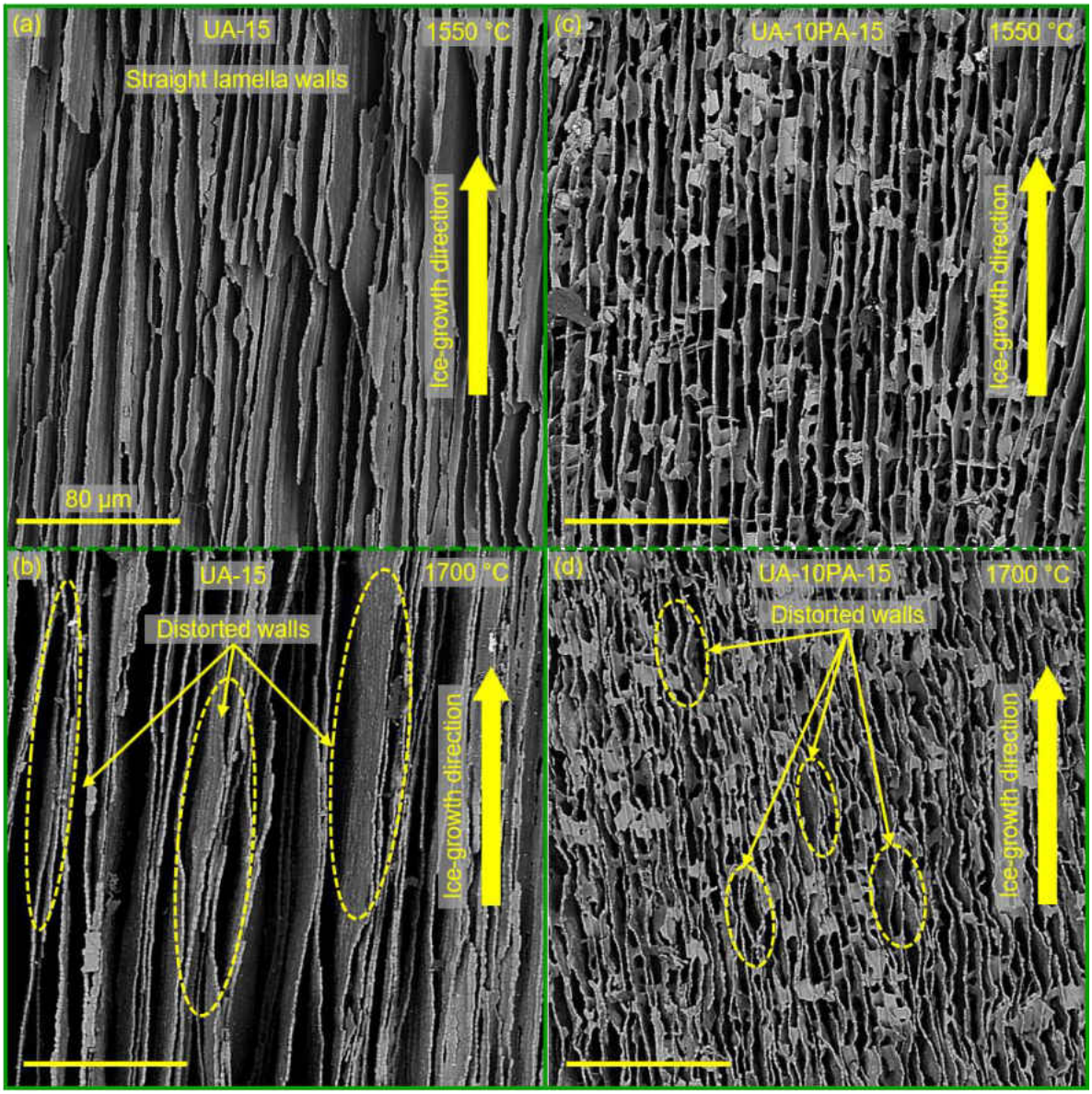

Figure 13: SEM images of vertical cross-sections (parallel to the growth direction of ice crystals) of (a) UA-15 and (b) UA-10PA-15 materials sintered at 1550 and 1700 °C.

We recall here the results shown in Figs. 1 and 3, which revealed a significant difference in the densification behavior between ice-templated porous Al_2O_3 materials and Al_2O_3 pellets. While the pellets did not exhibit any considerable increase in density above 1550 °C, ice-templated materials exhibited a significant increase in density above 1550 °C. Based on the microstructural

observations, we can state that the considerable enhancement of density in ice-templated Al_2O_3 materials above 1550 °C may not necessarily be due to the increased densification of Al_2O_3 but more of the dominant effect of the bending of the lamella walls and thereby the resulting shrinkage in the ice-templated samples.

Table 3: Values of d_{10}, d_{50}, d_{90} (estimated from distribution plots) for pore major axis (a), pore minor axis (b), and pore area (A_p), for the UA-15 and UA-10PA-15 materials sintered at 1550 and 1700 °C.

Composition		Temperature (°C)	$\boldsymbol{d_{10}}$	$\boldsymbol{d_{50}}$	$\boldsymbol{d_{90}}$
UA-15	Pore major axis (a), µm	1550	11.8	35.7	90.5
		1700	12.3	29.2	77.9
	Pore minor axis (b), µm	1550	4	6.9	9.6
		1700	2.6	4.8	11.4
	Pore area (A_p), µm^2	1550	33.7	194.2	645
		1700	19.2	105.1	528
UA-10PA-15	Pore major axis (a), µm	1550	4.9	22.8	66.1
		1700	6.3	26.3	86.8
	Pore minor axis (b), µm	1550	3.8	7.3	10.4
		1700	4	7.6	11.5
	Pore area (A_p), µm^2	1550	21.6	131.1	502.4
		1700	20.6	139.3	589.3

Also, recall from Fig. 2 that for the UA-15 materials above 1500 °C variations in the radial and axial shrinkages were dissimilar. The radial shrinkage was drastically higher compared to axial shrinkage. And, the origin of this difference could be due to the greater extent of the deformation

(bending) of the lamella walls (and resulting sintering between the adjacent walls) perpendicular to the ice-growth direction relative to parallel to the ice-growth direction. With the increasing temperature above 1500 °C the deformation of the walls increased which facilitated sintering between the adjacent walls and radial shrinkage increased markedly. Similarly, recall from Fig. 2 that the UA-10PA-15 materials sintered above 1650 °C exhibited a sharp increase of both radial and axial shrinkage, which we could attribute to the deformation of the lamella walls. However, in the UA-10PA-15 materials, radial and axial shrinkage were similar even at higher temperatures, suggesting that deformation (bending) of the lamella walls was similar both parallel and perpendicular to the ice-growth direction. Thus, the presence of platelets (and perhaps the corresponding lamellar bridges) not only increased the thermal stability of ice-templated structures at elevated temperatures but also prevented dissimilar shrinkage which occurred in the materials without platelets.

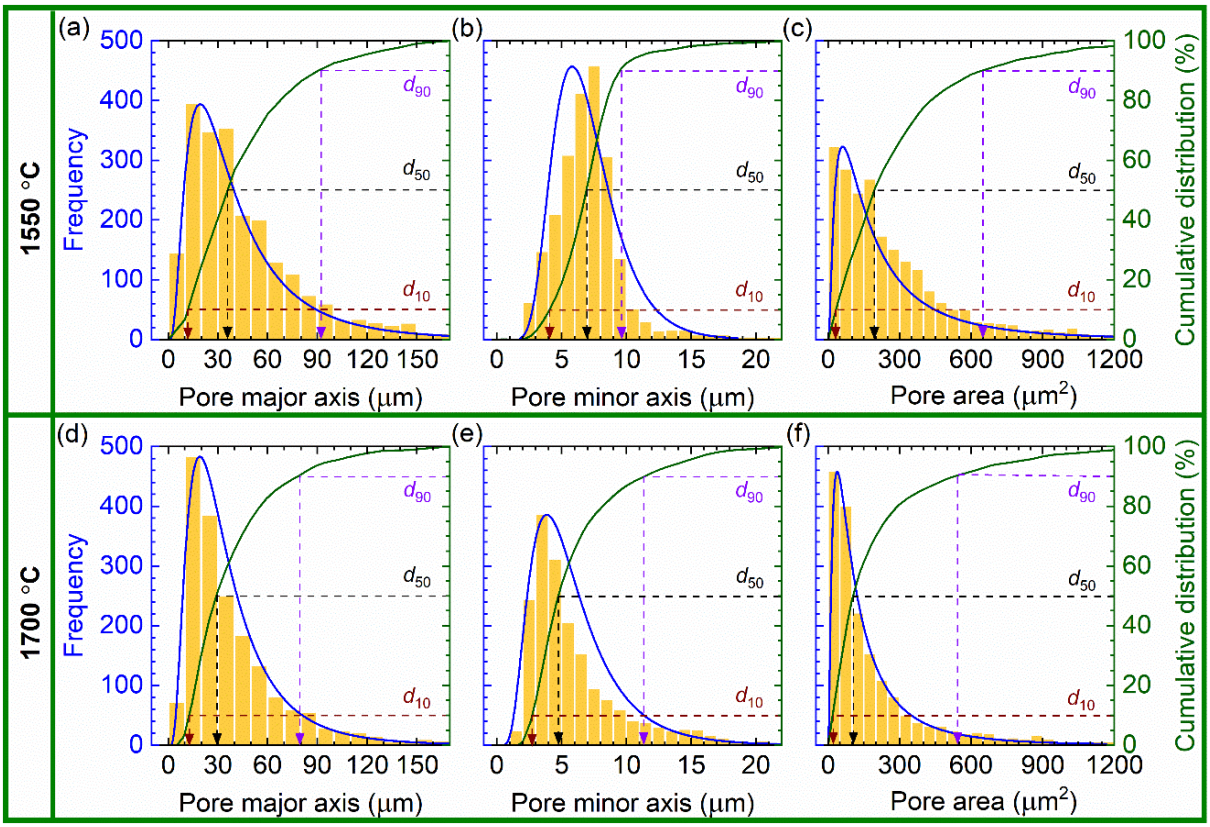

Figure 14: A comparison of the distribution of pore major axis (a), minor axis (b), and pore area ($A_\mathrm{p} = \frac{\pi}{4}ab$) in between the UA-15 materials sintered at 1550 °C (a–c) and 1700 °C (d–f).

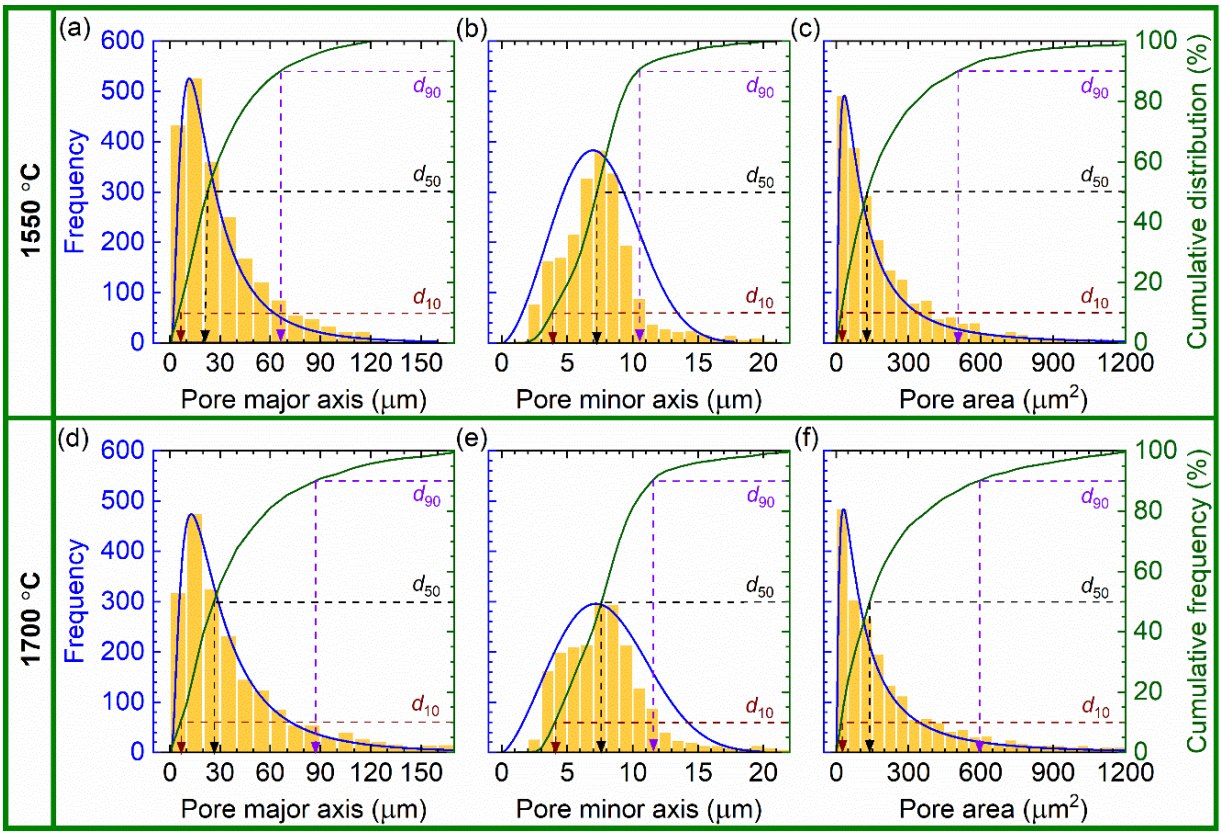

Figure 15: A comparison of the distribution of pore major axis (a), minor axis (b), and pore area ($A_\mathrm{p} = \frac{\pi}{4}ab$) in between the UA-10PA-15 materials sintered at 1550 °C (a–c) and 1700 °C (d–f).

Figure 14 shows the distribution of pore major axis (a), pore minor axis (b), and pore area ($A_\mathrm{p} = \frac{\pi}{4}ab$) in between the UA-15 materials sintered at 1550 °C (a-c) and 1700 °C (d-f). Similarly, in Fig. 15 shows the distribution of a, b, and A_p in between the UA-10PA-15 materials sintered at 1550 °C (a-c) and 1700 °C (d-f). In each figure, d_{10} represents that 10% of the pores are smaller than the value indicated by the vertical arrow, corresponding to pore major axis/pore minor axis/pore area. d_{50} represents that 50% of the pores are smaller than and 50% of the pores are larger than the value indicated by the vertical arrow, corresponding to pore major axis/pore minor axis/pore area. d_{90} represents that 90% of the pores are larger than the value indicated by the

vertical arrow, corresponding to pore major axis/pore minor axis/pore area. These values are provided in Table 3. In the UA-15 materials, for each of the parameters, with the increasing sintering temperature, the corresponding distribution shifted to an extent to the left-hand side which is attributed to increased radial shrinkage with temperature. For the *a*, the distribution became narrow with the increasing temperature and d_{50} decreased from 1550 °C to 1700 °C. For the *b*, the distribution became more asymmetric at the higher temperature and a significant change thus occurred in the cumulative distribution as well, which is attributed to the observed microstructural distortion with the increasing temperature. Similarly, a considerable change occurred in the A_{p} also. These measurements quantitatively reflect on the microstructural changes that occurred in the UA-15 materials between 1550–1700 °C as a result of the deformation of the lamella walls. Whereas, the changes of distributions in the UA-10PA-15 materials between 1550 °C and 1700 °C are observed to be less significant, further suggesting that structural thermal stability was enhanced in the latter materials.

7.3.5 Effects of temperature and platelets on the uniaxial compressive mechanical response

Figures 16a and 16b show uniaxial compressive stress-strain curves for different sintering temperatures for the UA-15 and UA-10PA-15 materials, respectively. The UA-15 materials sintered at 1200 °C were too weak to handle, and thus compression tests could not be performed. Figure 16c shows the variation of maximum compressive strength (referred to here as peak stress, σ_{p}) with temperature for both the compositions. The general features of the stress-strain curves are an elastic regime, which is followed by a plateau where stress decreased gradually with the increasing strain and a densification region where stress increased sharply with the increasing

strain. The apparent stress plateau regime is associated with the progressive failure of the materials by brittle crushing.

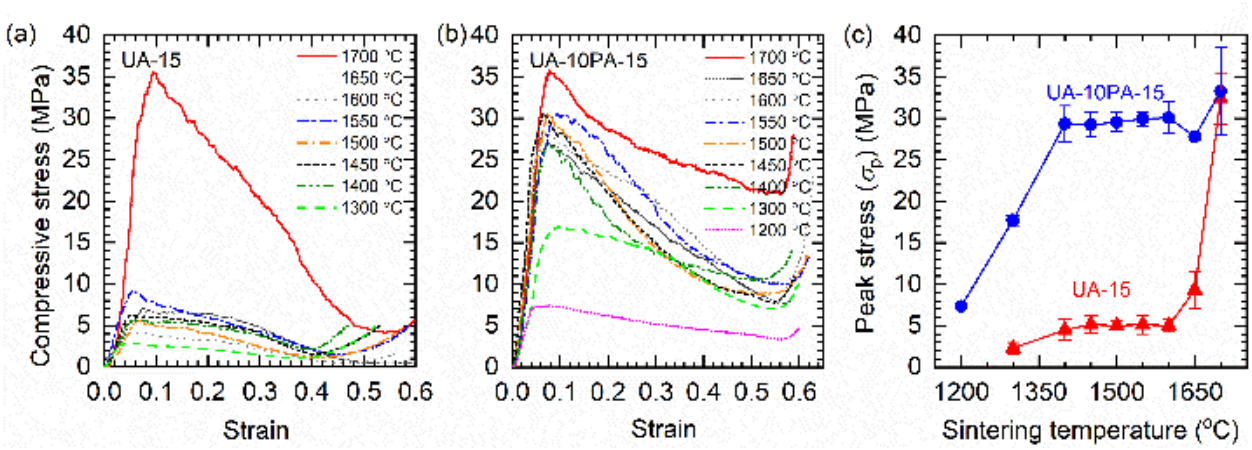

Figure 16: Variation of uniaxial compressive stress-strain curves with sintering temperature for (a) UA-15 and (b) UA-10PA-15 materials, and (c) variation of peak stress (σ_p) with temperature.

For the UA-15 materials, up to 1650 ºC, with the increasing sintering temperature both σ_p and compressive stress in the plateau regime exhibited a marginal increase only. In between 1300–1650 ºC, σ_p is observed to be below 10 MPa. However, as the temperature increased to 1700 ºC, UA-15 exhibited a drastic increase in σ_p but in the progressive failure stage stress decreased sharply with the increasing strain. The UA-10PA-15 materials exhibited significantly enhanced strength compared to the UA-15 materials. Both σ_p and fracture stress in the plateau regime increased considerably up to 1400 ºC, whereas beyond that compressive stress-strain curves are observed to be similar and only a marginal increase of the strength occurred at 1700 ºC. The UA-10PA-15 materials were also able to better sustain the applied load in the progressive failure regime compared to the UA-15 materials. In Fig. 17c, the general trend in the change of σ_p with

temperature for both the compositions can be seen more clearly. In between 1200–1650 °C, σ_p of the UA-10PA-15 materials remained significantly greater compared to that of the UA-15 materials, whereas at 1700 °C both the compositions exhibited comparable σ_p. Since the density of the materials increased with temperature, in Fig. 17 we compared the variation of specific σ_p (σ_p/ρ_r) with temperature. In between 1300–1600 °C specific σ_p values for the UA-15 materials remained comparable, but a substantial increase in specific σ_p occurred as the temperature increased to 1700 °C. On the other hand, for the UA-10PA-15 materials specific σ_p increased monotonically from 1200–1400 °C, but decreased gradually beyond 1400 °C. Over the entire sintering temperature range, specific σ_p for UA-10PA-15 remained greater compared to that of UA-15.

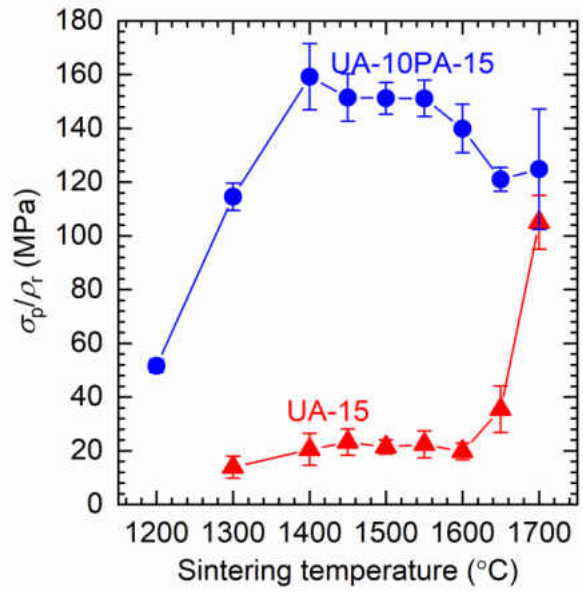

Figure 17: Variation of specific σ_p (σ_p/ρ_r) with the sintering temperature.

This investigation revealed several interesting aspects of the effects of temperature and Al_2O_3 platelets on the uniaxial compressive response of ice-templated ceramics. Compressive strength of

porous solids is strongly influenced by relative density (ρ_r) and increases with the increasing relative density (i.e., decreasing porosity) [110]. According to Gibson and Ashby models [110], compressive strength (σ) of brittle cellular solids is related to ρ_r as

$$\frac{\sigma}{\sigma_s} \propto \rho_r \text{ (for closed-cell)}, \quad (2)$$

$$\frac{\sigma}{\sigma_s} \propto (\rho_r)^{1.5} \text{ (for open-cell)}, \quad (3)$$

and

$$\frac{\sigma}{E_s} \propto (\rho_r)^3 \text{ (for honeycomb, out-of-plane deformation)}, \quad (4)$$

where σ_s and E_s are compressive strength and Young's modulus, respectively, of cell wall material. Therefore, with the increase of relative density from ρ_{r1} to ρ_{r2}, compressive strength is expected to increase from σ_1 to σ_2 as

$$\frac{\sigma_2}{\sigma_1} = \frac{\rho_{r2}}{\rho_{r2}} \text{ (for closed-cell)}, \quad (5)$$

$$\frac{\sigma_2}{\sigma_1} = \left(\frac{\rho_{r2}}{\rho_{r2}}\right)^{1.5} \text{ (for open-cell)}, \quad (6)$$

and

$$\frac{\sigma_2}{\sigma_1} = \left(\frac{\rho_{r2}}{\rho_{r2}}\right)^{3} \text{ (for honeycomb, out-of-plane deformation)}. \quad (7)$$

Although this is a simplified approach and pore morphology of ice-templated materials is not well-defined, the above equations do provide some useful guidance into the increase of strength with relative density. Moreover, these models have been utilized to compare experimentally measured strength and theoretical estimates to understand the mechanical behavior of ice-templated ceramics, and it has been shown that model estimations for open-cell and honeycomb (out-of-plane) morphologies are in reasonable agreement with the measured data [106,121,175]. As seen in Fig. 16c, by 1450 °C the UA-15 materials reached σ_p of about 5 MPa but the maximum strength

remained about the same up to 1600 °C. In between 1450–1600 °C, ρ_r of the UA-15 materials only marginally increased from 0.223 to 0.253 and therefore the empirical models would also predict a marginal strength increase, thus in reasonable agreement with the experimental measurements. Therefore, between 1450–1600 °C, the density of the materials marginally increased, grain growth occurred within lamella walls, and eventually each lamella wall became a single layer of grains. However, such changes had an insignificant impact on the compressive mechanical response. Thus, for the UA-15 materials, grain size and lamella wall microstructure can be significantly tailored in between 1450–1600 °C but without impacting compressive mechanical response.

Whereas in between 1600–1700 °C, the UA-15 materials exhibited a dramatic strength increase from 5 MPa to 32 MPa, by a factor greater than 6. Whereas, for an increase of ρ_r from 0.253 at 1600 °C to 0.309 at 1700 °C, the empirical models predict a moderate strength increase only by a factor of 1.2 to 1.82, depending on the type of pore morphology. In this temperature range, the UA-15 materials exhibited a considerable increase in density (Fig. 1) and significant normal grain growth as well as abnormal grain growth (Figs. 4, 5). However, the extensive microstructure investigation revealed significant distortion of lamella walls and evidence of temperature-induced structural instability. Therefore, drastic strength gain in the UA-15 materials was accompanied by significant structural distortion and shrinkage particularly in the direction perpendicular to the growth direction of ice crystals. We suggest that the marked increase of strength at elevated temperature is associated with the distortion and joining of the walls, and hence the measured strength enhancement is well-above that predicted by the empirical models.

In Fig. 18, we schematically showed the scenarios where the compressive load is applied to ice-templated ceramic with undistorted (Fig. 18a) and highly distorted lamella walls where some of

the walls being joined together (Fig. 18b). The schematics of structures shown in Figs. 18a and 18b approximately represent the UA-15 materials sintered at 1550 °C and 1700 °C, respectively. For uniaxial compression direction parallel to the ceramic lamella walls, lamella walls tend to carry the applied load whereas lamellar bridges provide mechanical support to walls [9,121,175]. Recall from the SEM images in Fig. 4 that lamellar bridges are negligible in the UA-15 materials. Due to high porosity and lack of lamellar bridges, the UA-15 materials are inherently weak and thus exhibited low strength. At 1700 °C, significant bending of the lamella walls resulted in the joining of a significant number of adjacent walls through sintering. It is possible that the sintered regions present between the adjacent lamella acted as local lamellar bridges as indicated in Fig. 18b and provided an improved level of mechanical support to the walls under compressive loading, which enhanced the load-bearing capacity of the walls and resulted in a drastic strength enhancement. However, the drastic gain in compressive strength was achieved at the expense of significant structural deformation and thus increased pore tortuosity.

A significant amount of literature exists on the processing and characterization of ice-templated ceramics; however, a systematic study is lacking in the influence of sintering temperature on the ice-templated porous ceramic structure and mechanical response. Toward this end, we investigated the combined effects of sintering temperature and Al_2O_3 platelets (large anisometric particles) on relative density, lamella wall microstructure, grain size and grain size distribution in lamella walls, structural deformation, and uniaxial compressive response of ice-templated Al_2O_3 materials. This investigation revealed a profound influence of both the processing variable and material variable on the several aspects of ice-templated ceramics, enabling an improved understanding of the structure-mechanical property relationships in these materials and limitations in the development of the ice-templated porous ceramic structure.

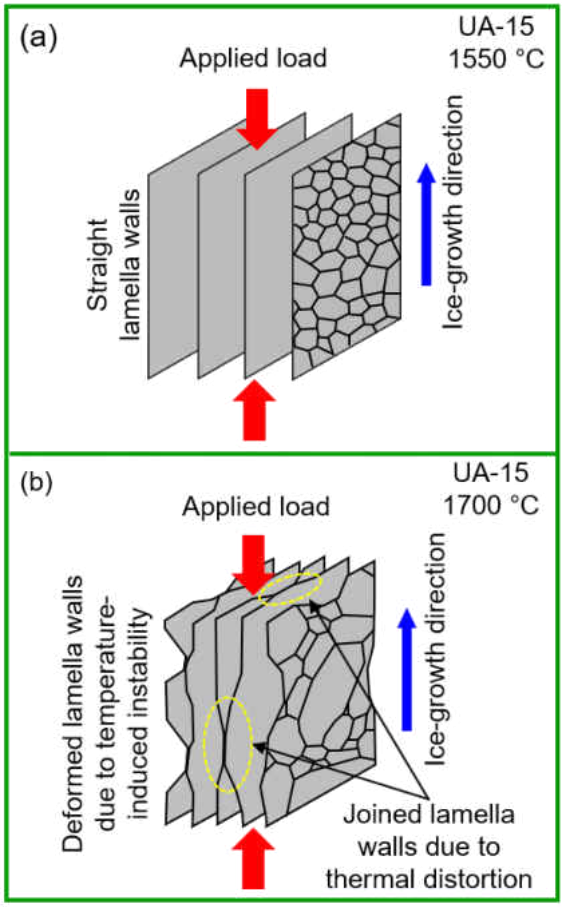

Figure 18: Schematic representation of the compressive load applied to UA-15 materials (a) with undistorted and (b) highly distorted lamella walls with some of the walls being joined together. The schematics of structures shown in Figs. 18a and 18b approximately represent the UA-15 materials sintered at 1550 °C and 1700 °C, respectively.

In the UA-15 materials (materials without platelets), with the increasing temperature, the polycrystalline lamella wall microstructure transitioned through different stages. At low-temperature regime, walls were highly porous with grain size comparable to the size of the staring UA particles. Whereas, at intermediate temperature regime, a pore-free lamella wall with fine-grained microstructure developed. And at high-temperature, along with grain growth, significant

abnormal grain growth occurred as well resulting in the development of large, elongated grains within the walls.

While the current investigation on the UA-15 materials provides insights into the tailorability of ice-templated structure with temperature, more dramatic was the combined effects of temperature and platelets. The effects of platelets on the ice-templated structure are realized at two length scales. During the templating process, some of the platelets develop lamellar bridges between lamella walls and these platelet particles remained similar to the starting particles over the entire sintering temperature range. Whereas, the platelets that became part of the lamella walls (oriented in the plane of the walls) remarkably impacted wall microstructure with the variation of temperature, which is attributed to the growth of the platelet particles as a result of diffusion of UA particles to platelets. Although the diffusion of UA particles to platelets caused microporosity in the walls, the micropores were eliminated at elevated temperatures and the walls became pore-free. The average grain size in walls was greater in UA-10PA-15 compared to UA-15. While the platelets grew into large particles, the morphology of the large particles is observed to be equiaxed (on the plane of wall) and the development of long, elongated grains was significantly less prominent compared to the UA-15 materials.

The current results strongly suggest that there are significant structural and mechanical strength advantages in the incorporation of large anisometric particles in ice-templated ceramics. The addition of large platelets resulted in a marked increase of compressive strength. A significant structural advantage is that the ice-templated ceramics containing platelets exhibited improved stability to structural deformation at higher temperatures compared to the materials without the platelets. By 1400 °C the UA-10PA-15 materials reached σ_p of about 30 MPa and at the higher temperatures the materials were able to maintain the strength with only a moderate decrease of

specific σ_p. Recall from Fig. 6 that by 1400 °C the UA-10PA-15 materials exhibited significant interactions between the UA and PA particles. With the increasing sintering temperature, the interactions enhanced and significant microstructural changes occurred, but the materials exhibited only a marginal increase of strength. Thus, at the early stages of sintering, the interactions between the UA and PA particles are crucial for strength gain, but at the latter stages the interactions could be exploited for tailoring lamella wall microstructure.

The current study provides insights into microstructure development as a function of sintering temperature within the lamella walls of ice-templated ceramics, effects of ceramic platelets on wall microstructure, and the influence of those developments on the compressive mechanical response. For each composition, a temperature range exists where it is possible to significantly tailor lamella wall microstructure but without affecting strength. Ice-templated lamellar structures are observed to be highly prone to thermal distortion at higher sintering temperatures, but the structural distortion could be reduced through the incorporation of large ceramic platelets. This study shows the importance of deeply probing into the structure-mechanical property relationships of ice-templated ceramics as a function of temperature and composition, providing valuable guidance into the microstructure design of these materials.

7.4 Conclusions

This study revealed that sintering temperature (a processing variable) and large anisometric particles (a material variable) can be judiciously employed in tailoring porosity, microstructure, and compressive mechanical response of ice-templated porous ceramic materials. In the ice-templated Al_2O_3 materials without platelets, increase of sintering temperature resulted in a gradual decrease of lamella wall porosity and thus total porosity, enhanced grain growth within the walls,

and caused significant abnormal grain growth at higher sintering temperatures. Sintering at elevated temperatures also resulted in significant deformation (bending) of lamella walls and thereby structural distortion and reduced pore directionality. Ice-templated materials without platelets exhibited low strength but gained significant strength at higher temperature, which is, however, attributed to the increased density due to structural deformation. On the other hand, addition of large Al_2O_3 platelets significantly modified ice-templated structure by increasing lamellar bridge density and remarkebly impacting lamella wall microstructure including limiting abnormal grain growth. Ceramic platelets caused drastic strength enhancement which was achieved at intermediate sintering temperature regime and the strength gain was maintained at higher temperatures. Moreover, in the presence of platelets, ice-templated materials exhibited significant resistance to temperature-induced structural instability, further illustrating the critical role of large anisometric particles in the development of mechanically robust ice-templated directionally porous ceramic materials.

Acknowledgment

This work was partially supported by the Thomas F. and Kate Miller Jeffress Memorial Trust, Bank of America, Trustee.

CHAPTER 8

SUMMARY AND FUTURE WORK

Over the ages, materials have been playing a predominant role in the advancement of civilizations. Everlasting quests and continuous endeavors are leading to the development of materials that are tailored to our needs. Even though we have advanced significantly, we are still far from our future necessities related to materials. Thus, directional porous ceramics are candidate materials for various applications including biomedical, structural, and energy-related applications. Ice-templating is one of the techniques to process such directional porous ceramics. However, the processing-structure-property relationships in these materials have not been explored fully. Therefore the present research work is focused on investigating the role of anisometric particles in aqueous ceramic suspensions during ice-templating of porous ceramics, microstructure evolution, and mechanical properties in them. The following are the summaries of findings and suggestions for future work in this area.

8.1 Summary

8.1.1 Effects of platelet-shaped particles and FFV on the microstructural evolution and mechanical properties in ice-templated porous ceramics

Replacing a small fraction of equiaxed particles with platelet-shaped particles in the aqueous suspensions of ice-templated ceramics resulted in dendritic pore morphology and enhanced compressive mechanical strength. Further, the systematic variation in FFV and platelet content is

found to greatly influence the structure-mechanical property in these materials. The following are the findings from this study:

- For a given solids loading, increasing FFV resulted in more dendritic morphology and the interlamellar bridges formed predominantly by the platelets only.
- Pore morphology gradually transitioned from lamellar to dendritic by increasing platelets content in the aqueous suspension of particular solids loading.
- Rigorous microstructural analysis revealed that the fraction of lamellar bridges containing platelets increased substantially with increasing platelet content.
- An innovative method is proposed to calculate the ratio of interlamellar vs. interlamellar platelets. Interestingly, it showed that by increasing the platelet content in the suspension, this ratio remained the same.
- Uniaxial compressive mechanical properties of these materials improved over 200% for an addition of 5 vol.% platelets of total solids loading.
- Overall, this investigation revealed a unique strategy that can be implemented to stiffen and strengthen the ice-templated porous ceramics.

8.1.2 Role of matrix phase particle size

Further, variation in the particle size of ceramic powder showed a significant influence on the microstructure and mechanical response of ice-templated porous ceramics. Finer, equiaxed ceramic powder particles sintered better than those of coarse particles. Also, significant interactions occurred between fine, equiaxed particles and platelets that are present in the lamella walls. Due to the better sinterability of fine particles, platelets-induced ice-templated porous

ceramics processed from fine, equiaxed particles showed enhanced mechanical properties compared to the materials processed from coarse matrix particles.

8.1.3 Fracture mechanisms within the lamella walls of platelets-induced ice-templated ceramics

This investigation revealed the fracture mechanisms within the polycrystalline lamella walls of platelets-induced ice-templated porous ceramics. Intergranular cracking was found to be the dominant fracture mechanism. Rigorous microstructural analyses suggested that intergranular cracks evolved mainly in two orientations, parallel and perpendicular to the compressive loading direction. In the lamella walls of platelets-induced ice-templated materials, crack deflection at the interface of fine equiaxed grain and large grain formed by platelet is observed. Probably, this crack deflection could lead to an extrinsic toughening of the lamella wall and might have contributed to the enhancement of compressive strength along with the contribution from the presence of platelet-bridges.

8.1.4 Effects of porosity and strain rate on the compressive response of ice-templated materials without platelets

A transition from cellular-like failure to brittle-like failure in ice-templated porous ceramics as the porosity decreases from 70 vol.% to 54 vol.%. When the materials with 70 vol.% porosity are uniaxially compressed, due to limited resistance to buckling lamella walls undergo localized failure, whereas the macroscopic structure remains intact at peak stress. Upon further compression beyond peak stress, the structure continues to undergo localized failure and the measured compressive response proceeds through a prominent plateau region where stress decreases

progressively with increasing strain. On the other hand, due to thick lamella walls and extensive lamellar bridging, lamella walls of the porous materials with 54 vol.% porosity exhibited marked resistance to buckling-induced instability. In the vicinity of peak stress, the applied load could be sufficient enough to cause the failure of the bridges and simultaneous axial splitting of the lamella walls throughout the structure. Thus, the ice-templated porous ceramics containing no platelets exhibited an abrupt drop of compressive stress beyond the peak stress which can be termed as brittle-like failure. Interestingly, in the dynamic or high-strain rate regimes of loading, ice-templated materials of 70 and 54 vol.% porosities showed enhanced peak stress and cellular-like compressive response beyond peak stress. Such behavior can be attributed to the inherent strain rate-sensitivity of the constituent material and micro-inertia effects.

8.1.5 Effects of strain rate on the compressive response of ice-templated porous ceramics containing platelets

Strain rate remarkably influenced the compressive mechanical properties of platelets-induced ice-templated porous ceramics. In the quasistatic loading conditions, the ice-templated materials containing platelets with 75 vol.% porosity showed brittle-like failure. However, in the high-strain rate loading conditions, these materials showed cellular-like compressive behavior. Also, these materials showed different strain rate-sensitivity at different loading regimes depending upon elastic vs. inelastic deformation.

8.1.6 Effects of temperature on microstructure evolution and structural stability of ice-templated porous ceramics containing platelets

In the ice-templated porous Al_2O_3 ceramics, increasing sintering temperature resulted in a gradual reduction in lamella wall porosity, enhanced grain growth, and caused significant abnormal grain growth at higher temperatures. Sintering at elevated temperatures also resulted in significant deformation (bending) of lamella walls and thereby structural distortion and reduced pore directionality. This excessive deformation caused the resintering of lamella walls which resulted in a marked increase in compressive strength in these materials which are sintered at the elevated temperatures. On the other hand, the addition of platelets significantly modified the ice-templated structure by increasing lamellar bridge density and remarkably impacted the lamella wall microstructure including limiting abnormal grain growth. Moreover, in the presence of platelets, ice-templated materials exhibited significant resistance to temperature-induced structural stability.

8.2 Direction for future research

8.2.1 Explore the effects of other processing parameters on the structure of ice-templated porous ceramics

As stated in this study, the interaction of particle-freezing front plays a major role in the microstructural development in ice-templated porous ceramics. The observed increase in bridge density of ice-templated ceramics structures in this dissertation has been rationalized based on the variation in few intrinsic parameters such as particle size and morphology, FFV, and solids loading that influenced the particle-freezing front interactions. However, other parameters such as different solvents and additives to the suspension can significantly influence those interactions [10,46]. Also, external fields such as magnetic field and electric fields are used to tailor the microstructure

of ice-templated porous ceramics [10,46]. Thus, systematic studies on the effects of variation in these intrinsic and extrinsic parameters on the microstructure evolution and mechanical properties can significantly enhance the understanding of processing-structure-property relationships of ice-templated porous ceramics.

8.2.2 Effects of variation in platelets content on microstructure evolution and mechanical response in ice-templated materials

During the ice-templating process, the presence of a small fraction of platelet particles in aqueous suspensions containing mainly fine equiaxed particles affected the particle packing in the lamella walls and resulted in a slight increase in the porosity of the materials. On the other hand, in spite of higher porosity, the presence of interlamellar bridges formed by the platelets markedly enhanced the compressive strength of ice-templated porous ceramics. While a small number of platelets in the matrix of fine equiaxed particles improves the compressive strength, the particle packing may deteriorate by increasing the platelet content that may result in the increase in porosity and thereby decrease in compressive strength. Thus, the enhancement in compressive strength may go through a maximum. A future study can be directed to understand this aspect by systematically varying the platelets' content for a given solids loading suspension. Also, this dissertation investigated the effects of platelets in ice-templated ceramics containing porosities between 75 to 82 vol.%. An important question is whether the platelets will also lead to the marked compressive property enhancement in ice-templated materials having porosities below 75 vlo.% and above 82 vol.%? To answer this, further studies are required that focus on the effects of platelets in ice-templated ceramics over a wide range of porosity.

8.2.3 Direct observation of failure in platelets-induced ice-templated ceramics

The understanding of the origin of elastic compressive response and compressive behavior in ice-templated ceramics after reaching the peak stress in quasistatic and dynamic loading conditions can be further enhanced by probing into the fracture events with the help of high-speed image capturing techniques.

8.2.4 Effects of platelets on functional properties in ice-templated porous ceramics

Ice-templated porous ceramics can provide several functional advantages such as less pore tortuosity with easily accessible porosity and high surface area. While the addition of platelets to the ice-templated porous materials can further enhance the surface area of the materials, the entrapment of platelets between lamella walls may affect the accessibility of pores. As such the pore tortuosity and permeability of the ice-templated porous ceramics can be affected by the addition of platelets. Therefore, it can be interesting to further study the effects of platelets on functional properties such as pore tortuosity and permeability in ice-templated porous ceramics.

8.2.5 Platelets-induced composites prepared from ice-templated porous preforms

Ice-templated porous materials can be used as preforms to prepare composite materials by infiltrating the porous structures with varieties of materials such as metals, polymers, and ceramics. By taking the advantages of mechanical or functional properties of both constituent materials, the composite materials result in enhanced material properties. Since the ice-templated preforms provide a laminar type of skeleton to the composites, the resulted composite materials form a laminar composite structure. Mechanical properties such as strength and toughness of composite materials depend on several factors such as adhesion between the interfaces of constituent phases,

the morphology of reinforcement phase material, and volume fraction and distribution of phases. Thus, further studies can be focused on the understanding of the role of platelets in strength enhancement and toughening mechanisms such as crack deflection or bridging in ice-templated preforms of composite materials.

REFERENCES

[1] T. Fukasawa, Z. Deng, M. Deng, M. Ando, T. Ohji, Y. Goto, Pore structure of porous ceramics synthesized from water-based slurry by freeze-dry process, J. Mater. Sci. 36 (10) (2001) 2523-2527.

[2] T. Fukasawa, M. Ando, T. Ohji, S. Kanzaki, Synthesis of porous ceramics with complex pore structure by freeze-dry processing, J. Am. Ceram. Soc. 84 (1) (2001) 230-232.

[3] T. Fukasawa, M. Ando, T. Ohji, Filtering properties of porous ceramics with unidirectionally aligned pores, Nippon 110 (7) (2002) 627-631.

[4] T. Fukasawa, Z.Y. Deng, M. Ando, T. Ohji, S. Kanzaki, Synthesis of porous silicon nitride with unidirectionally aligned channels using freeze-drying process, J. Am. Ceram. Soc. 85 (9) (2002) 2151-2155.

[5] J. Moon, H. Hwang, M. Awano, K. Maeda, S. Kanzaki, Preparation of dense thin-film solid electrolyte on novel porous structure with parallel pore channel, J. Ceram. Soc. Jpn. 110 (5) (2002) 479-484.

[6] J. Moon, H. Hwang, M. Awano, K. Maeda, S. Kanzaki, Preparation of NiO-YSZ tubular support with radially aligned pore channels, Mater. Lett. 57 (8) (2002) 1428-1434.

[7] S. Deville, E. Saiz, R.K. Nalla, A.P. Tomsia, Freezing as a path to build complex composites, Science 311 (2006) 515-518.

[8] S. Deville, E. Saiz, A. P. Tomsia, Ice-templated porous alumina structures, Acta Mater. 55 (2007) 1965-1974.

[9] D. Ghosh, N. Dhavale, M. Banda, H. Kang, A comparison of microstructure and uniaxial compressive response of ice-templated alumina scaffolds fabricated from two different particle sizes, Ceram. Inter. 42 (2016) 16138-16147.

[10] S. Deville, Freezing Colloids: Observations, Principles, Control, and Use: Applications in Materials Science, Life Science, Earth Science, Food Science, and Engineering, Springer, 2017.

[11] F. Zhang, C. He, L. Cao, W. Feng, H. Wang, X. Mo, J. Wang, Fabrication of gelati-hyaluronic acid hybrid scaffolds with tunable porous structures for soft tissue engineering, J. Biol. Macromol. 48 (3) (2011) 474-481.

[12] S. Flauder, U. Gbureck, F.A. Muller, β-TCP scaffolds with an interconnected and aligned porosity fabricated via ice-templating, Key Eng. Mater. 529-530 (2012) 129-132.

[13] A. Zamanian, S. Farhangdoust, M. Yasaei, M. Khorami, M. Abbasabadi, The effects of temperature on the microstructural and mechanical characteristics of hydroxyapatite macroporous scaffolds prepared via freeze-casting, Key Eng. Mater. 529-530 (2012) 133-137.

[14] M.K. Ahn, K.H. Shin, Y.W. Moon, Y.H. Koh, W.Y. Choi, H.E. Kim, Highly porous biphasic calcium phosphate (BCP) ceramics with large interconnected pores by freezing vigorously foamed BCP suspensions under reduced pressure, J. Am. Ceram. Soc. 94 (12) (2011) 4154-4156.

[15] W.Y. Choi, H.E. Kim, Y.H. Koh, Production, mechanical properties and in vitro biocompatibility of highly aligned porous poly (Ɛ-caprolactane) (PCL)/hydroxyapatite (HA) scaffolds, J. Porous Mater. 20 (2013) 701-708.

[16] S.C. Rodrigues, C.L. Salgado, A. Sahu, M.P. Garcia, M.H. Fernandes, F.J. Monteiro, Preparation and characterization of collagen-nanohydroxyapatite biocomposite scaffolds by cryogelation method for bone tissue engineering applications, J. Biomed. Mater. Res. Part A 101A (4) (2013) 1080-1094.

[17] S.M.H. Ghazanfari, A. Zamanian, Phase transformation, microstructural and mechanical properties of hydroxyapatite/alumina nanocomposite scaffolds produced by freeze casting, Ceram. Int. 39 (8) (2013) 9835-9844.

[18] M.K. Lee, N.O. Chung, J. Lee, Membranes with through-thickness porosity prepared by unidirectional freezing, Polymer 51 (26) (2010) 6258-6267.

[19] J.Z. Hamad, R. Dua, N. Kurniasari, M.D. Kennedy, P. Wang, G.L. Amy, Irreversible membrane fouling abatement through pre-deposited layer of hierarchical porous carbons, Water Res. 65 (2014) 245-256.

[20] C. Gaudillere, J. Garcia-Fayos, J.M. Serra, Enhancing oxygen permeation through hierarchically-structured perovskite membranes elaborated by freeze-casting, J. Mater. Chem. A 2 (2014) 3828-3833.

[21] C. Gaudillere, J. Garcia-Fayos, M. Balaguer, J.M. Serra, Enhanced oxygen separation through freeze-cast bilayered dual-phase membranes, ChemSusChem 7(9) (2014) 2554-2561.

[22] Z. Liu, K. Xu, P. She, S. Yin, X. Zhu, H. Sun, Self-assembly of 2D MnO_2 nanosheets into high-purity aerogels with ultralow density, Chem. Sci. 7(3) (2016) 1926-1932.

[23] I. Ogino, S. Kazuki, S.R. Mukai, Marked increase in hydrophobicity of monolithic carbon cryogels via HCl aging of precursor resorcinol-formaldehyde hydrogels: application to 1-butanol recovery from dilute aqueous solutions, J. Phy. Chem. C 118(13) (2014) 6866-6872.

[24] S.R. Mukai, Y. Kimura, S. Yoshida, I. Ogino, Development of a novel cesium adsorbent which causes minimal hydraulic resistance through the immobilization of Prussian blue analogues in a monolithic silica-alumina microhoneycomb, Chem. Eng. Trans. 42 (2014) 181-186.

[25] A. Ojuva, F. Akhtar, A.P. Tomsia, L. Bergstrom, Laminated adsorbents with very rapid CO_2 uptake by freeze-casting of zeolites, ACS Appl. Mater. Interfaces 5(7) (2013) 2669-2679.

[26] X. Guo, H. Bi, A. Zafar, Z. Liang, Z. Shi, L. Sun, Z. Ni, Investigation of dodecane in three-dimensional porous graphene sponge by Raman mapping, Nonotechnology 27(5) (2016) 055702.

[27] I. Corni, T.J. Harvey, J.A. Wharton, K.R. Stokes, F.C. Walsh, R.J.K. Wood, A review of experimental techniques to produce a nacre-like structure, Bioinspir. Biomim. 7(3) (2012) 031001.

[28] M.E. Launey, E. Munch, D.H. Alsem, E. Saiz, A.P. Tomsia, R.O. Ritchie, A novel biomimetic approach to the design of high-performance ceramic-metal composites, J. R. Soc. Interface 7(46) (2009) 741-753.

[29] S. Akurati, N. Tennant, D. Ghosh, Characterization of dynamic and quasistatic compressive mechanical properties of ice-templated alumina-epoxy composites, Journal of Materials Research 34(6) (2019) 959-971.

[30] D. Cai, S. Wang, L. Ding, P. Lian, S. Zhang, F. Peng, H. Wang, Superior cycle stability of graphene nanosheets prepared by freeze-drying process as anodes for lithium-ion batteries, J. Power Sources 254 (2014) 198-203.

[31] L. Pei, Q. Jin, Z. Zhu, Q. Zhao, J. Liang, J. Chen, Ice-templated preparation and sodium storage of ultrasmall SnO_2 nanoparticles embedded in three-dimensional graphene, Nano Res. 8(1) 2014 184-192.

[32] J. Cheng, G. Gu, Q. Guan, J.M. Razal, Z. Wang, X. Li, B. Wang, Synthesis of a porous sheet-like V_2O_5-CNT nanocomposite using an ice-templating 'brick-and-mortar' assembly

approach as high-capacity, long cycle life cathode material for lithium-ion batteries, J. Mater. Chem. A 4 (2016) 2729-2737.

[33] K.H. Lee, Y.W. Lee, S.W. Lee, J.S. Ha, S.S. Lee, J.G. Son, Ice-templated self-assembly of $VOPO_4$-graphene nanocomposites for vertically porous 3D supercapacitor electrodes, Sci. Rep. 5 (2015) 13696-13705.

[34] Y. Huang, D. Wu, J. Wang, S. Han, L. Lv, F. Zhang, X. Feng, Amphiphilic polymer promoted assembly of macroporous graphene/SnO_2 frameworks with tunable porosity for higher performance lithium storage, Small 10(11) (2014) 2226-2232.

[35] J.H. Um, M. Choi, H. Park, Y.H. Cho, D.C. Dunand, H. Choe, Y.E. Sung, 3D macroporous electrode and high-performance in lithium-ion batteries using SnO_2 coated Cu foam, Sci. Rep. 6 (2016) 18626-18634.

[36] K. Hamamoto, M. Fukushima, M. Mamiya, Y. Yoshizawa, J. Akimoto, T. Suzuki, Y. Fujishiro, Morphology control and electrochemical properties of LiFePO4/C composite cathode for lithium ion batteries, Solid State Ionics 225 (2012) 560-563.

[37] A.D. Roberts, S. wang, X. Li, H. Zhang, Hierarchical porous nitrogen-rich carbon monoliths via ice-templating: high capacity and high-rate performance as lithium-ion battery anode materials, J. Mater. Chem. A 2 (2014) 17787-17796.

[38] K. Shu, C. Wang, S. Li, C. Zhao, Y. Yang, H. Liu, G. Wallace, Flexible free-standing graphene paper with interconnected porous structure for energy storage, J. Mater. Chem. A 3 (2015) 4428-4434.

[39] Y. Huang, D. Wu, J. Jiang, Y. Mai, F. Zhang, H. Pan, X. Feng, Highly oriented macroporous graphene hybrid monoliths for lithium ion battery electrodes with ultrahigh capacity and rate capability, Nano Energy 12 (2015) 287-295.

[40] A.D. Roberts, X. Li, H. Zhang, Hierarchically porous sulfur-containing activated carbon monoliths via ice-templating and one-step pyrolysis, Carbon N. Y. 95 (2015) 268-278.

[41] R. Sahore, L.P. Estevez, A. Ramanujapuram, F.J. DiSalvo, E.P. Giannelis, High-rate lithium–sulfur batteries enabled by hierarchical porous carbons synthesized via ice templation, J. Power Sources 297 (2015) 188-194.

[42] Y. Wang, D. Kong, W. Shi, B. Liu, G.J. Sim, Q. Ge, H.Y. Yang, Ice templated free-standing hierarchically WS_2/CNT-rGO aerogel for high-performance rechargeable lithium and sodium ion batteries, Adv. Energy Mater. 6(21) (2016) 1601057.

[43] Y. Lin, F. Liu, G. Casano, R. Bhavsar, I.A. Kinloch, B. Derby, Pristine Graphene Aerogels by Room-Temperature Freeze Gelation, Adv. Mater. 28(36) (2016) 7993-8000.

[44] G. Li, J. Sun, W. Hou, S. Jiang, Y. Huang, J. Geng, Three-dimensional porous carbon composites containing high sulfur nanoparticle content for high-performance lithium–sulfur batteries, Nat. Commun. 7 (2016) 10601.

[45] S. Deville, The lure of ice-templating: Recent trends and opportunities for porous materials, Scripta Mater. 147 (2018) 119-124.

[46] K.L. Scotti, D.C. Dunand, Freeze casting – A review of processing, microstructure and properties via the open data repository, FreezeCasting.net, Prog. Mater. Sci. 94 (2018) 243-305.

[47] B.E. Novich, C.A. Sundback, R.W. Adams, Quickset injection molding of high performance ceramics, Ceram. Trans. 26 (1992) 157–64.

[48] B.E. Novich, R.R. Lee, G.V. Franks, D. Ouellette, M.K. Ferber, Fabrication of low cost and high performance ceramic gas turbine engine components, Proceedings of the Annual

Automotive Technology Development Contractors' Coordination Meeting Society of Automotive Engineers, Dearborn, MI, P-243 (1991) 111-123.

[49] M.A. Occhionero, B.E. Novich, C.A. Sundback, Forming of complex high performance ceramic and metallic shapes, US Patent No. 5, 047, 181, 1991.

[50] C.A. Sundback, B E. Novich, A.E. Karas, R.W. Adams, Complex ceramic and metallic shaped by low pressure forming and sublimative drying, US Patent No. 5, 047,182, 1991.

[51] T.Y. Yang, J.M. Lee, S.Y. Yoon, H.C. Park, Hydroxyapatite scaffolds processed using a TBA-based freeze-gel casting/polymer sponge technique, J. Mater. Sci. Mater. Med. 21(5) (2010) 1495-1502.

[52] T.T. Xu, C.A. Wang, R. Guo, Microstructure and electrical properties of porous PZT ceramics with unidirectional pore channel structure fabricated by freeze-casting, Key Eng. Mater. 512-515 (2012) 1347-1350.

[53] T.Y. Yang, H.B. Ji, S.Y. Yoon, B.K. Kim, H.C. Park, Porous mullite composite with controlled pore structure processed using a freeze casting of TBA-based coal fly ash slurries, Resour. Conserv. Recycl. 54(11) (2010) 816-820.

[54] T. Xu, C.A. Wang, Control of pore size and wall thickness of 3-1 type porous PZT ceramics during freeze-casting process, Mater. Des. 91 (2016) 242-247.

[55] B.H. Yoon, E.J. Lee, H.E. Kim, Y.H. Koh, Highly Aligned Porous Silicon Carbide Ceramics by Freezing Polycarbosilane/Camphene Solution, J. Am. Ceram. Soc. 90(6) (2007) 1753-1759.

[56] X. Liu, M.N. Rahaman, Q. Fu, Oriented bioactive glass (13-93) scaffolds with controllable pore size by unidirectional freezing of camphene-based suspensions: Microstructure and mechanical response, Acta Biomater. 7(1) (2011) 406-416.

[57] B.H. Yoon, W.Y. Choi, H.E. Kim, J.H. Kim, Y.H. Koh, Aligned porous alumina ceramics with high compressive strengths for bone tissue engineering, Scr. Mater. 58(7) (2008) 537-540.

[58] Y.M. Soon, K.H. Shin, Y.H. Koh, W.Y. Choi, H.E. Kim, Assembling unidirectionally frozen alumina/camphene bodies for aligned porous alumina ceramics with larger dimensions, J. Eur. Ceram. Soc. 31(3) (2011) 415-419.

[59] C. Hong, J. Du, J. Liang, X. Zhang, J. Han, Functionally graded porous ceramics with dense surface layer produced by freeze-casting, Ceram. Int. 37(8) (2011) 3717-3722.

[60] Y.H. Koh, J.J. Sun, H.E. Kim, Freeze casting of porous Ni–YSZ cermets, Mater. Lett. 61(6) (2007) 1283-1287.

[61] J.W. Kim, K. Taki, S. Nagamine, M. Ohshima, Preparation of poly(L-lactic acid) honeycomb monolith structure by unidirectional freezing and freeze-drying, Chem. Eng. Sci. 63(15) (2008) 3858-3863.

[62] C. Schugens, V. Maquet, C. Grandfils, R. Jerome, P. Teyssie, Biodegradable and macroporous polylactide implants for cell transplantation: 1. Preparation of macroporous polylactide supports by solid-liquid phase separation, Polymer 37(6) (1996) 1027-1038.

[63] P.A. George, K. Quinn, J.J. Cooper-White, Hierarchical scaffolds via combined macro- and micro-phase separation, Biomaterials 31(4) (2010) 641-647.

[64] R. Okaji, K. Taki, S. Nagamine, M. Ohshima, Preparation of porous honeycomb monolith from UV-curable monomer/dioxane solution via unidirectional freezing and UV irradiation. J. Appl. Polym. Sci. 125(4) (2012) 2874-2881.

[65] Y.Q. Goh, C.P. Ooi, Fabrication and characterization of porous poly(L-lactide) scaffolds using solid–liquid phase separation, J. Mater. Sci. Mater. Med. 19(6) (2008) 2445-2452.

[66] H.J. Choi, T.Y. Yang, S.Y. Yoon, B.K. Kim, H.C. Park, Porous alumina/zirconia layered composites with unidirectional pore channels processed using a tertiary-butyl alcohol-based freeze casting, Mater. Chem. Phys. 133(1) (2012) 16-20.

[67] K. Araki, J.W. Halloran, Porous Ceramic Bodies with Interconnected Pore Channels by a Novel Freeze Casting Technique, J. Am. Ceram. Soc. 88(5) (2005) 1108-1114.

[68] T. Waschkies, R. Oberacker, M.J. Hoffmann, Investigation of structure formation during freeze-casting from very slow to very fast solidification velocities, Acta Mater. 59 (2011) 5135-5145.

[69] N.D. Dhavale, A comparison of microstructure and uniaxial compressive response of ice-templated porous alumina scaffolds fabricated from two different particle sizes, MS thesis, Aerospace engineering, Old Dominion University, Summer 2016.

[70] S. Leo, C. Tallon, N. Stone, G.V. Franks, Near-net-shaping methods for ceramic elements of (body) armor systems, J. Am. Ceram. Soc. 97(10) (2014) 3013-3033.

[71] S. Deville, Freeze-casting of porous ceramics: A review of current achievements and issues, Adv. Eng. Mater. 10(3) (2008) 155-169.

[72] P.V. Hobbs, Ice physics, Oxford University Press, Cambridge, UK, 1974.

[73] R. Asthana, S.N. Tewari, The engulfment of foreign particles by a freezing interface, J. Eng. Mater. 28 (1993) 5414-5425.

[74] U.G.K. Wegst, M. Schecter, A.E. Donius, P.M. Hunger, Biomaterials by freeze casting, Phil. Trans. R. Soc. A 368 (2010) 2099-2121.

[75] H. Zhang, I. Hussain, M. Brust, M.F. Butler, S.P. Rannard, A.I. Cooper, Aligned two- and three-dimensional structures by directional freezing of polymers and nanoparticles, Nat. Mater. 4 (2005) 787-793.

[76] S.N. Omenyi, R.P. Smith, A.W. Neumann, Determination of solid/melt interfacial tensions and of contact angles of small particles from the critical velocity of engulfment, J. Colloid Interf. Sci. 75(1) (1980) 117-125.

[77] G.F. Bolling, J. Cisse, A theory for the interaction of particles with a solidifying front, J. Cryst. Growth 10 (1971) 56-66.

[78] Ch. Korber, G. Rau, M.D. Cosman, E.G. Cravalho, Interaction of particles and a moving ice-liquid interface, J. Cryst. Growth 72 (1985) 649-662.

[79] D.M. Stefanescu, B.K. Dhindaw, S.A. Kacar, A. Moitra, Behavior of ceramic particles at the solid-liquid metal interface in metal matrix composites, Metall. Trans. A 19A (1988) 2847-2855.

[80] D.R. Uhlmann, B. Chalmers, Interaction between particles and a solid-liquid interface, J. Appl. Phys. 35 (1964) 2986-2993.

[81] A.W. Rempel, M.G. Worster, The interaction between a particle and an advancing solidification front, J. Crys. Growth 205 (1999) 427-440.

[82] D. Ghosh, N. Dhavale, M. Banda, H. Kang, A comparison of microstructure and uniaxial compressive response of ice-templated alumina scaffolds fabricated from two different particle sizes, Ceram. Int. 42(14) (2016) 16138-16147.

[83] M.M. Porter, R. Imperio, M. Wen, M.A. Meyers, J. McKittrick, Bioinspired scaffolds with varying pore architectures and mechanical properties, Adv. Func. Mater. 24 (2014) 1978-1987.

[84] I.O. Ozer, E. Suvaci, B. Karadenir, J.M. Missiaen, C.P. Carry, D. Bouvard, Anisotropic shrinkage in alumina ceramics containing oriented platelets, J. Am. Ceram. Soc. 89(6) (2006) 1972-1976.

[85] T. Carisey, A. Laugier-Werth, D.G. Brandon, Control of texture in Al_2O_3 by gel-casting, J. Eur. Ceram. Soc. 15 (1995) 1-8.

[86] D. Brandon, D. Chen, H. Chan, Control of texture in monolithic alumina, Mater. Sci. Eng. A 195 (1995) 189-196.

[87] E. Suvaci, G.L. Messing, Critical factors in the templated grain growth of textured reaction-bonded alumina, J. Am. Ceram. Soc. 83(8) (2000) 2041-2048.

[88] X.N. Huang, P.S. Nicholson, Mechanical properties and fracture toughness of α-Al_2O_3-platelet-reinforced Y-PSZ composites at room temperatures, J. Am. Ceram. Soc. 76(5) (1993) 1294-1301.

[89] K. Morsi, B. Derby, Mechanical Properties of pressureless sintered alumina containing platelets, Br. Ceram. Trans. 98(2) (1999) 72-76.

[90] M. Wei, D. Zhi, D.G. Brandon, Microstructure and texture evolution in gel-cast α-alumina/alumina platelet ceramic composites, Scr. Mater. 53 (2005) 1327-1332.

[91] E. Feilden, T. Giovannini, N. Ni, C. Ferraro, E. Saiz, L. Vandeperre, F. Giuliani, Micromechanical strength of individual Al_2O_3 platelets, Scr. Mater. 131 (2017) 55-58.

[92] G.L. Messing, S. Trolier-McKinstry, E.M. Sabolsky, C. Duran, S. Kwon, B. Brahmaroutu, P. Park, H. Yilmaz, P.W. Rehrig, K.B. Eitel, E. Suvaci, M. Seabaugh, K.S. Oh, Templated grain growth of textured piezoelectric ceramics, Crti. Rev. Solid State 29 (2004) 45-96.

[93] M.M. Seabaugh, I.H. Kerscht, G.L. Messing, Texture development by templated grain growth in liquid-phase-sintered α-alumina, J. Am. Ceram. Soc. 80(5) (1997) 1181-1188.

[94] M.M. Seabaugh, G.L. Messing, Texture development and microstructure evolution in liquid-phase-sintered α-alumina by templated grain growth, J. Am. Ceram. Soc. 83(12) (2000) 3109-3116.

[95] J.A. Horn, S.C. Zhang, U. Selvaraj, G.L. Messing, S. Trolier-McKinstry, Templated grain growth of textured Bismuth Titanate, J. Am. Ceram. Soc. 82(4) (1999) 921-926.

[96] E. Suvaci, M.M. Seabaugh, G.L. Messing, Reaction-based processing of textured alumina by templated grain growth, J. Eur. Ceram. Soc. 19 (1999) 2465-2474.

[97] E. Suvaci, K.S. Oh, G.L. Messing, Kinetics of templated growth in alumina during the process of templated grain growth (TGG), Acta Mater. 49 (2001) 2075-2081.

[98] Y. Chang, S. Poterala, D. Yener, G.L. Messing, Fabrication of highly textured fine-grained α-alumina by templated grain growth of nanoscale precursors, J. Am. Ceram. Soc. 96(5) (2013) 1390-1397.

[99] P.M. Hunger, A.E. Donius, U.G.K. Wegst, Platelets self-assemble into porous nacre during freeze casting, J. Mech. Behav. Biomed. Mater. 19 (2013) 87-93.

[100] F. Bouville, E. Maire, S. Deville, Self-assembly of faceted particles triggered by a moving ice front, Langmuir 30 (2014) 8656-8663.

[101] F. Bouville, E. Portuguez, Y. Chang, G.L. Messing, A.J. Stevenson, E. Maire, L. Courtois, S. Deville, Templated grain growth in macroporous materials, J. Am. Ceram. Soc. 97(6) (2014) 1736-1742.

[102] S. Deville, E. Saiz, A.P. Tomsia, Freeze casting of hydroxyapatite scaffolds for bone tissue engineering, Biomaterials 27 (2006) 5480-5489.

[103] V. Naglieri, H.A. Bale, B. Gludovatz, A.P. Tomsia, R.O. Ritchie, On the development of ice-templated silicon carbide scaffolds for nature-inspired structural materials, Acta Mater. 61 (2013) 6948-6957.

[104] A. Ojuva, M. Järveläinen, M. Bauer, L. Keskinen, M. Valkonen, F. Akhtar, E. Levänenc, L. Bergström, Mechanical performance and CO_2 uptake of ion-exchanged zeolite A structured by freeze-casting, J. Euro. Ceram. Soc. 35 (2015) 2607-2618.

[105] A. Lichtner, D. Roussel, D. Jauffrès, C.L. Martin, R.K. Bordia, Effect of macropore anisotropy on the mechanical response of hierarchically porous ceramics, J. Am. Ceram. Soc. 99 (2016) 979-987.

[106] J. Seuba, S. Deville, C. Guizard, A.J. Stevenson, Mechanical properties and failure behavior of unidirectional porous ceramics, Sci. Rep. 6:24326 (2016) 1-11.

[107] P.M. Hunger, A.E. Donius, U.G.K. Wegst, Structure–property-processing correlations in freeze-cast composite scaffolds, Acta Biomater. 9 (2013) 6338-6348.

[108] D. Ghosh, M. Banda, H. Kang, N. Dhavale, Platelets-induced stiffening and strengthening of ice-templated highly porous alumina scaffolds, Scr. Mater. 125 (2016) 29-33.

[109] S. Deville, G. Bernard-Granger, Influence of surface tension, osmotic pressure and pores morphology on the densification of ice-templated ceramics, J. Euro. Ceram. Soc. 31 (2011) 983-987.

[110] L.J. Gibson, M.F. Ashby, Cellular Solids: Structure and Properties, 2nd ed., Cambridge University Press, Cambridge, UK, 1999.

[111] Q.M. Li, I. Magkiriadis, J.J. Harrigan, Compressive strain at the onset of densification of cellular solids, J. Cell. Plast. 42 (2006) 371-392.

[112] D. Ghosh, A. Wiest, R.D. Conner, Uniaxial quasistatic and dynamic compressive response of foams made from hollow glass microspheres, J. Euro. Ceram. Soc. 36 (2016) 781-789.

[113] T. Carisey, I. Levin, D.G. Brandon, Microstructure and mechanical properties of textured Al_2O_3, J. Euro. Ceram. Soc. 15 (1995) 283-289.

[114] M. Klecka, G. Subhash, Grain size dependence of scratch-induced damage in alumina ceramics, Wear 265 (2008) 612-619.

[115] J.A. Salem, J.L. Shanon Jr., R.C. Bradt, NASA technical memorandum 100250, Presented 89th Annual meeting of the American Ceramic Society, 1987.

[116] R.M. Spriggs, J.B. Mitchell, T. Vasilos, Mechanical properties of pure, dense aluminum oxide as a function of temperature and grain Size, J. Am. Ceram. Soc. 47 (1964) 323-327.

[117] L.J. Bonderer, A.R. Studart, L.J. Gauckler, Bioinspired design and assembly of platelet reinforced polymer films, Science 319 (2008) 1069-1073.

[118] R.C Bradt, D.P.H. Haselman, D. Munz, M. Sakai, V.Y. Sherchenko, Fracture mechanics of ceramics, 14 (2005).

[119] M.E. Launey, R.O. Ritchie, On the fracture toughness of advanced materials, Adv. Mater. 21 (2009) 2103-2110.

[120] A.R. Boccaccini, V. Winkler, Fracture surface roughness and toughness of Al_2O_3-platelet reinforced glass matrix composites, Composites: Part A 33 (2002) 125-131.

[121] S. Deville, S. Meille, J. Seuba, A meta-analysis of the mechanical properties of ice-templated ceramics and metals, Sci. Technol. Adv. Mater. 16 (2015) 043501.

[122] R.N. Mohamed, Sintering of Ceramics, CRC press, Boca Raton, USA 2007.

[123] S. Deville, E. Maire, A. Lasalle, A. Bogner, C. Gauthier, J. Leloup, C. Guizard, In situ X-ray radiography and tomography observations of the solidification of aqueous alumina particle suspensions—part I: Initial instants, J. Am. Ceram. Soc. 92(11) (2009) 2489-2496.

[124] D. Ghosh, H. Kang, M. Banda, V. Kamaha, Influence of anisotropic grains (platelets) on the microstructure and uniaxial compressive response of ice-templated sintered alumina scaffolds, Acta Mater. 125 (2017) 1-14.

[125] H. Horri, S. Nemat-Nesser, Brittle failure in compression: Splitting, faulting, and brittle-ductile transition, Philos. Trans. R. Soc. A139 (1986) 337-374.

[126] G. Ravichandran, G. Subhash, A micromechanical model for high strain rate behavior of ceramics, Int. J. Solids Struct. 32 (1995) 2627-2646.

[127] S. Nemat-Nasser, M. Obata, A microcrack model of dilatancy in brittle materials, J. Appl. Mech. 55 (1988) 24-35.

[128] T. Sadowski, Modelling of semi-brittle MgO ceramic behaviour under compression, Mech. Mater. 18(1) (1994) 1-16.

[129] Y.M. Tan, Microstructure and dynamic failure properties of freeze-cast materials for thermobaric warhead cases, Ph.D. thesis, Naval Postgraduate School, Monterey, CA 2012.

[130] Y.M. Tan, O. Cervantes, S.W. Nam, J.D. Molitoris, J.P. Hooper, Dynamic fragmentation of cellular, ice-templated alumina scaffolds, J. Appl. Phys. 119 (2016) 024901-1.

[131] Q. Fu, M.N. Rahaman, F. Dogan, B.S. Bal, Freeze casting of porous hydroxyapatite scaffolds. II. Sintering, microstructure, and mechanical behavior, J. Biomed. Mater. Res. B Appl. Biomater. 86B (2008) 514-522.

[132] S. Meille, M. Lombardi, J. Chevalier, L. Montanaro, Mechanical properties of porous ceramics in compression: on the transition between elastic, brittle, and cellular behavior, J. Eur. Ceram. Soc. 32 (2012), 3959-3967.

[133] G. Subhash, Q. Liu, X.-L. Gao, Quasistatic and high strain rate uniaxial compressive response of polymeric structural foams, Int. J. Impact Eng. 32 (2006) 1113-1126.

[134] V.S. Deshpande, N.A. Fleck, High strain rate compressive behavior of aluminum alloy foams, Int. J. Impact Eng. 24 (2000), 277-298.

[135] W. Chen, B. Zhang, M.J. Forrestal, A split Hopkinson bar technique for low-impedance materials, Exp. Mech. 39 (1999) 81-85.

[136] D. Ghosh, M. Banda, S. Akurati, H. Kang, V. O. Fakharizadeh, On the brittle fracture characteristics of lamella walls of ice-templated sintered alumina scaffolds and effects of platelets, Scripta Mater. 138 (2017) 139-144.

[137] H. Park, M. Choi, H. Choe, D.C. Dunand, Microstructure and compressive behavior of ice-templated copper foams with directional, lamellar pores, Mater. Sci. Eng. A, 679 (2017) 435-445.

[138] A.E. Donius, A. Liu, L.A. Berglund, U.G.K. Wegst, Superior mechanical performance of highly porous, anisotropic nanocellulose–montmorillonite aerogels prepared by freeze casting, J. Mech. Behav. Biomed. Mater. 37 (2014) 88-99.

[139] M. Vural, G. Ravichandran, Dynamic response and energy dissipation characteristics of balsa wood: experiment and analysis, Int. J. Solids Struc. 40 (2003) 2147-2170.

[140] P.J. Tan, J.J. Harrigan, S.R. Reid, Inertia effects in uniaxial dynamic compression of a closed cell aluminum alloy foam, Mater. Sci. Technol. 18 (2002) 480-488.

[141] W.M. Hinckley, J.C.S. Yang, Analysis of rigid polyurethane foam as a shock mitigator, Exp. Mech. (1975) 177-183.

[142] N.C. Hilyard, Shock mitigation–material behavior, in: Mechanics of Cellular Plastics, Applied Science, London, 1982.

[143] V.P.W. Shim, K.Y. Yap, Static and impact crushing of layered foam-plate systems, Int. J. Mech. Sci. 39 (1997) 69-86.

[144] J.J. Harrigan, S.R. Reid, C. Peng, Inertia effects in impact energy absorbing materials and structures, Int. J. Impact Eng. 22 (1999) 955-979.

[145] J. Lankford, Compressive stress and microplasticity in polycrystalline alumina, J. Mater. Sci. 12 (1977) 794-796.

[146] Z. Wang, P. Li, Dynamic failure and fracture mechanism in alumina ceramics: experimental observations and finite element modelling, Ceram. Inter. 41 (2015) 12763-12772.

[147] W. Zhihua, M. Hongwei, Z. Longmao, Y. Guitong, Studies on the dynamic compressive properties of open-cell aluminum alloy foams, Scr. Mater. 54 (2006) 83-87.

[148] D.D. Luong, O.M. Strbik III, V.H. Hammond, N. Gupta, K. Cho, Development of high performance lightweight aluminum alloy/SiC hollow sphere syntactic foams and compressive characterization at quasi-static and high strain rates, J. Alloy Compounds 550 (2013) 412-422.

[149] J.P. Schramm, M.D. Demetriou, W.L. Johnson, B. Poon, G. Ravichandran, D. Rittel, Effect of strain rate on the yielding mechanism of amorphous metal foam, Appl. Phys. Letts. 96 (2010) 021906.

[150] R.A.W. Mines, Strain rate effects in crushable structural foams, Appl. Mech. Mater. 7-8 (2007) 231-236.

[151] Y.D. Liu, J.L. Yu, Z.J. Zheng, J.R. Li, A numerical study on the rate sensitivity of cellular metals, Int. J. Solids Struc. 46 (2009) 3988-3998.

[152] K.A. Dannemann, J. Lankford, High strain rate compression of closed-cell aluminium foams, Mater. Sci. Eng. A 293 (2000) 157-164.

[153] I. W. Hall, M. Guden, C.J. Yu, 2000. Crushing of aluminum closed cell foams: density and strain rate effects, Scr. Mater. 43 (2000) 515-521.

[154] F.S. Han, H.F. Cheng, Z.B. Li, Q. Wang, The strain rate effect of an open cell aluminum foam, Metall. Mater. Trans. A 36 (2005) 645-650.

[155] P. Li, N. Petrinic, C. R. Siviour, R. Froud, J. M. Reed, Strain rate dependent compressive properties of glass microballoon epoxy syntactic foams, Mater. Sci. Eng. A 515 (2009) 19-25.

[156] L. Peroni, M. Scapin, M. Avalle, J. Weise, D. Lehmhus, Dynamic mechanical behavior of syntactic iron foams with glass microspheres, Mater. Sci. Eng. A 552 (2012) 364-375.

[157] P.J. Tan, J.J. Harrigan, S.R. Reid, Inertia effects in uniaxial dynamic compression of a closed cell aluminum alloy foam, Mater. Sci. Tech. 18 (2002) 480-488.

[158] P.J. Tan, S.R. Reid, J.J. Harrigan, Z. Zou, S. Li, Dynamic compressive strength properties of aluminium foams. Part I – experimental data and observations, J. Mech. Phys. Solids 53 (2005a) 2174-2205.

[159] P.J. Tan, S.R. Reid, J.J. Harrigan, Z. Zou, S. Li, Dynamic compressive strength properties of aluminium foams. Part II – 'shock' theory and comparison with experimental data and numerical models, J. Mech. Phys. Solids 53 (2005) 2206-2230.

[160] H. Zhao, I. Elnasri, S. Abdennadher, An experimental study on the behavior under impact loading of metallic cellular materials, Int. J. Mech. Sci. 47 (2005) 757-774.

[161] A. Honig, W.J. Stronge, In-plane dynamic crushing of honeycomb. Part I: crushband initiation and wave trapping, Int. J. Impact Eng. 30 (2002) 1665-1696.

[162] S.R. Reid, C. Peng, Dynamic uniaxial crushing of wood. Int. J. Impact Eng. 19 (1997) 531-570.

[163] W. Goldsmith, J.L. Sackman, An experimental study of energy absorption in impact on sandwich plates, Int. J. Impact Eng. 12 (1992) 241-262.

[164] E. Wu, W.S. Jiang, Axial crush of metallic honeycombs, Int. J. Impact Eng. 19 (1997) 439-456.

[165] H. Zhao, G. Gary, Crushing behavior of aluminium honeycombs under impact loading. Int. J. Impact Eng. 21 (1998) 827-836.

[166] M.F. Ashby, A. Evans, N.A. Fleck, L.J. Gibson, J.W. Hutchinson, H.N.G. Wadley, Metal Foams: A Design Guide. Butterworth-Heinemann, 2000.

[167] W.E. Baker, T.C. Togami, J.C. Weydert, Static and dynamic properties of high-density metal honeycombs, Int. J. Impact Eng. 21 (1998) 149-163.

[168] J.J. Harrigan, S.R. Reid, C. Peng, Inertia effects in impact energy absorbing materials and structures, Int. J. Impact Eng. 22 (1999) 955-979.

[169] C.R. Calladine, R.W. English, Strain-rate and inertia effects in the collapse of two types of energy absorbing structure, Int. J. Mech. Sci. 26 (1984) 689-701.

[170] T.G. Zhang, T.X. Yu, A note on a velocity sensitive energy absorbing structure, Int. J. Impact Eng. 8 (1989) 43-51.

[171] L.L. Tam, C.R. Calladine, Inertia and strain-rate effects in a simple plate-structure under impact loading, Int. J. Impact Eng. 11 (1991) 349-377.

[172] X.Y. Su, T.X. Yu, S.R. Reid, Inertia-sensitive impact energy-absorbing structures Part I: Effects of inertia and elasticity. Int. J. Impact Eng. 16 (1995) 651-672.

[173] X.Y. Su, T.X. Yu, S.R. Reid, Inertia-sensitive impact energy-absorbing structures Part II: Effects of strain-rate. Int. J. Impact Eng. 16 (1995) 673-689.

[174] D. Karagiozova, N.A. Jones, A note on the inertia and strain-rate effects in Tam and Calladine model, Int. J. Impact Eng. 16 (1995) 637-649.

[175] M. Banda, D. Ghosh, Effects of porosity and strain rate on the uniaxial compressive response of ice-templated sintered macroporous alumina, Acta. Mater. 149 (2018) 179-192.

[176] J. Marx, A. Rabiei, Overview of Composite Metal Foams and Their Properties and Performance, Adv. Eng. Mater. 19(11) (2017) 1600776.

[177] A. Paul, U. Ramamurthy, Strain rate sensitivity of a closed-cell aluminum foam, Mater. Sci. Eng. A 281 (2000) 1-7.

[178] C. Xiao-qing, W. Zhi-hua, M. Hong-wei, Z. Long-Mao, Y. Gui-tong, Cell size effect on the compressive properties of aluminum foam, Metals Soc. China 16 (2006) 351-356.

[179] W. Zhihua, M. Hongwei, Z. Longmao, Y. Guitong, Studies on the dynamic compressive properties of open-cell aluminum alloy foams, Scr. Mater. 54 (2006) 83-87.

[180] J. Shen, G. Lu, D. Ruan, Compressive behaviour of closed-cell aluminium foams at high strain rates, Compos. Part B 41 (2010) 678-685.

[181] R.E. Raj, V. Parameswaran, B.S.S. Daniel, Comparison of quasi-static and dynamic compression behavior of closed-cell aluminum foam, Mater. Sci. Eng. A 526 (2009) 11-15.

[182] M.D. Goel, M. Peroni, G. Solomos, D.P. Mondal, V.A. Matsagar, A.K. Gupta, M. Larcher, S. Marburg, Dynamic compression behavior of cenosphere aluminum alloy syntactic foam, Mater. Des. 42 (2012) 418-423.

[183] J.A.S. Maria, B.F. Schultz, J.B. Ferguson, N. Gupta, P.K. Rohatgi, Effect of hollow sphere size and size distribution on the quasi-static and high strain rate compressive properties of Al-A380–Al_2O_3 syntactic foams, J. Mater. Sci. 49(3) (2014) 1267-1278.

[184] Z.Y. Dou, L.T. Jiang, G.H. Wu, Q. Zhang, Z.Y. Xiu, G.Q. Chen, High strain rate compression of cenosphere-pure aluminum syntactic foams, Scr. Mater. 57 (2007) 945-948.

[185] C. Park, S.R. Nutt, Strain rate sensitivity and defects in steel foam, Mater. Sci. Eng. A 323 (2002) 358-366.

[186] A. Rabiei, M. Gracia-Avila, Effect of various parameters on properties of composite steel foams under variety of loading rates, Mater. Sci. Eng. A 564 (2013) 539-547.

[187] Y. Alvandi-Tabrizi, D.A. Whisler, H. Kim, A. Rabiei, High strain rate behavior of composite metal foams, Mater. Sci. Eng. A 631 (2015) 248-257.

[188] U.G.K. Wegst, H. Bai, E. Saiz, A.P. Tomsia, R.O. Ritchie, Bioinspired structural materials, Nat. Mater. 14 (2015) 23-36.

[189] S.S. Peppin, J.A.W. Elliott, M.G. Worster, Solidification of colloidal suspensions, J. Fluid Mech. 554 (2006) 147-166.

[190] K.H. Zuo, Y.P. Zeng, D. Jiang, Effect of polyvinyl alcohol additive on the pore structure and morphology of the freeze-cast hydroxyapatite ceramics, Mater. Sci. Eng. C 30 (2010) 283-287.

[191] C.M. Pekor, P. Kisa, I. Nettleship, Effect of polyethylene glycol on the microstructure of freeze-cast alumina, 91 (2008) 3185-3190.

[192] Y. Zhang, L. Hu, J. Han, Z. Jiang, Freeze casting of aqueous alumina slurries with glycerol for porous ceramics, 36 (2010) 617-621.

[193] S. Deville, E. Maire, A. Lasalle, A. Bogner, C. Gauthier, J. Leloup, C. Guizard, Influence of particle size on ice nucleation and growth during the ice-templating process, J. Am. Ceram. Soc. 93 (2010) 2507–2510.

[194] S. Deville, E. Maire, G. Bernard-Granger, A. Lasalle, A. Bogner, C. Gauthier, J. Leloup, C. Guizard, Metastable and unstable cellular solidification of colloidal suspensions, Nat. Mater. 8 (2009) 966–972.

[195] D. Ghosh, M. Banda, J.E. John, D.A. Terrones, Dynamic strength enhancement and strain rate sensitivity in ice-templated ceramics processed with and without anisometric particles, Scr. Mater. 154 (2018) 236-240.

[196] I. Bae and S. Baik, Abnormal grain growth of alumina, J. Am. Ceram. Soc. 80 (1997) 1149-1156.

[197] M.P. Harmer, S.J. Bennison, C. Narayan, Microstructure characterization of abnormal grain growth development in Al_2O_3, Mater. Sci. Res. 15 (1983) 309-320.

[198] W.S. Patrick, I.B. Cutler, Grain growth in sintered alumina, J. Am. Ceram. Soc. 48 (1965) 541- 542.

[199] D.W. Susnitzky, C.B. Carter, Localization of potassium in Al_2O_3, J. Am. Ceram. Soc. 68 (1985) 569-574.

VITA

Mahesh Banda was born in Pembarthy, Janagaon, Telangana, India. He completed his Bachelor of Technology (B.Tech) in Mechanical Engineering from DRK Institute of Science and Technology (affiliated to Jawaharlal Nehru Technological University Hyderabad, India) in 2012. He earned his Master of Technology (M.Tech.) in Metallurgical and Materials Engineering from National Institute of Technology Warangal (NITW), India, in 2015. During this period, he learned fundamentals of materials science and metallurgy in NITW and carried out research on high-temperature ceramics at Bhabha Atomic Research Center, Mumbai, India.

Upon graduating from NITW, Mr. Banda joined Indian Institute of Technology Bombay (IITB), Mumbai, India for further studies. Sooner, Mr. Banda got an opportunity to pursue his Ph.D. in Mechanical Engineering at Old Dominion University, USA, under the supervision of Dr. Dipankar Ghosh. Mr. Banda successfully completed his Ph.D. dissertation in 2020.